UNIVERSITY OF BELGRADE
FACULTY OF PHYSICS

Iva Bačić

SELF-ORGANIZATION IN COUPLED EXCITABLE SYSTEMS: INTERPLAY BETWEEN MULTIPLE TIMESCALE DYNAMICS AND NOISE

Doctoral Dissertation

Belgrade, 2020

UNIVERZITET U BEOGRADU

FIZIČKI FAKULTET

Iva Bačić

SAMOORGANIZACIJA U SPREGNUTIM EKSCITABILNIM SISTEMIMA: SADEJSTVO VIŠESTRUKIH VREMENSKIH SKALA I ŠUMA

Doktorska disertacija

Beograd, 2020.

Thesis Defense Committee

Thesis advisor:
Dr. Igor Franović
Associate Research Professor
Institute of Physics Belgrade
University of Belgrade

Committee member:
Prof. Dr. Đorđe Spasojević
Professor
Faculty of Physics
University of Belgrade

Committee member:
Prof. Dr. Milan Knežević
Professor
Faculty of Physics
University of Belgrade

Committee member:
Dr. Antun Balaž
Research Professor
Institute of Physics Belgrade
University of Belgrade

"We can lift ourselves out of ignorance, we can find ourselves as creatures of excellence and intelligence and skill. We can learn to be free!"

Richard Bach, Seagull Jonathan Livingston

Acknowledgements

In addition to my own hard work and persistence, the completion of the present thesis would not have been possible without the immense support that I have received both professionally and privately.

The presented research was conducted at the Scientific Computing Laboratory of the National Center of Excellence for the Study of Complex Systems at the Institute of Physics Belgrade under the supervision of Dr. Igor Franović. Financial support for the research was provided by the Ministry of Education, Science, and Technological Development of the Republic of Serbia under the National Project ON171017 *Modeling and Numerical Simulations of Complex Many-Body Systems*, and partially by the DAAD bilateral project *Emergent dynamics in systems of coupled excitable units*.

I wish to express my appreciation to my supervisor for introducing me to the world of research, writing, and publishing, as well as for imparting his broad scientific expertise to me, providing me with the foundation upon which I will build my international scientific career. I would also like to express my gratitude to our senior collaborators from Berlin, Dr. Serhiy Yanchuk and Dr. Matthias Wolfrum, whose expertise and valuable insights, shared through numerous discussions, helped me broaden my scientific horizons. I also sincerely thank dr Antun Balaž, head of our lab, to whom I am indebted for his encouragement and assistance throughout all stages of my PhD studies.

Finally, I owe lots of gratitude to my friends and family. The support of every single one of you has been very valuable to my completion of this journey. I thank my father for teaching me the importance of erudition by setting his own example, and my mother for teaching me to aim for the stars while adamantly following my dreams.

Self-Organization in Coupled Excitable Systems: Interplay Between Multiple Timescale Dynamics and Noise

Abstract

The dynamics of complex systems typically involves multiple spatial and temporal scales, while emergent phenomena are often associated with critical transitions in which a small parameter variation causes a sudden shift to a qualitatively different regime. In the vicinity of such transitions, complex systems are highly sensitive to external perturbations, potentially resulting in dynamical switching between different (meta)stable states. Such behavior is typical for many biological systems consisting of coupled excitable units. In neuronal systems, for instance, self-organization is influenced by the interplay between noise from diverse sources and a multi-timescale structure arising from both local and coupling dynamics.

The present thesis is devoted to several types of self-organized dynamics in coupled stochastic excitable systems with multiple timescale dynamics. The excitable behavior of single units is well understood, in terms of both the nonlinear threshold-like response to external perturbations and the characteristic non-monotonous response to noise, embodied by different resonant phenomena. However, the excitable behavior of coupled systems, as a new paradigm of emergent dynamics, involves a number of fundamental open problems, including how interactions modify local dynamics resulting in excitable behavior at the level of the coupled system, and how the interplay of multiscale dynamics and noise gives rise to switching dynamics and resonant phenomena. This thesis comprises a systematic approach to addressing these issues, consisting of three complementary lines of research.

In particular, within the first line of research, we have extended the notion of excitability to coupled systems, considering the examples of a small motif of locally excitable units and a population of stochastic neuronal maps. In the case of the motif, we have classified different types of excitable responses and, by applying elements of singular perturbation theory, identified what determines the motif's threshold-like response. Regarding the neuronal population, we have established the concept of macroscopic excitability whereby an entire population of excitable units acts like an excitable element itself. To examine the stability and bifurcations of the macroscopic excitability state, as well as the associated stimulus-response relationship, we have derived the first effective mean-field model for the collective dynamics of coupled stochastic maps.

The second line of research concerns switching dynamics induced by the interplay of noise and multiplicity of timescales in small systems of locally excitable units. Our analysis, carried out on two paradigmatic models, has revealed that the coaction of noise and a large, but finite timescale separation gives rise to two different types of switching dynamics, namely slow stochastic fluctuations and stochastic bursting. In the former case, demonstrated for a motif of two adaptively coupled stochastic units with excitable local dynamics, we have found that the fluctuation forms qualitatively depend on the scale separation. In one of the scenarios, noise induces two characteristic time scales, giving rise to switching between two modes of noise-induced oscillations. Concerning the latter, by introducing the model of a stochastic excitable unit with a slowly adapting feedback, we have demonstrated that switching between metastable states derived from deterministic attractors gives rise to a bursting regime, whose stability boundaries we have calculated by introducing a new stochastic averaging method which extends singular perturbation theory to stochastic multiscale systems.

Within the third line of research, we have studied resonant phenomena in coupled systems with local dynamics near the bifurcation threshold. By considering the influence of noise on a paradigmatic model of two units with excitable or oscillatory local dynamics, we have identified two generic scenarios for the onset of inverse stochastic resonance: one based on biased switching, and the other associated with the noise-enhanced stabilization of a deterministically unstable fixed point. We have also demonstrated a novel method of efficient control of coherence resonance, showing how the effect may be enhanced or suppressed by adjusting the strength of the slowly adapting feedback.

Keywords: excitability, noise, multiscale dynamics, macroscopic excitability, switching dynamics, resonant phenomena
Scientific field: Physics
Research area: Statistical physics
UDC number: 536

Samoorganizacija u spregnutim ekscitabilnim sistemima: sadejstvo višestrukih vremenskih skala i šuma

Sažetak

Dinamika kompleksnih sistema se tipično odigrava na nekoliko prostornih i vremenskih skala, pri čemu su emergentni fenomeni često povezani sa kritičnim prelazima, pri kojima mala promena vrednosti parametra izaziva naglu i kvalitativnu promenu dinamičkog režima. U blizini takvih prelaza, kompleksni sistemi su vrlo osetljivi na eksterne peturbacije, što može izazvati dinamiku alterniranja (*switching*) između različitih (meta)stabilnih stanja. Takvo ponašanje je tipično za mnoštvo bioloških sistema sačinjenih od spregnutih ekscitabilnih jedinica, među kojima su i neuronski sistemi, kod kojih na samoorganizaciju utiču koefekti šuma iz raznolikih izvora i višestrukosti vremenskih skala koja potiče od lokalne dinamike i dinamike interakcija.

Ova disertacija je posvećena proučavanju nekoliko vrsta samoorganizujuće dinamike u spregnutim stohastičkim ekscitabilnim sistemima sa dinamikom koja se odvija na višestrukim vremenskim skalama (*multiscale* dinamika). Ekscitabilno ponašanje pojedinačnih jedinica je detaljno istraženo, kako u pogledu nelinearnog pragovskog (*threshold-like*) odgovora na eksterne perturbacije, tako i u pogledu karakterističnog nemonotonog odgovora na šum, manifestovanog kroz razne rezonantne fenomene. Međutim, pri razmatranju ekscitabilnog ponašanja spregnutih sistema kao nove paradigme emergentne dinamike, na fundamentalnom nivou postoje brojna otvorena pitanja, uključujući kako interakcije modifikuju lokalnu dinamiku rezultujući ekscitabilnošću na nivou spregnutog sistema, kao i kako sadejstvo *multiscale* dinamike i šuma dovodi do *switching*-a i rezonantnih fenomena. U ovoj disertaciji, sačinjenoj od tri komplementarne linije istraživanja, sistematično pristupamo traženju odgovora na navedena pitanja.

U sklopu prve linije istraživanja, proširili smo koncept ekscitabilnosti na spregnute sisteme, razmatrajući primere malog motiva sačinjenog od lokalno ekscitabilnih jedinica i populacije stohastičkih neuronskih mapa. U slučaju motiva, klasifikovali smo različite vrste ekscitabilnih odgovora i pokazali šta određuje pragovsko ponašanje, primenivši elemente teorije singularnih perturbacija. U slučaju populacije, uveli smo koncept makroskopske ekscitabilnosti pri kojoj se cela populacija ekscitabilnih jedinica ponaša kao ekscitabilni element. Kako bismo ispitali stabilnost i bifurkacije stanja makroskopske ekscitabilnosti, kao i odgovor sistema na perturbaciju, izveli smo prvi efektivni model srednjeg polja (*mean-field*) za kolektivnu dinamiku spregnutih stohastičkih mapa.

Druga linija istraživanja se tiče *switching* dinamike indukovane interakcijom šuma i razdvajanja vremenskih skala u malim sistemima lokalno ekscitabilnih jedinica. Sprovevši analizu na dva paradigmatska modela, pokazali smo da koefekti šuma i velikog, ali konačnog razdvajanja vremenskih skala dovode do dve vrste alternirajuće dinamike: sporih stohastičkih fluktuacija i stohastičkog burstovanja. U prvom slučaju, razmatranom na motivu koji se sastoji od dve adaptivno spregnute stohastičke jedinice sa ekscitabilnom lokalnom dinamikom, pokazali smo da forma sporih fluktuacija kvalitativno zavisi od razdvajanja skala. U jednom od scenarija, šum uvodi dve nove vremenske skale, izazivajući *switching* između dve mode oscilacija izazvanih šumom. U drugom slučaju, uvevši model stohastičke ekscitabilne jedinice sa sporo adaptirajućom povratnom spregom (*feedback*), pokazali smo da se *switching* između metastabilnih stanja izvedenih iz determinističkih atraktora manifestuje kao režim burstovanja, čije granice stabilnosti smo izračunali koristeći novi metod stohastičkog usrednjavanja, proširivši teoriju singularnih perturbacija na stohastičke sisteme sa *multiscale* dinamikom.

U sklopu treće linije istraživanja, proučavali smo rezonantne fenomene u spregnutim sistemima sa lokalnom dinamikom blizu bifurkacionog praga. Razmatrajući uticaj šuma na paradigmatski model dve jedinice sa ekscitabilnom ili oscilatornom lokalnom dinamikom, identifikovali smo dva generička scenarija za pojavu inverzne stohastičke rezonance: jedan zasnovan na neuravnoteženom *switching*-u, a drugi povezan sa stabilizacijom deterministički nestabilne fiksne tačke šumom. Pored toga, uveli smo novi metod kontrole rezonance koherencije, pokazavši kako se rezonantni efekat može pojačati ili suzbiti prilagođavanjem jačine sporo adaptirajuće povratne sprege.

Ključne reči: ekscitabilnost, šum, dinamika na višestrukim vremenskim skalama, makroskopska ekscitabilnost, switching dinamika, rezonantni fenomeni
Naučna oblast: Fizika
Uža naučna oblast: Statistička fizika
UDK broj: 536

Contents

Thesis Defense Committee **i**

Acknowledgements **v**

Abstract **vii**

Sažetak **ix**

Contents **xi**

List of Figures **xv**

1 Introduction **1**

- 1.1 Multiple timescale dynamics . . . 6
  - 1.1.1 Singular perturbation theory and slow-fast analysis . . . 7
    - 1.1.1.1 Geometric singular perturbation theory . . . 8
    - 1.1.1.2 Asymptotic singular perturbation theory . . . 11
- 1.2 The concept of excitability . . . 11
  - 1.2.1 Phenomenology . . . 11
  - 1.2.2 Dynamical features of excitable systems . . . 12
  - 1.2.3 Minimal models of excitability . . . 16
    - 1.2.3.1 Type I Excitability: The active rotator model . . . 16
    - 1.2.3.2 Type II Excitability: The FitzHugh-Nagumo model . . . 18
- 1.3 Effects of noise in excitable systems . . . 24
- 1.4 This thesis . . . 26

2 The Excitability of Coupled Systems **29**

- 2.1 Excitability of a motif of two adaptively coupled units . . . 32
  - 2.1.1 Model . . . 32
  - 2.1.2 Deterministic dynamics: stationary states . . . 33
    - 2.1.2.1 Stability of fixed points on the synchronization manifold . . . 34
    - 2.1.2.2 β-dependence of the number and stability of fixed points . . . 36
  - 2.1.3 Stimulus-response relationship and threshold-like behavior . . . 38
- 2.2 Macroscopic excitability: assembly of coupled neuronal maps . . . 39

2.2.1 Local map dynamics and the population model 40
2.2.2 Derivation of the mean-field model 43
2.2.3 Stability and bifurcation analysis for the macroscopic excitability state 47
2.2.4 Response to external stimuli 53
2.3 Chapter summary and discussion 56

3 Switching Dynamics Induced by the Interplay of Adaptivity and Noise 59
3.1 Switching in a motif of two adaptively coupled excitable units 62
3.1.1 Model and deterministic dynamics of the full system 62
3.1.1.1 Stationary states 63
3.1.1.2 The onset of oscillations 63
3.1.2 Slow-fast analysis of deterministic dynamics 65
3.1.2.1 Dynamics of the fast flow: the layer problem 65
3.1.2.2 Dynamics of the slow flow: the reduced problem 68
3.1.3 Switching dynamics 70
3.1.3.1 Switching dynamics for slower adaptation 71
3.1.3.2 Switching dynamics for faster adaptation 72
3.2 Switching in an excitable unit with a slowly adapting feedback 73
3.2.1 Model 74
3.2.2 Slow-fast analysis of deterministic dynamics 74
3.2.2.1 Stable equilibrium in the fast flow and the method of adiabatic elimination 75
3.2.2.2 Stable periodic solution of the fast flow and averaging over fast oscillations 76
3.2.2.3 Combined dynamics of the slow variable 78
3.2.3 Slow-fast analysis of stochastic dynamics: stochastic averaging approach 79
3.2.4 Switching dynamics 84
3.3 Chapter summary and discussion 87

4 Resonant Phenomena in Coupled Systems with Local Dynamics near the Bifurcation Threshold 91
4.1 ISR due to biased switching 94
4.1.1 Model and deterministic dynamics of the full system 94
4.1.1.1 The onset of emergent oscillations 95
4.1.2 Numerical results on ISR 96
4.1.2.1 Characterization of ISR 96
4.1.2.2 Biased switching as a mechanism of ISR 98
4.1.2.3 Local stability of the limit cycle attractor: the impact of scale separation 100
4.1.3 Facilitatory role of adaptivity in the resonant effect: slow-fast analysis 101
4.2 ISR due to noise-enhanced stabilization of an unstable fixed point 104

4.2.1 Model and deterministic dynamics of the full system 104
4.2.1.1 Stationary states 105
4.2.1.2 Multistability of oscillatory regimes in the full system 105
4.2.2 Slow-fast analysis 106
4.2.2.1 Layer problem: stationary states and periodic orbits of the fast flow 108
4.2.2.2 Time-reversal symmetry of the fast flow 110
4.2.3 Numerical observation of ISR and the trapping effect 112
4.2.3.1 Degradation of ISR for different rules of adaptation 113
4.3 Two mechanisms of ISR in classical neuronal models 114
4.4 Controlling CR by nonlinear feedback 116
4.4.1 Paradigmatic model for the control of CR via a slowly adapting feedback 116
4.4.1.1 Slow-fast analysis of the deterministic system 117
4.4.1.2 Slow-fast analysis of the stochastic system 118
4.4.2 Enhancing or suppressing CR by adjusting the feedback strength . . . 119
4.5 Chapter summary and discussion 121

5 Conclusions **125**
5.1 Conceptual advancements 125
5.2 Methodological advancements 127
5.3 Outlook 127

Bibliography **129**

Curriculum Vitae **143**

List of Figures

1.1 Schematic representation of adaptivity. 7

1.2 Excitable behavior illustrated by the example of neuronal dynamics: membrane potential. 13

1.3 SNIPER and supercritical Hopf bifurcation scenarios and the associated stimulus-response curves pertaining to Type I and Type II excitable behavior. 14

1.4 Dynamical regimes of the active rotator model. 17

1.5 Phase portraits and trajectories of the FHN model in the excitable and oscillatory regime. 21

1.6 Canard explosion in the FHN system. 22

2.1 Stationary values of the coupling strengths as a function of the phase difference. 35

2.2 Bifurcation diagram for the fixed points of the fast flow. 37

2.3 Modalities of the response to external perturbation for two adaptively coupled active rotators. 38

2.4 Time series and phase portraits corresponding to the spiking responses from Fig. 2.3 for system (2.1). 40

2.5 Dynamical regimes of the neuron map model (2.10). 41

2.6 Impact of noise on a single map neuron in the excitable regime. 42

2.7 Dependencies of the (a) oscillation amplitudes $A(J,\beta)$ and b(c) average inter-spike intervals $T(J,\beta)$ obtained by stochastic averaging for a network alongside analogous results for the *MF* model shown in (c) and (d). 48

2.8 The macroscopic excitability feature. 49

2.9 Comparison of $R(J)$ curves for a network and the *MF* model, alongside time series for the spiking and bursting collective modes. 49

2.10 Family of $R(J)$ curves over σ for a network of $N = 100$ neurons under fixed $\beta = 0.2$. 51

2.11 Noise-induced phenomena within the J interval in the vicinity of the deterministic threshold. 52

2.12 Comparison of $A(J,\sigma)$ and $T(J,\sigma)$ dependencies for a network and the *MF* model. 52

2.13 $R(J)$ dependencies for increasing N under fixed $(\beta,\sigma) = (0.2, 0.05)$. 53

2.14 Assembly phase resetting. 54

2.15 Stimulus-response relationship in the excitable regime. 55

3.1 Emergence of oscillations in a motif of two adaptively coupled rotators. 64

3.2 Attractors of the fast flow in a motif of two adaptively coupled active rotators. . . 66
3.3 Schematic phase portraits corresponding to the characteristic regimes of the fast flow. 68
3.4 The vector field of the slow flow obtained by taking only the stable attractors of the fast flow into account. 69
3.5 Switching dynamics under the variation of timescale separation. 71
3.6 Switching dynamics between the two modes of noise-induced oscillations (slow adaptation). 72
3.7 Time traces of the phases (a) and weights (b) associated with noise-induced switching between the coexisting attractors of the deterministic system (fast adaptation). 73
3.8 Dynamics of the fast flow of an excitable active rotator with a slowly adapting feedback. 75
3.9 Graphical solution of the fixed point equation (3.26) and scheme of the slow-fast dynamics of system (3.9). 78
3.10 Fixed points of the slow dynamics (3.17) for varying feedback strength η. 80
3.11 Average frequency $\Omega_D(\mu)$ of the fast dynamics obtained by using numerical solutions of the stationary Fokker-Planck equation. 80
3.12 Branches of fixed points of the slow dynamics for different noise values. 82
3.13 Branches of fixed points of the slow dynamics for different feedback strength values. 82
3.14 Dynamical regimes of the stochastic excitable active rotator with a slowly adapting feedback for different choices of the feedback strength. 83
3.15 Histograms of interspike intervals of the phase variable for the full system and the fast subsystem. 85
3.16 Stationary distributions sampled from numerical simulations of the full system. . 85
3.17 Long-time averages $\langle\mu\rangle_T$ obtained from numerical simulations of the full system with fixed noise intensity and varying feedback strength for different values of timescale separation. 86
3.18 The balanced switching regime illustrated by time series of the fast $\varphi(t)$ and slow $\mu(t)$ variable. 87

4.1 The onset of emergent oscillations in (4.1) for $I_0 = 0.95, D = 0$. 96
4.2 Inverse stochastic resonance in (4.1) with $I_0 = 0.95, \beta = 4.2$. 97
4.3 Stationary distribution $P(\varphi_1)$ for noise levels below, at, and above the resonant value. 98
4.4 Mean spiking rate $\langle f\rangle$ as a function of β and D for fixed $\varepsilon = 0.09$, presented as a 3D plot and a heat map. 99
4.5 (a) Fraction of time spent in the oscillatory metastable state as a function of noise. (b) and (c) Numerically estimated transition rates from the oscillatory to the quasi-stationary metastable states and *vice versa*. 99

4.6 Determinant of the Jacobian calculated along the limit cycle orbit as a function of the phase variable. 101
4.7 (a) Attractors of the fast flow (4.2) in terms of κ_1 and κ_2. (b) Vector field of the slow flow (4.3). (c) and (d) time traces of phases and couplings during the switching episode. 103
4.8 Conditional probability. 103
4.9 The dependence of the maximal real part of the eigenvalues of the two foci on timescale separation. 106
4.10 Multistability of the full system (4.5) for $I_0 = 1.05, \beta = \pi, \varepsilon = 0.01, D = 0$. 107
4.11 Numerical bifurcation diagram obtained by determining the first return times T_n to the Poincare cross-section $\varphi_1 = 4.5$ for system (4.5) with $I_0 = 1.05, \beta = \pi, D = 0$. 107
4.12 (a) Variation of the number of fixed points of the fast flow (4.7) in the (κ, I_0) plane. (b)-(c) saddle-center bifurcation scenario. 109
4.13 Multistable dynamics of the fast flow (4.7) for $I_0 = 1.05$ below and above the saddle-center bifurcation. 109
4.14 Time-reversal symmetry of the fast flow for $I_0 = 1.05, \kappa = -0.8$. 111
4.15 Observation of inverse stochastic resonance in system (4.4) with $I_0 = 1.05$. 111
4.16 Noise-induced switching between metastable states. 112
4.17 Numerically estimated fraction of time spent in the vicinity of the unstable fixed point as a function of noise. 113
4.18 Family of $\langle f \rangle (D)$ curves over $\beta \lesssim \pi$ for system (4.4) with $I_0 = 1.05, \varepsilon = 0.05$. . . . 114
4.19 Bifurcation diagrams for the Morris-Lecar model in the vicinity of the supercritical and subcritical Hopf bifurcations, along with the $\langle f \rangle (D)$ dependence for selected values for both cases. 115
4.20 Comparison between the bifurcation diagram obtained within singular perturbation theory and numerical simulations for the full system with finite scale separation. 119
4.21 Enhancement or suppression of CR by a slowly adapting feedback control. 121

Chapter 1

Introduction

The spontaneous emergence of increased organization in a system led only by its own dynamics, referred to as **self-organization**, is a fundamental feature of our world [1, 2, 3, 4]. Many forms of fascinating self-organized behavior are encountered across all scales, including the formation of planetary systems and galaxies [5], crystal growth [6], sand dunes [7], flocking behavior in birds and fish [8], the development of living organisms [9], traffic flow [10], the stock market [11], the Internet [12], and the evolution of language [13]. Brain functionality also heavily relies on self-organizing processes [14] [15], and even consciousness can be considered a result of self-organization [16] [17]. In physics, self-organization is often related to phase transitions and spontaneous symmetry breaking, typically manifested as the formation of complex spatio-temporal patterns, with examples ranging from the synchronization transition in coupled oscillators, crystal growth, and spontaneous magnetization in classical physics to superconductivity, lasers, and Bose-Einstein condensation in quantum physics [18].

The idea of order spontaneously appearing from disorder has sparked human curiosity for centuries and millennia [19]. The oldest known reference to this notion reaches back to ancient Greek philosophers, when thinkers belonging to the atomist intellectual tradition, such as Lucretius and Democritus, speculated that, given enough matter, space and time, order emerges on its own without divine intervention [20]. Centuries later, several classical philosophers including René Descartes [21], Immanuel Kant [22], and Friedrich Wilhelm Joseph von Schelling [19] also pondered over this concept. In his *Critique of Judgment* from 1787, Kant was the first to propose the term self-organization, recognizing the possibility of an organization at the systemic level which cannot be explained by reducing the behavior of the system as a whole to the behavior of its constituents. For Schelling, self-organization was essential in considerations of the philosophy of nature.

As far as contemporary science is concerned, in 1947 the cyberneticist W. Ross Ashby introduced the concept to general systems theory by applying the term "self-organizing" to describe self-induced changes in organization in determinate systems [23]. Indeed, the main contributions in the initial stages of theoretical developments came from general systems theory and cybernetics, lead by prominent theorists such as Heinz von Förster, Gordon

Pask, and Norbert Wiener [24, 25, 26, 27, 28]. During the following decades, the idea was embraced by physicists and chemists within research on phase transitions. Eventually, physical chemist Ilya Prigogine bridged the gap between general systems theory and thermodynamics with his pioneering work on self-organization in chemical systems [29], for which he was awarded the Nobel Prize in 1977 [30].

Another major contribution was provided by Hermann Haken, founder of the interdisciplinary field of "synergetics", dedicated to self-organization and pattern formation in open systems far from equilibrium [1, 2]. Alongside the development of synergetics, a new interdisciplinary field of research emerged, termed "complexity science" [3, 4]. The focal point of this discipline is the investigation of **complexity** – collective behavior which arises as a result of local interactions between constituents of a complex system, as well as the interactions of the system and its environment. Complexity characterizes diverse phenomena relevant to a wide variety of both natural and social sciences, from the climate to transportation systems to the human body. While an intuitive grasp on the notion of complexity seems quite straightforward, it is rather difficult, if not impossible, to construct an universal definition. Indeed, the definition of complexity has been the subject of many debates [31].

Despite disagreements about the precise formulation of a universal definition of complexity, there are several general features that are generally agreed upon to be common characteristics of complex systems, such as that they all consist of *interacting components* [32]. Another intrinsic feature of complex systems is **emergence**, which refers to system traits that arise exclusively due to interactions of the constituents of the system, and which cannot be inferred by considering those parts in isolation [33]. Although emergence and self-organization are closely related concepts, the following distinction should be emphasized: while emergence refers to the appearance of a novel property on a global level arising from local interactions, self-organization concerns the increase in order resulting from internal dynamics in the absence of external influences [34].

Ever since it was established that complexity is a crucial feature of systems capable of exhibiting self-organizing behavior, research on self-organization and complex systems has become deeply interwoven [4]. Since these studies typically concern systems with many degrees of freedom which are impossible to treat mathematically, the analysis often consists of a qualitative approach, significantly relying on computer simulations [35]. In the early 2000s, empirical studies of real-world complex systems motivated a convenient representation of complex systems within the framework of **networks** in which the interactions between the constituents are described by links between nodes [36, 37, 38], providing an intuitive depiction of any system consisting of related components.

The mathematical field of *nonlinear dynamics*, devoted to the qualitative behavior of nonlinear dynamical systems [39], has turned out to be essential to the study of self-organization and, in general, the dynamics of complex systems. Within nonlinear dynamics, one aims to qualitatively understand the long-term behavior of systems, classifying the stable solutions for a given set of parameters (attractors). Dynamical systems which exhibit the coexistence of several attractors are referred to as **multistable** systems [40]. If a multistable system is exposed to a sufficiently strong perturbation and/or rapid parameter change, it may **switch** between different attractors [41]. Under the action of noise, the attractors of a multistable system become **metastable states**. Sufficiently strong noise may induce large fluctuations due to which the system exhibits continuous switching between different metastable states [42].

The dynamical structure of complex systems often involves multiple characteristic timescales, whereby such **multiscale dynamics** may arise from the local dynamics of the system's constituents and/or may appear due to the dynamics of the interactions (coupling dynamics). Coupling dynamics may involve mechanisms such as feedback or adaptivity in which the system's structure adaptively reorganizes itself in response to the dynamics [43, 44, 45, 46]. Systems whose dynamics involves a strong separation of characteristic timescales are referred to as slow-fast systems within the mathematical framework of *singular perturbation theory* [47, 48, 49, 50, 51].

Let us now establish a link between the fields of nonlinear dynamics and *statistical physics*, associated with critical transitions. Critical transitions occur at so-called tipping points, where the system suddenly shifts from one stable state to another qualitatively different stable regime [41, 52, 53, 54]. While critical transitions may, on one hand, result in undesired catastrophic outcomes, on the other hand, being in the vicinity of a tipping point may also have favorable consequences. For instance, in the brain, the transition from normal to epileptic brain activity is undesired [55], while transitions which contribute to switching between mutually exclusive motor programs are desired [56].

Deeper insight into critical transitions has been provided within the theory of nonlinear dynamics by considering stochastic multiscale (slow-fast) models [57]. Within this approach, a critical transition corresponds to a bifurcation – a qualitative change in the dynamics due to a small smooth variation of system parameter(s) [39] – such that the tipping point coincides with the bifurcation condition. In the vicinity of critical transitions, complex systems are extremely sensitive to perturbations, and may, depending on the dynamical character of the transition, exhibit two qualitatively different types of fluctuations [54]. In particular, they may either exhibit slow (critical) fluctuations, featuring a slow recovery to a stable state after a perturbation, or multistable fluctuations, manifested as stochastic switching (flickering) between metastable states [52]. The two types yield qualitatively different statistics: critical fluctuations are characterized by a scale-free power-law distribution, while multistable fluctuations follow an exponential distribution akin to a Poisson process. If we invoke an analogy with statistical physics, critical fluctuations mathematically correspond to a second-order (continuous) phase transition, whereas metastable fluctuations coincide with a first-order (discontinuous) one.

One of the key examples of self-organizing phenomena in complex systems is provided by the **synchronization transition** in coupled oscillators. The synchronization transition is typically described using the Kuramoto paradigmatic minimal model [58], which has been applied to analyze problems from a wide range of disciplines, including physics [59], engineering [60], chemistry [61], and biology [62]. The Kuramoto model consists of globally coupled oscillators described by their phases, each with its intrinsic natural frequency given by a common distribution. Under the variation of the coupling strength, the model displays a second-order (continuous) transition from an unsynchronized state of phase turbulence to partial synchrony [63], corresponding to a Hopf bifurcation of the complex order parameter. From the standpoint of statistical physics, synchronization is a non-equilibrium phase transition, since the dynamics settles to non-equilibrium stationary states [64].

Having provided a general introduction to the notion of self-organization in complex systems, describing central concepts such as emergence, multiscale dynamics, multistability and switching, as well as explaining the crucial role of stochastic effects in complex dynamics, a few words should be said about emergence and self-organization in **coupled excitable systems** to which this thesis is devoted to. In general, coupled excitable systems exhibit a variety of self-organized behaviors, including oscillations, pulses and (rotating, spiral, and scroll) waves, as well as localized and propagative spatio-temporal patterns such as localized spots and periodic or chaotic patterns [65, 66]. However, the governing principles of self-organization in coupled excitable systems are different from those in coupled oscillators because in the absence of input, an excitable unit settles into a stationary state.

In conceptual terms, the excitable behavior of single units influenced by different types of noise is well understood. However, much remains to be understood about the *excitable behavior of coupled systems*, where open questions concern the details of the nonlinear threshold-like behavior, the characteristic non-monotonous response to noise (resonant phenomena), as well as noise-induced switching dynamics. In particular, in the case of populations of excitable units, an interesting problem involves the scenario in which a whole population of coupled excitable units becomes an excitable system itself, a feature relevant to both theory and applications. We will refer to this emergent phenomenon as *macroscopic excitability*. Nonetheless, an equally interesting open issue concerns the interplay of noise and adaptivity-induced multiple timescale dynamics in small motifs consisting of locally excitable units. Moreover, although it is well-known that noise plays a constructive role in a variety of applications [67], including stochastic facilitation in neural systems [68, 69, 70] which mainly involves resonant phenomena, phenomena such as coherence resonance and inverse stochastic resonance have mostly been considered in the case of single units.

Studies of these effects in coupled systems are still lacking, despite their relevance in the context of neural networks [71, 72]. Indeed, our motivation for considering coupled stochastic multiscale excitable systems arises primarily from studies of neuronal systems, such as small network motifs and neural networks, whose activity is shaped by the interaction of multiple timescale dynamics, facilitated e.g. by synaptic plasticity, and diverse sources of intrinsic or external noise. The particular **types of self-organized dynamics explored within this thesis** include:

- the excitability of coupled systems,

- synchronization of noise-induced oscillations, namely the ordering transition accounting for the onset of a collective mode via a stochastic bifurcation,
- noise-induced multistability,
- noise-enhanced stabilization of deterministically unstable structures,
- noise-induced switching, and
- resonant phenomena,

whereby the **main conceptual novelties** include

- the introduction of the notion of macroscopic excitability, and
- the discovery of generic mechanisms of inverse stochastic resonance.

From a methodological standpoint, this study relies on standard methods from nonlinear dynamics and statistical physics, including the following **analytical and numerical techniques**:

- stability and bifurcation analysis,
- multiple timescale analysis for deterministic systems,
- numerical modeling of systems of deterministic and stochastic differential equations,
- calculation of phase response curves for coupled systems, and
- the Fokker-Planck method,

as well as **newly introduced analytical methods**, such as

- the application of mean-field theory to coupled time-discrete systems, and
- stochastic averaging for the analysis of stochastic multiscale systems.

The analysis of the above-mentioned phenomena will be carried out on several models with stochastic multiple timescale dynamics. In fact, each phenomenon will be studied with reference to more than one model in order to demonstrate its generality. To this end, the following **paradigmatic models** will be taken into consideration:

- an assembly of coupled stochastic map neurons,
- a stochastic slow-fast system of two adaptively coupled units,
- a stochastic excitable unit with a slowly adapting feedback, and
- the Morris-Lecar neuron model.

The remainder of this chapter contains an overview of the fundamental concepts underlying the present thesis, whereby section 1.1 concerns *multiple timescale dynamics*, including an introduction to geometric and asymptotic singular perturbation theory. Section 1.2 concerns the *concept of excitability*, including the phenomenology and dynamical features of excitable behavior. Furthermore, *the effect of noise on excitable systems* is discussed in section 1.3. Finally, section 1.4 contains an outline of the thesis.

1.1 *Multiple timescale dynamics*

In many complex systems, the components evolve on different characteristic timescales, giving rise to various forms of multiple timescale dynamics. For instance, in neural networks, the interplay of biochemical synaptic mechanisms and electrical spiking activity gives rise to complex phenomena which involve more than one timescale [73]. Considering single neurons, the membrane potential typically changes faster than the recovery variables [74]. Similarly, the optical and electrical components of optoelectronic devices operate on different timescales [75, 76]. Additional examples of multi-timescale systems include chemical reactors [77, 78], mechanical systems [79, 80], and ecological systems [81, 82].

Generally speaking, the multiplicity of timescales may appear (i) as a feature of the *local dynamics* of a single unit, and/or (ii) due to the *coupling dynamics* of interacting units. In the latter case, the interactions between the constituents of a system are time-dependent, whereby the system's structure responds to its dynamics by adaptively reorganizing itself [43, 44, 45, 46]. The interactions typically evolve slower than the state of the system, naturally invoking a distinction between the fast local dynamics and the slow dynamics of the couplings. Nevertheless, the evolution of such systems involves a feedback mechanism in which the couplings adapt to the dynamical processes at the units, but the changes in couplings in turn influence the evolution of the units itself. This interplay, illustrated in Fig. 1.1, is referred to as *adaptivity* or adaptation.

In neuronal systems, the concept of adaptivity is embodied in *synaptic plasticity*, a biological mechanism accounting for the changes in the strength of neural connections [83]. Depending on relative spike times of presynaptic and postsynaptic neurons, synaptic strengths may increase or decrease over time, resulting in short- or long-term potentiation or depression of synapses. Synaptic plasticity makes self-organization in neuronal systems a multi-timescale process: short-term spiking activity unfolds on a quasi-static coupling configuration, while the slow adjustment of couplings depends on the time-averaged evolution of units. In the interplay of neuronal activity and synaptic dynamics, the spiking pattern influences the synaptic connections, which results in new spiking patterns. In this context, plasticity has been modeled by different rules, such as Hebbian learning and spike-time-dependent plasticity (STDP) [84, 85, 86].

Dynamical systems involving a strong separation of timescales are referred to as *slow-fast systems* and are treated within the mathematical framework of *singular perturbation theory*

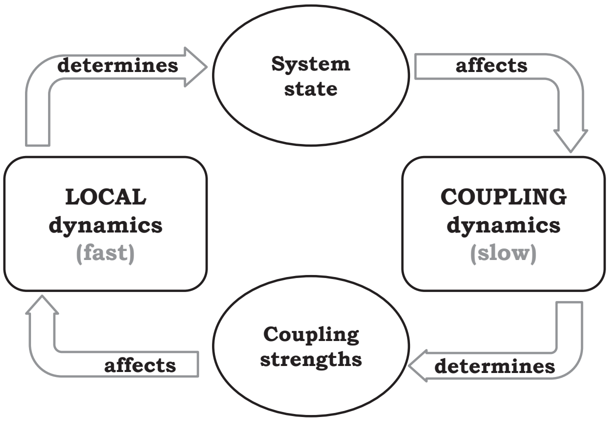

Figure 1.1: Schematic representation of adaptivity. The interplay between the local dynamics, occurring on the fast timescale, and the coupling dynamics, evolving on a slower timescale, gives rise to a feedback loop whereby the local dynamics determines the state of the system, which affects the coupling dynamics. The subsequent slow changes in coupling strengths in turn influence the system state.

[47, 48, 49, 50, 51].

1.1.1 Singular perturbation theory and slow-fast analysis

For simplicity, let us consider dynamical systems involving only two characteristic timescales, the fast and the slow one. Ordinary differential equations in which one set of variables has derivatives of a much larger magnitude than the remaining variables may be written in the following general form [47]:

$$\begin{aligned} \varepsilon\frac{d\overrightarrow{x}}{d\tau} &= \varepsilon\dot{\overrightarrow{x}} = f(\overrightarrow{x},\overrightarrow{y},\varepsilon) \\ \frac{d\overrightarrow{y}}{d\tau} &= \dot{\overrightarrow{y}} = g(\overrightarrow{x},\overrightarrow{y},\varepsilon), \end{aligned} \tag{1.1}$$

where $f : \mathbb{R}^m \times \mathbb{R}^n \to \mathbb{R}^m$, $g : \mathbb{R}^m \times \mathbb{R}^n \to \mathbb{R}^n$. The timescale separation is defined by the small positive parameter $0 < \varepsilon \ll 1$, implying that the $\overrightarrow{x}$ variables are the **fast variables**, while the $\overrightarrow{y}$ variables are the **slow variables**. By rescaling time as $t = \tau/\varepsilon$, we obtain the following equivalent formulation:

$$\begin{aligned} \frac{d\overrightarrow{x}}{dt} &= \overrightarrow{x}' = f(\overrightarrow{x},\overrightarrow{y},\varepsilon) \\ \frac{d\overrightarrow{y}}{dt} &= \overrightarrow{y}' = \varepsilon g(\overrightarrow{x},\overrightarrow{y},\varepsilon), \end{aligned} \tag{1.2}$$

such that t corresponds to the **fast timescale** while τ refers to the **slow timescale**. Both (1.1) and (1.2) are referred to as the **full system**.

It is important to emphasize that the dynamics of slow-fast systems cannot be analyzed within the framework of regular perturbation theory, where the small parameter ε would be simply approximated with zero. Rather, slow-fast systems belong to the class of singularly perturbed problems, i. e. those involving a qualitative difference between the solutions of the problem at a limiting value of the parameter and limit of the solutions of the general problem. In this case, **the singular limit** $\varepsilon = 0$ corresponds to an infinite timescale separation. Nevertheless, a natural first step in the analysis of such systems is to consider the singular limit such that the full system reduces to the fast and slow subsystems evolving on separate timescales t and τ.

1.1.1.1 Geometric singular perturbation theory

GSPT provides a framework for a mathematically rigorous treatment of solutions of singularly perturbed systems. In the singular limit, the dynamics of the full system reduces to lower-dimensional problems on the fast or the slow timescale, which are used to predict the behavior of the full system for small, but finite scale separation ε.

In particular, by setting $\varepsilon = 0$ in (1.2), we obtain the **layer problem** or **fast subsystem**, a *parametrized system of ordinary differential equations* defined on the fast timescale:

$$\begin{aligned} \overrightarrow{x}' &= f(\overrightarrow{x}, \overrightarrow{y}, 0) \\ \overrightarrow{y}' &= 0, \end{aligned} \tag{1.3}$$

whose vector flow is called the **fast flow**. The dynamics of the fast subsystem is obtained by treating the slow variables y as parameters, whereby each fixed value of y describes one "layer" of the fast subsystem.

Conversely, setting $\varepsilon = 0$ in (1.1) yields the **reduced problem** or **slow subsystem**, a *differential-algebraic equation* defined on the slow timescale:

$$\begin{aligned} 0 &= f(\overrightarrow{x}, \overrightarrow{y}, 0) \\ \dot{\overrightarrow{y}} &= g(\overrightarrow{x}, \overrightarrow{y}, 0), \end{aligned} \tag{1.4}$$

such that the corresponding vector flow is the **slow flow**. A natural way to analyze the orbits of the full system for finite $0 < \varepsilon \ll 1$ is to divide them into singular limit segments, such that, depending on the region of phase space, the dynamics of the full system converges to either the solution of the layer problem or the reduced one. Determining the dynamics of the slow flow involves time-averaging over the stable regimes of the fast flow of the layer problem. If the fast flow exhibits several attractors, multiple stable sheets of the slow flow emerge from the averaged dynamics of the different attractors of the fast flow. The initial conditions $\{\overrightarrow{x}(0), \overrightarrow{y}(0)\} = \{\overrightarrow{x_0}, \overrightarrow{y_0}\}$ must satisfy the constraint $0 = f(\overrightarrow{x}, \overrightarrow{y}, 0)$ in order to ensure the existence of the solution.

In the vicinity of the set described by the algebraic equation $f(\overrightarrow{x}, \overrightarrow{y}, 0) = 0$, referred to as the *critical set* $C_0 = \{(\overrightarrow{x}, \overrightarrow{y}) \in \mathbb{R}^m \times \mathbb{R}^n : f(\overrightarrow{x}, \overrightarrow{y}, 0) = 0\}$, a trajectory of the full system is approximately described by the solutions of the slow flow. On the other hand, sufficiently far from C_0, approximate trajectories of the full system are given by the fast flow. If C_0 is a submanifold of $\mathbb{R}^m \times \mathbb{R}^n$, C_0 is called the **critical manifold**. The proximity to C_0 determines which subsystem provides an appropriate approximation of the full system, whereas combining such singular limit segments should result in an approximated trajectory of the full system. Moreover, C_0 *is equivalent to the set of equilibria of the fast flow*. Trajectories of the layer problem approach C_0 along the **fast fibres**, such that C_0 comprises the set of base points of the fast fibres, connecting the fast and slow flow.

The structure of slow-fast systems typically involves segments where the fast dynamics unfolding orthogonal to the critical manifold dominates the slow dynamics tangential to the critical manifold. **Normal hyperbolicity** refers to the general feature of manifolds where the linearized dynamics in the orthogonal direction prevails over that in the tangential direction. In other words, perturbations applied in the direction orthogonal to the manifold grow exponentially with a larger rate than that of the exponential growth of tangential perturbations.

Considering that C_0 consists of equilibria, a subset $S \subset C_0$ is normally hyperbolic if and only if all points $p \in S$ are hyperbolic equilibria of the fast subsystem, i. e. none of the eigenvalues of the associated Jacobian matrix $D_x f(p, \varepsilon = 0)$ have zero real parts. A normally hyperbolic subset $S \subset C_0$ is **attracting** if all points $p \in S$ are *stable* equilibria of the fast subsystem (all eigenvalues have negative real parts), **repelling** if all $p \in S$ are *unstable* equilibria (all eigenvalues have positive real parts), and of **saddle type** otherwise. The slow and fast dynamics are tangent at local extrema of C_0, meaning that there is locally no separation of timescales. Although classic GSPT falls apart in such points, there are methods for desingularizing nonhyperbolic equilibrium points, such as the blow-up method [87].

Fenichel's theorem [88] establishes a correspondence between invariant manifolds obtained for $\varepsilon = 0$ and analogous invariant slow manifolds obtained for $\varepsilon > 0$. In particular, if $S \in C_0$ is normally hyperbolic, then S perturbs to $\mathcal{O}(\varepsilon)$-nearby invariant **slow manifolds** S_ε of the singularly perturbed system, whereas the flow on S_ε converges to the slow flow on S as $\varepsilon \to 0$. Note that S_ε is not unique; rather, it is a family of curves that lie within an $\mathcal{O}(e^{-\frac{K}{\varepsilon}}), K \in \mathbb{R}$ distance from each other.

Bifurcations of the layer problem result in the *loss of normal hyperbolicity* of the critical manifold since the eigenvalues of the Jacobian $D_x f(p, \varepsilon = 0)$ change sign in a bifurcation. Under certain circumstances, this results in the appearance of a special class of solutions of singularly perturbed systems. Generally, the loss of normal hyperbolicity of invariant critical manifolds often accounts for the generation of complex patterns in slow-fast systems, especially those which involve *folded critical manifolds* [89]. The fold point of a critical manifold is a **folded singularity** if it is a nondegenerate fold and an equilibrium (singular point) of the full system. Moreover, the folded singularity is **generic** if the g-nullcline (i) intersects C_0 transversally and (ii) passes through the folded singularity at nonzero speed.

The simplest example in $\mathbb{R}^2$ is provided by a parabolic critical manifold comprised of an attractive branch C^a and a repelling one C^r, separated by a fold point L in which normal hyperbolicity is lost (the layer problem undergoes a saddle-node bifurcation), i. e. $C_0 = C^a \cup L \cup C^r$. For finite ε, the corresponding slow manifolds are C^a_ε and C^r_ε. A **maximal canard** is a trajectory which lies at the intersections of the slow manifolds $C^a_\varepsilon \cap C^r_\varepsilon$ in the vicinity of a non-hyperbolic point $p \in L$. Such trajectories consist of motion along an attracting slow manifold followed by motion along a repelling slow manifold after passing near a folded singularity. In general, a **canard** is a trajectory which remains within $\mathcal{O}(\varepsilon)$ distance to a repelling slow manifold for an $\mathcal{O}(1)$ amount of time on the slow timescale $\tau = \varepsilon t$. In the singular limit, the maximal canard is unique and corresponds to a canard which stays in the vicinity of C^r for as long as it exists. However, for finite ε, the maximal canard consists of an exponentially thin layer of trajectories. Under the variation of a bifurcation parameter, the maximal canard is path-followed by tracing the solution which has the longest period. In practice, it is not easy to detect such solutions, since they appear in exponentially small regions of the parameter space. It should also be noted that *canards constitute separatrices for trajectories of the slow subsystem*, separating different forms of dynamical behavior.

Finally, let us consider one scenario of global dynamics involving canards in a planar system. Assume that a fast-slow system of the form

$$\begin{aligned} \varepsilon\dot{x} &= f(x,y,\lambda) \\ \dot{y} &= g(x,y,\lambda), \lambda \in \mathbb{R}, \end{aligned}$$

undergoes a singular Hopf bifurcation at $\lambda = \lambda_H$ (eigenvalues are singular as $\varepsilon \to 0$) and that the following holds:

(1) the critical manifold $C_0 = \{(x,y) \in \mathbb{R}^2 : f(x,y) = 0, y = h(x)\}$ is a smooth S-shaped curve comprised of normally hyperbolic attracting $C_0^{a\pm}$ and repelling C_0^r subsets connected by two generic fold points $p_\pm = (x_\pm, y_\pm)$, namely $C_0 = C_0^{a-} \cup \{p_-\} \cup C_0^r \cup \{p_+\} \cup C_0^{a+}$;

(2) p_- (p_+) is a local maximum (minimum) of h. At $\lambda = \lambda_c$, p_+ (p_-) is a generic folded singularity (generic fold point), namely

$$\begin{gathered} \frac{\partial f}{\partial x}(p_\pm,\lambda) = 0, \frac{\partial f}{\partial y}(p_\pm,\lambda) \neq 0 \\ \frac{\partial^2 f}{\partial x^2}(p_-,\lambda) > 0, \frac{\partial^2 f}{\partial x^2}(p_+,\lambda) < 0 \\ \frac{\partial g}{\partial x}(p_-,\lambda_c) \neq 0, \frac{\partial g}{\partial \lambda}(p_-,\lambda_c) \neq 0 \\ g(p_+,\lambda_c) = 0, g(p_-,\lambda) \neq 0; \end{gathered}$$

(3) at $\lambda = \lambda_c$, the slow flow fulfills $\dot{x} < 0$ ($\dot{x} > 0$) on $C_0^{a+} \cup C_0^r$ (C_0^{a-}).

The singular Hopf bifurcation at $\lambda = \lambda_H$ creates small-amplitude limit cycles of order $\mathcal{O}(\varepsilon)$, typically referred to as **subthreshold oscillations**. However, under assumptions (1)–(3), with varying λ the amplitude of the limit cycle rapidly increases at the maximal canard value $\lambda = \lambda_C$. Moreover, further variation of λ results in large-amplitude $\mathcal{O}(1)$ order **relaxation oscillations**. A relaxation oscillation converges to a singular trajectory comprised of continuous concatenations of alternating slow and fast segments forming a closed loop in the singular limit. For finite ε, limit cycles of intermediate size, between subthreshold and relaxation oscillations, are perturbations of **singular canard cycles** found for $\varepsilon = 0$. This scenario, accounting for the transition between small- and large-amplitude limit cycles, occurs within an exponentially small parameter range and is called a **canard explosion** [87, 90, 91, 92].

1.1.1.2 Asymptotic singular perturbation theory

Analytical approximations of singularly perturbed problems are derived within *asymptotic analysis*, where the goal is to obtain an asymptotic expansion of a function, describing its limiting behavior in terms of a sequence of gauge functions. A *gauge function* $\delta(\varepsilon)$ is a positive, monotonically decreasing function (as $\varepsilon \to 0$), continuously differentiable in the neighborhood of $\varepsilon = 0$. For instance, $\delta(\varepsilon) = \varepsilon^n, n \in \mathbb{N}$ is a standard choice for a gauge function. Moreover, if $\delta_{n+1}(\varepsilon) = o(\delta_n(\varepsilon))$ for all n as $\varepsilon \to 0$, then the sequence of gauge functions $\{\delta_n(\varepsilon)\}_{n=0}^{\infty}$ is called an *asymptotic sequence*. The **asymptotic expansion** of the function $v(x,\varepsilon)$ at x_0 up to order $\delta_N(\varepsilon)$ as $\varepsilon \to 0$ is given by

$$v(x_0,\varepsilon) = \sum_{n=0}^{N} a_n(x_0)\delta_n(\varepsilon) + b_N(x_0) \cdot o(\delta_N(\varepsilon)), \tag{1.5}$$

where the functions $b_N(x)$ and $\{a_n(x)\}_{n=0}^{N}$ are finite in x_0. Moreover, if (1.5) holds for all x_0 and $b_N(x)$ is a uniformly bounded function, then the uniformly valid asymptotic expansion of v up to order $\delta_N(\varepsilon)$ is given by:

$$v(x,\varepsilon) = \sum_{n=0}^{N} a_n(x)\delta_n(\varepsilon) + o(\delta_N(\varepsilon)). \tag{1.6}$$

If (1.6) holds for all $n \in \mathbb{N}$, then we have the **asymptotic series** of v:

$$v(x,\varepsilon) \sim \sum_{n=0}^{\infty} a_n(x)\delta_n(\varepsilon).$$

In general, asymptotic series are not convergent and the accuracy of the approximation is the highest only near a certain value of x_0 and for small ε. It is not possible to *a priori* determine the optimal number of terms for approximating a function with its asymptotic series.

1.2 *The concept of excitability*

1.2.1 Phenomenology

The concept of excitability refers to a system with a rest state that, when perturbed, displays **nonlinear threshold-like behavior** [74, 67].

Historically, the notion of excitability was first introduced by Norbert Wiener and Arturo Rosenblueth in 1946 within research on propagating contractions in the cardiac muscle. Without making any reference to the theory of nonlinear dynamical systems, they proposed a simple phenomenological paradigm by which all excitable systems have three characteristic states: **rest** (excitable), **excitatory**, and **refractory** [93]. Although the rest state classically refers to a stable equilibrium, it can also be a stable periodic orbit [94]. In the absence of external stimuli, an excitable system remains in the rest state. However, when perturbed, it may exhibit two qualitatively different types of behavior, whereby the introduced perturbation evokes either a small- or a large-amplitude deviation before the system relaxes to the rest state. This threshold-like response naturally invokes the following distinction:

- **subthreshold perturbations** cause a small-amplitude *linear* response after which the system rapidly relaxes back to the rest state;
- **superthreshold perturbations** evoke a large-amplitude *nonlinear* response, referred to as an excitation, whereby the system performs a large excursion in the phase space before returning to the rest state, followed by a refractory period during which the system cannot be excited again. If the rest state is a stable equilibrium, the excitation is pulse-like and referred to as a "spike".

Therefore, marginally different perturbations within a narrow range of stimuli magnitudes near the threshold may result in qualitatively different responses of the system. The concept of excitability is best understood in analogy to neuronal dynamics, as shown by the example of the membrane potential's response to external stimulus in Fig. 1.2. In the case of a subthreshold perturbation, the membrane potential exhibits a small-amplitude linear response in the form of a subthreshold (small graded) postsynaptic potential, whereas a suprathreshold perturbation elicits an order of magnitude larger, nonlinear response, generating a spike or action potential.

Since it was originally believed that the phenomenon of excitability is exclusive to biological systems, initial studies concerned the excitable behavior of biophysical systems such as nervous tissue [95], the myocardium [96], and the response of the human eye to a light stimulus [97, 98]. Nevertheless, research carried out during the following decades revealed that excitability is encountered in a much wider variety of systems. Nowadays, the concept of excitability provides a universal framework for explaining the behavior of a whole class of systems. Apart from biological systems such as neuronal networks, cardiac tissue, pancreatic beta cells, and gene regulatory networks [73, 99, 100, 101, 102], examples of excitable systems include lasers [103], semiconductors [104], models of chemical kinetics [105], social interactions [106, 107], climate dynamics [108], and earthquake faults [109].

1.2.2 Dynamical features of excitable systems

Historically, following the phenomenological paradigm of Wiener and Rosenblueth, another significant contribution to understanding excitable behavior was provided by the physiologist and biophysicist Alan Hodgkin, who proposed a *classification of excitability* in 1948 [110]. Based on purely experimental observations of the excitable response of crustacean nerves to external stimuli, Hodgkin had classified excitable behavior into distinct classes or types. This classification, relevant to this day, recognizes that the transition from small- to large-amplitude responses may be abrupt or continuous [73, 74].

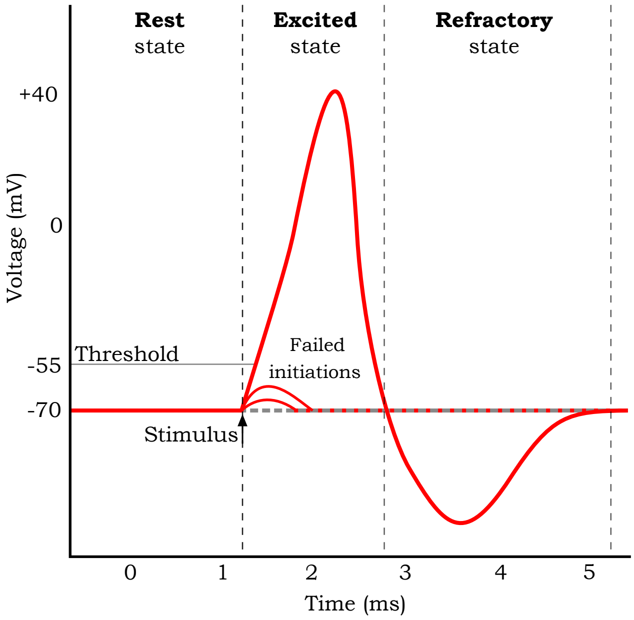

Figure 1.2: Excitable behavior illustrated by the example of neuronal dynamics. The plot shows a qualitative scheme of the membrane potential's response to stimulus, depicting three characteristic states of an excitable system: rest, excited, and refractory. Depending on whether the applied stimulus is below or above the threshold, the membrane potential displays either a linear response corresponding to subthreshold (small graded) postsynaptic potentials, or undergoes a nonlinear response in the form of an action potential or spike, followed by a refractory period during which no further spikes can be elicited.

The next milestone in the development of the theory of excitability emerged as a result of the collaborative research between Alan Hodgkin and fellow physiologist and biophysicist, Andrew Huxley, on the propagation of nerve impulses in the squid giant axon. In their legendary paper from 1952 [111], the duo provided *the first description of excitability within the framework of nonlinear dynamical systems*, having derived a mathematical model consisting of four nonlinear differential equations in order to describe the ionic mechanism of generating action potentials. For this discovery, today referred to as the Hodgkin-Huxley model, they were jointly awarded the 1963 Nobel Prize in Physiology or Medicine [112].

Several decades later, mathematicians John Rinzel and Bard Ermentrout explained Hodgkin's classification in mathematical terms by establishing a *correspondence between the different forms of experimentally observed behavior and bifurcations occurring in two-dimensional systems* [74, 113]. In general, the notion of bifurcation refers to a qualitative change in the dynamics of a system resulting from a small smooth change made to one or multiple system parameters [39]. In scenarios relevant to this thesis, the change in dynamics occurs as a result of a change in the number and stability of fixed points and limit cycles (isolated periodic solutions) in the phase space. In particular,

1. at the **saddle-node infinite period (SNIPER) bifurcation** (Fig. 1.3a), a saddle point and stable node collide and annihilate on an invariant circle, giving rise to an infinite-period limit cycle which appears as a homoclinic orbit. The SNIPER bifurcation is also

(a) **S**addle-**N**ode **I**nfinite **Per**iod bifurcation

(b) Type I excitability

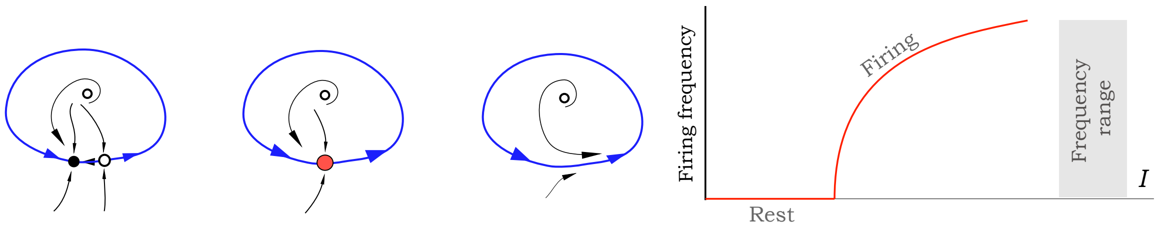

(c) Hopf bifurcation (supercritical)

(d) Type II excitability

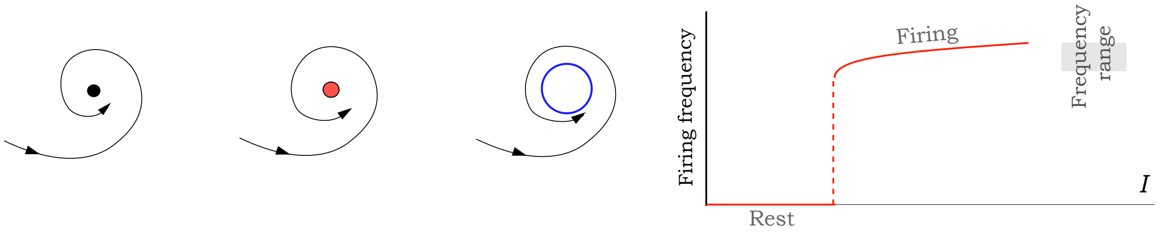

Figure 1.3: In the (a) SNIPER bifurcation scenario, two fixed points collide and annihilate on the invariant circle, giving rise to (b) Type I excitable behavior, characterized by a continuous change in firing frequencies within a wide range. On the other hand, in the (c) supercritical Hopf scenario, a small-amplitude limit cycle is born from a fixed point which loses its stability, leading to (d) Type II excitable behavior, in which the emerging limit cycle has a finite frequency assuming values from a narrow range. The figure is adapted from [73].

referred to as the saddle-node on invariant circle bifurcation.

2. in the **Hopf bifurcation** scenario (Fig. 1.3b), a fixed point changes its stability via a pair of imaginary eigenvalues as a small-amplitude limit cycle is born. Depending on the stability of the emerging limit cycle, we distinguish between the subcritical (unstable) and the supercritical (stable) Hopf bifurcation. In the former case, the stable equilibrium coexists with an unstable limit cycle, losing its stability as the unstable limit cycle engulfs it, while in the latter case, the stable equilibrium loses its stability in the bifurcation as a stable limit cycle is born.

Rinzel and Ermentrout primarily determined that the **necessary condition for observing excitable behavior in a dynamical system is that it lies near a bifurcation from the rest state to sustained oscillatory motion**. Moreover, they demonstrated that different types of bifurcations mediating the transition between stationary and oscillatory dynamics give rise to different types of excitable behavior. Based on Hodgkin's findings enriched by the mathematical characterization, we distinguish between two classes or types of excitability of a stable equilibrium, namely:

1. **Type I excitability**, which involves systems that lie close to the *SNIPER bifurcation* (Fig. 1.3a-b); and

2. **Type II excitability** (Fig. 1.3c-d), which refers to systems whose local dynamics is near the *Hopf bifurcation*.

These two mechanisms result in different dependencies of the spiking frequency on the stimulation amplitude in the vicinity of the bifurcation point, explaining Hodgkin's observations. Specifically, in Type I excitable systems, as the period of the limit cycle approaches infinity, the frequency of the oscillations becomes arbitrarily low, tending to zero. This is not the case for Type II excitable systems, in which the oscillation frequency always remains finite near the bifurcation point. Moreover, **the threshold separating small- and large-amplitude responses is more apparent in Type I than in Type II excitable systems** [74, 114]. From a mathematical point of view, thresholds are not points, but rather manifolds, whereby the mechanism of the threshold-like behavior depends on the geometric structure of the phase space of the system as follows:

1. Type I excitability involves a *separatrix* associated with *stable manifolds of saddle structures*, such as those found in the saddle-node or subcritical Hopf bifurcations. Such a structure accounts for a sharp distinction between small- and large-amplitude responses ("all-or-none" spiking), and the shape of the spike is completely independent of the stimulation properties.

2. Type II excitability, found in systems with a timescale separation, involves a *threshold manifold* or *ghost separatrix* related to the existence of *canard separatrices* [73, 74, 89, 114, 115]. Although such a structure results in a smooth crossover between the two types of responses within a narrow range of stimuli amplitudes, the system may still display a high sensitivity to perturbations given a sufficiently large timescale separation.

The details regarding the first point will be presented in section 1.2.3.1, whereas the notion of the threshold manifold will be explained within the framework of singular perturbation theory in section 1.2.3.2.

The concept of excitability has recently been extended to a relaxation limit cycle attractor [94]. In this case, the system's response to perturbations is *phase-sensitive*, i. e. non-uniform along the periodic orbit: the maximal canard provides the threshold, and the nonlinear response occurs only if superthreshold perturbations are applied to a certain part of the periodic orbit and in the appropriate direction.

Finally, regardless of the excitability type, all excitable systems share the following two **generic features**:

1. a nonlinear threshold-like response to external perturbation;

2. a non-monotonous dependence of the system's response to continuous random perturbations (*noise*).

The details concerning the second point will be elaborated in section 1.3. Here we just mention that noise may, in general, change the deterministic behavior of systems in two ways, one of which involves the crossing of thresholds or separatrices.

1.2.3 Minimal models of excitability

The generic features of excitability arise from the fact that excitable systems lie close to a bifurcation threshold. Although the specific processes accounting for the excitability of the wide variety of systems from the end of section 1.2.1 are diverse, their features are essentially alike on a fundamental level: they are all either Type I or Type II excitable.

Therefore, the significance of the classification of excitability from section 1.2.2 lies in the convenience of representing the behavior of a wider class of systems by a limited number of minimal models. Indeed, the nonlinear dynamical mechanisms responsible for *all* excitable behavior can be reduced to either the SNIPER bifurcation or the singular Hopf bifurcation, rendering it sufficient to consider only two classes of models in order to describe the entirety of excitable phenomena. This is mathematically formulated though the notion of the *normal form* of a bifurcation, i. e. the minimal dynamical system to which all other systems exhibiting this type of bifurcation are locally topologically equivalent [39].

Since the focus of this thesis concerns the mathematical properties of excitability regardless of the particular details of a system, I will consider two paradigmatic minimal models of excitability, corresponding to each excitability type.

1.2.3.1 Type I Excitability: The active rotator model

The active rotator is a simple one-dimensional model canonical for Type-I excitability. It was originally suggested by physicists Shigeru Shinomoto and Yoshiki Kuramoto in the context of the development of a statistical description of the synchronization process of a large population of oscillatory or excitable units [116]. Despite its simplicity, the active rotator model is capable of describing the behavior of an assortment of systems, including phase-locked loops in electronics, the flashing rhythms of fireflies, the mechanics of an overdamped pendulum driven by a constant torque, Josephson junctions, and lasers, to name but a few [39]. Moreover, as a one-dimensional model exhibiting the SNIPER bifurcation, it is equivalent to the biologically plausible theta model of neuronal dynamics, also known as the Ermentrout–Kopell canonical model. Although it was initially developed to describe the propagation of action potentials in the neurons of *Aplysia* sea slugs [117], it has since been applied to computational neuroscience [118, 119] as well as artificial intelligence [120].

Mathematically, the active rotator model is given by the following differential equation:

$$\frac{d\varphi}{dt} \equiv \dot{\varphi} = I - \sin\varphi \tag{1.7}$$

in which the phase state variable $\varphi \in S^1 \equiv \frac{\mathbb{R}}{2\pi\mathbb{Z}}$ is 2π-periodic, while the bifurcation parameter $I \in \mathbb{R}$ governs the local dynamics. In the context of neuroscience, φ qualitatively describes the oscillations of the neuronal membrane potential and I corresponds to the external bias current. The active rotator exhibits rather simple behavior (cf. Fig. 1.4) [73].

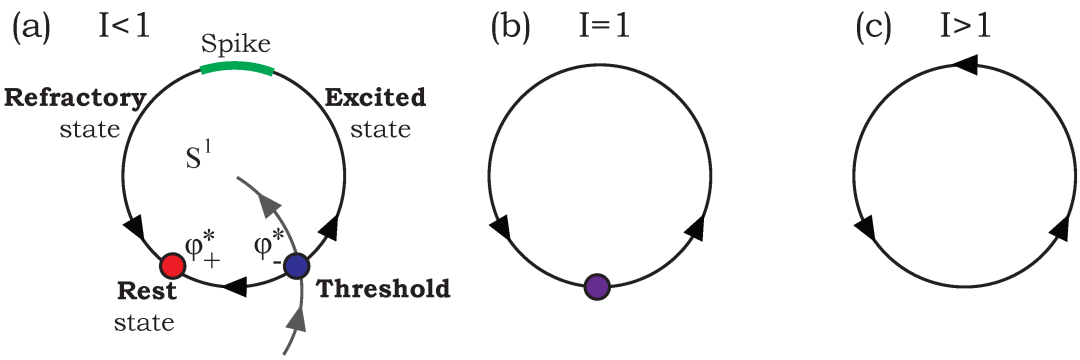

Figure 1.4: Dynamical regimes of the active rotator model (1.7) with respect to the bifurcation parameter I. The model is (a) excitable for $I < 1$, with a stable node φ_+^* corresponding to the rest state (red) and a threshold determined by the stable manifold (grey) of the saddle point (blue) φ_-^*. If φ_-^* is crossed, the system enters the excited state and emits a spike, followed by the refractory state before returning to the rest state. At (b) $I = 1$ the fixed points collide in the SNIPER bifurcation, whereas for (c) $I > 1$ the model exhibits oscillations.

Excitable regime for $I < 1$. In this regime, the system has two equilibria, a stable node φ_+^* and a saddle point φ_-^*:

$$\varphi_+^* = \arcsin I$$
$$\varphi_-^* = \pi - \varphi_+$$

corresponding to the rest state and the threshold, respectively. Small perturbations around the rest state that do not cause φ to cross the threshold value φ_-^* vanish exponentially. However, sufficiently large perturbations that lead φ beyond the stable manifold of the saddle induce a spike, whereby φ is driven to a large-amplitude excursion before returning to φ_+^*.

SNIPER bifurcation at $I = 1$. As $I \to 1^-$, the fixed points φ_+^* and φ_-^* approach each other on the invariant circle. The qualitative behavior of the system changes exactly at the bifurcation point in which the fixed points coalesce and the limit cycle becomes a homoclinic orbit to a saddle-node.

Oscillatory regime for $I > 1$. In this case, the system is a nonlinear oscillator with a unique limit cycle attractor. The oscillation period T can be obtained analytically by applying the substitution $u = tg\frac{\varphi}{2}$ to equation (1.7) as follows [39] :

$$T = \int dt = \int_0^{2\pi} \frac{dt}{d\varphi} d\varphi = \int_0^{2\pi} \frac{d\varphi}{I - sin\varphi} = 2\int_{-\infty}^{+\infty} \frac{du}{I + u^2 - 2u} = \frac{2\pi}{\sqrt{I^2 - 1}}, \qquad (1.8)$$

from which we see that the period T diverges as a square-root $(I-1)^{-1/2}$ as $I \to 1^+$, a scaling law which characterizes all systems near a saddle-node bifurcation.

The analysis presented above clarifies the origin of the well-defined threshold behavior found in Type I excitable systems: the perturbation must be strong enough to drive the system beyond the stable manifold of the saddle point; otherwise it remains in the resting state. This sharp threshold accounts for the all-or-nothing spiking response described in section 1.2.2 and explains why all realized spikes have the same shape and amplitude regardless of the form of the applied perturbation.

1.2.3.2 Type II Excitability: The FitzHugh-Nagumo model

The FitzHugh–Nagumo (FHN) model is a mathematical model of neuronal excitability. Derived by FitzHugh in 1961, the model was obtained by simplifying the Hodgkin–Huxley model to a two-dimensional system [121]. The following year, Jin-Ichi Nagumo, Suguru Arimoto, and Shuji Yoshizawa created an equivalent tunnel diode circuit [122]. Although the FHN model was initially derived in order to analyze the mathematical properties of neuronal excitability, subsequent research revealed that it can be applied to a variety of other phenomena, including excitability in Belousov–Zhabotinsky chemical reactions [123, 124, 125], cardiac arrhythmias [126], flutter and fibrillation of the myocardium [127], as well as cortisol secretion [128].

The significance of the FHN model, canonical for Type II excitability, lies in the fact that it is analytically tractable. It consists of (i) an *activator* variable x whose dynamics involves a cubic nonlinearity, and (ii) a *recovery* variable y with linear dynamics unfolding on a slower timescale, evolving according to

$$\begin{aligned} \frac{dx}{d\tau} &\equiv x' = x - \frac{x^3}{3} - y \\ \frac{dy}{d\tau} &\equiv y' = \varepsilon(x+b). \end{aligned} \tag{1.9}$$

The separation of timescales between the fast variable x and slow variable y is mediated by the small parameter $0 < \varepsilon \ll 1$, whereas the excitability of the system is controlled by the parameter b. In the context of neuroscience, the activator variable represents the membrane potential, while the recovery variable corresponds to the coarse-grained action of the potassium ion gating channels.

System (1.9) is defined on the fast timescale, whereas rescaling time as $\tau = t/\varepsilon$ yields the equivalent slow timescale formulation of the system,

$$\begin{aligned} \varepsilon\frac{dx}{dt} &\equiv \varepsilon\dot{x} = x - \frac{x^3}{3} - y \equiv \varepsilon f(x,y,\varepsilon,b) \\ \frac{dy}{dt} &\equiv \dot{y} = x + b \equiv g(x,y,\varepsilon,b). \end{aligned} \tag{1.10}$$

The system's unique fixed point FP, corresponding to the neuron's rest membrane potential

$$FP \equiv \{-b, -b + \frac{b^3}{3}\}, \tag{1.11}$$

lies at the intersection of the nullclines, curves which divide the phase plane into regions where $\dot{x}$ and $\dot{y}$ have opposing signs, namely

$$\begin{aligned} \dot{x} = 0 &\Rightarrow y = x - x^3/3 \\ \dot{y} = 0 &\Rightarrow x = -b, \end{aligned} \tag{1.12}$$

whereby the former is referred to as the *cubic* or fast nullcline, whereas the latter is the *linear* or slow nullcline. Moreover, FP is characterized by the following eigenvalues

$$\lambda_{\pm} = \frac{b^2 - 1 \pm \sqrt{(b^2-1)^2 - 4\varepsilon}}{2\varepsilon},$$

which reveal that it is stable for $|b| > 1$ and unstable for $|b| < 1$. It is sufficient to consider $b > 0$ due to the invariance of Eq. (1.9) under $(x, y, b) \to (-x, -y, -b)$. Given that $\lambda_{\pm}$ become singular when $\varepsilon = 0$, the bifurcation occurring at $b_H = 1$ has a *singular* nature. In particular, the system undergoes a singular supercritical Hopf bifurcation that gives rise to a small-amplitude stable limit cycle. Nevertheless, the system's multiscale structure gives rise to a *canard explosion* at $b_C < b_H$ in which these subthreshold harmonic oscillations exhibit a rapid transition to large-amplitude relaxation oscillations. Therefore, in order to elucidate the effect of b on the dynamical features of the FHN system, it is essential to analyze it within the framework of **geometric singular perturbation theory** [47, 89, 115, 129]. Indeed, without taking the singular nature of the FHN system into account, one can neither explain the absence of all-or-none spikes nor, consequentially, the absence of a well-defined firing threshold.

Recall from section 1.1.1 that, in the singular limit, a trajectory is comprised of continuously concatenated slow and fast segments, such that during fast motion, the trajectories of the full system converge to the solutions of the *layer (fast) problem*, obtained by setting $\varepsilon = 0$ in (1.9)

$$\begin{aligned} \dot{x} &= x - \frac{x^3}{3} - y \\ \dot{y} &= 0, \end{aligned} \tag{1.13}$$

whereas substituting $\varepsilon = 0$ into (1.10) yields the *reduced (slow) problem*, to whose solutions trajectories of the full system converge during slow motion:

$$\begin{aligned} 0 &= x - \frac{x^3}{3} - y \\ y' &= x + b. \end{aligned} \tag{1.14}$$

Moreover, the set of equilibria of (1.13) define the critical manifold,

$$C = \{(x, y) \in \mathbb{R} \times \mathbb{R} | x - \frac{x^3}{3} - y = 0\}.$$

The cubic-shaped manifold C, shown on Fig 1.5, consists of two stable (attracting) outer branches, namely the *refractory* C_R and *spiking* C_S branch, separated by an unstable (repelling) middle branch C_U. The branches are connected via two local extrema, fold points $F^{\pm}$ in which normal hyperbolicity is lost,

$$C = C_R \cup F^- \cup C_U \cup F^+ \cup C_S. \tag{1.15}$$

Trajectories of the layer problem (1.13) approach C along horizontal *fast fibres*. Note that C coincides with the cubic nullcline (1.12). The stability properties of C as a set of equilibria of (1.13) confirm that C_R and C_S are normally hyperbolic, given that

$$\begin{aligned} \frac{\partial f}{\partial x}(x,y,0,b) &= 1-x^2 < 0 \quad \text{for} \quad (x,y) \in \{C_R, C_S\} \Leftrightarrow |x| > 1, \\ \frac{\partial f}{\partial x}(x,y,0,b) &= 1-x^2 > 0 \quad \text{for} \quad (x,y) \in C_U \Leftrightarrow |x| < 1, \end{aligned} \tag{1.16}$$

while the layer problem undergoes saddle-node bifurcations at $F^{\pm} = (x^{\pm}, y^{\pm}) = (\pm 1, \pm\frac{2}{3})$, where the flow changes direction, such that

$$\begin{aligned} \frac{\partial f}{\partial x}(x^+,y^+,0,b) &= 1-x^2 = 0, \quad \frac{\partial^2 f}{\partial x^2}(x^+,y^+,0,b) = -2x^+ = -2 < 0 \\ \frac{\partial f}{\partial x}(x^-,y^-,0,b) &= 1-x^2 = 0, \quad \frac{\partial^2 f}{\partial x^2}(x^-,y^-,0,b) = -2x^- = 2 > 0, \end{aligned} \tag{1.17}$$

whereby the fold point F^- coincides with FP (1.11) for $b = 1$. Moreover,

$$\begin{aligned} \frac{\partial g}{\partial x}(x^+,y^+,0,b_C) &= 1 \neq 0, \\ \frac{\partial g}{\partial b}(x^+,y^+,0,b_C) &= 1 \neq 0, \\ g(x^-,y^-,0,b_C) &= x^- + b_C = -1 + b_C = 0, \\ g(x^+,y^+,0,b) &= x^+ + b = 1 + b \neq 0, \end{aligned} \tag{1.18}$$

from which we derive the condition $b_C = 1$. The slow flow is restricted to motion along C, i. e. $y = x - \frac{x^3}{3} \equiv \Phi(x)$. Considering

$$y = \Phi(x) \;\Rightarrow\; \dot{y} = \dot{x}\Phi_x^{'}(x) = g(x, \Phi(x), b, 0) \;\Rightarrow\; \dot{x} = \frac{g(x, \Phi(x), b, 0)}{\Phi_x^{'}(x)},$$

the following holds for the slow flow at $b = b_C = 1$:

$$\dot{x}|_{b=b_C} = \frac{1+x}{1-x^2} = \frac{1}{1-x} \Rightarrow \begin{cases} \dot{x} < 0 & \text{for} \quad x > 1 \Leftrightarrow (x,y) \in C_S \\ \dot{x} > 0 & \text{for} \quad x < 1 \Leftrightarrow (x,y) \in C_R \cup C_U, \end{cases}$$

implying that the slow flow changes direction in F^+.

Eqs. (1.15), (1.16), (1.17), (1.18), (1.19) fully determine the geometry of the phase space. Furthermore, the FHN model satisfies the conditions for the existence of a *canard solution* as well as those for a *canard explosion* at $b = b_C$, both of which crucially influence the dynamics of the non-singular FHN system: in the excitable regime, a canard-like trajectory accounts for the system's threshold-like response to perturbation, while in the oscillatory regime, the canard explosion gives rise to large-amplitude relaxation oscillations.

Let us now consider the dynamical regimes of the FHN system in detail [129, 130], see Fig. 1.5.

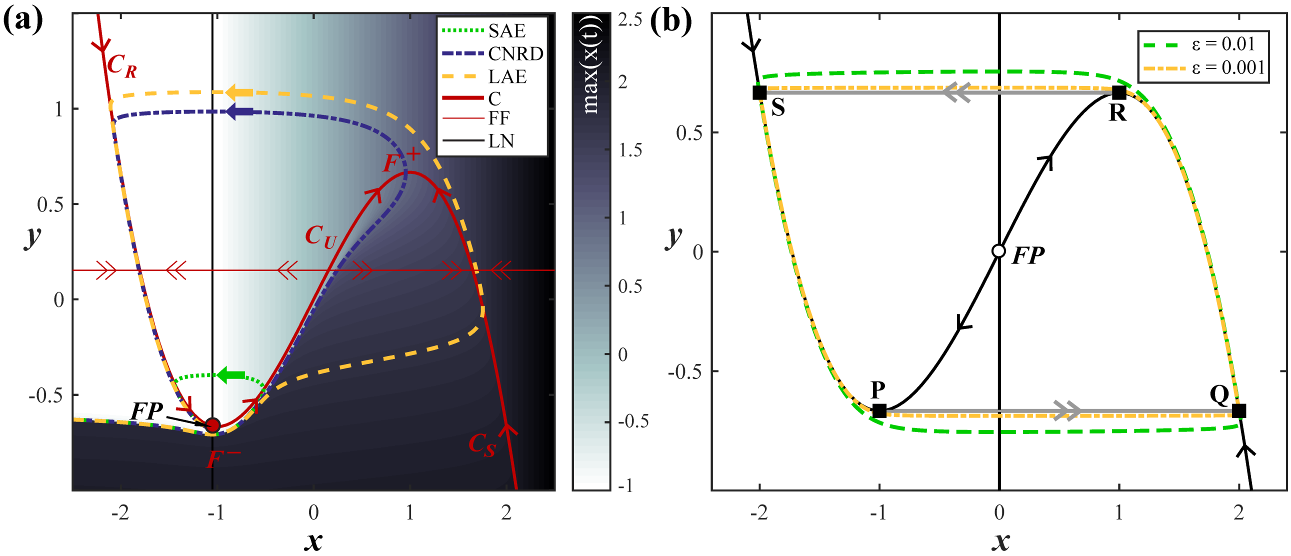

Figure 1.5: Phase portraits and trajectories of the FHN model in the (a) excitable and (b) oscillatory regime. The background of subplot (a) shows the model's response in terms of $max(x)$ depending on the initial conditions $\{x(0), y(0)\}$, demonstrating the absence of all-or-none spikes (obtained for $\varepsilon = 0.05, b = 1.05$). The trajectories are obtained by varying $y(0) \in \{-0.6204, -0.620482000763042, -0.6206\}$ with fixed $x(0) = -3$, for SAE, LAE and $CNRD$ (small-, large-amplitude responses, and a canard-like trajectory accounting for the threshold, respectively). Slow motion occurs along the critical manifold C, comprised of the stable refractory C_R, unstable C_U, and stable spiking C_S branches, connected by fold points $F^{\pm} = (\pm 1, \pm\frac{2}{3})$, whereas fast motion occurs along the horizontal fast fibres FF. Arrows indicate the direction of motion. The linear nullcline LN intersects the cubic nullcline (which coincides with C) at the fixed point $FP = (-b, -b + \frac{b^3}{3})$. Subplot (b) shows the phase portrait for $b = 0$ with two relaxation oscillation trajectories, obtained for $\varepsilon \in \{0.001, 0.01\}$. The unstable FP lies at the intersection of the nullclines. Between the turning points P and Q, as well as R and S, the system rapidly jumps between the branches along the fast fibres in the direction indicated by the arrows, while motion along the branches is much slower.

Excitable regime for $b > 1$. The stable focus FP (1.11), as the sole attractor, is the rest state. When perturbed, the system typically displays either a small-amplitude excitation (SAE, green curve on Fig 1.5a)) or large-amplitude excitation or spike (LAE, yellow curve), whereby the threshold separating the SAE and LAE is not as clearly defined as it is in Type I excitability. Indeed, the Hopf bifurcation does not provide an object which could account for a well-defined boundary, such as the stable manifold of the saddle in the previously considered class of models.

Nevertheless, the details of the threshold-like response can be explained by considering the singular limit where global trajectories consist of continuously concatenated solutions of the layer and reduced and problems, cf. Fig 1.5a). Starting from initial conditions away from FP, any trajectory will first rapidly approach an attracting segment of C along a fast fibre (layer problem), forming a new initial condition for the slow dynamics on C (reduced problem). For $\varepsilon = 0$, the threshold separating SAE and LAE is a canard trajectory which follows C_U and separates nearby trajectories into those that sharply diverge to the left or

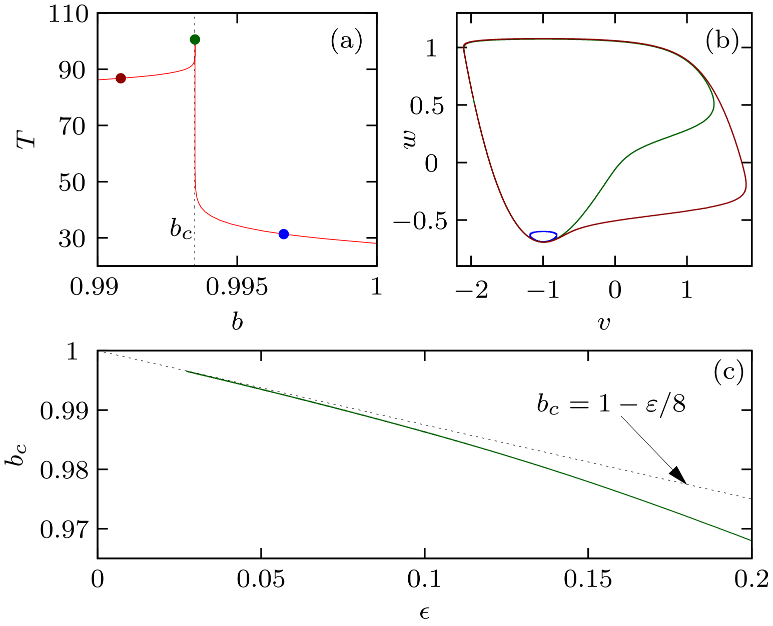

Figure 1.6: Canard explosion in the FHN system, adopted from [131]. Subplot (a) shows the dependence of the period T on b for fixed $\varepsilon = 0.05$, (b) contains the phase portraits of a subthreshold oscillation ($b_C < b < b_H$, blue), the canard trajectory ($b = b_C$, green), and a relaxation oscillation ($b > b_C$, red), whereas (c) shows a comparison of the $b_C(\varepsilon)$ dependence obtained by path-following of the canard solution (green solid) and the asymptotic formula Eq. (1.19) (black dashed). Symbols in (a) denote chosen b values for (b).

right of the canard, reaching either the refractory C_R or spiking C_S branch. In other words, the canard is a separatrix for solutions of the reduced problem, such that, depending on the position of the base point of the fast fibre relative to the singular canard trajectory, the system exhibits

- either a **SAE**, in which the trajectory returns to FP before reaching the spiking branch C_S, such that a singular global trajectory consists of motion along C_U, followed by a rapid jump via a fast fibre to C_R, along which it approaches FP;
- or a **LAE (spike)**, whereby the trajectory involves partial motion along C_S before returning to FP, such that it consists of motion along C_U, followed by a jump via a fast fibre to C_S, along which it slowly moves to F^+, from where it jumps along a fast fibre back to C_R, from where it reaches FP.

When the timescale separation is finite $0 < \varepsilon \ll 1$, the system inherits a so-called "ghost separatrix" structure from the singular limit [114], comprised of an exponentially thin layer of trajectories around C_U. Such canard-like trajectories ($CNRD$, blue curve in Fig 1.5a)) follow C_U and separate (a) trajectories which jump along the fast fibres to the left to C_S and produce a spike or LAE from (b) those that jump along the fast fibres to the right to C_R, resulting in a SAE. Given a sufficient separation of timescales, the system still displays a high sensitivity to perturbations, allowing the approximation of the ghost separatrix by a threshold in the conventional sense. Therefore, canards and repelling slow manifolds approximate the spiking threshold [74], explaining the absence of a well-defined spiking threshold in the FHN model. Although the crossover between these two types of responses is continuous, intermediate-amplitude responses of the system are rather difficult to detect. FitzHugh himself had observed this behavior, calling it the“quasi-threshold” [132], whereas he named the region of the phase plane which contains trajectories starting in the vicinity of the quasi-threshold “No Man’s Land”.

Let us now consider the absence of an all-or-none spiking response. The background of Fig. 1.5a) shows the peak value of the activator variable x depending on the initial conditions $\{x(0), y(0)\}$, such that dark regions indicate a LAE whereas white regions indicate a SAE, clearly indicating that the model exhibits a continuous but rapid blow-up of $max(x(t))$ in a small region near C_U, corresponding to intermediate-amplitude responses. See [133] for an overview of such behavior in other neuronal models.

Supercritical *singular* Hopf bifurcation at $b = b_H = 1$. As FP loses its stability, $FP = F^-$, and a small-amplitude harmonic limit cycle characterized by an ε-dependent period and amplitude of orders $\mathcal{O}(1/\sqrt{\varepsilon})$ and $\mathcal{O}(\varepsilon)$, respectively, emerges around FP.

Oscillatory regime for $b < 1$. The now unstable focus FP has crossed F^-, moving from C_R to C_U, whereas the stable limit cycle accounts for self-sustained oscillatory motion, derived from the local features of the unstable focus. Nevertheless, such a limit cycle persists only for a narrow range of values $b < b_H$, whereas further reducing b leads to a blow-up of the oscillation amplitude to the order $\mathcal{O}(1)$, accompanied by a change in the order of the period from $\mathcal{O}(1/\sqrt{\varepsilon})$ to $\mathcal{O}(1/\varepsilon)$. Specifically, considering (a) a cubic shaped critical manifold $C = C_R \cup F^- \cup C_U \cup F^+ \cup C_S$ such that C_R, C_S (C_U) are normally hyperbolic attracting (repelling), whereby (b) $F-$ ($F+$) is a folded singularity (generic fold point), and that (c) at $b = b_c$ the slow flow on C changes direction in $F+$ such that $\dot{x} < 0$ for $(x, y) \in C_S$ and $\dot{x} > 0$ for $(x, y) \in C_R \cup C_U$, the system fulfills the conditions for a *canard explosion* at $b = b_C$ (recall section 1.1.1 and conditions given by Eqs. (1.15), (1.16), (1.17), (1.18), (1.19)). In the singular limit, $b_C = b_H = 1$, but for $0 < \varepsilon \ll 1$, $b_C < b_H$, accounting for an abrupt increase in the amplitude of the limit cycle born in the Hopf bifurcation [134, 135, 136], see Fig. 1.6(a)-(b). The first-order asymptotic approximation for $b_C(\varepsilon)$ is given by [137, 138],

$$b_C \approx 1 - \frac{\varepsilon}{8}. \tag{1.19}$$

whereas Fig. 1.6(c) shows a comparison of analytically calculated and numerically obtained results. Nevertheless, periodic solutions of intermediate amplitude (canard cycles) are hard to detect because they occur only for a narrow range of values. Neuroscientifically, the canard explosion accounts for a transition route from rest to spiking through subthreshold oscillations.

The large-amplitude limit cycle, as a relaxation oscillation, consists of segments of slow and fast motion. In contrast to the local nature of harmonic oscillations born in the supercritical Hopf bifurcation, relaxation oscillations arise from the global structure of the phase space. In the singular limit, see Fig. 1.5 b), the relaxation trajectory involves turning points of the trajectory, namely $\{P, Q, R, S\} = \{(-1, -\frac{2}{3}), (2, -\frac{2}{3}), (1, \frac{2}{3}), (-2, \frac{2}{3})\}$, such that slow motion is confined to the slow manifold ($Q \rightarrow R$ and $S \rightarrow P$), whereas fast motion consists of the trajectory jumping along the fast fibres between different parts of the slow manifold ($P \rightarrow Q$ and $R \rightarrow S$) in the direction indicated by the gray arrows. With increasing ε, the fast segments of the trajectory deviate from those obtained in the singular limit, and the system "overshoots" the horizontal straight line in the vicinity of the turning points, extending the oscillation period T (cf. trajectories in Fig. 1.5 b) for different ε). Nevertheless, the $T(b)$ dependence may be approximated by neglecting the fast transitions and including only the motion along the slow manifold, cf. Eq. (1.14), namely

$$y = x - \frac{x^3}{3} \Rightarrow \dot{y} = \dot{x}(1 - x^2) = x + b \Rightarrow \dot{x} = \frac{x + b}{1 - x^2}.$$

The system spends T_S and T_R amounts of time on the spiking branch and refractory branch, respectively,

$$\begin{aligned} T_S &= \int_2^1 dx \frac{x + b}{1 - x^2} = (b^2 - 1) \ln \frac{b + 2}{b + 1} - b + \frac{3}{2} \\ T_R &= \int_{-2}^{-1} dx \frac{x + b}{1 - x^2} = (b^2 - 1) \ln \frac{b - 2}{b - 1} + b + \frac{3}{2}, \end{aligned}$$

yielding the following estimation for the period of oscillations:

$$T = T_S + T_R = (b^2 - 1) \ln \frac{b^2 - 4}{b^2 - 1} + 3.$$

Although with increasing ε this formula predicts a shorter period compared to that obtained from numerical simulations, it turns out that the additional time has a similar dependence on b, allowing one to rescale the period with a constant parameter $e \in \mathbb{R}$ as follows [129]

$$T = \left((b^2 - 1) \ln \frac{b^2 - 4}{b^2 - 1} + 3 \right) (1 + e).$$

1.3 *Effects of noise in excitable systems*

The dynamics of far-from-equilibrium systems inherently involves fluctuations or noise, which may originate from the embedding environment (external sources) or describe the system's inherent fluctuations (intrinsic sources) [67]. Moreover, noise may derive from coarse-graining over the degrees of freedom associated with small spatial and temporal scales. In excitable systems, instances of internal fluctuations include the quasi-random release of neurotransmitters by the synapses in neurons, quantum fluctuations in lasers [139], and finite-size effects in chemical reactions [140]. On the other hand, an example of external noise is provided by synaptic bombardment in which each neuron is impacted by a large number of uncorrelated presynaptic inputs [141].

The deterministic behavior of excitable systems is rather well understood. However, given that noise may substantially modify their nonlinear threshold-like behavior, many issues concerning the effects of noise on such systems still remain open. Since noisy signals consist of successive sub- and super-threshold perturbations occurring in an unpredictable fashion, excitable systems are considerably sensitive to the influence of noise. Indeed, noise-induced fluctuations may give rise to a variety of dynamical behaviors, essentially influencing systems by [67]:

1. either *modulating the deterministic behavior* by acting non-uniformly on different states of the system thus amplifying or suppressing some of its features; or
2. *giving rise to completely novel forms of behavior*, typically based on crossing the thresholds or separatrices, or involving an enhanced stability of deterministically unstable structures.

In particular, the key effects of noise in excitable systems include:

1. the onset of **noise-induced oscillations** [142, 143, 144, 145, 146, 147, 148]; and
2. different types of **resonant phenomena**, manifested as a characteristic non-monotonous dependence on the noise level, associated with noise introducing a new characteristic timescale to the dynamics.

Under certain circumstances, noise may increase the coherence or regularity of the system's dynamics [149]. For instance, in excitable systems exhibiting *noise-induced oscillations*, a notable example is *coherence resonance* (CR), in which the regularity of noise-induced oscillations becomes maximal at an optimal noise intensity [149, 150, 151, 152, 153, 154, 155, 156]. The prevalence of CR is well established for the case of single excitable units, coupled stochastic units [157], as well as at the level of collective variables in coupled systems [158]. CR has been found in a variety of neural models, laser models, excitable biomembrane models and climate models, and has been experimentally observed in systems as diverse as electronic circuits, laser diodes, excitable chemical reactions, and the cat's cortical dynamics [108, 159, 160, 161, 162, 163, 164, 165, 166, 167, 168, 169, 170]. The mechanism of the effect relies on a particular balance between the noise-dependent variabilities of the (i) activation process, which describes the escape from the vicinity of the stable equilibrium, and the (ii) relaxation process, which corresponds to the return to the fixed point [67]. CR is observed when the noise intensity is simultaneously large enough to ensure a short activation time and small enough to maintain the deterministic nature of the relaxation process.

Another resonant phenomenon appearing in noisy dynamics of a single excitable unit is *self-induced stochastic resonance* (SISR) [171]. While both CR and SISR lead to increased coherence in the system, the underlying mechanisms are different, due to the fact that noise perturbs the deterministic slow-fast structure of the underlying system in a different way.

A more recent development concerns the observation of resonant phenomena in oscillating units near the bifurcation threshold. In contrast to the previously considered excitable regime in which such phenomena involve noise-induced oscillations, in this scenario, resonant effects are related to *noise-perturbed oscillations*. A curious example of such behavior is *inverse stochastic resonance* (ISR), where the frequency of noise-perturbed oscillations becomes minimal at an optimal noise intensity [94, 68, 172, 173, 174, 175, 176, 177, 178]. In ISR, the effect of noise is inhibitory: it may either induce bursting-like behavior in which oscillations are interrupted with quiescent episodes, or completely quench the oscillations. Such an inhibitory effect of noise has recently been explicitly corroborated for cerebellar Purkinje cells [178, 179, 42, 180]. Moreover, ISR has been indicated to play important functional roles in neuronal systems, including the reduction of spiking frequency in the absence of neuromodulators, suppression of pathologically long short-term memories, triggering of on-off tonic spiking activity, and even optimization of information transfer along the signal propagation pathways [68, 174, 176, 178].

1.4 *This thesis*

Having introduced the fundamental concepts underlying this thesis, we shall now provide an outline of its contents. The complementary directions of research which the thesis is comprised of concern **three groups of emergent phenomena**, namely:

1. the excitability of coupled systems,
2. switching dynamics induced by the interplay of adaptivity and noise, and
3. resonant phenomena in coupled systems with local dynamics near the bifurcation threshold.

The remainder of the thesis consists of three chapters, each devoted to one group of considered emergent phenomena, followed by a final concluding chapter. Since different aspects of the same models are relevant to phenomena explored in particular chapters, there is a partial overlap between the chapters in the sense that certain analyses rely on previously presented results. The outline of the thesis is as follows.

Chapter 2 addresses the problem of extending the notion of excitability to coupled systems by considering the following issues:

- the excitable dynamics of an adaptively coupled motif of two locally excitable units, and
- the *macroscopic excitability* feature in a population of stochastic map neurons,

where the fundamental question is how interactions modify the local excitability feature. In the former case, our analysis concerns deterministic excitable regimes of two adaptively coupled active rotators [181, 182, 183, 184], whereby our goal is to classify the modalities of the system's response to external perturbation and explain them in terms of bifurcation analysis. These results have been published in [181].

Concerning macroscopic excitability, we have derived a mean-field approach in order to systematically analyze the emergent behavior, underlying bifurcations, and the stimulus-response relationship of a population of stochastic map neurons, whereby the derivation of the effective model relies on a cumulant approach complemented by the Gaussian closure hypothesis [67, 185, 186, 187, 188, 189, 190]. Our goal here will be to demonstrate that the reduced model captures the qualitative and quantitative features of the spontaneous and induced collective dynamics of the exact system. These results have been published in [191].

Chapter 3 presents a systematic analysis of stochastic switching arising due to the interplay of multiple timescale dynamics and noise. To this end, we investigate two simplified yet paradigmatic models that incorporate three basic ingredients of neurodynamics, namely, excitability, plasticity, and noise. The considered systems include:

- two adaptively coupled stochastic active rotators; and
- a self-coupled stochastic active rotator with slowly adapting feedback.

In the case of two coupled rotators, our central discovery is the appearance of slow stochastic fluctuations, whereby their form qualitatively depends on the scale separation between the fast and the slow variables. These results have been published in [181]. The analysis of the deterministic structure of the system, as well as our methods for obtaining a qualitative insight into the mechanisms guiding the switching dynamics, rely on geometric singular perturbation theory.

In the case of the self-coupled stochastic active rotator with adaptation, our main finding is that the system is capable of displaying stochastic bursting due to noise-induced switching. We have explained the mechanism behind the stochastic bursting regime, its stability boundaries, and the means of controlling its features by introducing a novel method of stochastic averaging. These results have been published in [192].

Chapter 4 is devoted to the investigation of resonant phenomena in small motifs of units whose local dynamics is set close to the bifurcation threshold. Essentially, the goal of this chapter is to extend previous research of non-monotonous responses to noise in single units presented in section 1.3. In particular, we investigate:

- new generic scenarios for *inverse stochastic resonance* (ISR) in two adaptively coupled stochastic active rotators; and
- *coherence resonance* (CR) in a stochastic active rotator with slowly adapting feedback.

Concerning ISR, we have discovered two generic mechanisms of the effect, whereby one is based on biased switching between metastable states associated with coexisting attractors of the corresponding deterministic system, whereas the other is due to noise-enhanced stabilization of a deterministically unstable fixed point. Moreover, by showing that the same phenomena can be found in a single Morris-Lecar unit, we have established that the effects are independent on the excitability class. These results have been published in [193, 194].

As far as the latter point is concerned, we have introduced a novel method of control of CR in excitable systems via a slowly adapting feedback. The control mechanism has been explained by extending the methods of multiscale analysis to stochastic systems. These results have been published in [192].

Finally, **Chapter** 5 concludes the thesis by summarizing the main conceptual and methodological advances of the presented results and providing an outlook for future research.

Chapter 2

The Excitability of Coupled Systems

One method of exciting an excitable unit is by coupling it to other units. Systems comprised of interacting excitable elements – widely encountered in physics, chemistry, and biology – are capable of exhibiting a rich variety of self-organizing phenomena in which novel features emerge at the collective level [195]. Spatially coupled excitable units comprise excitable media, capable of supporting localized or propagative patterns. In general, coupling in networks or arrays (spatially distributed systems) may give rise to oscillations, manifested either as the onset of collective mode or cluster states; pulses; wavefronts and circular, spiral, and scroll waves; as well as patterns such as localized spots, periodic and chaotic spatio-temporal patterns [65, 66]. Another interesting discovery concerns chimera states, characterized by coexisting domains of spatially coherent and incoherent dynamics, recently found in nonlocally coupled excitable systems [196]. Given the prevalence of coupled excitable systems, investigating their collective behavior is relevant to a broad range of fields, whereby understanding the emergent features of such systems requires going far beyond the analysis of constituent elements. The fundamental question to which this chapter is devoted to is how interactions modify the local excitability feature.

In neuroscience, for instance, gaining a comprehensive understanding of the emergent dynamics of neuronal populations and their interactions is a topical issue [71, 72]. According to contemporary neuroscientific paradigms, the key functional unit of the mammalian CNS is comprised of distributed ensembles of neurons rather than single neurons [197]. Indeed, the brain is a complex system characterized by a nontrivial hierarchical organization over multiple temporal and spatial scales, whereby neurobiological research indicates that processes occurring at different organizational levels are distributed across anatomically segregated, but functionally integrated moduli [14, 198, 199].

Nevertheless, although excitability is well-understood at the level of individual units, the excitable behavior of interacting systems remains an open problem. In this context, the present chapter concerns the following fundamental questions:

1. Can excitability be found at the level of coupled systems, i.e. does macroscopic excitability exist? If yes, how does it relate to local excitability features? In particular, how do interactions modify local excitability and what are the differences between

macroscopic and microscopic excitability?

2. What determines the nonlinear threshold-like behavior of coupled systems?
3. What are the stability boundaries of such an excitable state and which bifurcations account for the transitions to other states? Can one derive a reduced model to identify the conditions giving rise to collective excitability?

As a first step, it seems reasonable to study the influence of coupling on the excitable behavior of a small network *motif*. Motifs are basic building blocks of complex networks, consisting of a small number of coupled elements [14, 200]. In neurobiology, for instance, a single structural motif can support multiple functional motifs [201, 202, 203, 204], each characterized by a particular weight configuration and direction of information flow. Bridging the gap between research on individual excitable units and our understanding of the excitability of coupled systems, this chapter concerns

1. the **excitability of an adaptively coupled motif** of two locally excitable units [181]; and
2. the **macroscopic excitability** feature in a population of locally excitable elements [191].

The main motivation for studying problem (1) comes from neuroscience, where network motifs of just a few neurons involve synaptic connections whose strength is slowly modified by synaptic plasticity, dependent on the averaged dynamics of pre- and postsynaptic neurons. Although our setup is simple, it is also paradigmatic: the active rotator model is canonical for Type I excitability, whereas the chosen phase-dependent adaptivity rule mimics the typical properties of synaptic plasticity [182, 205, 206, 207]. The considered system can be interpreted as a binary neuron motif.

Our aim regarding problem (1) is to (i) determine which plasticity rules facilitate the excitability of the coupled system, as well as (ii) understand the details of the associated threshold-like behavior. Our results indicate that the threshold-like behavior is determined by the manifolds of the saddle structures of the coupled system. It turns out the system is capable of displaying several distinct types of responses to external perturbation, characterized by different patterns with respect to the spiking of individual units. We explain the modalities of the system's response to external perturbation in terms of the interplay of the thresholds of individual units and asymmetry in the coupling.

A detailed analysis of this issue is provided in section 2.1, which is organized as follows. The details of the model are introduced in section 2.1.1, whereas section 2.1.2 contains a detailed analysis of deterministic dynamics, focusing on the stationary states which may exhibit excitable behavior. The final section 2.1.3 provides a classification of the different excitable regimes displayed by the binary motif.

Problem (2), considering a population of excitable neurons, concerns a population of coupled stochastic maps, which may be considered as a model of a mesoscopic neuronal population. At the level of collective dynamics, an important open issue relevant to both theoretical and experimental considerations involves the macroscopic excitability scenario in which a whole population of excitable units acts as an excitable element itself. The idea of macroscopic excitability is analogous to an often-invoked paradigm in nonlinear dynamics by which a population of coupled oscillators displaying a collective mode is treated as a macroscopic oscillator [208]. Within this approach, the goal is to describe the collective mode by developing a reduced and analytically tractable description of the population's behavior based on different forms of mean-field (*MF*) approximations. This is typically done by applying a bottom-up strategy [209], starting from a high-dimensional system of (stochastic) differential equations which describes local neuronal dynamics.

The *MF* approach and its generalization to spatially extended systems have become a standard tool for analyzing diverse problems in neuroscience and other fields [210, 211, 212, 213, 214, 215, 216]. Nevertheless, it has thus far been applied only to systems described by coupled ordinary or delay differential equations, while effective models for assemblies of coupled maps have been lacking. In particular, although the collective motion of spiking or bursting neurons influenced by noise has been extensively studied in different models of coupled discrete systems, such as Rulkov [202, 217, 218, 219, 220, 221, 222, 204] or Izhikevich neuron maps [223, 224], this has not been complemented by an appropriate *MF* theory, most likely because the Fokker-Planck formalism cannot be applied to discrete-time systems. Our analysis is the first *MF* theory obtained for a population of coupled stochastic neuronal maps. The derivation relies on the cumulant approach complemented by the Gaussian closure hypothesis [67, 185, 186, 187, 188, 189, 190]. Our immediate goal is to establish the regime of macroscopic excitability, as a new form of emergent behavior, study its stability boundaries and bifurcations to other regimes, as well as to examine the related stimulus-response relationship of the population.

Section 2.2 of this chapter is devoted to this corpus of problems. In particular, section 2.2.1 contains an overview of the local map dynamics and introduces the population model, whereas section 2.2.2 outlines the derivation of the *MF* model. Then, in section 2.2.3, we provide proof of the the qualitative and quantitative agreement between the dynamics of the exact and the *MF* model, in terms of appropriate bifurcation diagrams as well as a comparison of the characteristic features of the associated regimes. Section 2.2.4 concerns the assembly's stimulus-response relationship, where we first investigate the analogy between the respective phase-response curves (*PRCs*) of the exact system and the effective model in spiking and bursting regimes and then consider the extent to which the *MF* model reproduces the population's response to perturbations of finite amplitude and duration.

A summary and discussion of our results concerning the excitability of the adaptively coupled motif, as well as the neuronal population are provided in the concluding section 2.3 of this chapter.

2.1 *Excitability of a motif of two adaptively coupled units*

In this section, we classify the excitable regimes of a motif consisting of two active rotators interacting by phase-dependent adaptive couplings. The active rotator model is canonical for Type I local excitability, whereas the slower dynamics of the coupling strengths plays the role of plasticity in neuronal systems. Our first goal is to identify conditions that give rise to excitable behavior at the level of the motif. To this end, we perform stability and bifurcation analysis and find that the considered plasticity rule supports a parameter regime admitting two excitable equilibria. In terms of coupling strengths, these fixed points effectively correspond to master-slave configurations, characterized by an asymmetry in the influence the units have on each other. Our findings reveal that the system is capable of generating several distinct threshold-like responses to external perturbation, whereby these modalities can be explained in terms of the threshold behavior of individual units and the disparity of the coupling strengths.

2.1.1 Model

In our model, the dynamics of the phases $\{\varphi_1(t), \varphi_2(t)\}$ and the couplings $\{\kappa_1(t), \kappa_2(t)\}$ is described by the following system of ordinary differential equations:

$$\begin{aligned}
\dot{\varphi_1} &= I_0 - \sin\varphi_1 + \kappa_1 \sin(\varphi_2 - \varphi_1) \\
\dot{\varphi_2} &= I_0 - \sin\varphi_2 + \kappa_2 \sin(\varphi_1 - \varphi_2) \\
\dot{\kappa_1} &= \varepsilon(-\kappa_1 + \sin(\varphi_2 - \varphi_1 + \beta)) \\
\dot{\kappa_2} &= \varepsilon(-\kappa_2 + \sin(\varphi_1 - \varphi_2 + \beta)),
\end{aligned} \tag{2.1}$$

where $\varphi_1, \varphi_2 \in S^1$ and $\kappa_1, \kappa_2 \in \mathbb{R}$. The rotators are assumed to be identical, with the local dynamics governed by the excitability parameter I_0. In particular, isolated units undergo the SNIPER bifurcation at the critical value $I_0 = 1$, separating the excitable ($I_0 < 1$) and oscillatory ($I_0 > 1$) regimes. Since this section concerns excitable local dynamics, $I_0 = 0.95$ will be kept fixed for simplicity. In the excitable regime, the uncoupled system always converges to a steady state, whereas the interactions may induce emergent oscillations in the coupled system. The parameter $0 < \varepsilon \ll 1$ defines the timescale separation between the fast dynamics of the phases and the slow dynamics of adaptation. In the context of neuroscience, I_0 can be interpreted as an external bias current. The system has $\mathbb{Z}_2$ symmetry since the equations are invariant to the exchange of indices $1 \leftrightarrow 2$.

The plasticity rule is controlled by the phase shift parameter β, which describes the modality of the plasticity rule with respect to the phase difference $\Delta\varphi = \varphi_2 - \varphi_1$, allowing one to interpolate between different adaptation modalities. The analogy between the adaptivity dynamics in classical neuronal systems and the systems of coupled phase oscillators has been addressed in [205, 206, 207], whereas a deeper analysis of the correspondence between the phase-dependent plasticity rules and the STDP has been provided in [182]. From these studies, it follows that the scenario found for $\beta = 3\pi/2$, where the stationary weights increase for smaller phase differences and decrease for larger ones ("like-and-like" form of behavior), qualitatively resembles the Hebbian learning rule [206, 207]. Nevertheless, in the case $\beta = \pi$, the two couplings always change in opposite directions, which may be interpreted as promoting an STDP-like plasticity rule. This is shown in Fig. 2.1. Our interest lies in the β interval between these two limit cases, since it admits two coexisting excitable fixed points.

2.1.2 Deterministic dynamics: stationary states

We will now consider the system's fixed points in order to understand the excitable behavior of the motif. Note that due to $\mathbb{Z}_2$, fixed points always appear in pairs which share the same stability features.

In line with a standard slow-fast approach (singular perturbation theory), we may consider the *layer problem (fast subsystem) fast subsystem*, defined on the fast timescale:

$$\begin{aligned} \dot{\varphi_1} &= I_0 - \sin\varphi_1 + \kappa_1 \sin(\varphi_2 - \varphi_1) \\ \dot{\varphi_2} &= I_0 - \sin\varphi_2 + \kappa_2 \sin(\varphi_1 - \varphi_2), \end{aligned} \tag{2.2}$$

in which κ_1 and κ_2 are treated as fixed parameters; as well as the associated *reduced problem (slow subsystem)*, defined on the slow timescale, whose dynamics is given by:

$$\begin{aligned} \dot{\kappa_1} &= -\kappa_1 + \sin(\varphi_2 - \varphi_1 + \beta) \\ \dot{\kappa_2} &= -\kappa_2 + \sin(\varphi_1 - \varphi_2 + \beta), \end{aligned} \tag{2.3}$$

In general, the fixed points $(\varphi_1^*, \varphi_2^*, \kappa_1^*, \kappa_2^*)$ of the full system (2.1) are given by the solutions of the following set of equations:

$$\begin{aligned} \sin\varphi_1^* - \sin(\varphi_2^* - \varphi_1^* + \beta)\sin(\varphi_2^* - \varphi_1^*) &= I_0, \\ \sin\varphi_2^* - \sin(\varphi_1^* - \varphi_2^* + \beta)\sin(\varphi_1^* - \varphi_2^*) &= I_0, \end{aligned} \tag{2.4}$$

with

$$\begin{aligned} \kappa_1^* &= \sin(\varphi_2^* - \varphi_1^* + \beta), \\ \kappa_2^* &= \sin(\varphi_1^* - \varphi_2^* + \beta). \end{aligned} \tag{2.5}$$

Equations (2.4) can be numerically solved for any fixed parameter set, while numerical path-following allows one to study the dependence of the coordinates of the fixed points on the parameters. The fast flow is useful because it allows for analytical tractability, whereas the exchange symmetry can be taken into account by considering the solutions on and off the synchronization manifold of the fast subsystem ($\varphi_1 = \varphi_2$).

The following subsections contain a brief analysis of the stability of the fixed points on the synchronization manifold of the fast subsystem for four paradigmatic values of β which reduce the dimension of the full system (2.1), as well as a more rigorous analysis on the fast flow which explicitly considers the β-dependence of the number and stability of fixed points. The explicit study of the points on and off the synchronization manifold is motivated by the system's $\mathbb{Z}_2$ exchange symmetry.

2.1.2.1 Stability of fixed points on the synchronization manifold

The fixed points on the synchronization manifold can be obtained from the equations for the fast flow by setting $\varphi_1 = \varphi_2$ in the fast subsystem (2.2). The following holds for $i \in \{1, 2\}$:

$$\dot{\varphi}_i = I_0 - \sin\varphi_i = 0 \Rightarrow \sin\varphi_i = I_0 \iff \varphi_i = (-1)^n \arcsin I_0 + \pi n, n \in \mathbb{Z}$$

implying that the *fast subspace always contains fixed points on the synchronization manifold for* $I_0 \in (0, 1)$. Indeed, the fast flow has two fixed points on the synchronization manifold, both independent of the stationary values of the couplings:

$$\begin{aligned} P1 &\equiv \{\varphi_1, \varphi_2\} = \{\arcsin I_0, \arcsin I_0\} \\ P2 &\equiv \{\varphi_1, \varphi_2\} = \{\pi - \arcsin I_0, \pi - \arcsin I_0\}. \end{aligned} \tag{2.6}$$

The stability of these fixed points along the transversal $\lambda_\perp$ and longitudinal $\lambda_{||}$ directions follows from the eigenvalues of the Jacobian. In particular, the corresponding eigenvalues of $P1$ are given by:

$$\begin{aligned} \lambda_\perp &= -\sqrt{1 - {I_0}^2} - \kappa_1^* - \kappa_2^* \\ \lambda_{||} &= -\sqrt{1 - {I_0}^2} < 0, \end{aligned}$$

whereas those of $P2$ read:

$$\begin{aligned} \lambda_\perp &= \sqrt{1 - {I_0}^2} - \kappa_1^* - \kappa_2^* \\ \lambda_{||} &= \sqrt{1 - {I_0}^2} > 0, \end{aligned}$$

revealing that both $P1$ and $P2$ change transversal stability depending on the stationary values of the couplings, whereas $P1$ ($P2$) is always longitudinally stable (unstable) for $I_0 < 1$. Thus, the synchronization manifold contains one fixed point ($P1$) which always remains longitudinally stable, whereas its transversal stability depends on the coupling.

Since β determines the stationary values of the weights (2.5), the plasticity rule has a nontrivial impact on the dynamics of the full system. Let us first consider four paradigmatic values $\beta \in \{0, \pi/2, \pi, 3\pi/2\}$ which give rise to symmetrical behavior of the coupling strengths ($\kappa_1 = \pm\kappa_2$), reducing the dimension of the full system by one. By analyzing the impact of the global stability of the longitudinally stable fixed point on the synchronization manifold $P1$ (2.6), as well as the impact of β on the stationary couplings, we arrive to the following conclusions, see also Fig. 2.1.

1. $\beta = \frac{\pi}{2} :\Rightarrow {\kappa_1}^* = {\kappa_2}^* = +1$:

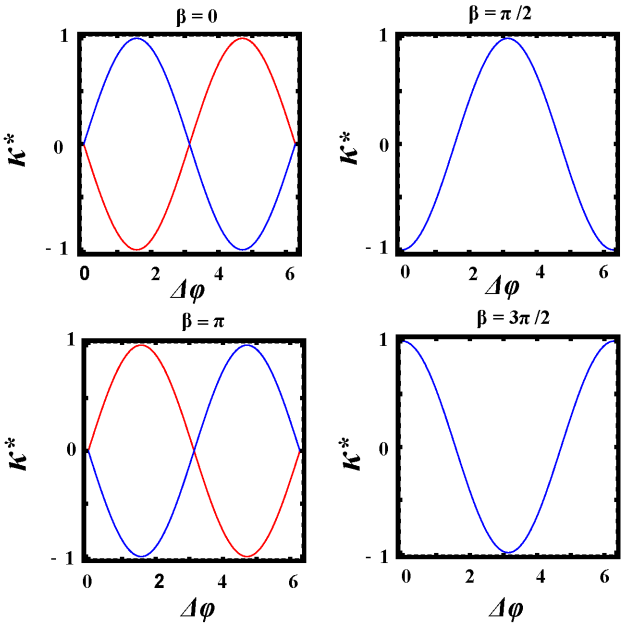

Figure 2.1: The stationary values of the coupling strengths (2.5) as a function of $\Delta\varphi = \varphi_2 - \varphi_1$ for several paradigmatic β values: $\beta \in \{0, \pi/2, \pi, 3\pi/2\}$. According to [206], the scenario for $\beta = 3\pi/2$, where the stationary weight increases for smaller phase differences and decreases for larger ones ("like-and-like" form of behavior), qualitatively corresponds to the well-known Hebbian learning rule. By the same token, the case $\beta = \pi/2$ qualitatively corresponds to the anti-Hebbian learning rule, whereas the $\kappa^*(\Delta\varphi)$ profiles for $\beta \in \{0, \pi\}$ may be interpreted as STDP-like plasticity rules.

- Attractive coupling.
- $P1$ is a transversally stable node.
- The full system converges to the completely synchronized state $(\varphi_1^*, \varphi_2^*, \kappa_1^*, \kappa_2^*) = (\arcsin I_0, \arcsin I_0, +1, +1)$.
- No emergent oscillations.
- Anti-Hebbian learning rule.

2. $\beta \in \{0, \pi\} :\Rightarrow \kappa_1^* = -\kappa_2^* = 0$:
   - Decoupled state.
   - $P1$ is a transversally stable node.
   - No emergent oscillations.
   - STDP-like learning rules.

3. $\beta = \frac{3\pi}{2} \Rightarrow {\kappa_1}^* = {\kappa_2}^* = -1$:
   - Repulsive coupling.
   - $P1$ is a transversally unstable node.
   - The system exhibits emergent oscillations.
   - Hebbian learning rule.

2.1.2.2 β-dependence of the number and stability of fixed points

Let us rewrite the equations of the fast flow (2.2) by applying the following transformation of coordinates $(\varphi_1, \varphi_2) \mapsto (\delta\varphi, \Phi)$:

$$\begin{aligned}\delta\varphi &= \frac{1}{2}(\varphi_1 - \varphi_2)\\ \Phi &= \frac{1}{2}(\varphi_1 + \varphi_2).\end{aligned}$$

The dynamics of the fast flow in terms of the new variables is then given by

$$\begin{aligned}\dot{\delta\varphi} &= -\sin\delta\varphi(\cos\Phi + (\kappa_1 + \kappa_2)\cos\delta\varphi)\\ \dot{\Phi} &= I_0 - \cos\delta\varphi(\sin\Phi + (\kappa_1 - \kappa_2)\sin\delta\varphi),\end{aligned}$$

where κ_1 and κ_2 are fixed parameters. The dependence of the number of fixed points of the fast flow, as well as their stability in terms of β, can be analyzed by substituting the stationary weight values into the equations of fast flow. In particular, the slow flow (2.5) in terms of $(\delta\varphi, \Phi)$ reads

$$\begin{aligned}\dot{\kappa_\pm} &= \varepsilon(-\kappa + \sin(\pm\delta\varphi + \beta))\\ &= \varepsilon(-\kappa + \sin\beta\cos\delta\varphi \pm \cos\beta\sin\delta\varphi)\end{aligned}$$

meaning that the stationary weights are given by

$$\begin{aligned}\kappa_1^* &= \cos\beta\sin\delta\varphi + \sin\beta\cos\delta\varphi\\ \kappa_2^* &= \cos\beta\sin\delta\varphi - \sin\beta\cos\delta\varphi.\end{aligned} \tag{2.7}$$

Finally, by substituting (2.7) into (2.2), the fast subsystem becomes

$$\begin{aligned}\dot{\varphi_1} &= I_0 - \sin\varphi_1 + \cos\beta(\sin\delta\varphi)^2 + \sin\beta\cos\delta\varphi\sin\delta\varphi\\ \dot{\varphi_2} &= I_0 - \sin\varphi_2 + \cos\beta(\sin\delta\varphi)^2 - \sin\beta\cos\delta\varphi\sin\delta\varphi.\end{aligned} \tag{2.8}$$

Note that the synchronization manifold is once again invariant due to (2.8) being symmetrical with respect to the exchange of indices 1 ↔ 2. Due to this symmetry, all fixed points outside of the synchronization manifold appear in pairs within which members share stability features.

We have verified that the number and stability of the fixed points of the full system (2.1) matches those of the fast subsystem (2.8). The complete bifurcation diagram showing the fixed points of (2.1) as a function of β, obtained in the described way, is provided in Fig. 2.2. With respect to the number of fixed points, the system admits seven distinct regimes:

1. $\beta \in (0, 0.156)$: **4 fixed points**, one stable on the synchronization manifold, one unstable, two saddles;

2. $\beta \in (0.156, 1.787)$: **2 fixed points**, one stable and one saddle on the synchronization manifold;

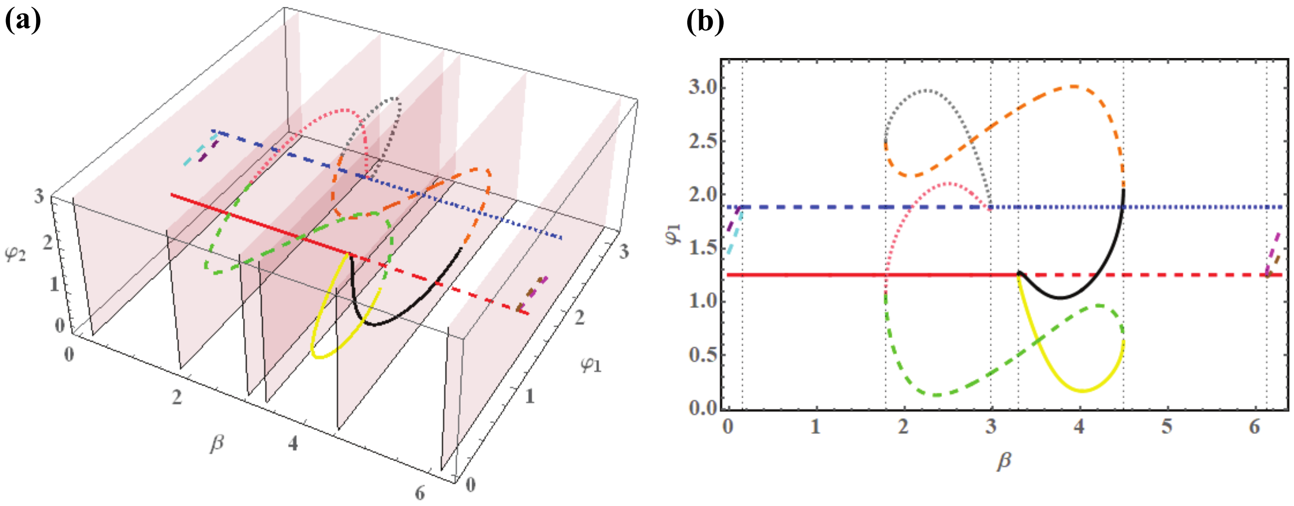

Figure 2.2: Subplot (a) shows the bifurcation diagram for the fixed points of the fast flow in the $(\beta, \varphi_1, \varphi_2)$ space, whereas (b) shows projection of the bifurcation diagram to (β, φ_1) plane. The two fixed points independent on β belong to the synchronization manifold: the red (blue) one is always longitudinally stable (unstable). The solid lines denote stable fixed points, whereas the dashed and dotted lines denote saddles of unstable dimension 1 and 2, respectively.

3. $\beta \in (1.787, 2.984)$: **6 fixed points**, one stable on the synchronization manifold, two unstable points and three saddles;

4. $\beta \in (2.984, 3.298)$: **4 fixed points**, one stable on the synchronization manifold, one unstable, two saddles;

5. $\beta \in (3.298, 4.495)$: **6 fixed points**, two stable outside of synchronization manifold, one unstable point and three saddles;

6. $\beta \in (4.495, 6.126)$: **2 fixed points**, one unstable and one saddle on the synchronization manifold;

7. $\beta \in (6.126, 2\pi)$: **4 fixed points**, one stable on the synchronization manifold, one unstable, two saddles.

Under increasing β, the associated bifurcations are as follows:

1. $\beta = 0.156$: **inverse supercritical pitchfork bifurcation** in which the longitudinally unstable fixed point on the synchronization manifold gains transversal stability;

2. $\beta = 1.787$: **two fold bifurcations** giving rise to two pairs of symmetry-related fixed points, each comprised of a saddle point and an unstable point;

3. $\beta = 2.984$: **subcritical pitchfork bifurcation** in which the longitudinally unstable fixed point on the synchronization manifold is destabilized in the transversal direction;

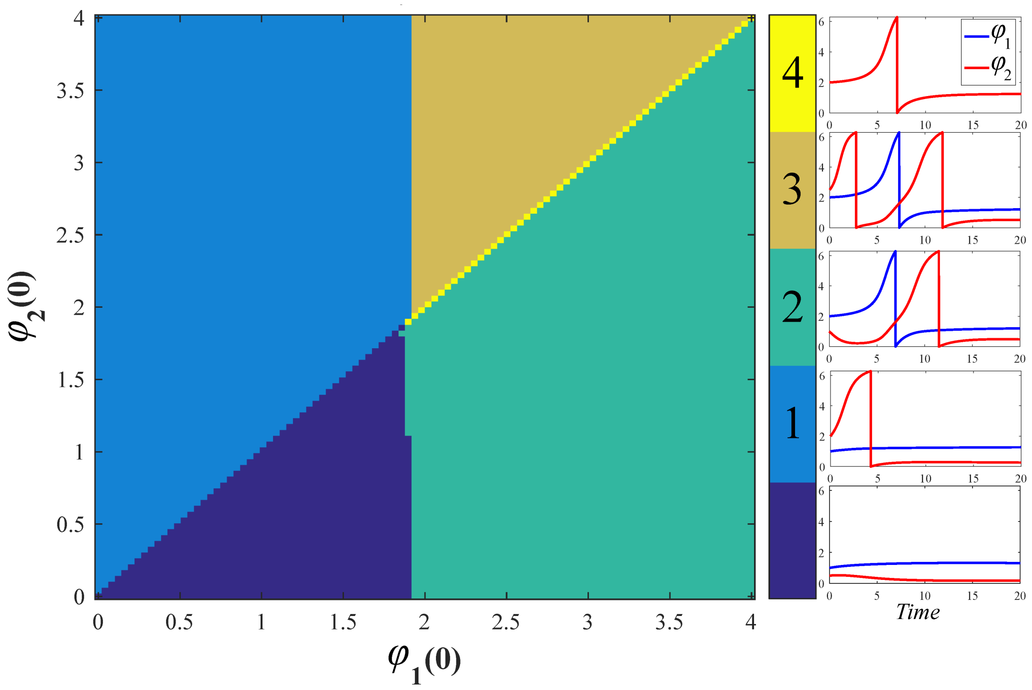

Figure 2.3: Modalities of the response to external perturbation for system (2.1). The system parameters are fixed to $I_0 = 0.95$, $\varepsilon = 0.01$ and $\beta = 4.212$, whereas the initial conditions for the couplings are set to $\kappa_1(0) = -0.0078$, $\kappa_2(0) = -0.8456$. Depending on the initial phases $(\varphi_1(0), \varphi_2(0))$, one may observe the following regimes: (0) no spikes; (1) the unit with larger $\varphi(0)$ emits one spike and the other does not; (2) both units emit a single spike, with the unit with larger $\varphi(0)$ firing first; (3) the unit with larger $\varphi(0)$ emits two spikes and the other unit emits one; (4) both units spike synchronously.

4. $\beta = 3.298$: **supercritical symmetry-breaking pitchfork bifurcation** in which two stable fixed points are created off the synchronization manifold;

5. $\beta = 4.495$: **two symmetrical inverse saddle node bifurcations** in which pairs consisting of a stable and an unstable fixed point off the synchronization manifold are destroyed;

6. $\beta = 6.126$: **inverse subcritical pitchfork bifurcation** which stabilizes the longitudinally stable fixed point on the synchronization manifold in the transversal direction.

2.1.3 Stimulus-response relationship and threshold-like behavior

Since our study concerns plasticity rules which support excitable fixed points, we have confined our analysis to interval (5) $\beta \in (3.298, 4.495)$, where the system has two stable fixed points off the synchronization manifold (i. e. $\varphi_1 \neq \varphi_2$), which are excitable, as well as four unstable fixed points. In further considerations, we shall fix β to a particular value within the relevant interval. For instance, for $\beta = 4.212$, the symmetry-related pair of stable foci is given by

$$\begin{aligned}(\varphi_1^*, \varphi_2^*, \kappa_1^*, \kappa_2^*) &= (1.2757, 0.2127, -0.0078, -0.8456) \\ (\varphi_1^*, \varphi_2^*, \kappa_1^*, \kappa_2^*) &= (0.2127, 1.2757, -0.8456, -0.0078)\end{aligned} \tag{2.9}$$

These asymmetric coupling strengths support effective *master-slave configurations* in which one unit exerts a much stronger influence on the other unit than vice versa.

The excitability of the two stable asymmetric foci (2.9) manifests itself as several different types of responses to external perturbations of the coupled system, as shown in the classification provided in Fig. 2.3 and the corresponding phase portraits 2.4. The perturbation is introduced by the setting of different initial conditions $\{\varphi_1(0), \varphi_2(0)\}$ with fixed $\kappa_1(0) = -0.0078, \kappa_2(0) = -0.8456$ to values from 2.9.

By analyzing the subsequent relaxation of the phases to the rest state, we observe that the excitability of the coupled system involves **well-defined threshold-like behavior**. The threshold set is partially determined by the unstable manifold of the saddle point on the synchronization manifold whose coordinates are given by:

$$(\varphi_1^*, \varphi_2^*, \kappa_1^*, \kappa_2^*) = (\pi - \arcsin I_0, \pi - \arcsin I_0, \sin\beta, -\sin\beta),$$

which means that the excitation threshold for individual units is given by the value $\varphi_{thr} = \pi - \arcsin I_0$. If the perturbation excites either φ_1 or φ_2 to values larger than φ_{thr}, the corresponding unit will emit a spike.

Moreover, the response of the coupled system is asymmetric due to the disparity of coupling strengths and phases of the two steady states (2.9). Namely, if the initial conditions are set to $\varphi_2(0) > \varphi_1(0)$, the steady state will be achieved only after a large excursion in the phase space (compare (0) and (1) from Fig. 2.3). The phase portraits shown in Fig. 2.4) clearly demonstrate that trajectories cannot directly cross the synchronization manifold $\varphi_1 = \varphi_2$ (dashed line) during relaxation; rather, a spike must occur before the system settles back to the rest state.

When both units are perturbed below threshold, neither unit fires (regime 0). In order to observe spiking behavior, at least one of the units must be perturbed at or above the threshold (regimes 1–4). This may be achieved either by crossing the unstable manifold of the saddle point on the synchronization manifold ($\varphi_1(0) > \varphi_{thr}$ or $\varphi_2(0) > \varphi_{thr}$) or by setting the initial conditions to $\varphi_2(0) > \varphi_1(0)$. Depending on the perturbation, the system emits between one and three spikes in total. In general, in scenarios in which both units respond with a spike, the order of firing is such that the unit with larger initial phase fires first (regimes 2–3). Nonetheless, if both units are set exactly onto the synchronization manifold by the perturbation with $\varphi_1(0) = \varphi_2(0) > \varphi_{thr}$, they will both emit a single spike synchronously (regime 4).

— 2.2 *Macroscopic excitability: assembly of coupled neuronal maps* —

In this section, we establish the concept of macroscopic excitability based on the idea of synchronized local activity, examine the stability boundaries of this regime and bifurcations to other regimes, as well as examine the population's stimulus-response relationship. To

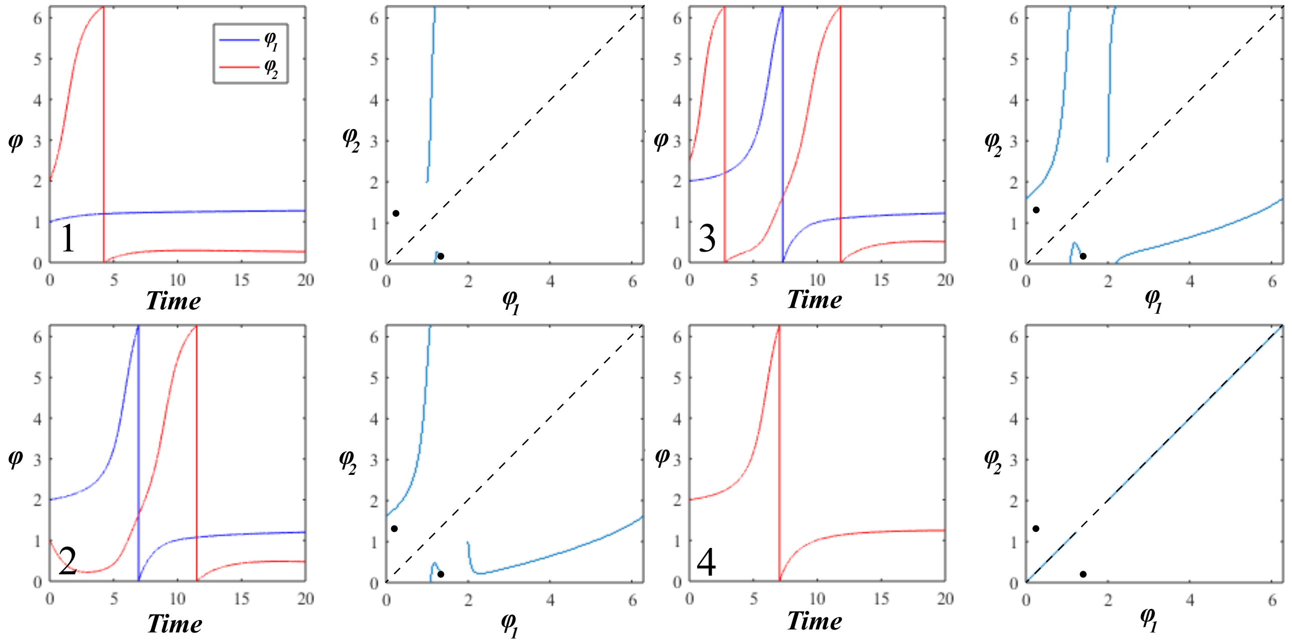

Figure 2.4: Time series $\{\varphi_1(t), \varphi_2(t)\}$ (blue and red, respectively) and trajectories in the (φ_1, φ_2) plane (light blue) corresponding to the spiking responses 1–4 from Fig. 2.3 for system (2.1). The system parameters are fixed to $I_0 = 0.95$, $\varepsilon = 0.01$ and $\beta = 4.212$, whereas the initial conditions for the couplings are set to $\kappa_1(0) = -0.0078$, $\kappa_2(0) = -0.8456$. Depending on the initial conditions, the system exhibits different modalities of relaxing to one of the excitable equilibria (black dots), emiting between one and three spikes in total. The black dashed line denotes the synchronization manifold ($\varphi_1 = \varphi_2$).

address these issues, we derive a reduced effective (mean field) model based on a cumulant approach complemented by the Gaussian closure hypothesis [191].

2.2.1 Local map dynamics and the population model

The local dynamics is represented by the map model:

$$
\begin{aligned}
x_{n+1} &= x_n + G(x_n) - \beta H(x_n - d) - y_n, \\
y_{n+1} &= y_n + \varepsilon(x_n - J),
\end{aligned}
\tag{2.10}
$$

where n denotes the iteration step. The variable x_n qualitatively accounts for the membrane potential, whereas the recovery variable y_n, whose rate of change is set by the small parameter $\varepsilon = 0.01$, mimics the behavior of ion-gating channels. The parameters a, β and d modify the oscillation profile, while J crucially influences the neural excitability, viz. the transitions from silence to active regimes. The model be considered as a discrete version of the FHN neuron model, and has first been introduced in [225, 226]. The local dynamics may exhibit a variety of regimes found in real neurons, including excitability, subthreshold oscillations, regular and chaotic spiking or bursting, as well as mixed spiking-bursting oscillations [227, 228, 229, 230].

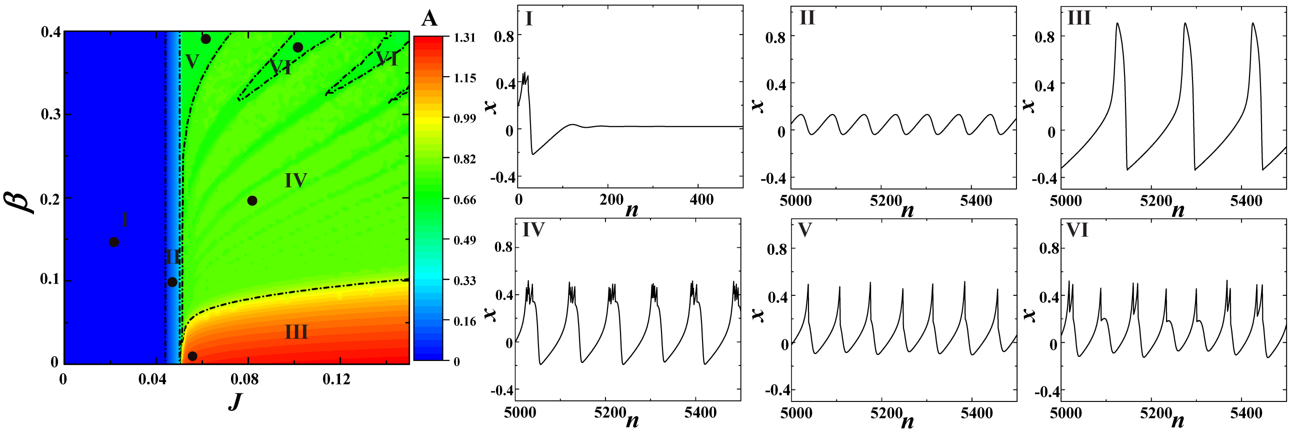

Figure 2.5: Dynamical regimes of the neuron map model (2.10). The heat map shows the variation of the amplitude of oscillations A of the x time series in the $J-\beta$ plane. The waveforms shown in subfigures $I-VI$ illustrate different generic forms of neuronal behavior, including excitability (I), subthreshold oscillations (II), regular spiking (III), chaotic bursting (IV), chaotic spiking (V), as well as mixed spike-burst activity (VI). The dots in the heat map indicate the particular (J,β) values for which the representative waveforms were obtained.

The evolution of x_n features two nonlinear terms: (i) a FitzHugh-Nagumo-like cubic nonlinearity $G(x_n) = x_n(x_n - a)(1 - x_n)$, which is complemented by (ii) a discontinuity term $-\beta H(x_n - d)$, where H stands for the Heaviside step function. The parameters $a = 0.1$ and $d = 0.45$ are kept fixed throughout the chapter. The discontinuity makes the fast subsystem (Eq. (2.10) with $\varepsilon = 0$) a Lorenz-type map within certain parameter domains [226, 231], due to which the model may exhibit chaotic spiking or bursting oscillations, typically absent in Fitzhugh-Nagumo type of systems.

Under the variation of J and β, the considered map (2.10) is capable of reproducing a rich repertoire of generic regimes displayed by real neurons, as demonstrated in Fig. 2.5. In particular, the main frame shows the amplitudes of the corresponding x time series as a function of (J,β), while the remaining subfigures illustrate characteristic waveforms corresponding to the excitable regime (region I), subthreshold oscillations (II), regular (III) or chaotic spiking (IV), chaotic bursting (V), as well as mixed chaotic spike-burst activity (VI). Some of the indicated boundaries, such as those involving domains IV, V and VI should be understood as tentative since the associated transitions are smooth and therefore difficult to discern.

A detailed phase plane analysis concerning the relevant unstable invariant curves and the mechanisms underlying the transitions between the different dynamical regimes can be found in [232]. Here we briefly mention that under increasing J, the equilibrium loses stability via the Neimarck-Sacker bifurcation which gives rise to subthreshold oscillations. These subthreshold oscillations may be considered excitable in the sense that a sufficiently strong perturbation elicits a spike, but the system relaxes to a closed invariant curve instead of a steady state.

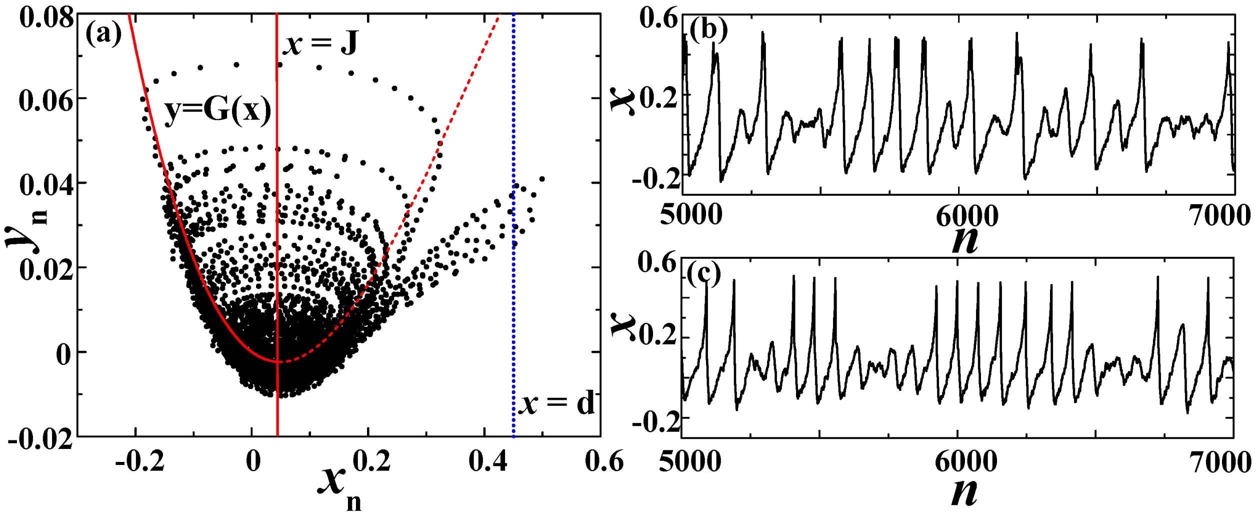

Figure 2.6: Impact of noise on a single map neuron in the excitable regime. (a) indicates the mechanism behind noise-induced spiking. The data are obtained for $J = 0.046, \beta = 0.4, \sigma = 0.005$. The equilibrium is deterministically stable given that the line $x = J$ intersects the invariant curve $y = G(x)$ below the curve's minimum. (b) shows the x_n series corresponding to noise-induced bursting ($J = 0.042, \beta = 0.2, \sigma = 0.008$), whereas (c) demonstrates stochastic spiking superimposed on subthreshold oscillations ($J = 0.048, \beta = 0.4, \sigma = 0.008$).

We are now interested in the behavior of an assembly of N globally electrically (diffusively) coupled stochastic neurons whose local dynamics conforms to (2.10). Each neuron receives input from all other units within the assembly through electrical synapses and is further influenced by synaptic noise, representing uncorrelated input from the embedding environment. Note that in multiscale neuron models, the term “synaptic noise” typically refers to external sources of noise acting on the fast (activator) variables, while the stochastic terms included in the slow (recovery) variables are interpreted as mimicking the influence of intrinsic (ion-channel) neuronal noise [69, 233]. The population activity is described by the following system:

$$\begin{aligned} x_{i,n+1} &= x_{i,n} + G(x_{i,n}) - \beta H(x_{i,n} - d) - y_{i,n} + I^{syn}_{i,n}, \\ y_{i,n+1} &= y_{i,n} + \varepsilon(x_{i,n} - J), \\ I^{syn}_{i,n} &= I^{coup}_{i,n} + I^{rand}_{i,n} = \frac{c}{N}\sum_{j=1, j\neq i}^{N}(x_{j,n} - x_{i,n}) + \sigma\xi_{i,n}, \end{aligned} \tag{2.11}$$

where i specifies the particular neuron. The synaptic currents $I^{syn}_{i,n}$ consist of two terms: (i) *diffusive couplings* $I^{coup}_{i,n}$ characterized by strength c, assumed to be uniform over the network and set to $c = 1$ in the remainder of the chapter; and (ii) *random inputs* $I^{rand}_{i,n}$ which involve uncorrelated white noise ($E[\xi_{i,n}] = 0, E[\xi_{i,n}\xi_{j,n'}] = \delta_{ij}\delta(n - n')$) of intensity σ.

Confined to a single unit, the stochastic component influences the dynamics either by perturbing the deterministic oscillatory regimes or by inducing oscillations in the excitable regime, cf. Fig. 2.6(b). The onset of noise-induced spiking or bursting within domain I in Fig. 2.5, where the fixed point is deterministically stable, corresponds to a *stochastic bifur-*

cation [189, 234, 235, 236, 237]. Stochastic bifurcations are noise-induced transitions. The present scenario is an instance of a P (phenomenological) stochastic bifurcation, characterized by a qualitative change in a time-averaged quantity (such as the asymptotic probability distributions of relevant variables or the associated power spectra) under the variation of noise intensity. Unlike deterministic bifurcations that occur at a clearly defined critical value of the control parameter, stochastic bifurcations involve a gradual change in the system's behavior [189]. Within region II, noise may perturb the regime of subthreshold oscillations by eliciting the dynamics similar to mixed-mode oscillations, with interspersed relaxation and subthreshold oscillations, cf. Fig. 2.6(c).

So far, models similar to (2.11) have been applied to address a number of problems associated with collective phenomena in networks of coupled neurons, including synchronization of electrically coupled units with spike-burst activity [238, 239], pattern formation in complex networks with modular architecture [227, 228, 240], transient cluster activity in evolving dynamical networks [230], as well as the basin stability of synchronization regimes in small-world networks [229]. In our analysis, the collective motion will be described in terms of the global variables $X_n = \frac{1}{N}\sum_{i=1}^{N} x_{i,n}$ and $Y_n = \frac{1}{N}\sum_{i=1}^{N} y_{i,n}$.

2.2.2 Derivation of the mean-field model

Considering a *MF* approximation, our main goal is to derive a reduced low-dimensional deterministic set of nonlinear difference equations whose dynamics is qualitatively analogous to the collective motion of the original system (2.11) comprised of $2N$ coupled stochastic maps. In particular, the *MF* model should should reproduce the qualitative and quantitative features of all the regimes displayed by the exact system, further allowing one to determine the respective stability domains and bifurcations outlining their boundaries. Regarding the explicit effects of noise, the *MF* model is expected to account for the onset or suppression of different types of collective modes associated with macroscopic spiking or bursting activity, which are mediated by synchronization or desynchronization of the dynamics of individual neurons, respectively. The synchronization processes may be influenced by noise in a variety of ways, including scenarios in which noise acts as a perturbation to mainly deterministic (and chaotic) local oscillations, as well as those in which noise plays a facilitatory role, in the sense that the collective mode emerges through the synchronization of noise-induced local dynamics.

Given that (2.11) is a system of discrete-time equations, the standard approach to deriving *MF* models which relies on the Fokker-Planck formalism cannot be applied [190]. Nevertheless, an analytically tractable *MF* model may still be built by considering the evolution of cumulants [67, 185, 186, 189], whereby the full density of states is factorized into a series of marginal densities. This approach allows us to truncate the underlying cumulant series by introducing simplifying approximations in a controlled fashion. Such approximations, stated in the form of a *closure hypothesis* [67], are required due to the nonlinearity of the original system causing the dynamics of cumulants of a given order to be coupled to those of the higher order.

In our case, the derivation of the effective model incorporates an explicit *Gaussian closure hypothesis* [67, 185, 186, 189], according to which all cumulants above second order are assumed to vanish. The collective dynamics is then described by a set of five variables (the first- and second-order cumulants), including

(i) the **means**, given by $m_{x,n} = \lim\limits_{N\to\infty} \frac{1}{N}\sum_{i=1}^{N} x_{i,n} \equiv \langle x_{i,n}\rangle$, $m_{y,n} = \lim\limits_{N\to\infty} \frac{1}{N}\sum_{i=1}^{N} y_{i,n} \equiv \langle y_{i,n}\rangle$;

(ii) the **variances**, defined as $S_{x,n} = \langle x_{i,n}^2\rangle - \langle x_{i,n}\rangle^2 = \langle x_{i,n}^2\rangle - m_{x,n}^2$ and $S_{y,n} = \langle y_{i,n}^2\rangle - \langle y_{i,n}\rangle^2 = \langle y_{i,n}^2\rangle - m_{y,n}^2$;

(iii) the **covariance** $U_n = \langle x_{i,n}y_{i,n}\rangle - m_{x,n}m_{y,n}$.

The expressions for higher order moments $\langle x_{i,n}^k\rangle$ in terms of the first- and second-order cumulants [241], such as

$$\begin{aligned}
\langle x_i^3\rangle &= m_x^3 + 3m_xS_x \\
\langle x_i^4\rangle &= m_x^4 + 6m_x^2S_x + 3S_x^2 \\
\langle x_i^2y_i\rangle &= m_yS_x + m_ym_x^2 + 2m_xU \\
\langle x_i^3y_i\rangle &= 3S_xU + 3S_xm_xm_y + 3m_x^2U + m_ym_x^3 \\
\langle x_i^5\rangle &= m_x^5 + 15m_xS_x^2 + 10m_x^3S_x \\
\langle x_i^6\rangle &= m_x^6 + 15S_x^3 + 15m_x^4S_x + 45m_x^2S_x^2,
\end{aligned} \tag{2.12}$$

can be derived using the closure hypothesis.

The Gaussian approximation effectively amounts to an assumption that the relation

$$\lim_{N\to\infty}\frac{1}{N}\sum_{i=1}^{N} x_{i,n}^k \approx E[x_{i,n}^k],$$

holds, whereby E refers to the expectation value obtained by averaging over an ensemble of different stochastic realizations. In other words, we suppose that the local variables are independent and are drawn from the normal distribution $\mathcal{N}(m_x, S_x)$. However, we cannot know *a priori* whether such an assumption is fulfilled or not. Rather, we may judge its validity by verifying whether the predictions on the population dynamics provided by the *MF* model are correct.

Since the effective model concerns the dynamics of the assembly in the thermodynamic limit $N \to \infty$, we can neglect the stochastic terms, as it can be shown that they contribute to finite size effects which scale as $1/N$. This means that the influence of noise in our *MF* model is felt only via the noise intensity, which assumes the role of an additional bifurcation parameter.

Let us illustrate the main technical points required for the derivation of the *MF* model. We begin by considering the dynamics of m_x, which is given by

$$m_{x,n+1} = m_{x,n} - m_{y,n} + \langle G(x_{i,n})\rangle - \beta\langle H(x_{j,n} - d)\rangle \tag{2.13}$$

It is easy to see that there is no contribution from the coupling term. As far as the third term on the r.h.s. of Eq. (2.13) is concerned, using Eq. (2.12), one arrives at

$$\langle G(x_i)\rangle = \langle -x_i^3 + (1+a)x_i^2 - ax_i\rangle = G(m_x) + S_x(1+a-3m_x). \tag{2.14}$$

In the last expression, we have dropped the time index for simplicity and have introduced the shorthand notation $G(m_x) \equiv -m_x^3 + (1+a)(m_x^2 + S_x)$.

The key problem is how to treat the final term in the r.h.s. of Eq. (2.13). Our approach consists in replacing the assembly average by the expectation value ($\langle H(x_i - d)\rangle \approx E[H(x_i-d)]$), obtained by assuming that the local variables at an arbitrary moment of time are normally distributed according to $P(x_i) \sim \mathcal{N}(m_x, S_x)$. The expectation may then be evaluated as

$$\begin{aligned}
&E[-\beta\langle H(x_i-d)\rangle] = \int dx_1 \int dx_2 ... \int dx_N (-\frac{\beta}{N}\sum_i H(x_i-d))p(x_1,x_2,...,x_N) = \\
&-\beta\int_{-\infty}^{\infty} dx_1 H(x_1-d)p(x_1) = -\beta\int_d^{\infty}\frac{1}{\sqrt{2\pi S_x}}e^{-\frac{(x_1-m_x)^2}{2S_x}} = -\frac{\beta}{2}(1-Erf\left[\frac{d-m_x}{\sqrt{2S_x}}\right]),
\end{aligned}$$

with the error function $Erf(x) = \frac{2}{\sqrt{\pi}}\int_0^x e^{-t^2}dt$. In the above calculation, we have explicitly used the assumption on the independence of distributions of local variables at any given moment of time.

In a similar fashion, one may consider the S_x dynamics, which constitutes the most demanding part of the derivation. In particular, proceeding from the S_x definition, we obtain

$$\begin{aligned}
S_{x,n+1} &= \langle x_{i,n+1}^2\rangle - \langle x_{i,n+1}\rangle^2 = \\
&= \langle[(1-c)x_{i,n} + G(x_{i,n}) - \beta H(x_{i,n}-d) - y_{i,n} + \xi_{i,n} + cm_{x,n}]^2\rangle \\
&- (m_{x,n} - m_{y,n} + G(m_{x,n}) + S_{x,n}(1+a-3m_{x,n}) - \beta\langle H(x_{i,n}-d)\rangle)^2.
\end{aligned} \tag{2.15}$$

As an illustration, let us evaluate one of the terms containing an average over the threshold function:

$$\begin{aligned}
&-2\beta E\left[\langle G(x_i)H(x_i-d)\rangle - \langle G(x_i)\rangle\langle H(x_i-d)\rangle\right] = \\
&-2\beta\left[\int dx_1 G(x_1)H(x_1-d)p(x_1) - \int dx_1 H(x_1-d)p(x_1)\left[G(m_x) + S_x(1+a-3m_x)\right]\right] \\
&\approx -2\beta\left[\int dx_1 (G(m_x) + G'(m_x)(x_1-m_x) + \frac{1}{2}G''(m_x)\times (x_1-m_x)^2)H(x_1-d)p(x_1) - \right. \\
&\left.\int dx_1 H(x_1-d)p(x_1)\times\left[G(m_x)+S_x(1+a-3m_x)\right]\right] = ... = \\
&-2\beta\left[(1+a)(m_x+d) - a - 3m_x d\right]\sqrt{\frac{S_x}{2\pi}}\exp\left[-\frac{(d-m_x)^2}{2S_x}\right].
\end{aligned}$$

Again, the time indices have been suppressed to simplify the notation.

Following some algebra, Eq. (2.15) can be transformed to

$$\begin{aligned}S_{x,n+1} &= (1-c)^2 S_{x,n} + S_{y,n} + \sigma^2 - 2(1-c)U_n + \underbrace{(\langle G(x_{i,n})^2\rangle - \langle G(x_{i,n})\rangle^2)}_{Var(G(x_{i,n}))} \\ &+ 2(1-c)(\langle x_{i,n}G(x_{i,n})\rangle - m_{x,n}\langle G(x_{i,n})\rangle) - 2(\langle y_{i,n}G(x_{i,n})\rangle - m_{y,n}\langle G(x_{i,n})\rangle) \\ &- 2\beta(1-c)\left[\langle x_{i,n}H(x_{i,n}-d)\rangle - m_{x,n}\langle H(x_{i,n}-d)\rangle\right] \\ &- 2\beta(\langle G(x_{i,n})H(x_{i,n}-d)\rangle - \langle G(x_{i,n})\rangle\langle H(x_{i,n}-d)\rangle) \\ &+ \beta^2 \underbrace{(\langle H(x_{i,n}-d)^2\rangle - \langle H(x_{i,n}-d)\rangle^2)}_{Var(H(x_{i,n}-d)))}.\end{aligned}$$

The partial results required for completing the calculation are given by

$$\begin{aligned}\langle x_i G(x_i)\rangle - m_x\langle G(x_i)\rangle &= G'(m_x)S_x - 3S_x^2 \\ \langle y_i G(x_i)\rangle - m_y\langle G(x_i)\rangle &= -3S_xU_{xy} - 3m_x^2U_{xy} + 2(1+a)m_xU_{xy},\end{aligned}$$

where $G'(m_x) \equiv -3m_x^2 + 2(1+a)m_x - a$. Note that the time indexes have been omitted for simplicity. After some straightforward calculations, it may also be shown that the expression for variance $Var(G(x_i))$ reads

$$Var(G(x_i)) = G'^2(m_x)S_x + S_x^2\left[36m_x^2 - 24(1+a)m_x + 2(1+a)^2 + 6a\right] + 15S_x^3.$$

Let us now explicitly calculate the terms containing the threshold function. First we have

$$\begin{aligned}&-2\beta(1-c)\left[\langle x_iH(x_i-d)\rangle - \langle x_i\rangle\langle H(x_i-d)\rangle\right] = \\ &-2\beta(1-c)\left[\int dx_1dx_2...dx_N\frac{1}{N}\sum_i x_iH(x_i-d)p(x_1,...,x_N)\right. \\ &\left.-m_x\int dx_1dx_2...dx_N\frac{1}{N}\sum_i H(x_i-d)p(x_1,...,x_N)\right] = \\ &... = -2\beta(1-c)\left[\int dx_1(x_1-m_x)H(x_1-d)p(x_1)\right] = -2\beta(1-c)\sqrt{\frac{S_x}{2\pi}}\exp\left[-\frac{(d-m_x)^2}{2S_x}\right].\end{aligned}$$

Finally, let us address the term $\beta^2 Var(H(x_i-d))$, which can be estimated by considering the associated expectation $\beta^2 Var(H(x_i-d)) \approx \beta^2\left[\langle H(x_i-d)^2\rangle - \langle H(x_i-d)\rangle^2\right]$. By applying the introduced technique, we obtain

$$\begin{aligned}&E[\beta^2H(x_i-d)^2] = \beta^2\int dx_1\int dx_2...\int dx_N(\frac{1}{N^2}\sum_i\sum_j H(x_i-d)H(x_j-d))p(x_1,x_2,...,x_N) \\ &= \underbrace{\frac{\beta^2}{N^2}N\int dx_1H(x_1-d)p(x_1)}_{N \text{ cases where } i=j} + \underbrace{\frac{\beta^2}{N^2}N(N-1)\int dx_1\int dx_2H(x_1-d)H(x_2-d)p(x_1)p(x_2)}_{N(N-1) \text{ cases where } i\neq j} \\ &= \frac{\beta^2}{2N}[1-Erf[\frac{d-m_x}{\sqrt{2S_x}}]] + \frac{\beta^2}{4N^2}N(N-1)[1-Erf[\frac{d-m_x}{\sqrt{2S_x}}]]^2.\end{aligned}$$

Given that $\beta^2\langle H(x_i-d)\rangle^2 = \frac{\beta^2}{4}\left[1-Erf[\frac{d-m_x}{\sqrt{2S_x}}]\right]^2$, one arrives at

$$\beta^2 Var(H(x_i-d)) = \frac{\beta^2}{4N}(1-Erf[\frac{d-m_x}{\sqrt{2S_x}}])([1+Erf[\frac{d-m_x}{\sqrt{2S_x}}]).$$

This shows that the variance of the threshold function ultimately contributes to a finite-size effect which can be neglected in the thermodynamic limit.

Ultimately, by combining all these elements, one arrives at the final equations of the *MF* model in the thermodynamic limit:

$$\begin{aligned}
m_{x,n+1} =& m_{x,n} - m_{y,n} + G(m_{x,n}) + S_{x,n}(1+a-3m_{x,n}) - \frac{\beta}{2}\left(1-Erf\left[\frac{d-m_{x,n}}{\sqrt{2S_{x,n}}}\right]\right) \qquad (2.16)\\
m_{y,n+1} =& m_{y,n} + \varepsilon(m_{x,n}-J)\\
S_{x,n+1} =& (1-c)^2 S_{x,n} + S_{y,n} + \sigma^2 - 2(1-c)U_n + S_{x,n}(-3m_{x,n}^2 + 2(1+a)m_{x,n} - a)^2\\
& - 2(1-c)(3m_{x,n}^2 S_{x,n} + 3S_{x,n}^2 - 2(1+a)m_{x,n}S_{x,n} + aS_{x,n})\\
& + 2(3S_{x,n}U_n + 3m_{x,n}^2 U_n - 2(1+a)m_{x,n}U_n)\\
& - 2\beta\left[(1+a)(m_{x,n}+d) - a - 3dm_{x,n}\right]\sqrt{\frac{S_{x,n}}{2\pi}}\exp\left[-\frac{(d-m_{x,n})^2}{2S_{x,n}}\right]\\
& - 2\beta(1-c)\sqrt{\frac{S_{x,n}}{2\pi}}\exp\left[-\frac{(d-m_{x,n})^2}{2S_{x,n}}\right]\\
& + S_{x,n}^2\left[36m_{x,n}^2 - 24(1+a)\ m_{x,n} + 2(1+a)^2 + 6a\right] + 15S_{x,n}^3\\
S_{y,n+1} =& S_{y,n} + \varepsilon^2 S_{x,n} + 2\varepsilon U_n\\
U_{n+1} =& U_n - (a+c+\varepsilon)U_n + \varepsilon(1-c-a)S_{x,n} - S_{y,n}\\
& - (U_n + \varepsilon S_{x,n})(3S_{x,n} + 3m_{x,n}^2 - 2(1+a)m_{x,n}) - \beta\varepsilon\sqrt{\frac{S_{x,n}}{2\pi}}\exp\left[-\frac{(d-m_{x,n})^2}{2S_{x,n}}\right].
\end{aligned}$$

2.2.3 Stability and bifurcation analysis for the macroscopic excitability state

This section focuses on the stability of the macroscopic excitability state and the bifurcations outlining the boundaries of its stability domain. To get a basic understanding of all the macroscopic regimes, we first examine the succession of macroscopic regimes in the $J-\beta$ parameter plane for σ fixed at an intermediate value $\sigma = 0.002$, see Fig. 2.7. As in the case of a single unit, J is relevant for the system's excitability, while β influences the waveforms of the active states (spiking, bursting, or mixed spike-bursting activity). The assembly is found to exhibit collective modes that qualitatively correspond to the dynamics of a single unit illustrated in plates $III-VI$ of Fig. 2.5. The heat maps in the left column of Fig. 2.7 provide a comparison between the oscillation amplitudes A of the global variable X (top row) and the *MF* variable m_x (bottom row) for the given (J,β). The right column indicates how well the average interspike interval (or the average bursting cycle) T of the exact system matches with the corresponding characteristics of the dynamics of the *MF* model (2.16).

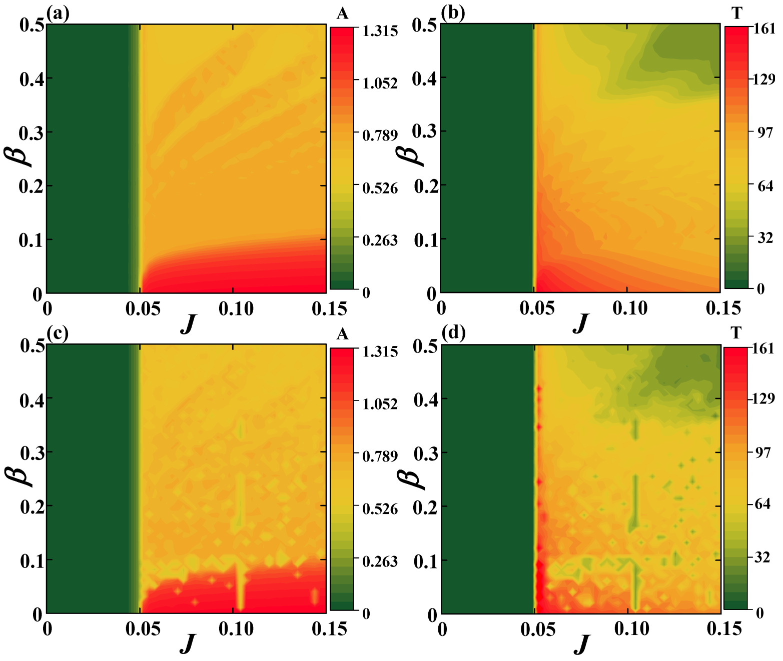

Figure 2.7: The heat maps in (a) and (b) show the dependencies of the oscillation amplitudes $A(J, \beta)$ and average interspike intervals $T(J, \beta)$ obtained by stochastic averaging for a network of $N = 100$ neurons, respectively. (c) and (d) illustrate the analogous results for the *MF* model. The noise intensity in all instances is $\sigma = 0.001$.

In our numerical experiments, the exact system is an assembly consisting of $N = 100$ units. We have obtained A by averaging over sufficiently long time series, whereas T is determined by averaging over an ensemble of 20 different stochastic realizations. To calculate T, we have selected the threshold value $X = \theta = 0.2$ ($m_X = \theta = 0.2$) for the exact system (MF model), since it is convenient for clearly detecting individual spikes, as well as unambiguously discerning the initiation stage of bursts, required for calculating the length of the bursting cycle.

In order to examine the phenomenon of macroscopic excitability, we focus on the domain of J values where the exact system exhibits a stochastically stable equilibrium, while the *MF* model has a stable stationary state. Stochastic stability physically implies that fluctuations around the deterministic fixed point are typically of the order of noise, though some rare spikes may still be evoked. For J sufficiently close to the region which admits subthreshold oscillations, the population manifests macroscopic excitability. The term "macroscopic" here refers to a form of emergent assembly behavior, rather than a characteristic spatial scale. To properly illustrate this feature, we have analyzed the assembly dynamics in the limit $\sigma = 0$, cf. Fig. 2.8. In particular, figures 2.8(a) and 2.8(b) show the maximum X and m_x values reached in the corresponding time series obtained for sets of different initial conditions (X_0, Y_0) and $(m_{x,0}, m_{y,0})$, respectively. A comparison of the two plots corroborates that the boundary defining the domain of the spiking response is appropriately anticipated by the *MF* model. An important remark is that for a particular value of J, the assembly may exhibit different forms of macroscopic excitability, generating a single spike or a burst of

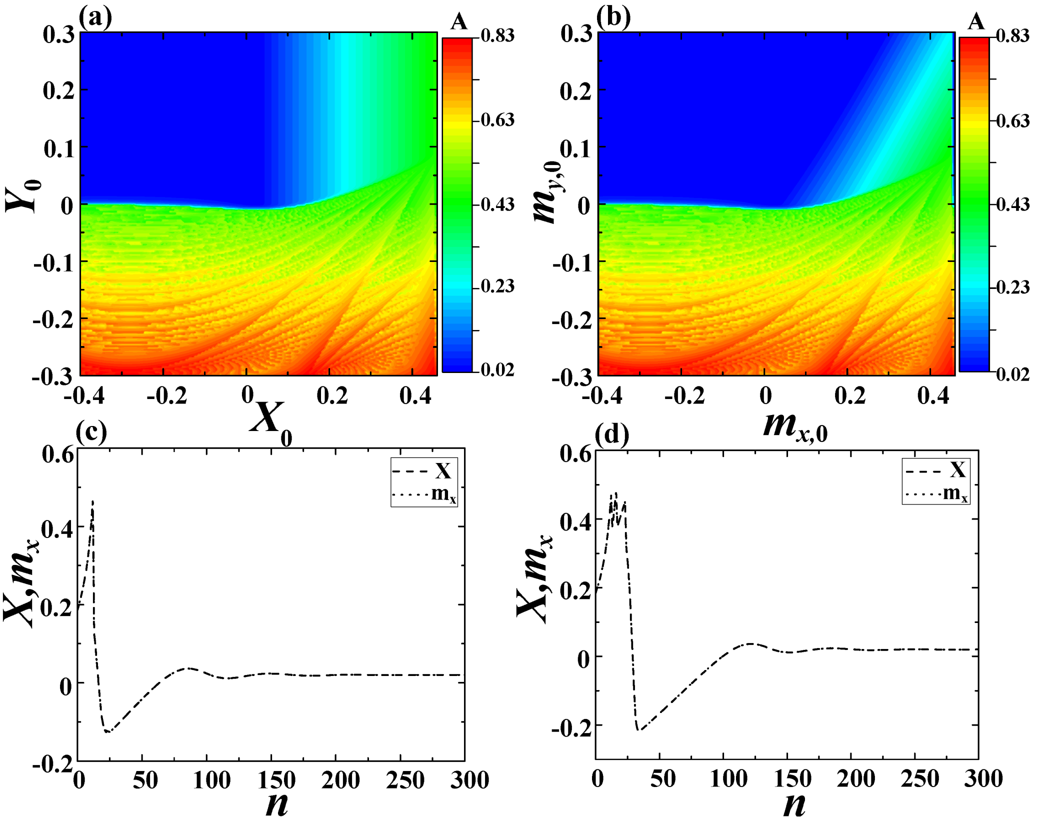

Figure 2.8: The macroscopic excitability feature. The heatmaps in (a) and (b) show the maximum values of X and m_x reached by the exact and the *MF* system, starting from analogous initial conditions (X_0, Y_0) and $(m_{x,0}, m_{y,0})$, respectively. The parameters are $J = 0.02, \beta = 0.4$. (c) illustrates the case where a strong enough perturbation elicits a single-spike response ($J = 0.02, \beta = 0.4$), whereas (d) corresponds to a bursting response made up of three spikes ($J = 0.02, \beta = 0.15$). In both instances, the time series of the *MF* model (dotted line) is indistinguishable from that of the exact system (dashed line).

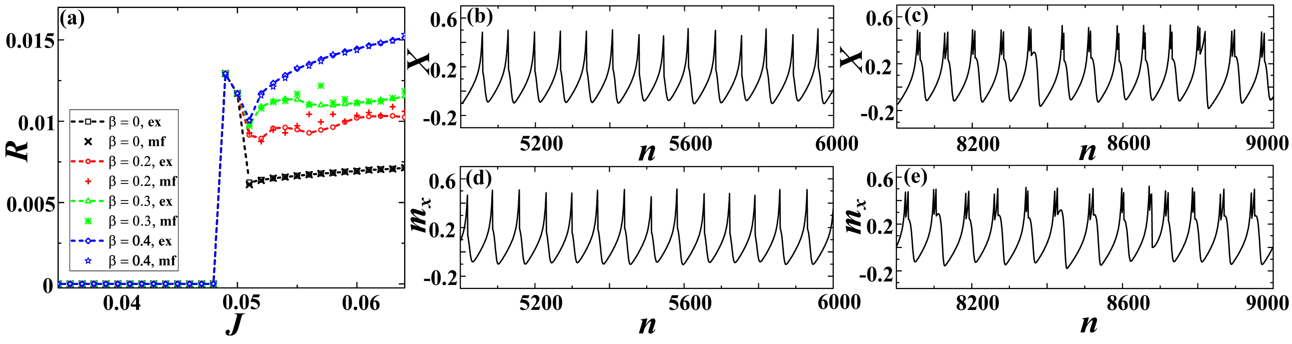

Figure 2.9: (a) shows a family of $R(J)$ curves for different β for a network of size $N = 100$ under fixed $\sigma = 0.001$ with the results for the *MF* model superimposed on the plot, whereby the symbols $\times, +, *, \star$ correspond to $\beta = 0, 0.2, 0.3$ and 0.4, respectively. (b) and (c) illustrate the time series of X associated with the spiking and the bursting collective modes. The considered network is made up of $N = 100$ neurons, with the parameters set to $J = 0.06, \beta = 0.4, \sigma = 0.001$ in (b), and $J = 0.08, \beta = 0.2, \sigma = 0.001$ in (c). (d) and (e) show the m_x series obtained for the parameters from (b) and (c).

spikes, depending on the value of β. This is demonstrated by the time series in figures 2.8(c) and 2.8(d). The former refers to a one-spike response in the case of $\beta = 0.4$. For smaller β, one observes responses comprising two or more closely packed spikes, with Fig. 2.8(d) illustrating a three-spike burst encountered for $\beta = 0.25$. Note that the time series of the full system and the *MF* model exactly coincide in the limit $\sigma = 0$.

The next relevant issue concerns noise-influenced transitions from quiescent to active regimes observed under increasing J. These transitions define the stability boundaries of the macroscopic excitability state, corresponding to gradual stochastic bifurcations in the exact system and proper bifurcations in the MF system. In particular, Fig. 2.9(a) shows how the firing (spiking or bursting) frequency R changes for an assembly consisting of $N = 100$. The average frequency is determined by considering an ensemble of 20 different stochastic realizations, having σ fixed to the moderate value $\sigma = 0.001$. The results from simulations of the full system (2.11) are compared against the data obtained for the *MF* model. In this context, two points should be stressed: (i) for moderate σ, the firing frequencies of the *MF* model lie in close agreement to those of the exact system; and (ii) one finds that the quantitative agreement also holds for different types of transitions from silent to active regimes. As already indicated, the waveforms of the active states depend on β and the associated transitions are mediated by distinct synchronization processes. For instance, synchronization at $\beta = 0$ involves time series of single units that conform to spiking activity of type III from Figure 2.5, which is quite resilient to the impact of noise. On the other hand, for $\beta = 0.3$ or $\beta = 0.4$, individual units exhibit chaotic bursting or spiking activity, respectively, such that the underlying synchronization process is more susceptible to stochastic effects. Typical time series of X for different collective modes are compared to the corresponding m_x series in figures 2.9(b)-(e). The top (bottom) row concerns the data for the exact system (*MF* model).

For a deeper understanding of the influence of noise for J in the vicinity of the transition from silence to active regimes, we examine how the profiles of $R(J)$ curves change under increasing σ. The results for a population comprised of $N = 100$ neurons with $\beta = 0.2$ are shown in Fig. 2.10. As expected, the transition is quite sharp for moderate noise ($\sigma = 0.001$), but is considerably flattened for larger σ (e. g. $\sigma = 0.05$). The crosses indicate the firing frequencies predicted by the *MF* model for $\sigma = 0.001$. For larger σ, the *MF* model fails to reproduce the behavior of the exact system in the vicinity of the threshold, in the sense that it overestimates the maximal value of R, as well as the actual critical J corresponding to the transition. Viewed from another angle, one may infer that for sufficiently large σ and J below the threshold given by the *MF* model, the *MF* model fails to capture the impact of synchronization processes taking place between the noise-induced oscillations of individual units. This especially refers to the J interval within which spikes or bursts (depending on β) are superimposed on the background of subthreshold oscillations. An example of such a discrepancy between the behavior of the exact and the effective system is provided in Fig. 2.11, cf. Fig. 2.11(a) and Fig. 2.11(c). Also, for strong σ and J values above the transition, the

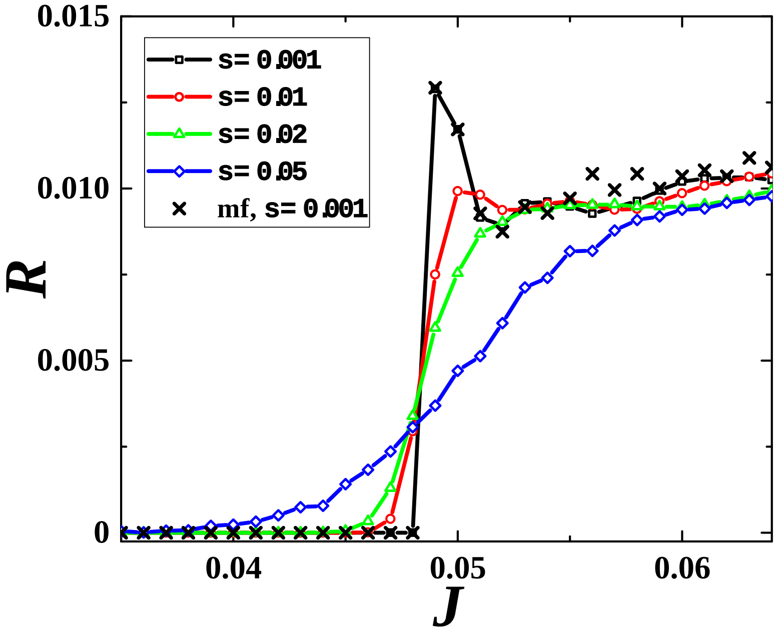

Figure 2.10: Family of $R(J)$ curves over σ for a network of $N = 100$ neurons under fixed $\beta = 0.2$. The different symbols correspond to cases $\sigma = 0.001$ (squares), $\sigma = 0.01$ (circles), $\sigma = 0.02$ (triangles) and $\sigma = 0.05$ (diamonds). The crosses connected by the dashed line highlight the $R(J)$ curve for the *MF* model at $\sigma = 0.001$.

firing frequencies anticipated by the effective model are typically higher than those of the exact system (not shown). Within this region, the stochastic effects suppress synchronization between the chaotic oscillations of single neurons, thereby reducing the corresponding R value. This is not accounted for with sufficient accuracy by the *MF* system. Note that such suppression of synchronization is reflected in the corresponding X series by the spike (burst) "skipping" mechanism, where the large-amplitude oscillations are occasionally replaced with subthreshold oscillations. For the associated J and σ values, such a phenomenon is absent in the dynamics of the effective model, cf. Fig. 2.11(b) and Fig. 2.11(d). In both scenarios illustrated in Fig. 2.11, the *MF* model fails because the Gaussian approximation breaks down due to large stochastic fluctuations.

In order to elucidate how the validity of the effective model's predictions deteriorates with increasing σ, we consider the $A(J, \sigma)$ and $T(J, \sigma)$ dependencies for the exact and the approximate system at fixed $\beta = 0.4$ and $N = 100$, see Fig. 2.12. A comparison between the respective A (left column) and T plots (right column) suggests that the range of σ values where the *MF* approximation applies is contingent on J. For instance, in the J region below the deterministic threshold, one may estimate this range by noting that the effective bifurcation diagram in Fig. 2.12(a) indicates that noise-induced macroscopic oscillations emerge for $\sigma \approx 0.003$. Since this point is not adequately represented by the effective model, cf. Fig. 2.12(c), one may state that the Gaussian approximation breaks down around $\sigma \approx 0.003$ within the given J region. Nevertheless, for J above the deterministic threshold, the validity of the *MF* model appears to depend rather strongly on the particular value of J, such that the Gaussian approximation effectively fails for $\sigma \in (0.002, 0.006)$.

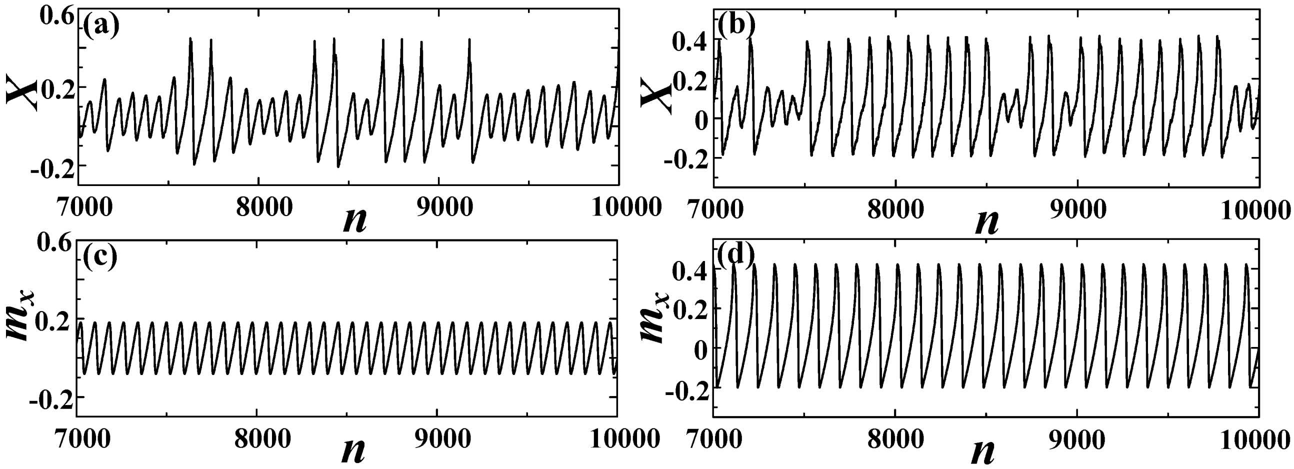

Figure 2.11: Noise-induced phenomena within the J interval in the vicinity of the deterministic threshold. X series in (a) show noise-induced spike-bursting activity on top of subthreshold oscillations ($J = 0.047, \beta = 0.2, \sigma = 0.02$). (b) illustrates the "skipping" phenomenon where the stochastic effects occasionally suppress the large-amplitude oscillations of the X variable ($J = 0.058, \beta = 0.2, \sigma = 0.01$). (c) and (d) show the m_x series corresponding to the parameter sets from (a) and (b), respectively.

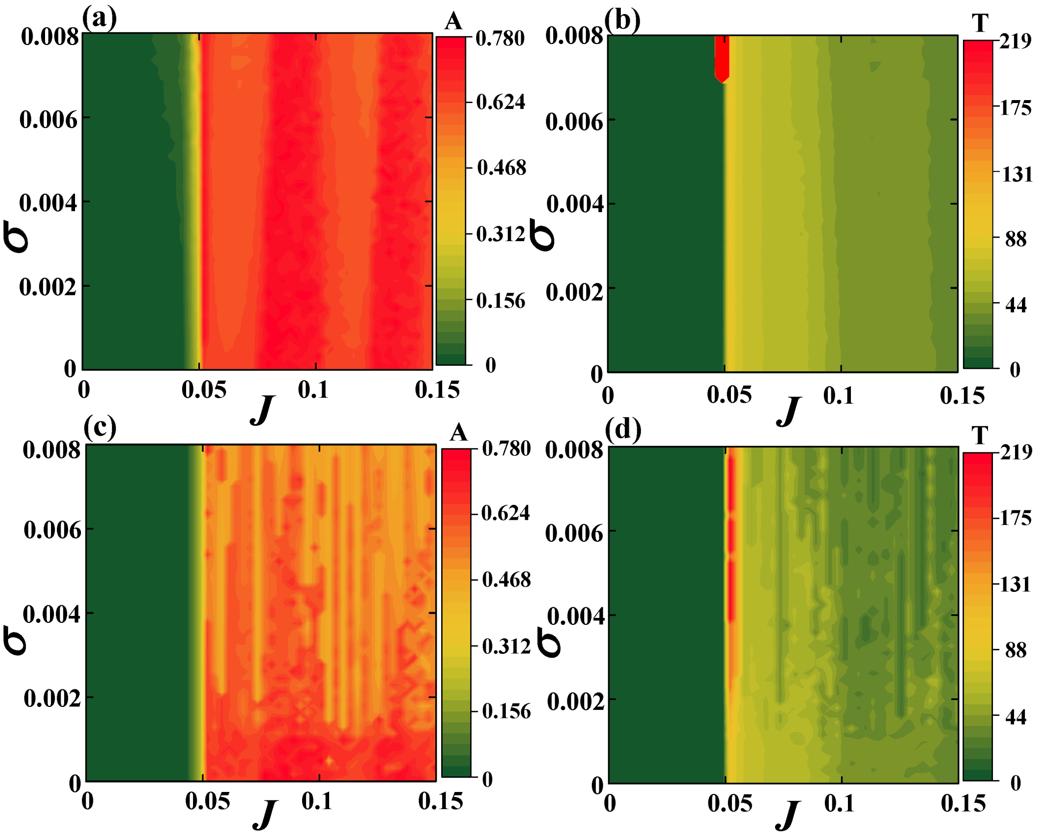

Figure 2.12: Subplots (a) and (b) respectively refer to the $A(J, \sigma)$ and $T(J, \sigma)$ dependencies for the network of $N = 100$ neurons at fixed $\beta = 0.4$. The results in (a) are obtained by averaging over sufficiently long time series, whereas data in (b) derive from averaging over an ensemble of 20 different stochastic realizations. The $A(J, \sigma)$ and $T(J, \sigma)$ dependencies determined by numerical simulations of the MF model are provided in (c) and (d).

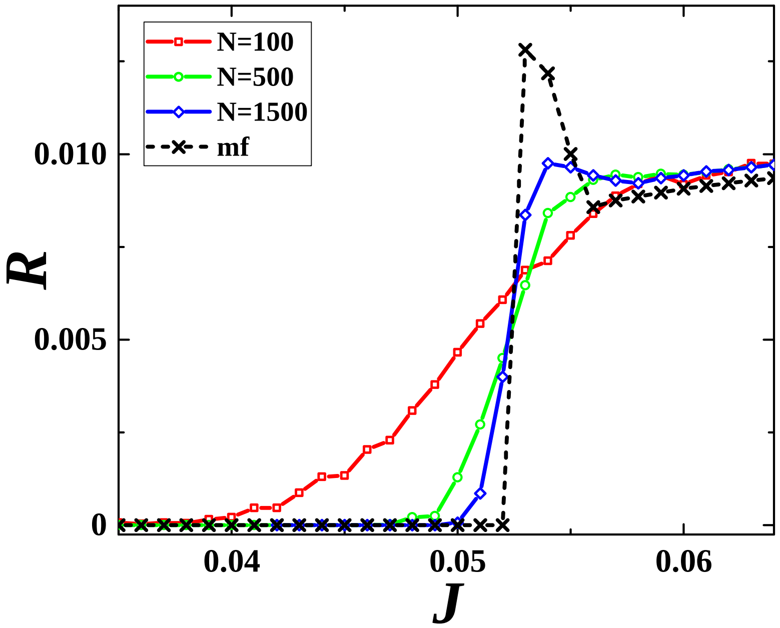

Figure 2.13: $R(J)$ dependencies for increasing N under fixed $(\beta, \sigma) = (0.2, 0.05)$. The squares, circles and diamonds correspond to cases $N = 100$, $N = 500$ and $N = 1500$, respectively. The results for the *MF* model, corresponding to the thermodynamic limit, are indicated by crosses connected with the dashed line.

So far, we have investigated the impact of noise by comparing the results for the network of size $N = 100$ to those obtained for the effective system. Nevertheless, it has already been emphasized in section 2.2.2 that the *MF* model, deterministic in character, refers to the system's behavior in the thermodynamic limit $N \to \infty$, whereas explicitly stochastic terms could only appear as finite-size effects. With this in mind, we have examined how the behavior of the exact system within the J domain around deterministic threshold changes for large and fixed σ under increasing N. Fig. 2.13 contains the $R(J)$ curves calculated for $N = 100$ (squares), $N = 500$ (circles) and $N = 1500$ (diamonds) at fixed $\beta = 0.2, \sigma = 0.05$. The curve for $N = 100$ indicates that the chosen σ value is quite large in the sense that it is sufficient to induce collective oscillations within the excitable regime. Alongside the dependencies for the full system, we also show the $R(J)$ curve associated with the *MF* model (dashed line with crosses). An interesting point regarding the latter is that the J threshold for the emergence of the collective mode is shifted toward a larger value compared to the case $\sigma \approx 0.01$. While the transition itself appears quite sharp, the curves corresponding to the exact system approach it with increasing N, both in terms of the J threshold and the R values above the transition, corroborating that the (J, σ) domain in which the Gaussian approximation fails expectedly reduces with system size.

2.2.4 Response to external stimuli

Within this section, we demonstrate that the *MF* model can be used to predict the stimulus-response relationship of an assembly exhibiting different macroscopic regimes, including the macroscopic excitability state as well as the spiking and bursting collective modes. Let

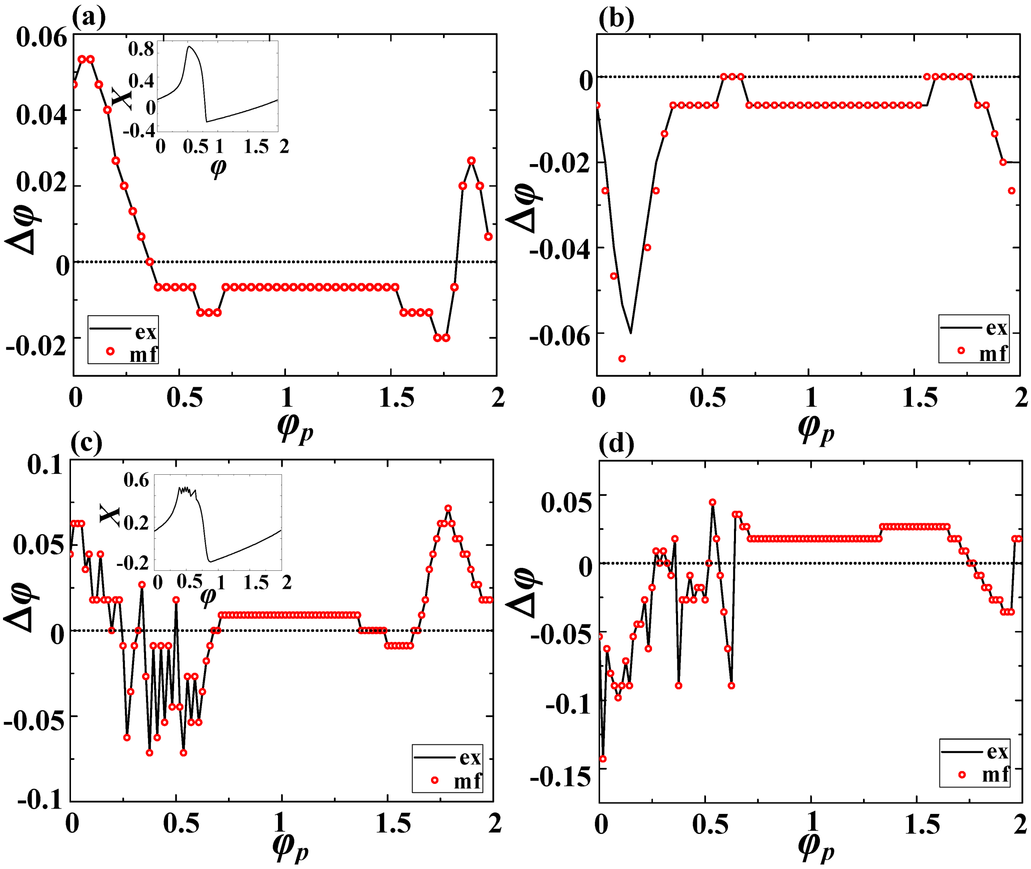

Figure 2.14: Assembly phase resetting. (a) and (b) show the PRCs for a population in spiking regime ($J = 0.055, \beta = 0$) under excitatory ($a = 0.008$) and inhibitory stimulation ($a = -0.008$), respectively. Results for the exact system ($N = 500$) are indicated by the solid line, whereas the data for the MF model are denoted by circles. The bottom row illustrates the PRCs for an assembly exhibiting macroscopic bursting ($J = 0.06, \beta = 0.1$), whereby (c) describes the effect of an excitatory ($a = 0.01$), and (d) of an inhibitory pulse perturbation ($a = -0.01$). The insets in (a) and (c) demonstrate how the phases are assigned to the points within the spiking and bursting cycles, respectively. The phase is expressed in units of π.

us first focus on the two latter instances and examine the sensitivity of a population to an external pulse perturbation within the framework of phase resetting theory [242, 243, 74, 244]. To compare the behavior of the exact system and the effective model, we determine the corresponding phase resetting curves (PRCs), which describe the phase shift $\Delta\varphi$, induced by the perturbation, in terms of the phase φ_p when the perturbation is applied. The considered stimulus has a form of a short pulse current $I_p = a_p H(n - n_i) H(n - n_f)$, whose magnitude a_p and width $\Delta = n_i - n_f$ are small compared to the amplitude and duration of the spiking (or bursting) cycle T_0, respectively. In the case of the exact system, the same pulse current is delivered to each neuron i, adding the term I_p to x_i dynamics, whereas, in the effective model, the stimulation is administered via the m_x variable. The phase φ_p is defined in reference to T_0 by $\varphi_p = n_p/T_0$. The associated phase difference following the reset is calculated as $\Delta\varphi = 1 - T_1/T_0$, where T_1 denotes the duration of the perturbed spiking or bursting cycle.

The PRCs characterizing the assembly response in the spiking regime are provided in

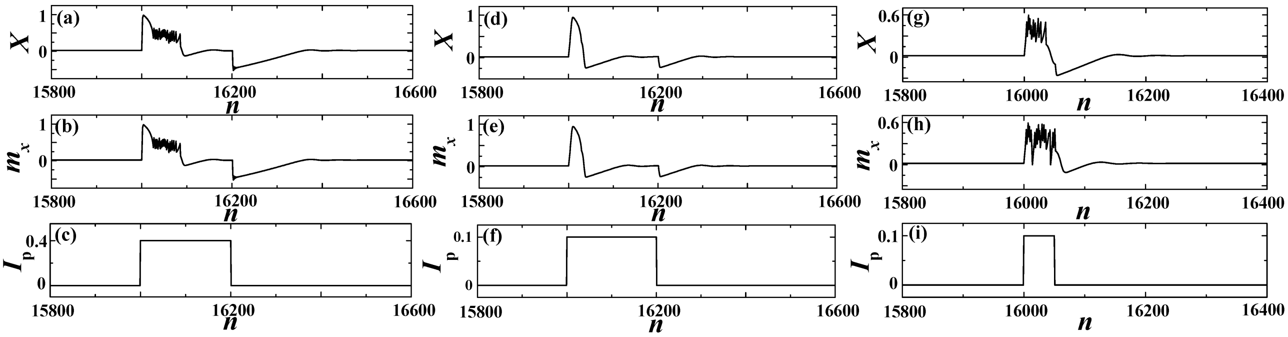

Figure 2.15: Stimulus-response relationship in the excitable regime ($J = 0.02$). The top (middle) row refers to the response of the full system (*MF* model), whereas the bottom row shows the profile of the external stimulation. In the panels (a)-(c), the system parameters are $\beta = 0.4, \sigma = 0$, while the perturbation is characterized by $a_p = 0.4, \Delta = 200$. Panels (d)-(f) concern the response of an assembly ($\beta = 0.1, \sigma = 0.001$) subjected to a rectangular pulse $a_p = 0.4, \Delta = 200$. Panels (g)-(i) illustrate the response of a population ($\beta = 0.4, \sigma = 0.001$) influenced by the external stimulation $a_p = 0.1, \Delta = 50$. The considered network is of size $N = 500$.

Fig. 2.14(a) and Fig. 2.14(b), whereby the former is obtained under the action of an excitatory ($a_p > 0$), and the latter under the influence of an inhibitory stimulation ($a_p < 0$). We stress that in both instances, the results derived from the effective model, denoted by circles, show excellent agreement with the data for the exact system (solid lines). In qualitative terms, one observes that excitatory stimulation may advance the phase of the spiking cycle if it arrives sufficiently close to the spike, but still before the sharp rising stage. However, an excitatory perturbation acting during the spike or within the effective refractory period has a suppression effect where the next spike is delayed. In contrast to excitatory stimulation, the inhibitory pulse postpones the next firing time if it is introduced within the interval close to the rising stage of the spike.

The *PRC*s determined for an assembly exhibiting collective bursting show qualitatively analogous effects to those described so far, see Fig. 2.14(c) and Fig. 2.14(d). This especially refers to the impact of perturbation delivered sufficiently close to a moment of burst initiation. An apparent difference compared to Fig. 2.14(a) and Fig. 2.14(b) emerges during the bursting stage itself, where the associated *PRC*s expectedly exhibit strong fluctuations. Apart from that, one finds an interesting effect: both the excitatory and the inhibitory stimulation have a facilitatory role, i. e. cause phase advancement during the relaxation stage of the bursting cycle.

For a population in the macroscopic excitability state, we consider scenarios in which the system is perturbed by a rectangular pulse of finite magnitude and duration, where finite means that it is comparable to corresponding features of typical spiking or bursting cycles. Note that the selected J value $J = 0.02$ lies sufficiently far from the interval admitting subthreshold oscillations. To determine whether the *MF* model correctly anticipates the response of the exact system, now in the presence of small to moderate noise, we have provided several illustrative examples of the stimulus-response relationship under finite perturbation in Fig. 2.15. The top and middle row refer to the X and corresponding m_x time series, respectively, while the bottom row shows the profile of the applied stimulus. We find that in the absence of noise or for sufficiently small σ, the effective model reproduces the induced dynamics of the full system quite accurately. This also refers to some highly complex forms of responses, as corroborated in Fig. 2.15(a)-(c), which concern relatively large a_p and Δ. Under increasing σ, the ability of the MF model to predict the dynamics of the exact system gradually reduces in a way which depends nontrivially on β. In particular, for smaller $\beta \approx 0.1$, which would facilitate the macroscopic spiking mode for supercritical J, it turns out that the dynamics of the MF model lies in close agreement to that of the exact system even for moderate noise $\sigma = 0.001$, cf. Fig. 2.15(d)-(f). However, for larger β, such an analogy between the responses of the exact and the MF system is lost, see Fig. 2.15(g)-(i). Naturally, the validity of the predictions given by the MF model deteriorates if the stimulation amplitude a_p and the duration Δ are large, especially in the presence of non-negligible noise.

2.3 *Chapter summary and discussion*

In the present chapter, we have extended the notion of excitability to coupled multiscale systems by studying two paradigmatic examples, namely a motif of adaptively coupled active rotators and a network of globally coupled map neurons.

In section 2.1, we have

- **identified the excitable equilibria** of a binary motif,
- determined the features of the associated **threshold-like behavior**, and
- examined its **stimulus-response relationship**.

Concerning the last point, we have determined four different types of excitable responses to external perturbation. Our findings indicate that the system exhibits *well-defined threshold behavior*, characteristic for Type I excitability, whereby the threshold set partially corresponds to the stable manifold of the saddle point on the synchronization manifold.

Moreover, in section 2.2, we have extended the notion of excitability, showing that an assembly of coupled excitable elements can act as a macroscopic excitable element. We have derived an effective mean field (*MF*) model to address

- the **stability domains and (noise-induced) bifurcations** associated with the macroscopic excitability regime, and
- the **stimulus-response relationship** of the population.

Our reduced low-dimensional model has been derived within the framework of Gaussian approximation, formally introduced in the form of a closure hypothesis. In physical terms, this approximation suggests that the local variables are independent and conform to a normal distribution centered about the assembly mean and characterized by the associated assembly variance. Although the validity of this approximation cannot be established *a priori*, it has been systematically verified by numerically corroborating that the *MF* model reproduces the behavior of the exact system with sufficient accuracy.

Nevertheless, the accuracy of the model has certain limitations, namely

- for too **large noise**, the collective variables of the exact system manifest large fluctuations, explicitly violating the Gaussian approximation, and
- in the vicinity of stochastic bifurcations, where the neglected **finite-size effects** are most prominent, the Gaussian approximation breaks down.

Finally, we have also verified that the *MF* model is capable of capturing the stimulus-response features of the exact system. In the macroscopic excitable regime, for scenarios where the assembly is stimulated by rectangular pulse perturbations of finite amplitude and duration, we have observed substantial analogies between the *PRC*s of the exact and reduced system. For short pulse-like perturbations, it has been found that the approximate system reproduces the *PRC*s of the exact system for both the spiking and bursting regimes of collective activity with high accuracy.

The *MF* model has enabled us to examine the stability and bifurcations of the emergent macroscopic regimes, most notably macroscopic excitability, in a *homogeneous* network of *globally* coupled stochastic maps, as well as to analyze the related stimulus-response relationship. Nevertheless, the remaining open questions are how the macroscopic excitability state is affected by the diversity (parameter heterogeneity) of units, as well as complex network topologies [227, 229].

Chapter 3

Switching Dynamics Induced by the Interplay of Adaptivity and Noise

The present chapter comprises a study of noise-induced switching dynamics in excitable systems with a multiple timescale structure, whereby we will consider the conditions that give rise to the phenomenon, as well as the mechanisms underlying it. Within this study, we will combine classical multiple timescale analysis for deterministic systems with standard concepts from stochastic systems, such as metastable states, escape processes, and noise-induced switching.

A feature common to many nonlinear dynamical systems is the coexistence of several stable states (attractors) for a given set of parameters, referred to as *multistability* [40]. Multistability may emerge due to a variety of mechanisms, including coupling or delayed feedback [41]. In such systems, each attractor has a corresponding basin of attraction, i. e. the set of external initial conditions from which the system's dynamics converges to that particular attractor. Due to a sufficiently strong perturbation and/or rapid change of a parameter, a multistable system may *switch* from one stable state to another [41]. Switching may also be induced by *noise*, in which case it connects metastable states derived from the attractors of the deterministic system. The process of noise-induced switching is characterized by an additional timescale introduced by noise.

The dynamics of many complex systems involves a multiple timescale structure, which may be inherent to local dynamics of the units and/or may be associated with the coupling dynamics. An example of the former is provided by classical neuronal models where the evolution of the recovery or gating variables is typically much slower than the changes in the membrane potential [74, 245], while the latter involves mechanisms such as feedback or adaptivity. Adaptivity refers to the feature of complex systems where the interactions between the constituents are affected by the constituents' states [43, 44, 45, 46]. Such self-organized dynamics involves complex feedback mechanisms where the structure of the couplings adapts to the dynamics of the constituent units, which in turn influences their evolution. The modeling of such systems is based on the paradigm of adaptive networks, where self-organization unfolds both at the level of the interactions and the constituents' collective dynamics. Typically, the dynamics of adaptive networks features multiple characteristic timescales, differing in orders of magnitude, whereby the faster/slower timescale is associated with the dynamics of the units/couplings. Such a separation of timescales implies that the short-term evolution of the units occurs on a quasi-static network, whereas the slow changes in couplings depend on the time-averaged dynamics of the units. For instance, at the level of neural networks, certain mechanisms of synaptic adaptation, such as spike-timing-dependent plasticity (STDP) [84, 85, 86, 246, 247, 248], are slower than the spiking dynamics of individual neurons. Investigating the dynamics of such multiple timescale systems has lead to the development of a number of useful asymptotic and geometric methods [47, 48, 49, 50, 51]. Subjecting an excitable system to additional feedback or coupling it to other such systems may give rise to the emergence of different forms of oscillations, patterns, propagating waves, and other self-organizing phenomena [67, 94, 130, 149, 181, 249, 250, 251, 252, 253].

Another essential feature of complex systems is stochasticity or randomness. In modeling, noise may describe the intrinsic randomness of the system, account for the fluctuations in the embedding environment, or derive from coarse-graining over the degrees of freedom associated with small spatial or temporal scales [2, 67]. Neural dynamics, for instance, is influenced by intrinsic sources of noise, such as the random opening of ion channels, as well as by external sources, like synaptic noise [69]. Recent years have witnessed a rapid expansion of stochastic models for a wide variety of important physical and biological phenomena, from sub-cellular processes and tissue dynamics, over large-scale population dynamics and genetic switching to optical devices, Josephson junctions, fluid mechanics, and climatology. These studies have demonstrated that the effects of noise manifest themselves on a broad range of scales, nevertheless displaying certain universal features. From a physical standpoint, noise either modifies the deterministic features of the system or induces qualitatively novel types of behavior [67], such as noise-induced switching.

To study the impact of noise on excitable systems with a multiple timescale structure, we have constructed the following two simplified models:

A. **two identical adaptively coupled stochastic active rotators with excitable local dynamics** [181, 193, 254], whereby adaptivity is modeled by phase-dependent plasticity [205, 206, 207];

B. **a stochastic excitable active rotator with a slowly adapting feedback**.

Both models incorporate the basic ingredients of neurodynamics such as excitability, plasticity, and noise. The active rotator model, common to both systems, is paradigmatic for Type I excitability, whereas the stochasticity, modeled by Gaussian white noise, accounts for synaptic noise. Model A may be interpreted as a binary neuron motif, while model B may describe a neuron with a slow recovery variable, a model of population dynamics influenced by a slowly varying environment, or, more generally, an excitable system under the influence of a nonlinear control mechanism. As far as adaptivity is concerned, the setup in model A allows for continuous interpolation between different plasticity rules such as those analogous to Hebbian learning or STDP, whereas the one considered in model B provides positive feedback for spiking behavior. In the following, we will provide a preview of the main results and methods applied.

Within our study on model A, we have discovered two qualitatively different types of slow stochastic fluctuations depending on the scale separation, or rather adaptivity rate. For slow adaptation, noise induces two characteristic timescales, one related to two modes of noise-induced oscillations, and the other giving rise to slow stochastic fluctuations between them. For faster adaptation, noise gives rise to bursting-like behavior, based on stochastic switching between the metastable states derived from coexisting attractors of the deterministic system.

Within our research on model B, we have found that the interplay of slowly adapting feedback and noise may give rise to three dynamical regimes, namely *noise-induced spiking, noise-perturbed oscillations, and stochastic busting*. The last is a new type of emergent behavior based on switching dynamics due to which the system alternates between episodes of spiking and relative quiescence. Moreover, we demonstrate that adjusting the feedback strength influences the form of the switching dynamics, providing a mechanism for the control of the statistical features of stochastic bursting.

In terms of theoretical methods, the main significance of the research on model B lies in the development of a novel approach which provides an extension of the classical singular perturbation theory to stochastic multiscale systems. In particular, we have first analyzed the noise-free system, employing a combination of two standard multiscale methods – *adiabatic elimination* in the regime where the fast subsystem has a stable equilibrium, and *averaging* when the fast subsystem is oscillatory. A bifurcation analysis of the resulting reduced slow system reveals that the two attractors of the fast flow give rise to bistable dynamics within the slow flow for a sufficiently strong feedback. Moreover, to perform a multiscale analysis of the system's noisy dynamics, we have applied the method of *stochastic averaging* [181, 182, 255, 256, 257] in which the dynamics of the slow flow is determined using the distribution density for the fast variable obtained from a stationary Fokker-Plank equation. This has allowed us to obtain averaged slow dynamics for which we have performed a complete numerical bifurcation analysis with respect to noise intensity and the control gain or feedback strength parameter, obtaining a bifurcation diagram with a characteristic bistability region of the slow flow, as well as the stability boundaries of the three dynamical regimes. In the case of finite scale separation, stochastic bursting is found to emerge due to noise-induced switching of Kramers type.

The chapter is organized as follows. Section 3.1 is devoted to the analysis of switching dynamics in model A. The model is presented in section 3.1.1 along with its deterministic dynamics, while section 3.1.2 contains the results of the corresponding slow-fast analysis. Finally, section 3.1.3 concerns the stochastic behavior of model A, whereby the features of the two generic types of switching behavior are considered within a multiscale framework.

Section 3.2 addresses the switching dynamics exhibited by model B. In particular, the details of the model are introduced in section 3.2.1, whereas section 3.2.2 contains an analysis of its deterministic dynamics within the framework of singular perturbation theory. Sections 3.2.3 and 3.2.4 address the influence of noise in model B, whereby the former concerns the extension of singular perturbation theory to stochastic systems by employing the method of stochastic averaging, while the latter provides an analysis of switching dynamics in the case of finite timescale separation. The concluding section 3.3 contains a summary and discussion of the presented results.

– 3.1 *Switching in a motif of two adaptively coupled excitable units* –

In this section, we will show that the interplay of noise and plasticity gives rise to slow stochastic fluctuations in a system of two coupled active rotators with excitable local dynamics. Depending on the scale separation (adaptation rate), we observe two qualitatively different types of switching behavior. For slower adaptation, one finds alternation between two modes of noise-induced oscillations, whereby the modes are distinguished by a different order of spiking between the units. In the case of faster adaptation, the system switches between four metastable states derived from coexisting attractors of the corresponding deterministic system, whereby the phases exhibit bursting-like behavior. The qualitative features of the switching dynamics are analyzed within the framework of slow-fast analysis [181].

3.1.1 Model and deterministic dynamics of the full system

The model considered in this section is a stochastic version of system (2.1) from the previous chapter. In particular, the dynamics of the phases $\{\varphi_1(t), \varphi_2(t)\}$ and the couplings $\{\kappa_1(t), \kappa_2(t)\}$ now reads

$$\begin{aligned}
\dot{\varphi}_1 &= I_0 - \sin\varphi_1 + \kappa_1 \sin(\varphi_2 - \varphi_1) + \sqrt{D}\xi_1 \\
\dot{\varphi}_2 &= I_0 - \sin\varphi_2 + \kappa_2 \sin(\varphi_1 - \varphi_2) + \sqrt{D}\xi_2 \\
\dot{\kappa}_1 &= \varepsilon(-\kappa_1 + \sin(\varphi_2 - \varphi_1 + \beta)) \\
\dot{\kappa}_2 &= \varepsilon(-\kappa_2 + \sin(\varphi_1 - \varphi_2 + \beta)),
\end{aligned} \tag{3.1}$$

where $\varphi_1, \varphi_2 \in S^1$, while $\kappa_1, \kappa_2 \in \mathbb{R}$, and $0 < \varepsilon \ll 1$ is the timescale separation parameter. Once again, the analysis will be confined to excitable local dynamics ($I_0 < 1$) with $I_0 = 0.95$ fixed, as well as the β interval which admits excitable fixed points, interpolating between the Hebbian learning rule $\beta = 3\pi/2$ [206, 207] and the STDP-like plasticity rule $\beta = \pi$. White noise of variance D acts only within the subspace of fast variables, whereby the terms $\xi_1(t)$ and $\xi_2(t)$ are independent ($\langle\xi_i(t)\xi_j(t')\rangle = \delta_{ij}\delta(t - t')$ for $i, j \in \{1, 2\}$). Recall that system (3.1) with $D = 0$ is invariant to exchange of units' indices ($\mathbb{Z}_2$ symmetry).

The noiseless uncoupled system always converges to a steady state, whereas oscillations may emerge due to interactions and/or noise. Let us first consider the impact of interactions by analyzing the deterministic dynamics of (3.1). To this end, we will evoke the previously obtained results on the stationary states and the associated excitability feature, see section 2.1, after which we will analyze the onset and waveform of emergent oscillations.

3.1.1.1 Stationary states

Recall that the fixed points $(\varphi_1^*, \varphi_2^*, \kappa_1^*, \kappa_2^*)$ of the full system (3.1) with $D = 0$ are given by the solutions of the following set of equations:

$$\sin\varphi_1^* - \sin(\varphi_2^* - \varphi_1^* + \beta)\sin(\varphi_2^* - \varphi_1^*) = I_0,$$
$$\sin\varphi_2^* - \sin(\varphi_1^* - \varphi_2^* + \beta)\sin(\varphi_1^* - \varphi_2^*) = I_0,$$

having used

$$\kappa_1^* = \sin(\varphi_2^* - \varphi_1^* + \beta),$$
$$\kappa_2^* = \sin(\varphi_1^* - \varphi_2^* + \beta).$$

Depending on β, there may be two, four or six fixed points, see Fig. 2.2. Nevertheless, our analysis concerns the interval $\beta \in (3.298, 4.495)$ in which the system has *two stable* fixed points lying off the synchronization manifold $\varphi_1 = \varphi_2$ as well as four unstable fixed points. The bifurcations associated with the boundaries of the given β interval are as follows: at $\beta = 3.298$ the system undergoes a supercritical symmetry-breaking pitchfork bifurcation where a symmetry-related pair of two stable fixed points off the synchronization manifold is created, whereas at $\beta = 4.495$, this pair meets a pair of unstable fixed points off the synchronization manifold, getting annihilated in symmetry-related inverse saddle-node bifurcations.

The two stable fixed points in the interval $\beta \in (3.298, 4.495)$ are *excitable foci*. Recall that the system may exhibit several different types of response to external perturbations as illustrated in Fig. 2.3. Once again, we will set the plasticity parameter to $\beta = 4.212$ for which the fixed points are given by

$$(\varphi_1^*, \varphi_2^*, \kappa_1^*, \kappa_2^*) = (1.2757, 0.2127, -0.0078, -0.8456)$$
$$(\varphi_1^*, \varphi_2^*, \kappa_1^*, \kappa_2^*) = (0.2127, 1.2757, -0.8456, -0.0078).$$

Note that these weight levels support effective master-slave configurations in which one unit exerts a much stronger influence on the other unit than vice versa.

3.1.1.2 The onset of oscillations

The onset of emergent oscillations in the full system (3.1) with $D = 0$ depends on the interplay between the plasticity rule, specified by β, and the adaptation rate, characterized by ε. We have determined the maximal stability region of the periodic solution in the (β, ε) parameter plane by numerical continuation, in which the final state reached for a certain set of (β, ε)

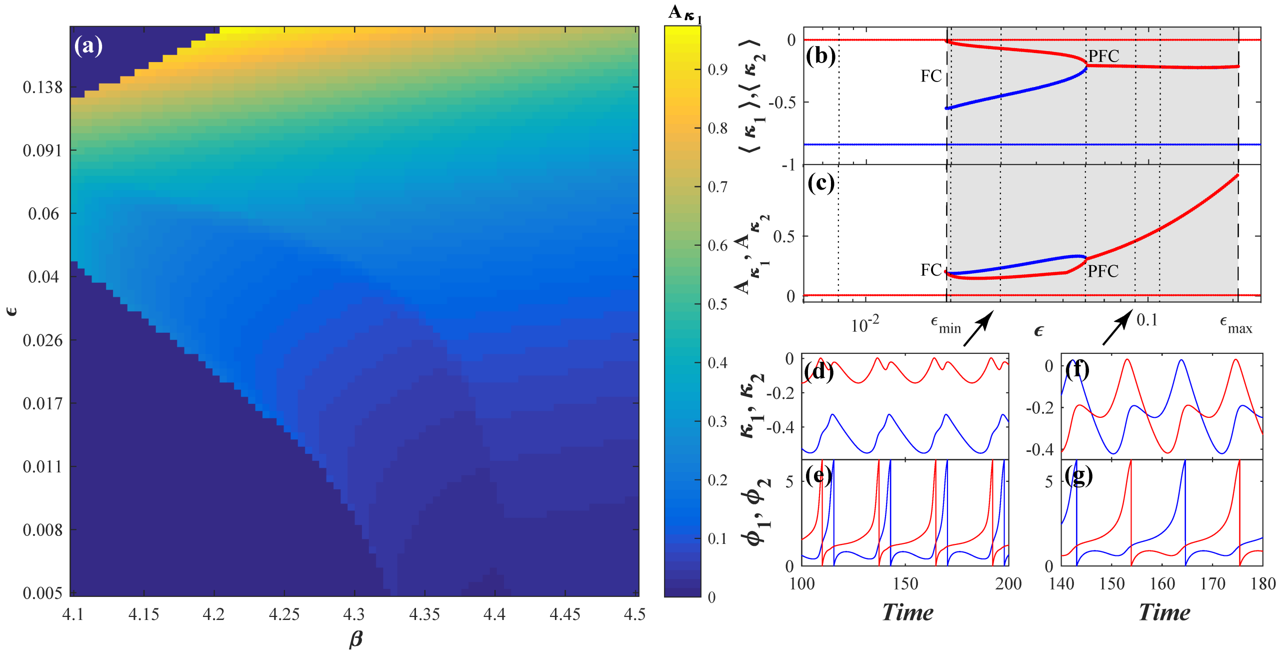

Figure 3.1: Emergence of oscillations in system (3.1) with $D = 0$ for $I_0 = 0.95$. The maximal stability region of the periodic solutions is indicated in panel (a), which shows how the variation A_{κ_1} of the coupling weight κ_1 changes in the (β, ε) plane. Panel (b) shows the dependencies $\langle\kappa_1\rangle(\varepsilon)$ and $\langle\kappa_2\rangle(\varepsilon)$, whereas panel (c) contains $A_{\kappa_1}(\varepsilon)$ and $A_{\kappa_2}(\varepsilon)$, both under fixed $\beta = 4.212$. In (b) and (c), the red and blue thick (thin) solid lines in correspond to the oscillatory (stationary) state, black dotted lines indicate ε values corresponding to the time traces in Fig. 3.5, gray shading designates the ε region supporting multistability of two symmetry-related equilibria and two limit cycles, while *FC* and *PFC* denote the fold of limit cycles and pitchfork of limit cycles bifurcations, respectively. Panels (d)-(g) show the waveforms before and after *PFC*, obtained for $\varepsilon = 0.03$ and $\varepsilon = 0.09$, respectively (indicated by the arrows).

values provides the initial conditions for the simulation of the system at incremented parameter values. A parameter scan indicating the variation of κ_1, $A_{\kappa_1} = \max(\kappa_1(t)) - \min(\kappa_1(t))$, in terms of (β, ε) is shown in Fig. 3.1(a). Positive values $A_{\kappa_1} > 0$ correspond to oscillations, whereas the steady states are characterized by $A_{\kappa_1} = 0$.

For fixed β within the relevant range, we find an interval of timescale separation values $\varepsilon \in (\varepsilon_{min}, \varepsilon_{max})$ admitting stable periodic solutions which appear as symmetry-related twins. The onset of oscillations at $\varepsilon = \varepsilon_{min}(\beta)$ corresponds to the appearance of *two* stable periodic solutions related via the exchange symmetry of the indices. These solutions are born via two symmetrical fold-cycle bifurcations, indicated by FC in Fig. 3.1(b). Under increasing ε, the two branches of oscillatory solutions eventually merge at $\varepsilon \approx 0.06$, where the system undergoes an inverse (symmetry-gaining) pitchfork bifurcation of limit cycles (PFC). The oscillations coexist with two symmetry-related stable stationary states, cf. Fig. 3.1(b)-(c). Moreover, under increasing β, the maximal stability region of oscillations changes such that the lower boundary value $\varepsilon_{min}(\beta)$ reduces, whereas the upper boundary value $\varepsilon_{max}(\beta)$ grows.

Below the PFC bifurcation, the phases $\varphi_1(t)$ and $\varphi_2(t)$ maintain a small phase-shift, while $\kappa_1(t)$ and $\kappa_2(t)$ have different oscillation profiles, see Fig. 3.1(d) and Fig. 3.1(e), respectively. Above the bifurcation, the system gains anti-phase space-time symmetry,

$$\begin{aligned}\varphi_1(t) &= \varphi_2(t+T/2)\\ \kappa_1(t) &= \kappa_2(t+T/2),\end{aligned}$$

where T denotes the oscillation period, cf. the associated waveforms in Fig. 3.1(g) and Fig. 3.1(f).

3.1.2 Slow-fast analysis of deterministic dynamics

The deterministic dynamics in case of sharp timescale separation between the fast and slow variables, which conforms to slow adaptation, may be analyzed within the framework of singular perturbation theory. This involves complementary treatments of the layer problem, defined on the fast timescale, and the reduced problem, which concerns the slow timescale. Within the layer problem, our aim is to determine the fast flow dynamics $(\varphi_1(t;\kappa_1,\kappa_2),\varphi_2(t;\kappa_1,\kappa_2))$ by treating the slow variables κ_1 and κ_2 as additional system parameters. The goal of the reduced problem is to determine the dynamics of the slow flow $(\kappa_1(t),\kappa_2(t))$ by assuming that the fast flow of the layer problem is either at a stable equilibrium or at the averaged value of a stable periodic solution. Note that multistability of the fast flow gives rise to multiple stable sheets of the slow flow.

3.1.2.1 Dynamics of the fast flow: the layer problem

Within the layer problem, we study the fast subsystem

$$\begin{aligned}\dot{\varphi}_1 &= I_0 - \sin\varphi_1 + \kappa_1 \sin(\varphi_2-\varphi_1)\\ \dot{\varphi}_2 &= I_0 - \sin\varphi_2 + \kappa_2 \sin(\varphi_1-\varphi_2),\end{aligned} \tag{3.2}$$

where $\kappa_1,\kappa_2 \in [-1,1]$ are considered as additional system parameters. Formally, system (3.2) is obtained by setting $\varepsilon = 0$ in (3.1) for $D = 0$.

The numerically obtained bifurcation diagram shown in Fig. 3.2(a) indicates that the fast flow is monostable for the majority of (κ_1,κ_2) values, exhibiting either a fixed point or a limit cycle attractor. The stability boundary of the periodic solution (red curves) has been obtained by numerical continuation of the stable periodic solution, using the final state reached for the given (κ_1,κ_2) set as initial conditions for the system dynamics at the next iteration step. The coexistence between a stable fixed point, lying on the synchronization manifold $\varphi_1 = \varphi_2$, and a limit cycle is found within a small region near the diagonal, shown white in Fig. 3.2(a). Let us now classify the fixed points of the fast flow and then examine the scenarios that give rise to oscillations.

Fixed points — It can be shown that the fast flow admits either two or four fixed points, with the associated (κ_1,κ_2) regions indicated in Fig. 3.2(b). In particular, there are two fixed

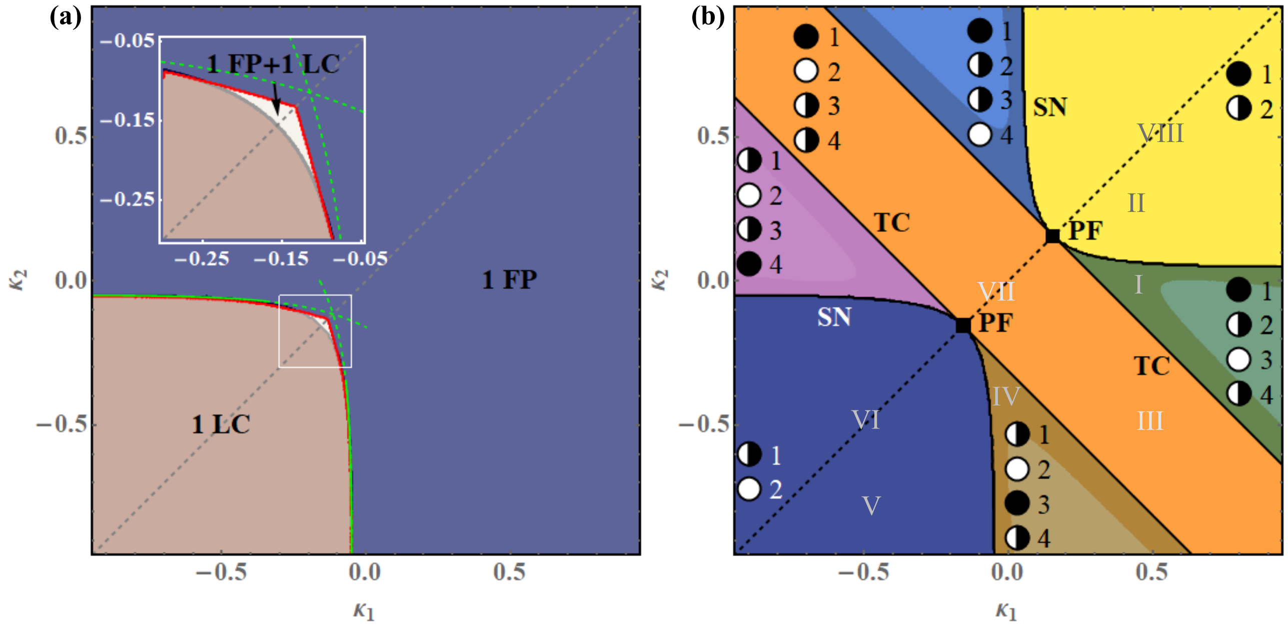

Figure 3.2: (a) Attractors of the fast flow (3.2) in terms of κ_1 and κ_2, now considered as parameters. The fast flow is typically monostable, supporting either a stable fixed point (*FP*) or a stable limit cycle (*LC*), apart from a small region near the main diagonal, indicated in white, where it exhibits bistable behavior. The green curves indicate approximations of two branches of SNIPER bifurcations obtained by the method described in the text. The red lines correspond to the numerically determined stability boundaries of the oscillatory solution. (b) Classification of the fixed points of the fast flow (3.2). The labels of the fixed points correspond to those referenced in the main text, with their stability indicated as follows: full circles denote stable fixed points, semi-full circles represent saddle points and white circles correspond to doubly unstable fixed points. Within the four light-shaded triangular-shaped regions, the node which lies off the synchronization manifold becomes a focus without changing stability. The notation I-VIII refers to parameter values corresponding to the phase portraits in Fig. 3.3.

points on the synchronization manifold, whose coordinates are independent of κ_1 and κ_2:

$$FP1 \equiv (\varphi_1^*, \varphi_2^*) = (\arcsin I_0, \arcsin I_0)$$
$$FP2 \equiv (\varphi_1^*, \varphi_2^*) = (\pi - \arcsin I_0, \pi - \arcsin I_0)$$

Moreover, the fast flow may contain two additional fixed points off the synchronization manifold, referred to as $FP3$ and $FP4$ in Fig. 3.2(b). The bifurcations affecting the number and stability of the fixed points, starting from the lower left region of the (κ_1, κ_2) plane, can be summarized as follows. Along the main diagonal $\kappa_1 = \kappa_2$, we find two points of *supercritical pitchfork bifurcations* (PF) in which the saddles $FP3$ and $FP4$ appear and disappear from symmetric fixed points. Off the main diagonal $\kappa_1 \neq \kappa_2$, the pitchforks unfold into curves of *saddle-node* (SN) and *transcritical bifurcations* (TC), as shown in Fig. 3.2(b).

Within regions of the phase plane where either $FP3$ or $FP4$ is a node, we find subregions where their character changes while retaining the stability features. In particular, in region IV from Fig. 3.2(b), the stable node $FP3$ becomes a stable focus, whereas in region I the unstable node $FP3$ becomes an unstable focus. Analogous scenarios concerning $FP4$ hold for the two regions symmetrical with respect to the main diagonal (purple and light blue).

Periodic solutions — The (κ_1, κ_2) region featuring stable oscillations almost exactly matches the lower left domain admitting two unstable fixed points. Within this region, each periodic solution obtained for (κ_1, κ_2) above the main diagonal $\kappa_1 = \kappa_2$ has a symmetry-related counterpart in the domain below the main diagonal. Depending on κ_1 and κ_2, we find three distinct scenarios by which the two periodic solutions emerge.

In particular, sufficiently far from the main diagonal $\kappa_1 = \kappa_2$, the oscillations emerge via two branches of *SNIPER bifurcations*, where either κ_1 or κ_2 remain nearly constant and close to zero. In either scenario, $FP3$ and $FP4$ collide and disappear as the limit cycle is born. Near the main diagonal, in the small (κ_1, κ_2) region admitting coexistence between fixed point and limit cycle attractors, the onset of oscillations cannot conform to the SNIPER bifurcation scenario, because the total number of fixed points remains unchanged. Instead, the oscillations there emerge via a *heteroclinic bifurcation* in which an orbit connects the two saddles $FP3$ and $FP4$ lying off the synchronization manifold. The orbit of the limit cycle follows the unstable manifold of the saddle point $FP2$ on the synchronization manifold. Slightly away from the main diagonal, one finds that Z_2 symmetry-related limit cycles are born from *homoclinic bifurcations* in which a saddle point, either $FP3$ or $FP4$, emerging as a homoclinic orbit to the saddle FP3 or FP4.

Schematic phase portraits indicating the fixed points along with their stability manifolds, as well as the representative limit cycle, for each of the characteristic regimes of the fast flow denoted by I-VIII in Fig. 3.2(b) are illustrated in Fig. 3.3.

The two branches of SNIPER bifurcations may readily be approximated for small values of κ_1 and κ_2 by a simple scheme which amounts to reducing the fast flow to the normal form of the saddle-node bifurcation. Let us first suppose that $\kappa_1 \ll 1$ and $I_0 - 1 \ll 1$. More specifically, let $\xi \ll 1$ be a small parameter such that $I_0 - 1 = \xi$, and $\kappa_1 = \gamma\xi$, where γ is a rescaling parameter of κ_1, allowing for a zoom in the neighborhood of zero. Then, the steady states are given by the system

$$\begin{aligned} 1 + \xi - \sin\varphi_1 + \xi\gamma\sin(\varphi_2 - \varphi_1) &= 0, \\ 1 + \xi - \sin\varphi_2 + \kappa_2\sin(\varphi_1 - \varphi_2) &= 0. \end{aligned} \tag{3.3}$$

In the zeroth order approximation, the first equation yields $\varphi_1 = \pi/2$. Using the perturbation technique, we obtain that the coordinates $(\varphi_1^*, \varphi_2^*)$ of the steady states satisfy

$$\begin{aligned} \varphi_1^* &= \frac{\pi}{2} + \sqrt{\xi}\Psi_1 + \cdots, \\ \varphi_2^* &= \Psi_2 + \cdots, \end{aligned} \tag{3.4}$$

where the $\sqrt{\xi}$ scaling follows from the Taylor expansion of the function $\sin\varphi_1$ at $\pi/2$. By inserting (3.4) into (3.3), we arrive at the following system of equations for Ψ_1 and Ψ_2

$$\begin{aligned} 1 + \frac{1}{2}\Psi_1^2 - \gamma\cos\Psi_2 &= 0, \\ 1 - \sin\Psi_2 + \kappa_2\cos\Psi_2 &= 0. \end{aligned}$$

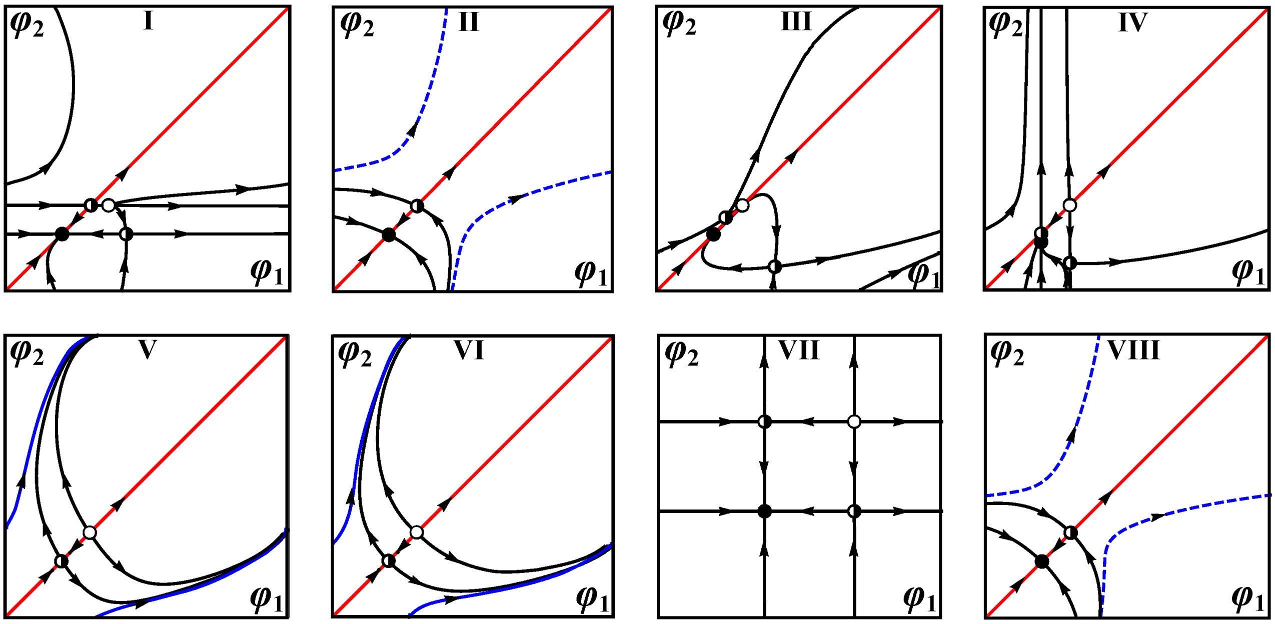

Figure 3.3: Schematic phase portraits corresponding to the characteristic regimes of the fast flow. The panels I-VIII refer to representative parameter values indicated in Fig. 3.2(b). Also, the stability of fixed points is presented the same way as in Fig. 3.2(b). The invariant synchronization manifold is denoted by the red color, whereas the orbit of a stable/unstable limit cycle is indicated by the solid/dashed blue lines.

The saddle-node bifurcation occurs if $\Psi_1 = 0$, i. e. when the condition $1 - \gamma \cos \Psi_2 = 0$ is satisfied. This leads to the following parametric representation of the saddle-node curve for small κ_1 values

$$\kappa_1 = \xi\gamma = \frac{I_0 - 1}{\cos \Psi_2},$$
$$\kappa_2 = \frac{\sin \Psi_2 - 1}{\cos \Psi_2},$$

where Ψ_2 plays the role of the parameter along the curve. An analogous approach may be used to capture the second branch of saddle-node bifurcations, cf. the green dashed lines in Fig. 3.2(a).

3.1.2.2 Dynamics of the slow flow: the reduced problem

We have numerically obtained the dynamics of the slow flow by applying the following two-step approach.

1. Determine the time-averaged dynamics of the fast flow (3.2), $\langle \varphi_2 - \varphi_1 \rangle_t = f(\kappa_1, \kappa_2)$ for fixed (κ_1, κ_2).

   The averaging $\langle \cdot \rangle_t$ must be performed over a sufficiently long time interval, having eliminated a transient. The resulting average depends on the type of attractor of the fast flow for given (κ_1, κ_2). In particular, if the fast flow has a stable fixed point, then

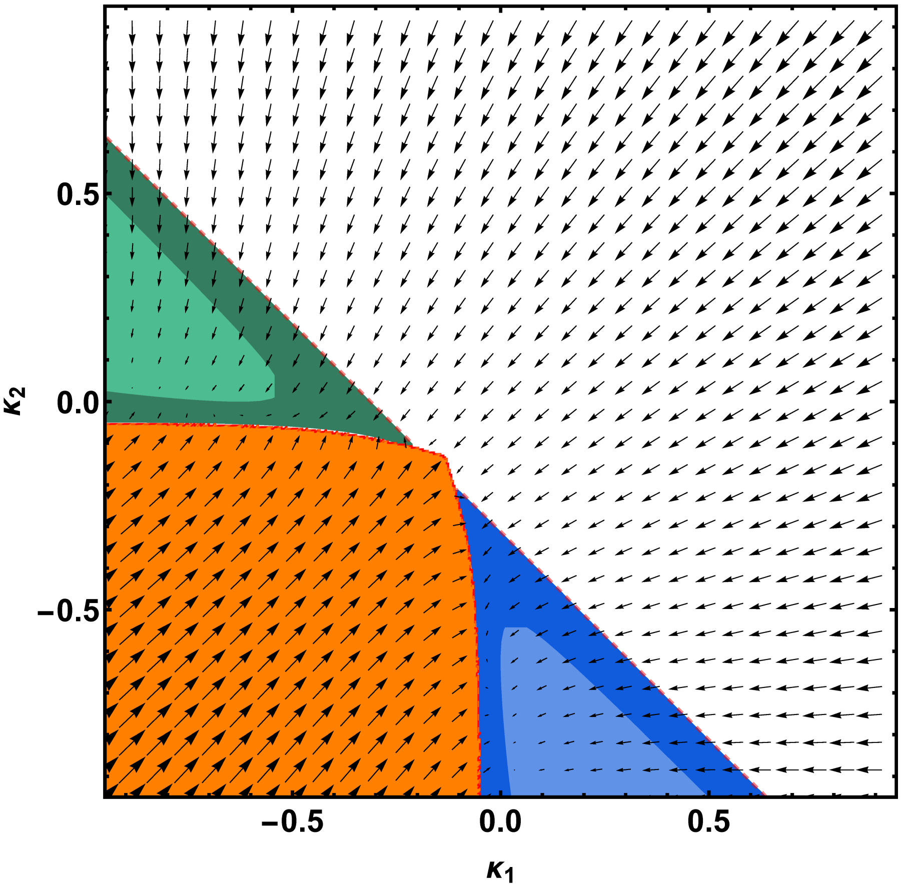

Figure 3.4: The vector field of the slow flow obtained by taking only the stable attractors of the fast flow into account. The color coding is as follows: orange color denotes the region associated with the stable limit cycle of the fast flow, white stands for the stable fixed point $FP1$ of the fast flow, whereas blue and green color correspond to the two stable fixed points $FP3$ and $FP4$. Within the lighter shaded regions, $FP3$ and $FP4$ are foci rather than nodes, cf. Fig. 3.2(b). The system parameters are $\beta = 4.212$, $I_0 = 0.95$.

$\langle \varphi_2 - \varphi_1 \rangle_t = \varphi_2^* - \varphi_1^*$, where $(\varphi_1^*, \varphi_2^*)$ is a solution of

$$\begin{aligned} I_0 - \sin \varphi_1^* + \kappa_1 \sin(\varphi_2^* - \varphi_1^*) &= 0 \\ I_0 - \sin \varphi_2^* + \kappa_2 \sin(\varphi_1^* - \varphi_2^*) &= 0. \end{aligned}$$

This procedure results in determining the slow critical manifold of the system. On the other hand, when the attractor of the fast flow is periodic, $\langle \varphi_2 - \varphi_1 \rangle_t$ presents the time average over the period. Approximating the the effect of the fast oscillations on the slow flow in this way constitutes a standard approach [182, 255], rather natural for describing the influence of oscillations in the fast flow on the dynamics of the slow flow.

2. Substitute the obtained time-averages into the coupling dynamics:

$$\begin{aligned} \dot{\kappa_1} &= \varepsilon[-\kappa_1 + \sin(f(\kappa_1, \kappa_2) + \beta)] \\ \dot{\kappa_2} &= \varepsilon[-\kappa_2 + \sin(-f(\kappa_1, \kappa_2) + \beta)]. \end{aligned} \tag{3.5}$$

We have plotted the vector field of the slow flow (3.5) associated with each attractor of the fast flow within its respective stability region, thus obtaining the stable sheets of the slow flow over the (κ_1, κ_2) parameter plane, cf. Fig. 3.4. In the (κ_1, κ_2) region which admits coexisting stable solutions of the fast flow, namely a stable equilibrium and a stable limit cycle, the corresponding vector field of the slow flow is given by multiple overlapping sheets, since the value of the average $f(\kappa_1, \kappa_2)$ depends on the initial conditions.

Fig. 3.4 shows two important features of the slow flow: (i) it exhibits two symmetry-related fixed points within the green and blue regions, and (ii) the slow vector field is pointed in opposing directions near the boundary between the oscillatory regime (orange region) and the steady states of the fast flow (blue, green, and white regions). The latter implies that we can expect nontrivial effects near the border separating the oscillatory and steady state regime of the fast flow. In particular, adding noise causes fluctuations around this boundary, leading to switching between the quasi-stationary and the fast spiking dynamics. Such effects are studied in more detail within the next section.

3.1.3 Switching dynamics

In this section, we demonstrate how the interaction of plasticity and noise gives rise to slow stochastic fluctuations (switching dynamics) in a motif of two excitable active rotators. Depending on the adaptation rate, we find two qualitatively different scenarios, namely:

1. switching between two modes of noise-induced oscillations for *slower* adaptation (small $\varepsilon \sim 0.01$);

2. switching between multiple coexisting attractors of the deterministic dynamics for *faster* adaptation (intermediate $\varepsilon \simeq 0.05$).

In the first case, the impact of noise is twofold: on a short timescale, it gives rise to spiking dynamics, while on a long time scale, it induces random transitions between the two oscillatory modes. In the second case, the switching dynamics involves metastable states derived from two fixed points, as well as two limit cycles associated with the emergent oscillations of the corresponding deterministic system. The key difference between these two scenarios is that for slower adaptation, the system switches between oscillatory modes that do not exist as deterministic attractors. Moreover, the two generic types of switching are characterized by distinct phase dynamics. In particular, for slower adaptation, there is an alternation of noise-induced oscillation modes that involve a different order of spiking between the units. On the other hand, in the case of faster adaptation, the phases effectively exhibit bursting behavior, involving a succession of spiking episodes and relative quiescence.

Fig. 3.5 provides an overview of how the typical dynamics of couplings changes with ε for fixed β and noise intensity. Note that, for the deterministic system, the difference between the average couplings of the stable periodic solutions is much smaller than the typical distance between the levels corresponding to the stationary states, see Fig. 3.1(b). Concerning the influence of ε on the prevalence of metastable states, intermediate adaptation favors

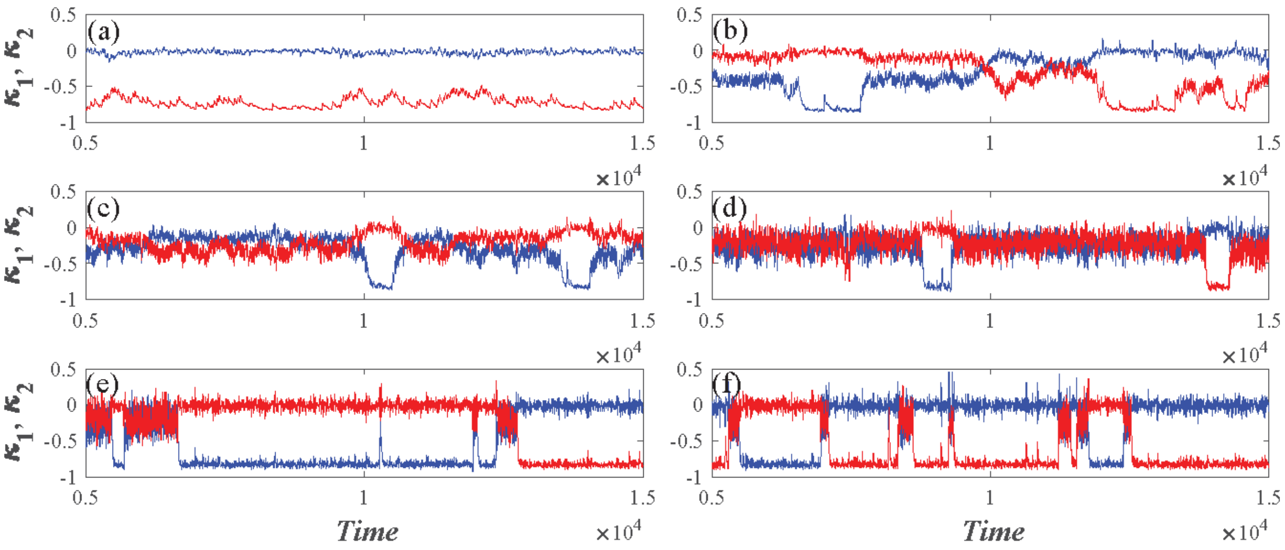

Figure 3.5: Switching dynamics under the variation of ε. The time traces $(\kappa_1(t), \kappa_2(t))$ are obtained for fixed $I_0 = 0.95$, $D = 0.006$, $\beta = 4.212$, whereas ε assumes the following values: (a) $\varepsilon = 0.008$, (b) $\varepsilon = 0.02$, (c) $\varepsilon = 0.03$, (d) $\varepsilon = 0.06$, (e) $\varepsilon = 0.09$, and (f) $\varepsilon = 0.11$.

oscillatory modes, whereas fast adaptation apparently promotes the two quasi-stationary states. The following subsections provide a deeper insight into the mechanisms underlying the switching dynamics.

3.1.3.1 Switching dynamics for slower adaptation

In this case, ε is sufficiently small, in the sense that it cannot facilitate emergent oscillations in the full system (3.1). Nevertheless, noise-induced oscillations may appear under appropriate noise levels for $\varepsilon \simeq 0.01$. These oscillations arise in a scenario that involves a multiple timescale stochastic bifurcation, whereby noise acts only within the fast subsystem of (3.1). The onset of oscillations under increasing D occurs in two stages. In the first stage, the phase dynamics gradually exhibits an increasing number of induced spikes, reflected in the fact that the stationary distributions of the phases eventually acquire a longer tail. Nevertheless, the stationary distributions of the couplings change considerably only at the second stage, reflecting the onset of oscillations of the couplings, which takes place for sufficiently large D. Note that the system (3.1) actually exhibits *two modes* of noise-induced oscillations, characterized by a different order of firing between the two units, as illustrated by the time traces of the phase dynamics and the associated evolution of the couplings in Fig. 3.6(a).

It is interesting to examine whether we can use the vector field of the slow flow, calculated in section 3.1.2.2 and shown on Fig. 3.4, to explain the slow stochastic fluctuations of the couplings. To this end, we have superimposed the $(\kappa_1(t), \kappa_2(t))$ orbits of the two noise-induced modes, as well as that of a switching episode, onto the vector field of the slow flow. Our first observation is that these orbits lie close to the boundary which outlines the transition between the two attractors of the fast flow, where the couplings are non-negligible. Moreover, the two modes are confined to small areas of the (κ_1, κ_2) plane symmetrical with

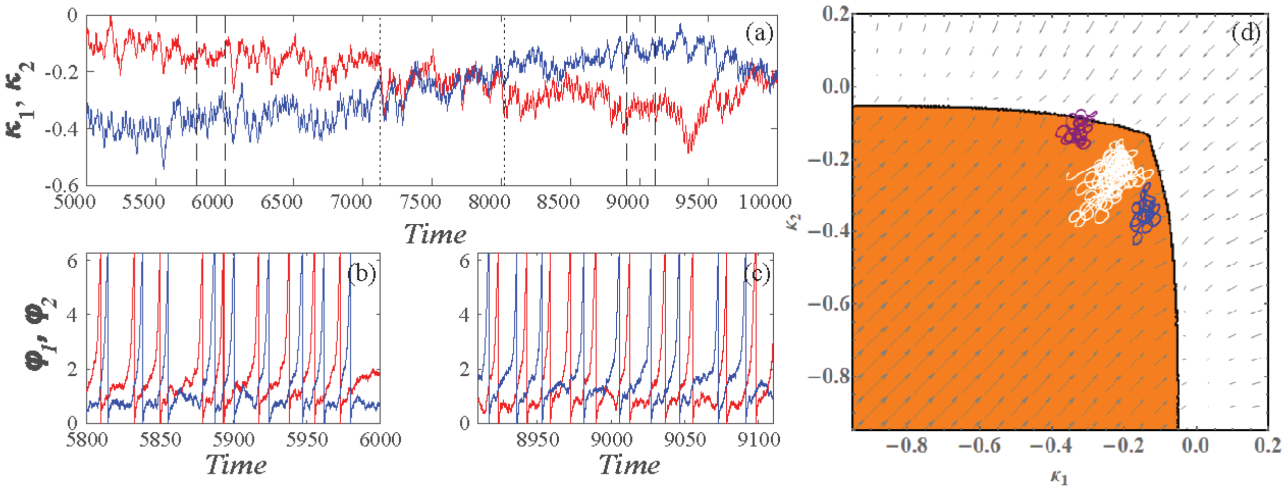

Figure 3.6: Switching dynamics between the two modes of noise-induced oscillations (slow adaptation) for $I_0 = 0.95, \beta = 4.212, \varepsilon = 0.01, D = 0.009$. Time traces of the weights are shown in panel (a), whereas panel (b) and (c) display the corresponding time traces of the phases during the intervals between the dashed lines in panel (a). Panel (d), we superimpose the $(\kappa_1(t), \kappa_2(t))$ projections of the orbits associated with each of the two modes (blue and purple), as well as the switching episode (white) onto the vector field of the slow flow from Fig. 3.4. The orange shaded area corresponds to the stable limit cycle.

respect to the main diagonal $\kappa_1 = \kappa_2$, whereas the switching episode virtually takes place on the diagonal. Apparently, the noise-induced modes occupy regions where the oscillations in the fast flow emerge via homoclinic bifurcations rather than by the SNIPER scenario. Nonetheless, the switching episode involves the domain featuring the coexistence of the two stable sheets of the slow vector field. Within these sheets, which correspond to the two attractors of the fast flow – a stable node and a stable limit cycle – the vector fields are oriented in opposing directions, thereby promoting the switching dynamics.

3.1.3.2 Switching dynamics for faster adaptation

The switching dynamics for faster adaptation involves four metastable states derived from the attractors of the deterministic system. Indeed, recall that for intermediate ε, deterministic multistability involves two symmetry-related stationary states and two symmetry-related limit cycles, cf. Fig. 3.1. While the two stable steady states exist for arbitrary small ε and are therefore visible in the slow flow in Fig. 3.4, the oscillatory solutions disappear for small ε and hence cannot be observed in the slow flow. The two oscillatory regimes are characterized by the same phase shift, however, the order of firing between the two units is reversed. Influenced by noise, the phases effectively engage in bursting behavior, manifesting slow stochastic fluctuations between episodes of intensive spiking activity and periods of relative quiescence, see Fig. 3.7(a). For a fixed noise level, the prevalence of metastable states changes with adaptation speed. In particular, for $\varepsilon \simeq 0.05$, the oscillatory dynamics is preferred, whereas the quasi-stationary states are dominant for $\varepsilon \simeq 0.1$.

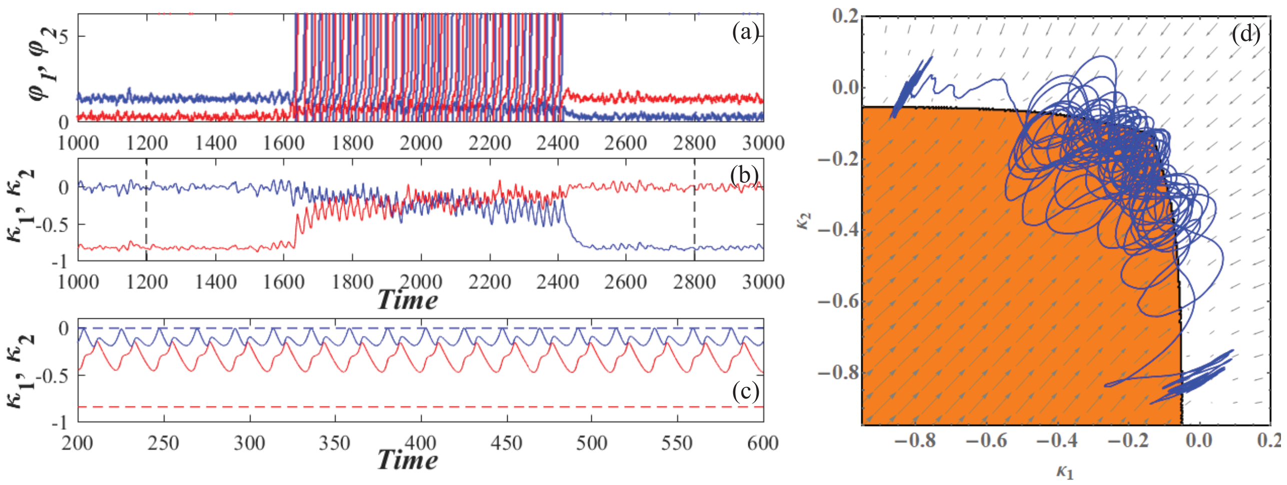

Figure 3.7: Time traces of the phases (a) and weights (b) associated with noise-induced switching between the coexisting attractors of the deterministic system (fast adaptation) for $I_0 = 0.95, \beta = 4.212, \varepsilon = 0.05, D = 0.004$. For comparison, panel (c) shows the deterministic dynamics of weights obtained for the same parameter values. In panel (d), the $(\kappa_1(t), \kappa_2(t))$ orbit corresponding to the interval between the dashed lines in (b) is superimposed onto the vector field of the slow flow, cf. Fig. 3.4.

Comparing the typical (κ_1, κ_2) orbits to the vector field of the slow flow from Fig. 3.4 reveals that the switching is again confined to the criticality region at the boundary between the stationary and oscillatory regimes of the fast flow, cf. Fig. 3.7. As far as the transitions between the different metastable states are concerned, it is clear from Fig. 3.7(b) that there can be no direct transitions between the two quasi-stationary states since the system must pass through the oscillatory states to reach the other stationary level. Moreover, the transition from oscillatory to quasi-stationary dynamics typically occurs once the couplings approach a “master-slave”-like configuration, where the coupling in one direction is much stronger than the other one. This scenario coincides with the SNIPER bifurcation of the fast flow described in section 3.1.2.1. The scenario accounting for transitions between the two metastable oscillatory states closely resembles the one occurring for slower adaptation.

- 3.2 *Switching in an excitable unit with a slowly adapting feedback* -

In this section, we study the model of an excitable system with a slowly adapting feedback to demonstrate how the interaction of noise and multiscale dynamics gives rise to a novel form of emergent behavior, *stochastic bursting*. By extending methods from multiscale analysis to stochastic systems, we have determined the existence domain of stochastic bursting regime, as well as the bifurcations underlying the transitions to other regimes. We also explain how the properties of the switching process, i. e. whether the switching is balanced or biased, influences the statistical features of stochastic bursting [192].

3.2.1 Model

In general, a stochastic excitable system influenced by a low-pass filtered feedback may be modeled as follows:

$$\begin{aligned}\dot{v} &= f(v,\mu) + \sqrt{D}\xi(t), \\ \dot{\mu} &= \varepsilon(-\mu + \eta g(v)),\end{aligned} \tag{3.6}$$

where the small parameter $0 < \varepsilon \ll 1$ defines the timescale separation between the fast variable $v(t)$ and the slow feedback variable $\mu(t)$. The fast dynamics $\dot{v} = f(v, 0)$ is excitable, whereby the excitability feature is influenced by the slow feedback variable $\mu(t)$. Gaussian white noise $\xi(t)$ of variance D acts within the fast subsystem. The parameter η featured in the slow dynamics is the feedback strength, such that for $\eta = 0$ one recovers a classical noise-driven excitable system [67]. An important example of a system conforming to (3.6) for $\eta \neq 0$ is the Izhikevich neuron model [258], in which the stochastic input to the fast variable would describe the action of synaptic noise.

Our analysis will be carried out on a simple, yet paradigmatic model belonging to the class of systems given by (3.6). In particular, the excitable local dynamics is represented by the Type I excitable active rotator model while the slow adaptation is introduced as a positive periodic function $g(\varphi) = 1 - \sin\varphi$, such that the complete model reads

$$\dot{\varphi} = I_0 - \sin\varphi + \mu + \sqrt{D}\xi(t), \tag{3.7}$$

$$\dot{\mu} = \varepsilon\left(-\mu + \eta\left(1 - \sin\varphi\right)\right). \tag{3.8}$$

In the presence of feedback, the deterministic dynamics of the active rotator depends on the term $I_0 + \mu$ involving the control variable $\mu(t)$, which can induce switching between the excitable equilibrium ($|I_0 + \mu| < 1$) and the oscillatory regime ($|I_0 + \mu| > 1$). The chosen adaptation rule provides positive feedback for spiking behavior, since μ increases when $\varphi(t)$ exhibits noise-induced oscillations, effectively driving the system towards the oscillatory regime. On the other hand, in the vicinity of the equilibrium ($\sin\varphi \approx 1$), the feedback effectively vanishes. In the following sections, we will first perform an analysis of the deterministic dynamics within the framework of singular perturbation theory, after which we will extend the analysis to the stochastic dynamics in the limit of infinite timescale separation.

3.2.2 Slow-fast analysis of deterministic dynamics

In this section, we analyze system (3.7)–(3.8) in the absence of noise $(D = 0)$

$$\begin{aligned}\dot{\varphi}(t) &= I_0 - \sin\varphi(t) + \mu(t), \\ \dot{\mu}(t) &= \varepsilon\left(-\mu(t) + \eta\left(1 - \sin\varphi(t)\right)\right),\end{aligned} \tag{3.9}$$

considering the limit $\varepsilon \to 0$ within the framework of singular perturbation theory. The dynamics on the fast timescale is described by the layer equation, formally obtained by

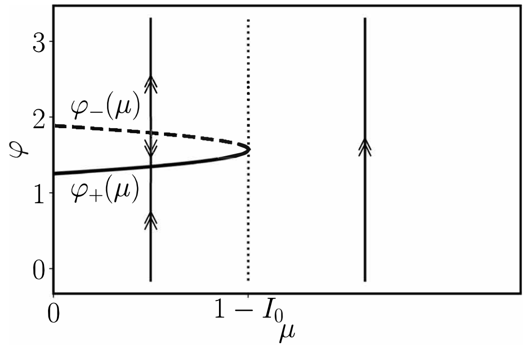

Figure 3.8: Dynamics of the fast flow (3.10). The critical manifold is comprised of the stable branch $\varphi_+(\mu)$, shown by the solid line, and the unstable branch $\varphi_-(\mu)$ (dashed line). For $\mu < 1 - I_0$, the fast dynamics converges to the stable branch of the critical manifold, while for $\mu > 1 - I_0$, it is oscillatory with periodic rotation of the phase φ. The bifurcation threshold $\mu = 1 - I_0$ is indicated by the dotted line.

setting $\varepsilon = 0$ in (3.9) and treating μ as an additional parameter:

$$\dot{\varphi}(t) = I_0 + \mu - \sin \varphi(t). \tag{3.10}$$

The subsequent analysis of the effects of the fast dynamics on the corresponding reduced problem will be based on a combination of two methods from multiple timescale analysis. In particular, depending on whether (3.10) exhibits a stable equilibrium or a limit cycle attractor, we will employ either adiabatic elimination or averaging over fast oscillations to obtain a reduced system capable of describing both regimes, as well as the transitions between them. A bifurcation analysis of the slow subsystem will show that, for sufficiently large η, the system exhibits bistability between the equilibrium and fast oscillations.

3.2.2.1 Stable equilibrium in the fast flow and the method of adiabatic elimination

In the case $\mu < 1 - I_0$, the layer equation (3.10) has two fixed points:

$$\varphi_+(\mu) = \arcsin(I_0 + \mu),$$
$$\varphi_-(\mu) = \pi - \varphi_+(\mu),$$

where φ_+ is stable and φ_- is unstable. As functions of the parameter μ, the two branches of equilibria, $\varphi_+(\mu)$and $\varphi_-(\mu)$ merge in the fold point $\mu = 1 - I_0$, see Fig. 3.8. Equivalently, the set of equililbria of the fast subsystem

$$\{(\varphi, \mu) : \sin \varphi = I_0 + \mu\} \tag{3.11}$$

comprises the *critical manifold* of (3.9), with the stable part $\varphi_+(\mu)$ and the unstable part $\varphi_-(\mu)$.

For $\mu < 1 - I_0$, the fast dynamics is rapidly attracted to the stable branch of the critical manifold $\varphi_+(\mu)$, along which it slowly drifts for $\varepsilon \gtrsim 0$. In order to describe this slow dynamics, we rescale time as $T = \varepsilon t$, obtaining

$$\varepsilon\varphi'(T) = I_0 + \mu(T) - \sin\varphi(T), \tag{3.12}$$

$$\mu'(T) = -\mu(T) + \eta(1 - \sin\varphi(T)), \tag{3.13}$$

where the prime denotes the derivative with respect to the slow time T. By setting $\varepsilon = 0$, we eliminate the $\sin\varphi = I_0 + \mu$ term and arrive at the equation for the slow dynamics on the critical manifold:

$$\mu'(T) = -\mu(T) + \eta(1 - I_0 - \mu(T)). \tag{3.14}$$

3.2.2.2 Stable periodic solution of the fast flow and averaging over fast oscillations

For $\mu > 1 - I_0$, the fast subsystem (3.10) has no fixed points, see Fig. 3.8. Instead, one finds periodic oscillations

$$\varphi_\mu(t) = 2\arctan\frac{1 + \Omega(\mu)\tan\frac{t}{2}\Omega(\mu)}{I_0 + \mu} \tag{3.15}$$

with the μ-dependent oscillation frequency (recall eq. (1.8) from section 1.2.3.1)

$$\Omega(\mu) = \sqrt{(I_0 + \mu)^2 - 1}.$$

In this case, the fast oscillations $\varphi_\mu(t)$ should be averaged in order to approximate their influence on the dynamics of the slow variable $\mu(T)$. Let us first provide a simplified explanation of the averaging procedure. First, we substitute the fast-oscillating solution $\varphi = \varphi_\mu(t)$ of (3.10) into the equation for the slow variable (3.13):

$$\mu'(T) = -\mu(T) + \eta(1 - \sin\varphi_\mu(t)).$$

Since the term $\sin(\cdot)$ oscillates rapidly, the last equation can be averaged over the fast timescale t, which leads to

$$\mu'(T) = -\mu(T) + \eta\left(1 - \left\langle\sin\varphi_\mu(t)\right\rangle_t\right). \tag{3.16}$$

The average $\left\langle\sin\varphi_\mu(t)\right\rangle_t$ can be found by integrating (3.10) over the oscillation period

$$\langle\dot\varphi(t)\rangle_t = \Omega(\mu) = I_0 + \mu - \langle\sin\varphi_\mu(t)\rangle_t \Rightarrow \langle\sin\varphi_\mu(t)\rangle_t = I_0 + \mu(T) - \Omega(\mu(T)),$$

which we substitute into (3.16) to obtain the slow averaged dynamics:

$$\mu'(T) = -\mu(T) + \eta(1 - I_0 - \mu(T) + \Omega(\mu(T))). \tag{3.17}$$

Equation (3.17) for the dynamics of the slow flow ca formally be derived within the so-called *two-timing approach* [39], based on introducing a general multiscale Ansatz of the form:

$$\begin{aligned}\varphi &= \bar\varphi(t, \varepsilon t) + \varepsilon\hat\varphi(t, \varepsilon t),\\ \mu &= \bar\mu(t, \varepsilon t) + \varepsilon\hat\mu(t, \varepsilon t).\end{aligned} \tag{3.18}$$

By substituting (3.18) into (3.9), we obtain up to the terms of the order ε

$$\begin{aligned}\partial_1\bar{\varphi}+\varepsilon\partial_2\bar{\varphi}+\varepsilon\partial_1\hat{\varphi} &= I_0-\sin\left(\bar{\varphi}+\varepsilon\hat{\varphi}\right)+\bar{\mu}+\varepsilon\hat{\mu},\\ \partial_1\bar{\mu}+\varepsilon\partial_2\bar{\mu}+\varepsilon\partial_1\hat{\mu} &= \varepsilon\left(-\bar{\mu}-\varepsilon\hat{\mu}+\eta\left(1-\sin\left(\bar{\varphi}+\varepsilon\hat{\varphi}\right)\right)\right),\end{aligned}$$

where the subscripts 1 and 2 refer to partial derivatives with respect to t and εt, respectively.

The coefficients of each power of ε must vanish separately. Collecting the terms of order $\mathcal{O}(1)$ yields:

$$\partial_1\bar{\varphi}=I_0-\sin\bar{\varphi}+\bar{\mu}, \tag{3.19}$$

$$\partial_1\bar{\mu}=0. \tag{3.20}$$

The equation (3.20) implies that $\bar{\mu}=\bar{\mu}(\varepsilon t)$ depends only on the slow time and acts as a parameter in (3.19). For $\bar{\mu}>1-I_0$, equation (3.19) has the oscillating solution $\bar{\varphi}=\varphi_{\bar{\mu}}(t)$ given by (3.15). Note that the parameters of this solution can depend on the slow time.

In the next step, we consider the terms of order ε:

$$\begin{aligned}\partial_2\bar{\varphi}+\partial_1\hat{\varphi} &= -\hat{\varphi}\cos\bar{\varphi}+\hat{\mu},\\ \partial_2\bar{\mu}+\partial_1\hat{\mu} &= -\bar{\mu}+\eta\left(1-\sin\bar{\varphi}\right),\end{aligned} \tag{3.21}$$

whereby the second equation of (3.21) can be rewritten as

$$\partial_2\bar{\mu}+\bar{\mu}=-\partial_1\hat{\mu}+\eta\left(1-\sin\bar{\varphi}\right), \tag{3.22}$$

where the left-hand side depends only on the slow time. Hence, the solvability condition for (3.22) is that its right-hand side is independent on the fast time t, i.e.

$$-\partial_1\hat{\mu}+\eta\left(1-\sin\bar{\varphi}\right)=u(T) \tag{3.23}$$

with some function $u(T)$, where $T=\varepsilon t$ is the slow time. By integrating (3.23) with respect to the fast time, we obtain

$$\hat{\mu}(t)=\hat{\mu}(0)+\eta\left(t-\int_0^t\sin\bar{\varphi}dt\right)-tu(T) \tag{3.24}$$

The integral in (3.24) can be computed using the intergal form of (3.19), namely:

$$\int_0^t\sin\bar{\varphi}dt=tI_0+t\bar{\mu}-\bar{\varphi}(t)+\bar{\varphi}(0),$$

so that

$$\hat{\mu}(t)=\hat{\mu}(0)+t\left[\eta\left(1-I_0-\bar{\mu}+\frac{\bar{\varphi}(t)-\bar{\varphi}(0)}{t}\right)-u(T)\right].$$

Taking into account that

$$\frac{\bar{\varphi}(t)-\bar{\varphi}(0)}{t}=\Omega(\bar{\mu})+\mathcal{O}\left(\frac{1}{t}\right),$$

we obtain the expression for $\hat{\mu}$:

$$\hat{\mu}(t)=\hat{\mu}(0)+t\left[\eta\left(1-I_0-\bar{\mu}+\Omega(\bar{\mu})\right)-u(T)\right]+\mathcal{O}(1),$$

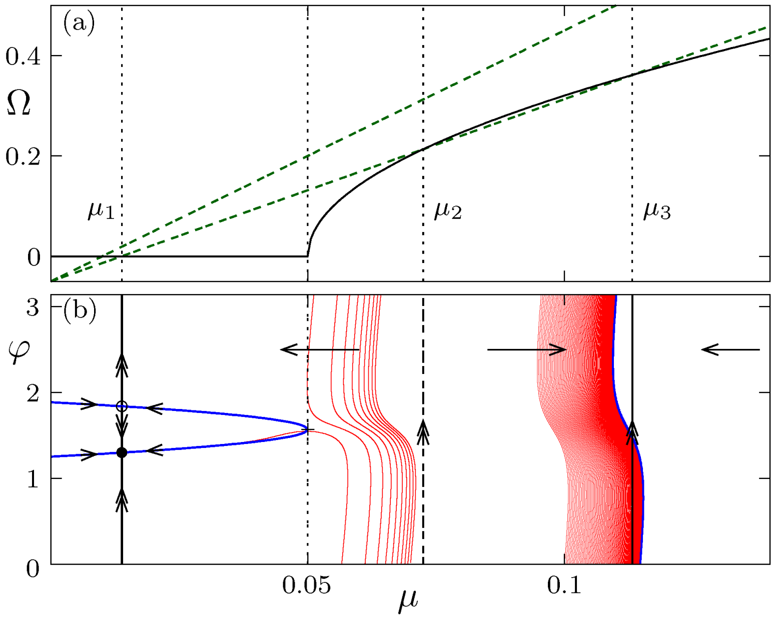

Figure 3.9: (a) Graphical solution of the fixed point equation (3.26): $\Omega(\mu)$ according to (3.25) (black solid line) and the right-hand side of (3.26) for two different choices of η (green dashed lines). Depending on η, the equation may have from one to three fixed points. (b) Scheme of the slow-fast dynamics of system (3.9) with parameters $I_0 = 0.95$ and $\eta = 0.38$ and the numerical sample trajectories for $\varepsilon = 0.005$ (red). For $\mu < 1 - I_0$, the trajectories are attracted to the stable branch of the slow manifold (blue curve) and subsequently slowly drift toward the stable fixed point $(\varphi_+(\mu_1), \mu_1)$ (black dot). For $\mu > 1 - I_0$, the sample trajectories show fast oscillations in φ with a slow average drift in μ in the direction indicated by the arrows.

where the linearly growing term must vanish for $\hat{\mu}(t)$ to be bounded. By setting this secular term to zero (even without computing explicitly $\hat{\mu}$), we have

$$u(T) = \eta\left(1 - I_0 - \bar{\mu} + \Omega(\bar{\mu})\right).$$

Therefore, taking into account (3.22) and (3.23), the equation for the leading order approximation of the slow variable reads

$$\partial_2\bar{\mu} + \bar{\mu} = \eta\left(1 - I_0 - \bar{\mu} + \Omega(\bar{\mu})\right).$$

Since $\bar{\mu}$ is a function of the slow time only, we have $\partial_2\bar{\mu} = \bar{\mu}'$, finally arriving at the equation for the slow dynamics given by (3.17),

$$\mu'(T) = -\mu(T) + \eta(1 - I_0 - \mu(T) + \Omega(\mu(T))).$$

3.2.2.3 Combined dynamics of the slow variable

Having obtained the dynamics of the slow variable for both $\mu < 1 - I_0$ and $\mu > 1 - I_0$ as given by equations (3.14) and (3.17), respectively, let us now combine these results into a single equation of the form (3.17) by extending the definition of the frequency $\Omega(\mu)$ to

$$\Omega(\mu) = \begin{cases} 0, & \mu < 1 - I_0 \\ \sqrt{(I_0 + \mu)^2 - 1}, & \mu > 1 - I_0 \end{cases}. \tag{3.25}$$

Since the slow dynamics is described by the scalar ordinary differential equation on the real line, the only possible attractors are fixed points, which are given by the zeros of the right-hand side of (3.17):

$$\Omega(\mu) = \frac{\eta+1}{\eta}\mu + I_0 - 1 \tag{3.26}$$

Geometrically, the fixed points correspond to the intersection points of the frequency profile $\Omega(\mu)$ and the line $\frac{\eta+1}{\eta}\mu + I_0 - 1$, as shown in Fig. 3.9(a). In particular, one fixed point always exists for $\Omega(\mu_1) = 0$, namely,

$$\mu_1 = \frac{\eta(1-I_0)}{1+\eta} < 1 - I_0, \tag{3.27}$$

corresponding to a pair of equilibria on the critical manifold (3.11). Since μ_1 is stable for the slow dynamics, the point $(\varphi_+(\mu_1), \mu_1)$ is also a stable equilibrium for the original system (3.9) with small ε. The other two fixed points of the slow equation

$$\mu_{2,3} = \frac{\eta\left(1+\eta-I_0 \mp \sqrt{(\eta+I_0)^2 - 1 - 2\eta}\right)}{1+2\eta}$$

with $\Omega(\mu_{2,3}) > 0$ appear in a saddle-node bifurcation at

$$\eta_{\mathrm{sn}} = 1 - I_0 + \sqrt{2(1-I_0)}, \tag{3.28}$$

and correspond to a pair of periodic orbits of the layer equation (3.10).

The results of our slow-fast analysis are schematically shown in Fig. 3.9(b) for $I_0 = 0.95$ and $\eta = 0.38$. The chosen parameter values admit two stable regimes, namely, the *fixed point* $(\varphi_+(\mu_1), \mu_1)$ and *fast oscillations* for which $\langle\mu(t)\rangle_t \approx \mu_3$ holds.

Finally, Fig. (3.10) presents the bifurcation diagram for the fixed points of the slow dynamics with respect to the feedback strength η. One observes that one branch of stable fixed points corresponding to the steady state always exists, while two stable fixed points corresponding to fast oscillations appear when $\eta > \eta_{\mathrm{sn}}$.

3.2.3 Slow-fast analysis of stochastic dynamics: stochastic averaging approach

This section contains details on how singular perturbation theory may be extended to the case where the fast flow dynamics is stochastically perturbed. In particular, to determine the dynamics of the slow flow, we will perform *stochastic averaging* over the stationary probability density of the fast variable obtained by solving the corresponding Fokker-Planck equation. This method allows us to numerically construct a bifurcation diagram in terms of D and η.

In analogy to the noise-free case, in the $\varepsilon \to 0$ limit we can consider the averaged fast dynamics

$$\langle \sin\varphi(t)\rangle_t = \lim_{t\longrightarrow\infty} \frac{1}{t}\int_0^t \sin\varphi(t)\mathrm{d}t'$$

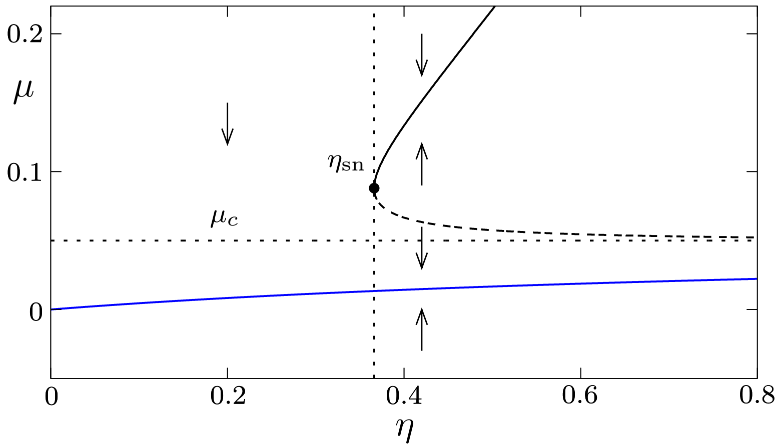

Figure 3.10: Fixed points of the slow dynamics (3.17) for varying feedback strength η. The values $\mu_{2,3}$ on the upper branch (black curve) correspond to periodic orbits of the layer equation (3.10), while μ_1 (blue curve) is the branch of fixed points (3.11). Solid and dashed lines indicate stable and unstable solutions, respectively. The direction of the motion in $\mu(T)$ is indicated by the arrows. The dotted lines indicate the onset of bistability for $\eta = \eta_{\mathrm{sn}}$ (3.28) and the transition at $\mu_c = 1 - I_0$ from equilibria to periodic orbits.

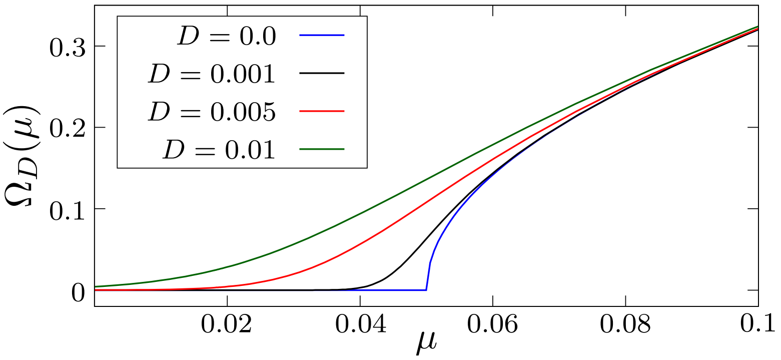

Figure 3.11: Average frequency of the fast dynamics (3.7) for $I_0 = 0.95$ given by (3.34)- (3.35) obtained by using numerical solutions of the stationary Fokker-Planck equation (3.31) in which μ acts as a time independent parameter.

for the stochastic layer dynamics

$$\dot{\varphi}(t) = I_0 + \mu - \sin\varphi(t) + \sqrt{D}\xi(t) \tag{3.29}$$

in order to approximate the slow flow (3.13) by

$$\mu'(T) = -\mu(T) + \eta(1 - \langle \sin\varphi(t)\rangle_t). \tag{3.30}$$

To calculate the average over stochastic fast dynamics, we use the *stationary probability density distribution* $\rho(\varphi; \mu, D)$, which is for fixed μ and noise intensity D given as a solution of the stationary Fokker-Planck equation

$$\frac{D}{2}\partial_{\varphi\varphi}\rho - \partial_\varphi\left[(I_0 + \mu - \sin\varphi)\rho\right] = 0, \tag{3.31}$$

complemented by the periodic boundary conditions

$$\rho(0) = \rho(2\pi) \tag{3.32}$$

as well as the normalization condition

$$\int_0^{2\pi} \rho(\varphi;\mu,D)\mathrm{d}\varphi = 1. \tag{3.33}$$

Then we can calculate the *stochastic average*

$$\langle \sin\varphi(t)\rangle_t = \int_0^{2\pi} \rho(\varphi;\mu,D)\sin\varphi \mathrm{d}\varphi \tag{3.34}$$

and obtain the mean frequency

$$\Omega_D(\mu) = I_0 + \mu - \langle \sin\varphi(t)\rangle_t, \tag{3.35}$$

which depends via (3.34) both on D and μ. Taking into account (3.30) and (3.35), the equation for the slow dynamics of $\mu(T)$ now reads

$$\mu'(T) = -\mu(T) + \eta(1 - I_0 - \mu + \Omega_D(\mu(T))), \tag{3.36}$$

i.e. it is of the same form as in the deterministic case (3.17). The corresponding fixed point equation for the stationary values of μ with respect to the slow dynamics is given by (3.26).

The stationary Fokker-Planck equation (3.31) can be solved directly by integral expressions. Integrating (3.31) once yields

$$\frac{D}{2}\partial_\varphi\rho - (I_0 + \mu - \sin\varphi)\,\rho = C \tag{3.37}$$

with the constant C to be determined. The solution of (3.37) with the normalization (3.33) and the boundary (3.32) conditions is given by

$$\begin{aligned}
\rho(\varphi;\mu,D) &= \frac{1}{g_\Lambda}\Lambda(\varphi), \text{where}\\
\Lambda(\varphi) &= \int_0^{2\pi} \frac{\Psi(\varphi)}{\Psi(\varphi+\lambda)} d\lambda,\\
g_\Lambda &= \int_0^{2\pi} \Lambda(\varphi) d\varphi,\\
\Psi(\varphi) &= \exp\left\{\frac{2}{D}\left[(I_0+\mu)\varphi + \cos\varphi - 1\right]\right\}.
\end{aligned} \tag{3.38}$$

For small non-vanishing D, the numerical evaluation of the integrals is difficult, so we have solved (3.31) as a first-order ODE boundary value problem with the software AUTO [259], which provides numerical solutions to boundary value problems by collocation methods together with continuation tools for numerical bifurcation analysis.

The numerically obtained effective frequencies $\Omega_D(\mu)$ for different noise levels D are shown in Fig. 3.11. Solving the stationary Fokker-Planck equation (3.31) together with the fixed point equation for $\mu(T)$ (3.26) yields branches of stationary solutions $(\mu^*, \rho(\varphi;\mu^*,D))$ for fixed values of D and varying feedback strength η, as shown in Fig. 3.12(a). For small noise intensities, these branches are folded, indicating the coexistence of up to three stationary solutions, similar to the noise-free case. Alternatively, we can also fix η and obtain

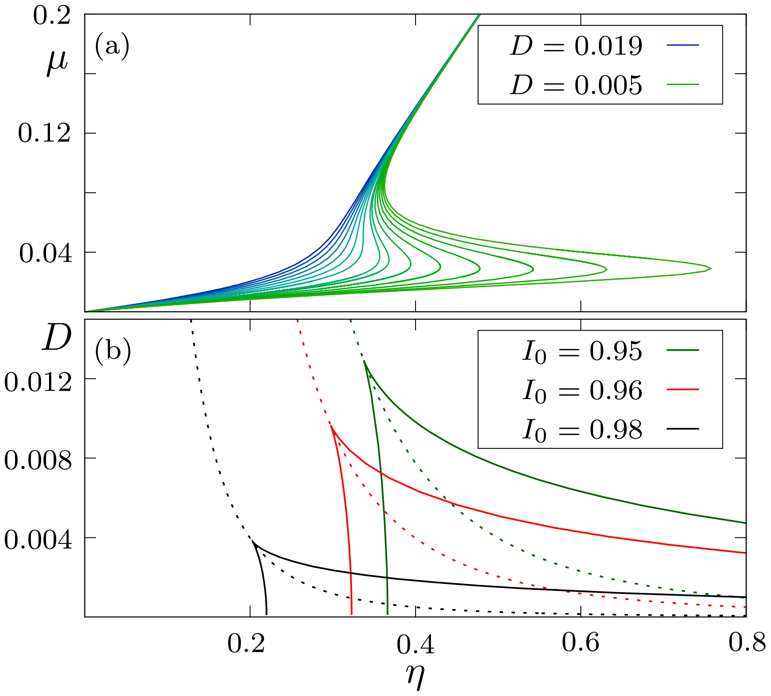

Figure 3.12: (a) Branches of fixed points $\mu^*(\eta)$ of the slow dynamics (3.36) for a set of noise values $D \in \{0.005, 0.006, \ldots, 0.019\}$ and $I_0 = 0.95$, calculated from (3.26) together with the stationary Fokker-Planck equation (3.31). (b) Two-dimensional bifurcation diagrams in terms of η and D for three different values of I_0 show the curves of fold bifurcations, which meet at the cusp point. The dashed curves indicate the case where $\mu = \mu_c = 1 - I_0$.

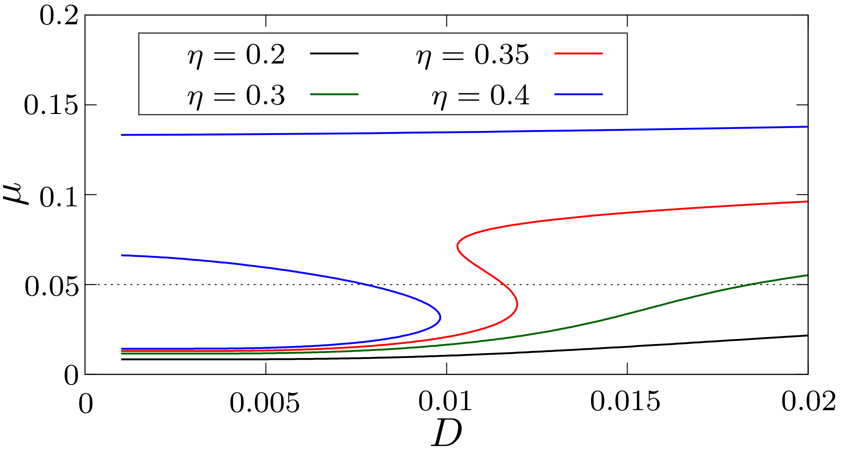

Figure 3.13: Branches of fixed points $\mu^*(D)$ of the slow dynamics (3.36) for a set of feedback strength values $\eta \in \{0.2, 0.3, 0.35, 0.4\}$ and fixed $I_0 = 0.95$, calculated from (3.26) together with the stationary Fokker-Planck equation (3.31).

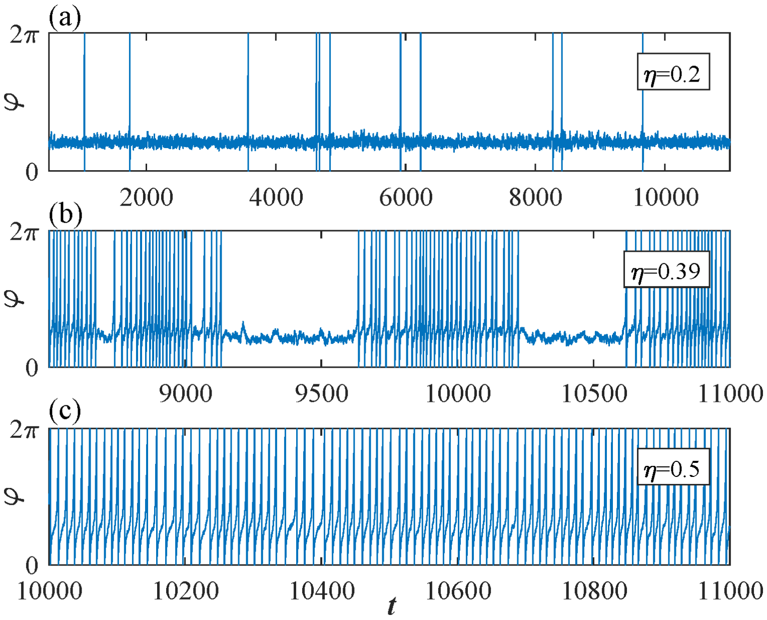

Figure 3.14: Different dynamical regimes in the stochastic excitable system subjected to a slowly adapting feedback (3.7)-(3.8) with $\varepsilon = 0.005$, $D = 0.008$, and different choices of the feedback strength η: noise-induced spiking (a), stochastic bursting (b), and noise-perturbed spiking (c).

branches for varying D, see Fig. 3.13. For small η they are monotonically increasing, while for larger η they are folded. For $\eta_{\text{sn}} < \eta$ there are two separate branches, emanating from the three solutions of (3.26) at $D = 0$.

Continuation of the folds in the (η, D) parameter plane provides the curves which outline the boundaries of the bistability region. Fig. 3.12(b) shows that the two branches of folds meet at the cusp point $(\eta_{\text{cu}}, D_{\text{cu}})$. For $D \to 0$, one of the branches approaches the value $\eta = \eta_{\text{sn}}$ calculated in (3.28), while the other one diverges to infinite values of η. When I_0 approaches the critical value $I_0 = 1$, the cusp point shifts to a smaller noise intensity D, decreasing the region of bistability. In terms of dynamical regimes, our study of stochastic dynamics reveals three characteristic (D, η) regions featuring noise-induced spiking, noise-perturbed spiking, and stochastic busting, see Figure 3.14.

For $D > 0$, all average frequencies satisfy $\Omega_D > 0$, so a clear distinction between the stationary and the oscillatory regime of the fast dynamics is no longer possible. However, one can compare the critical value of the deterministic fast dynamics

$$\mu_c = 1 - I_0$$

with the corresponding stationary value μ^* of the slow variable from (3.36) in order to distinguish between the regimes of noise-induced oscillations and oscillations originating from the deterministic component of the dynamics. If $\mu^* < \mu_c$, the oscillations are noise-induced and appear in the form of rare spikes, see Fig. 3.14(a), while for $\mu^* > \mu_c$ the deterministic oscillations are prevalent, see Fig. 3.14(c).

It turns out that the curves where the stationary values of μ satisfy the condition $\mu = \mu_c$, shown by dashed lines in Fig. 3.12(b), pass exactly through the corresponding cusp point. Moreover, in the bistability region, these curves correspond to the unstable solutions given by the middle part of the S-shaped curves in Fig. 3.12(a). This leads us to conclude that varying the parameters across this line outside the bistability region results in a gradual transition between the regimes of noise-induced oscillations and the deterministic-driven oscillations. At the boundary of the bistability region, there is a hysteretic transition between the two stable regimes. Moreover, within the region of bistability, stochastic fluctuations may induce transitions between the two stable regimes when the timescale separation is finite.

3.2.4 Switching dynamics

In this section, we will examine how the interplay of the finite timescale separation and fluctuations gives rise to switching dynamics in the full system. In particular, we will consider how the region of bistability found in the singular limit $\varepsilon \to 0$ affects the dynamics of the full system for finite timescale separation $\varepsilon > 0$.

The two basic deterministic regimes of the fast dynamics – the excitable equilibrium and the oscillations – naturally induce two corresponding metastable states of the stochastic system with small $\varepsilon > 0$, namely

- **noise-induced spiking**, characterized by a Poissonian-like distribution of interspike intervals (ISIs), see Fig. 3.15(a); and
- **noisy oscillations**, involving a Gaussian-like distribution of the ISIs, centered around the deterministic oscillation period, see Fig. 3.15(b).

These states are found for sufficiently small or sufficiently large values of η, respectively, where only one corresponding branch of solutions of the deterministic system is available. Accordingly, the fluctuations of μ around its average value have no substantial impact on the dynamics. This is confirmed by in Fig. 3.15 which shows that the ISI distributions for the fast subsystem (3.30) complemented by the stationary solutions of (3.36) coincide with those of the full system (3.7)-(3.8). For sufficiently large noise levels above the cusp $D > D_{cu}$ and intermediate values of η, we observe a gradual transition between these two regimes. However, for smaller noise $D < D_{cu}$, in the limiting case $\varepsilon = 0$ the system lies in the region of bistability, cf. Fig. 3.12(b). In the case of finite scale separation, the two coexisting attractors from the singular limit, associated with a stable stationary and a periodic solution, become metastable states. Sufficiently strong noise may then induce large deviations from metastable states, giving rise to switching dynamics, illustrated by the time series in Fig. 3.14(b).

Based on the slow-fast analysis laid out above, the mechanism of noise-induced switching may be understood as follows. The noisy fluctuations of $\varphi(t)$ around its average distribution, given by the stationary Fokker-Planck equation (3.31), induce fluctuations of $\langle \sin \varphi(t) \rangle_t$, and hence also of μ, around the stationary average values we have calculated.

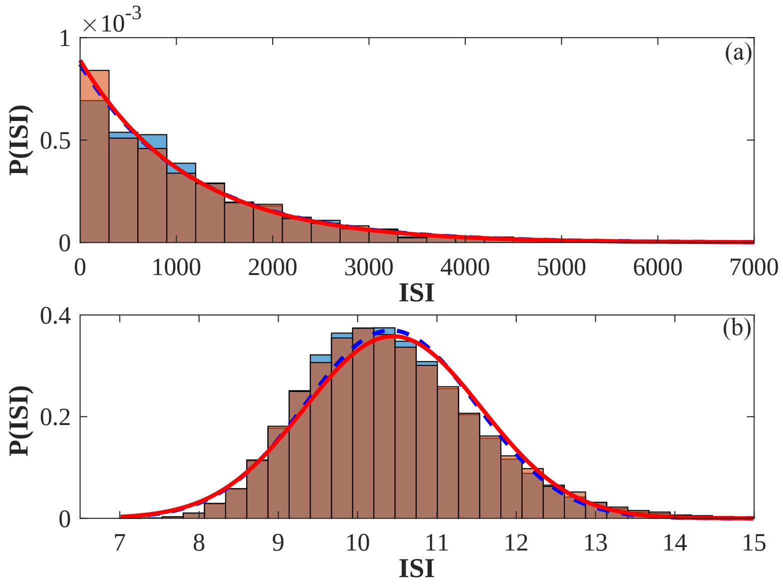

Figure 3.15: Histograms of interspike intervals (ISIs) of the phase variable for feedback strengths $\eta = 0.2$ (top panel) and $\eta = 0.5$ (bottom panel), obtained from numerical simulations of the full system (3.7)–(3.8) with $\varepsilon = 0.005$ (orange) and in the limit of infinite timescale separation (blue), using (3.29) with the stationary $\mu(T) \equiv \mu_D$ determined from the stationary Fokker-Planck equation (3.31). The solid red and dashed blue curves represent fits to (a) exponential decay and (b) Gaussian distributions for the ISI histograms of the full system and the limit of infinite scale separation, respectively.

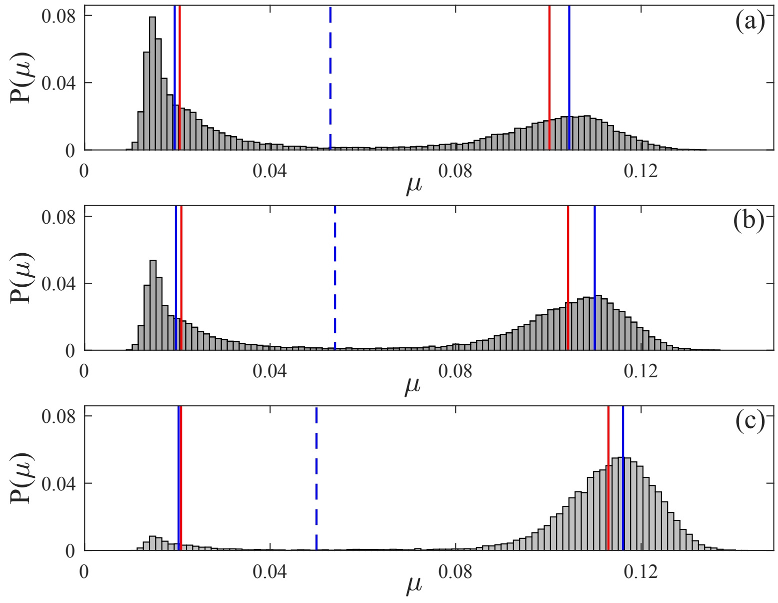

Figure 3.16: Stationary distributions $P(\mu)$, sampled from numerical simulations of the full system (3.7)–(3.8) with $\varepsilon = 0.005$. Parameters $\eta = 0.37$ in (a), $\eta = 0.373$ in (b) and $\eta = 0.38$ in (c) and fixed noise level $D = 0.009$ lie inside the bistability region from Fig. 3.12(b). Blue vertical lines indicate the fixed points of μ from the stationary Fokker-Planck equation (3.31) complemented with the fixed point equation (3.26) of the slow dynamics. Red vertical lines indicate the mean values of all μ in $P(\mu)$ below and of all μ above the unstable fixed point in the middle (dashed blue lines).

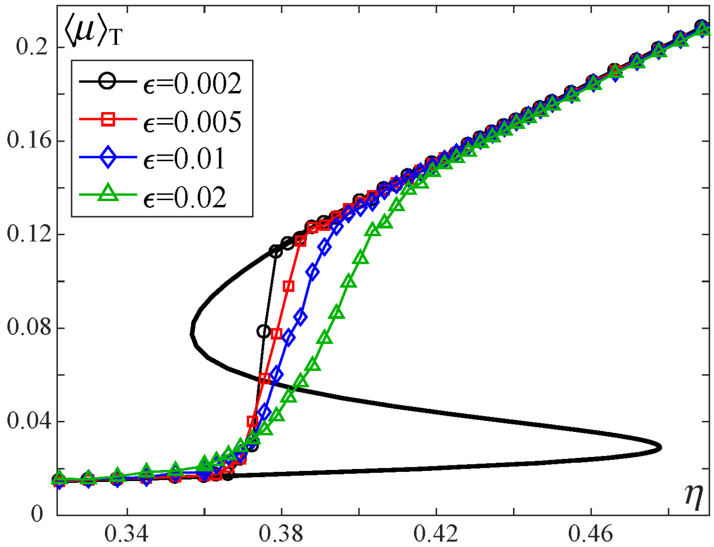

Figure 3.17: Long-time averages $\langle\mu\rangle_T$ obtained from numerical simulations of (3.7)–(3.8) with fixed noise intensity $D = 0.008$ and varying feedback strength η for different values of $\varepsilon \in \{0.002, 0.005, 0.01, 0.02\}$. The black curve represents the corresponding result for the infinite timescale separation, cf. Fig. 3.12(a).

For small ε, the corresponding distribution of μ consists of narrow peaks centered around the stable stationary values. However, with increasing ε, the nonlinear filtering induces a strong skewness of each peak in the distribution, and their overlapping indicates the possibility of noise-induced transitions between the two metastable states. Fig. 3.16 shows the distribution for $\varepsilon = 0.005$ and different values of the η within the bistability region. These transitions can be understood in analogy with the Eyring-Kramers process in a double-well potential [241, 256]: in the generic case of different energy levels corresponding to the two potential wells, transitions in one of the directions occur at a higher rate and the system prefers the state associated with the global minimum of the potential. Such **biased switching** behavior is very pronounced near the boundaries of the bistability region, where the transition to the state close to the fold is much less probable than the transition in the opposite direction.

To further investigate the properties of switching, we have numerically calculated the dependence of the time averages $\langle\mu(T)\rangle$ on the feedback strength η, shown in Fig. 3.17. For most values of η, the long time behavior is dominated by one of the two metastable states, indicating a biased switching process. Nevertheless, for intermediate values of η, the system exhibits **balanced switching** in which the transitions in both directions occur at an almost equal rate. An example of time series illustrating balanced switching is provided in Fig. 3.18. In the limit $\varepsilon \to 0$, the switching rate exponentially decreases to zero while the switching bias in the unbalanced regime increases. This results in the characteristic step-like behavior of the averages observed in Fig. 3.17 for smaller ε.

The noise-induced switching in Fig. 3.18 and Fig. 3.14(b) resembles the typical features of bursting dynamics found in neuronal systems. Here it emerges due to the interplay of slow adaptation and noise, whereby the bursts are triggered just by the stochastic fluctuations.

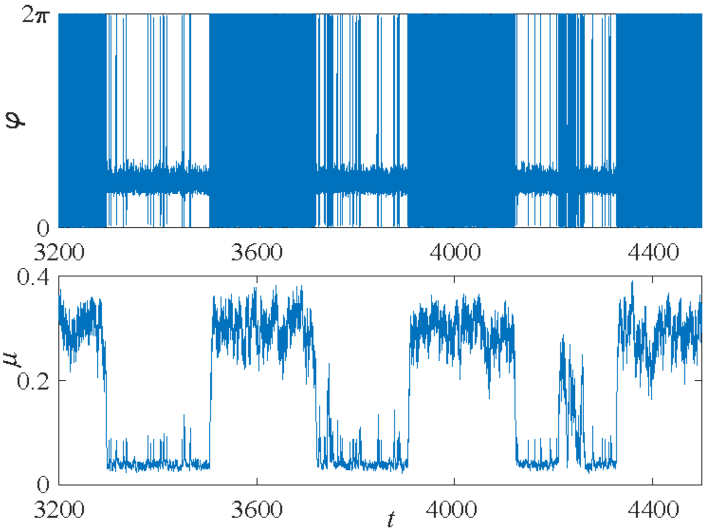

Figure 3.18: Time series $\varphi(t)$ (top panel) and $\mu(t)$ (bottom panel) illustrating the regime of balanced switching. The system parameters are $\eta = 0.38, D = 0.008, I_0 = 0.95, \varepsilon = 0.01$.

However, in the regime $\eta > \eta_{\text{cu}}$, the system is also quite susceptible to external inputs, which could initiate the bursts even without any intrinsic noise.

3.3 *Chapter summary and discussion*

In the present chapter, we have analyzed the switching dynamics in two paradigmatic stochastic multiscale systems with excitable fast dynamics.

First, we have analyzed a system consisting of locally excitable active rotators interacting by adaptive couplings, demonstrating that the interplay of plasticity and noise may give rise to slow stochastic fluctuations. In particular, we have identified two qualitatively different types of self-organized behavior depending on the adaptation rate. For slower adaptation, the switching dynamics features an alternation between two modes of noise-induced oscillations, associated with a preferred order of spiking between the two units. In this case, noise plays a twofold role: it gives rise to oscillations by perturbing the excitable local dynamics on a short timescale while causing alternation between the two oscillatory states on a long timescale. In the case of faster adaptation, the coupling elicits emergent oscillations in the deterministic system, which then exhibits complex multistable behavior involving two stationary and two oscillatory regimes. Under the influence of noise, the system undergoes switching between these four different metastable states, whose prevalence at a fixed noise level depends on the speed of adaptation. The deterministic attractors associated with metastable states are related by $\mathbb{Z}_2$ symmetry. Thus, a mismatch in excitability parameters would lead to symmetry-breaking, whereby a small mismatch would induce a bias in switching dynamics, whereas a larger mismatch, corresponding to the scenario involving one excitable and one oscillatory unit, would completely alter the observed dynamics.

Though the underlying phenomena are not found in the singular limit of infinite scale separation, the fast-slow analysis we have applied still explains the qualitative features of both considered types of switching behavior. Studying the layer problem, and in particular, the vector field of the slow flow has enabled us to gain insight into the metastable states and the transitions between them. We have demonstrated that the coupling dynamics is always in a state of "criticality", being confined to the boundary between the stationary and oscillatory regimes of the fast flow.

Given that excitability, plasticity, and noise are inherent to neuronal systems, the obtained results can be interpreted in the context of neuroscience. It is well known that the backbone of neural networks is made up of binary and ternary neuron motifs, whereby a single structural motif typically supports multiple functional motifs, essentially characterized by a particular weight configuration and underlying direction of the information flow. With this in mind, the scenario of switching under slow adaptation may be important, because it implies that a binary motif can display slow alternation between two effectively unidirectional weight configurations, promoting opposite directions of information flow. For faster adaptation, we find multistability between unidirectional coupling and bidirectional coupling of moderate strength. Nonetheless, the underlying phase dynamics, if extended to networks, may be considered as a paradigm for UP-DOWN states, typical for cortical dynamics [180, 260].

Next, we have analyzed the multiscale dynamics of a stochastic excitable system with a slowly adapting nonlinear feedback, taken from a low pass filter of a function that provides positive feedback for oscillations by pushing the excitability parameter towards the oscillatory regime. Our paradigmatic model provides a novel perspective on how the interaction of a slowly adapting feedback and noise influences the dynamics of an excitable system, giving rise to three different dynamical regimes, including noise-induced spiking, noise-perturbed oscillations, and stochastic bursting. The latter is a novel form of emergent behavior in stochastic multiscale systems. A deep insight into the mechanism giving rise to stochastic bursting, as well as the means of controlling its statistical properties, has been gained by extending singular perturbation theory to the case of stochastic layer dynamics.

Employing the multiple timescale analysis in the limit of infinite timescale separation has allowed us to perform a numerical bifurcation analysis and determine the stability domains of different dynamical regimes. Within the domain where the limiting problem $\varepsilon = 0$ indicates bistability between an equilibrium and fast oscillations, the stochastic fluctuations at finite values of $\varepsilon > 0$ give rise to switching between the associated metastable states which accounts for the onset of stochastic bursting. However, our analysis shows that for sufficiently large noise intensity, this bistability vanishes, such that noise-induced and noise-perturbed oscillations can no longer be distinguished.

From the standpoint of multiscale systems theory, the deterministic part of the presented model provides one of the simplest examples involving a combination of a stable equilibrium regime and oscillations within the fast subsystem. A rigorous mathematical treatment of the dynamical transitions between the two regimes and corresponding reductions by the standard adiabatic elimination method and the averaging technique is still missing. Also, our approach to the analysis of stochastic dynamics in multiscale systems based on introducing a stationary Fokker-Planck equation for the fast dynamics raises important questions concerning the limiting properties of the trajectories and the specific implications of the fluctuations. Nevertheless, we have only considered the case in which noise acts in the fast variable. An open problem is to study how noise in the slow variable influences the obtained results, where interesting new effects can be expected [261]. Since excitability, feedback, and noise are typical ingredients of neural systems, we believe that the application of our results to a specific neural model would be a next natural step, aiming to gain a deeper understanding of the onset of different dynamical regimes.

Chapter 4

Resonant Phenomena in Coupled Systems with Local Dynamics near the Bifurcation Threshold

Noise in excitable or bistable systems may induce two types of generic effects [67]. On one hand, it can modify the deterministic behavior by acting non-uniformly on different states of the system, thus amplifying or suppressing some of its features. For instance, noise may smoothen the threshold-like behavior, causing noise-induced linearization [262]. On the other hand, it may fundamentally change the deterministic dynamics by giving rise to qualitatively novel forms of behavior, typically based on crossing thresholds or separatrices or involving enhanced stability of deterministically unstable structures. In particular, the emergent dynamics may involve noise-induced oscillations and stochastic bursting [263, 264, 265], switching between metastable states [42, 181], or noise-enhanced stability of unstable and metastable states [266, 267, 268, 269, 270], to name but a few.

The constructive role of noise has been evinced in a wide range of real-world applications, from neural networks and chemical reactions to lasers and electronic circuits (see [67] and references therein). In neural systems, for instance, such phenomena are collectively referred to as *stochastic facilitation* [68, 69, 70]. The latter mainly refer to *resonant phenomena*, manifested as characteristic non-monotonous responses of the system to noise, whereby the most prominent examples include:

1. **coherence resonance** (CR) [149, 271, 272, 273, 274], where the regularity of *noise-induced oscillations* becomes maximal at an intermediate noise level;

2. **stochastic resonance** (SR) [70, 275], where the sensitivity of a system to a subthreshold periodic stimulation becomes maximal at a preferred noise level; and

3. **inverse stochastic resonance** (ISR) [94, 68, 172, 173, 174, 175, 176, 177, 178, 193], an inhibitory effect where the spiking frequency of *noise-perturbed oscillations* becomes minimal at a preferred noise level.

These effects are fundamentally related to the fact that noise induces an additional timescale compared to the deterministic system. For instance, in the case of ISR, noise introduces a timescale associated with the scale separation between the activation and relaxation processes.

In contrast to SR, the ISR effect concerns autonomous rather than periodically driven systems. ISR has recently been experimentally observed for cerebellar Purkinje cells [178], having explicitly demonstrated how the lifetimes of the spiking ("up") and the relative quiescence ("down") states [179, 42, 180] depend on the noise intensity. It has also been indicated that ISR plays a variety of important functional roles in neuronal systems, including the reduction of spiking frequency in the absence of neuromodulators, suppression of pathologically long short-term memories, triggering of on-off tonic spiking activity, and even optimization of information transfer along the signal propagation pathways [68, 174, 176, 178]. So far, the studies of ISR have described only one mechanism of the effect whereby a single neural oscillator exhibits bistable deterministic dynamics, featuring coexistence between a limit cycle and a stable equilibrium. Such bistability is typical for Type II neurons below the subcritical Hopf bifurcation, e.g. classical Hodgkin-Huxley and Morris-Lecar models [68, 173, 174, 175]. Influenced by noise, the deterministic attractors turn into metastable states between which the system then switches. The associated switching rates become strongly asymmetric at an intermediate noise level, favoring the quasi-stationary state rather than spiking activity. This is reflected in the characteristic non-monotone dependence of the spiking frequency on noise, a hallmark of ISR.

The issues unresolved prior to our research concern the mechanisms and robustness of the ISR effect. Is it dependent on the type of neuronal excitability? Can there be more than one mechanism of ISR? How does the effect depend on the form of couplings, e. g. can it be robust for adaptively changing couplings, typical for neuronal systems? Can the effect be observed in coupled excitable systems, in which noise influences *emergent* oscillations?

Having a longer history than ISR, both in terms of theoretical studies and experimental observations, CR has been explored in much more detail [108, 159, 160, 161, 162, 163, 164, 165, 166, 167, 168, 169, 170]. CR concerns noise-induced oscillations in (coupled) excitable or bistable systems. The resonant effect occurs when the noise intensity is simultaneously large enough to ensure a short activation time (escape from the vicinity of the stable equilibrium) and small enough to maintain the deterministic nature of the relaxation process (return to the fixed point), i. e. when the noise-dependent variabilities of the activation and relaxation processes are balanced in a certain way. A particularly relevant open issue concerns the mechanisms of enhancing (or in general, efficient *control* of) CR, whereby recent research has considered different mechanisms of control in networks of coupled oscillators, including time-delayed feedback [276, 277, 278, 279, 280, 281, 282], network topology [283, 284], and spatial heterogeneity of bifurcation parameters [285]. What we demonstrate is a novel efficient method of control of CR based on introducing a *slowly* adapting feedback to an excitable system, exploiting the multiscale dynamics to selectively enhance or suppress the noise-induced spiking.

This chapter is devoted to understanding the characteristic non-monotonous response to noise arising in systems near a bifurcation between stationary and oscillatory states. In the light of the aforementioned open questions, the particular two problems that we will consider include

1. **generic scenarios for inverse stochastic resonance**; and
2. the **control of coherence resonance** by a slowly adapting feedback.

Our studies will be conducted on the two simplified, yet paradigmatic models from chapter 3 that combine the three typical ingredients of neuronal dynamics – excitability, noise and coupling plasticity – as well as an additional neuronal model, namely:

A. **two identical adaptively coupled stochastic active rotators** [181, 193, 254]; and

B. **a stochastic excitable active rotator with a slowly adapting (low-pass filtered) feedback**.

As far as problem (1) is concerned, we have investigated model A in both the excitable and the oscillatory regime. Within these studies, we have discovered two different generic scenarios accounting for the onset of ISR: one based on *biased switching*, and the other on the *noise-enhanced stability* of a deterministically unstable fixed point [266, 267, 268, 269, 270]. The former occurs due to noise-induced crossing over the separatrix between the stationary and oscillatory states, whereas the latter takes place due to "tunneling" through the bifurcation. We have confirmed that these two mechanisms can account for the onset of ISR in the classical neuronal model B, demonstrating the generality of our results.

Regarding problem (2), our research has shown that a slowly adapting feedback is capable of efficiently enhancing or suppressing CR, whereby the mechanism of control is not a simple additive effect where the system is effectively pushed towards or away from the bifurcation threshold.

The present chapter is organized as follows. Section 4.1 is devoted to ISR due to biased switching, arising in the system of two coupled rotators with excitable local dynamics. In particular, section 4.1.1 contains the details of the model and numerical bifurcation analysis of its deterministic dynamics, already addressed in section 3.1 of the previous chapter, while section 4.1.2 concerns our numerical results on ISR, where we quantify the effect in terms of the average frequency, corresponding stationary distributions, transition probabilities, and several other quantities. Then, 4.1.3 presents a slow-fast approach to understanding the role of plasticity in the resonant effect. Moreover, section 4.2 is dedicated to ISR due to noise-induced trapping in the vicinity of a deterministically unstable fixed point, arising in the system of two coupled active rotators with oscillatory local dynamics. Section 4.2.1 provides an overview of the model and its deterministic dynamics, section 4.2.2 concerns slow-fast analysis of the system, whereas section 4.2.3 refers to our numerical results on ISR. Furthermore, in section 4.3 we demonstrate that a single neuron model may display two different scenarios for ISR, depending on the particular parameter values. Finally, section 4.4 concerns the control of CR by nonlinear adaptive feedback, whereby section 4.4.1 presents the model and its dynamics (from section 3.1 of the previous chapter), whereas section 4.4.2 shows how CR can be enhanced or suppressed by our scheme. In the concluding section 4.5, we overview the results and discuss their relevance.

4.1 *ISR due to biased switching*

In this section, we treat the problem of conditions giving rise to ISR in coupled excitable systems, where noise influences the emergent oscillations. Considering the example of emergent oscillations in two adaptively coupled active rotators with excitable local dynamics, we demonstrate a novel generic scenario for ISR in a multi-timescale system. The impact of plasticity is shown to be twofold. First, at the level of multiscale dynamics, one finds a range of intermediate adaptivity rates that give rise to the multistability of limit cycle attractors and stable equilibria, a condition necessary for the onset of the effect. Second, by applying slow-fast analysis, we show that the plasticity also plays a subtle facilitatory role by guiding the dynamics of the fast flow to parameter domains where its stable equilibria become foci rather than nodes, which effectively enhances the influence of noise. The described scenario persists for different plasticity rules, underlying its robustness in the light of potential applications to neuroscience and other types of cell dynamics. The following analysis strongly relies on our results on the slow stochastic fluctuations exhibited by this system presented in section 3.1 of the previous chapter.

4.1.1 Model and deterministic dynamics of the full system

As in section 2.1 of Chapter 2 and section 3.1 of Chapter 3, the considered model consists of two identical stochastic active rotators interacting by adaptive couplings [181, 182, 183, 184]

$$\begin{aligned}
\dot{\varphi}_1 &= I_0 - \sin\varphi_1 + \kappa_1 \sin(\varphi_2 - \varphi_1) + \sqrt{D}\xi_1(t) \\
\dot{\varphi}_2 &= I_0 - \sin\varphi_2 + \kappa_2 \sin(\varphi_1 - \varphi_2) + \sqrt{D}\xi_2(t) \\
\dot{\kappa}_1 &= \varepsilon(-\kappa_1 + \sin(\varphi_2 - \varphi_1 + \beta)) \\
\dot{\kappa}_2 &= \varepsilon(-\kappa_2 + \sin(\varphi_1 - \varphi_2 + \beta)),
\end{aligned} \tag{4.1}$$

where the phases $\{\varphi_1, \varphi_2\} \in S^1$, while the couplings $\{\kappa_1, \kappa_2\} \in \mathbb{R}$. The uncoupled units undergo a SNIPER bifurcation at $I_0 = 1$, separating the excitable ($I_0 < 1$) and oscillatory ($I_0 > 1$) regimes. In the present section, we will keep $I_0 = 0.95$ fixed. The small parameter $0 < \varepsilon \ll 1$ defines the scale separation between the fast (phase) dynamics and the slow (adaptation) dynamics. Recall that due to $\mathbb{Z}_2$ symmetry of the noiseless version of (4.1), attractors always appear in pairs characterized by the same stability features. The fast variables are influenced by independent white noise of variance D such that $\xi_i(t)\xi_j(t') = \delta_{ij}\delta(t-t')$ for $i, j \in \{1, 2\}$, which embodies the action of synaptic noise in neuronal systems

[69]. The parameter β controls the modality of the plasticity rule, whereby we will once again focus on the β interval interpolating between the two limiting cases corresponding to the Hebbian learning rule ($\beta = 3\pi/2$) [287] and an STDP-like plasticity rule ($\beta = \pi$) [84, 85, 86, 182, 206, 207, 288, 289].

Recall from section 2.1.2 that depending on β, the system may have two, four or six fixed points, and that our analysis concerns the interval $\beta \in (3.298, 4.495)$, where the system has two stable fixed points lying off the synchronization manifold $\varphi_1 = \varphi_2$. These fixed points are excitable foci, born in a supercritical symmetry-breaking pitchfork bifurcation at $\beta = 3.298$ and annihilated in two symmetry-related inverse fold bifurcations at $\beta = 4.495$. In the present section, we shall mainly refer to the case $\beta = 4.2$, for which the two stable foci of (4.1) with $D = 0$ are given by

$$EQ1 \equiv (\varphi_1^*, \varphi_2^*, \kappa_1^*, \kappa_2^*) = (1.177, 0.175, 0.032, -0.92),$$
$$EQ2 \equiv (\varphi_1^*, \varphi_2^*, \kappa_1^*, \kappa_2^*) = (0.175, 1.177, -0.92, 0.032).$$

Let us now provide a brief reminder about the results on stable stationary states from section 2.1.2 and explain the onset of emergent oscillations in detail.

4.1.1.1 The onset of emergent oscillations

The onset of emergent oscillations for the deterministic version of (4.1) depends on the interplay of the plasticity rule, controlled by β, and the adaptation rate, characterized by ε. Due to the invariance of the system to exchange symmetry, the periodic solutions appear in pairs, sharing the same stability features. The maximal stability region of the periodic solutions is illustrated in Fig. 4.1(a), which shows the variation of the κ_1 variable, $\sigma_{\kappa_1} = \max(\kappa_1(t)) - \min(\kappa_1(t))$, in the$(\beta, \varepsilon)$ parameter plane. This was obtained by numerical continuation starting from a stable periodic solution, such that the initial conditions for an incremented parameter value are given by the final state obtained for the previous iteration step. The scan reveals that for a given β, there exists an interval $\varepsilon \in (\varepsilon_{min}, \varepsilon_{max})$ of intermediate scale separation ratios supporting the oscillations, cf. the highlighted region in Fig. 4.1(b). At ε_{min}, two branches of stable periodic solutions emanate from fold of cycles bifurcations, denoted by FC in Fig. 4.1(b). Note that the associated threshold scale separation $\varepsilon_{min}(\beta)$ decreases with increasing β.

Recall from section 3.1.1.2 that the waveform of oscillations also changes as ε is increased under fixed β. In particular, for smaller ε, the waveforms corresponding to the two units are rather different. Nevertheless, the two branches of oscillatory solutions merge at $\varepsilon \approx 0.06$, where the system undergoes an inverse pitchfork bifurcation of limit cycles (PFC in Fig. 4.1(b)). This gives rise to anti-phase space-time symmetry $\varphi_1(t) = \varphi_2(t + T_{osc}/2), \kappa_1(t) = \kappa_2(t + T_{osc}/2)$ of the incipient stable limit cycle, with T_{osc} denoting the oscillation period.

Fig. 4.1(c) shows an example of the stability basins of the stationary and oscillatory solutions for $\varepsilon = 0.1$, obtained by fixing the initial values of the phases and varying the initial couplings within the range $\kappa_{i,ini} \in [-1, 1], i \in \{1, 2\}$. In the presence of noise, the coexist-

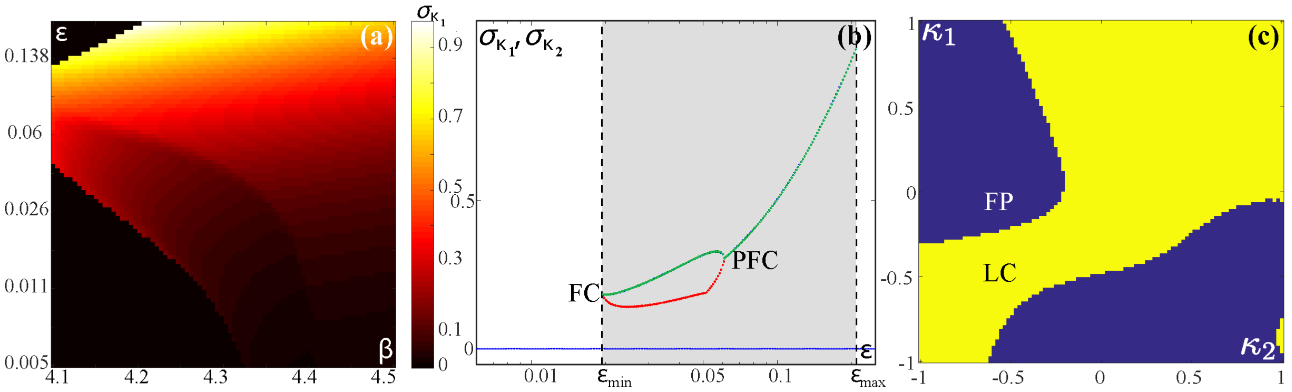

Figure 4.1: The onset of emergent oscillations in (4.1) for $I_0 = 0.95, D = 0$. (a) Variation $\sigma_{\kappa_1} = \max(\kappa_1(t)) - \min(\kappa_1(t))$ of the coupling weight κ_1 in the (β, ε) plane. (b) Dependencies $\sigma_{\kappa_i}(\varepsilon), i \in \{1, 2\}$ for the stationary (blue) and oscillatory solutions (red and green refer to the two units) for fixed $\beta = 4.2$. Shading indicates the interval $\varepsilon \in (\varepsilon_{min}, \varepsilon_{max})$ which supports the multistability of two symmetry-related stable equilibria and limit cycle(s), whereas *FC* and *PFC* denote the ε values where the fold of cycles and pitchfork of cycles occur. (c) Basins of stability of the stationary (*FP*, blue) and oscillatory solutions (*LC*, yellow) in the (κ_1, κ_2) plane, obtained by setting the initial phases to $(\varphi_1, \varphi_2) = (1.32, 0.58)$, with the remaining parameters fixed to $\beta = 4.2, \varepsilon = 0.1$.

ing attractors of the deterministic system give rise to metastable states, connected by noise-induced switching.

4.1.2 Numerical results on ISR

ISR occurs due to noise-mediated suppression of oscillations, whereby the frequency of noise-perturbed oscillations becomes minimal at a preferred noise level. For the considered motif of two adaptively coupled excitable active rotators (4.1), the characteristic non-monotone dependence on noise is generically found for intermediate adaptivity rates which support the multistability of stationary and oscillatory solutions. In the current section, we will quantify ISR in terms of the dependence of the average oscillation frequency on noise and analyze the corresponding stationary probability distributions, the noise dependence of the switching bias, as well as how the resonant effect changes with β and ε.

4.1.2.1 Characterization of ISR

A family of curves illustrating the dependence of the oscillation frequency on noise variance $\langle f \rangle(D)$ for several $\varepsilon \geq \varepsilon_{min}(\beta)$ values is shown in Fig. 4.2(a). The angular brackets $\langle \cdot \rangle$ refer to averaging over an ensemble of a 100 different stochastic realizations, having fixed a set of initial conditions within the basin of attraction of the limit cycle. Nonetheless, we have verified that qualitatively analogous results are obtained if for each realization of the stochastic process one randomly selects a new set of initial conditions from the same basin of attraction.

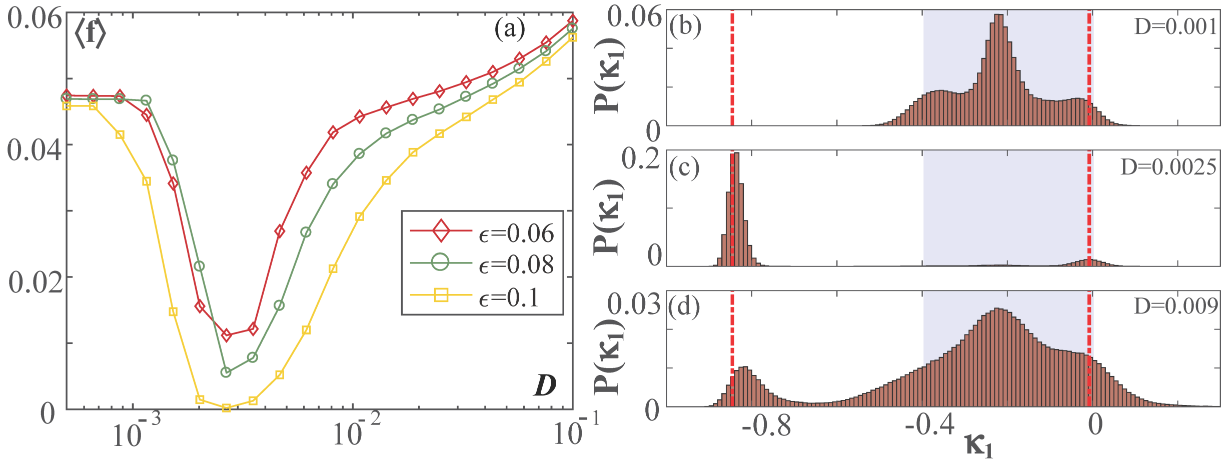

Figure 4.2: Inverse stochastic resonance in (4.1) with $I_0 = 0.95, \beta = 4.2$. (a) Dependencies of the mean oscillation frequency on noise $\langle f \rangle(D)$ for scale separation $\varepsilon \in \{0.06, 0.08, 0.01\}$. (b-d) show the stationary distributions $P(\kappa_1)$ for noise intensities below ($D = 0.001$), at ($D = 0.0025$), and above ($D = 0.009$) the resonant noise intensity for $\varepsilon = 0.1$. Dash-dotted red lines denote the κ_1 levels associated with the two stable equilibria, $\kappa_1^*(EQ1) = 0.032$ and $\kappa_1^*(EQ2) = -0.92$, while the blue shaded interval indicates the variation σ_{κ_1} of the unique stable periodic solution. For noise intensities near resonance, the system barely resides in the limit cycle metastable state.

In section 3.1.3.2, we have shown that noise-induced switching gives rise to bursting-like behavior. In particular, this occurs due to spiking being interrupted by quiescent episodes which correspond to the system residing in the vicinity of the quasi-stationary metastable states. These episodes are prevalent at noise levels around the minimum of $\langle f \rangle(D)$ from Fig. 4.2(a), essentially accounting for the appearance of inverse stochastic resonance in the system. For weaker noise $D \lesssim 10^{-3}$, the frequency of emergent oscillations remains close to the deterministic one, whereas for a much stronger noise, it increases above that of unperturbed oscillations. Moreover, the inhibitory effect of noise depends on the adaptivity rate, and is found to be more pronounced for faster adaptivity (cf. Fig. 3.5). Indeed, for smaller ε, $\varphi(t)$ series corresponding to the noise levels around the minimum of $\langle f \rangle(D)$ exhibit bursting-like behavior, whereas for larger ε, noise effectively quenches the oscillations, such that the minimal observed frequency approaches zero.

Let us now demonstrate how ISR is qualitatively reflected in the stationary distributions of the fast and the slow variables, considering their typical distributions below, at and above the resonant noise level. Using these distributions, which allow one to understand the features of the noise-induced switching process between the metastable states derived from coexisting attractors of the corresponding deterministic system, we will show that the mechanism of ISR is in fact based on biased switching between the oscillatory and quasi-stationary metastable states. Fig. 4.2(b)-(d) contains the stationary distributions $P(\kappa_1)$ for noise levels below, at and above the resonant level. For comparison with the noiseless system, we have indicated the weight levels associated with the two equilibria $\kappa_1^*(EQ1) = 0.032$ and $\kappa_1^*(EQ2) = -0.92$, as well as the variation σ_{κ_1} of the stable limit cycle. Note that the sta-

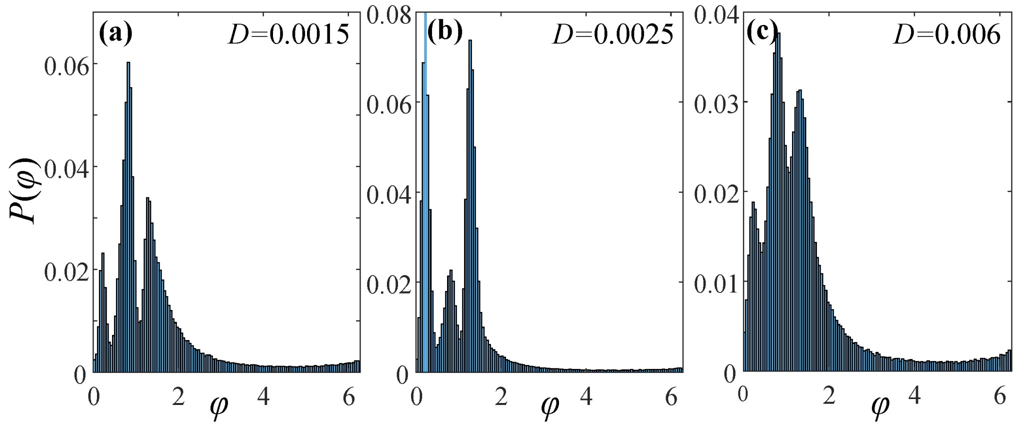

Figure 4.3: Stationary distribution $P(\varphi_1)$ for noise levels (a) below, (a) at, and (c) above the resonant value, with $I_0 = 0.95$, $\beta = 4.2$ and $\varepsilon = 0.06$. The middle peak, prevalent in (a) and (c), refers to the metastable state associated with the oscillatory mode of (4.1) for $D = 0$. The two lateral peaks, dominant in (b), correspond to quasi-stationary states derived from the stable equilibria.

ble periodic solution is unique for the considered timescale separation $\varepsilon = 0.1$ since the deterministic system lies above the pitchfork of cycles bifurcation, cf. PFC in Fig. 4.1(b). The stationary distribution $P(\kappa_1)$ at the resonant noise level expectedly shows a pronounced peak corresponding to one of the quasi-stationary states, while the distributions below and above the resonant noise level indicate a high occupancy of the oscillatory metastable state.

Fig. 4.3(a)-(c) shows the stationary distributions of one of the phase variables, $P(\varphi)$, for noise levels below, at and above the resonant value, with the remaining parameters set to $(\beta, \varepsilon) = (4.2, 0.06)$. The distribution $P(\varphi)$ is characterized by (i) two lateral peaks, corresponding to the two symmetry-related quasi-stationary states, and (ii) the area around the central peak, corresponding to the oscillatory mode. Expectedly, for small noise $D = 0.0015$, see Fig. 4.3(a), as well as very large noise $D = 0.006$, cf. Fig. 4.3(c), the central peak of $P(\varphi)$ is dominant. Nevertheless, the switching dynamics near the minimum of $\langle f \rangle(D)$ is fundamentally different. Indeed, the corresponding distribution $P(\varphi)$ for $D = 0.0025$ in Fig. 4.3(b) reveals that the system strongly prefers the quasi-stationary states to oscillations.

Note that the ISR effect is robust with respect to different modality rules. This is corroborated in Fig. 4.4, which illustrates how the average oscillation frequency changes with β and D for the fixed scale separation $\varepsilon = 0.09$. The nonlinear response to noise, conforming to a resonant effect with a minimum of oscillation frequency at an intermediate noise level, persists in a wide range of β, essentially interpolating between Hebbian-like and STDP-like adaptive dynamics.

4.1.2.2 Biased switching as a mechanism of ISR

To elucidate the mechanism behind ISR, we have calculated how the fraction of the total time spent in either of the oscillatory metastable states, T_{osc}/T_{tot}, changes with noise. Within our numerical experiments, the quasi-stationary and the oscillatory metastable states have

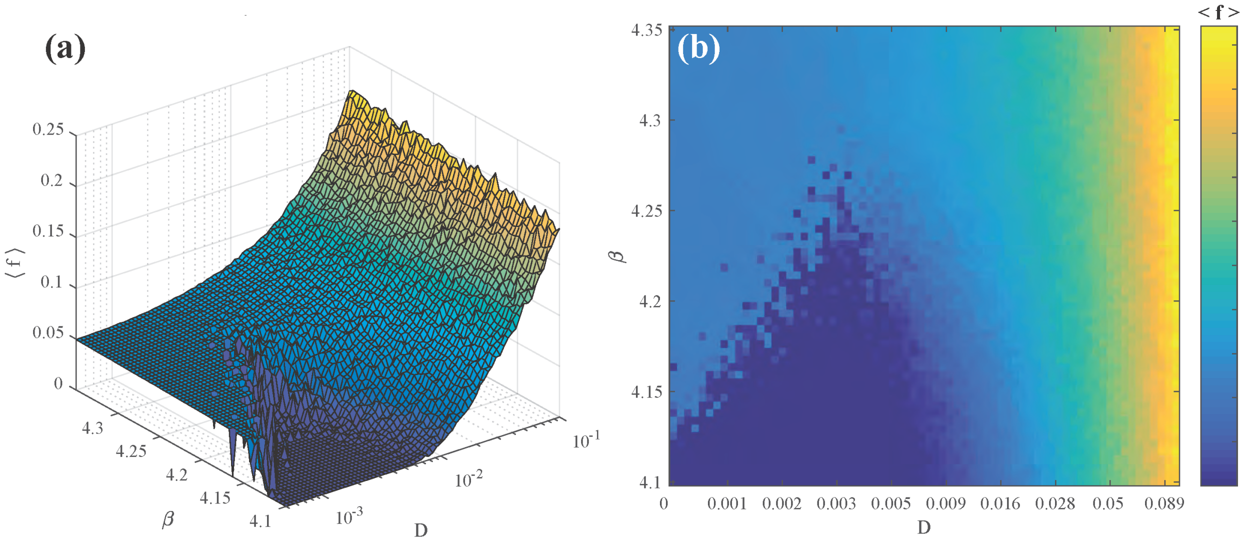

Figure 4.4: Mean spiking rate $\langle f \rangle$ as a function of β and D for fixed $\varepsilon = 0.09$, presented as (a) a 3D plot and (b) a heat map. The results corroborate the robustness of the effect with respect to different plasticity rules.

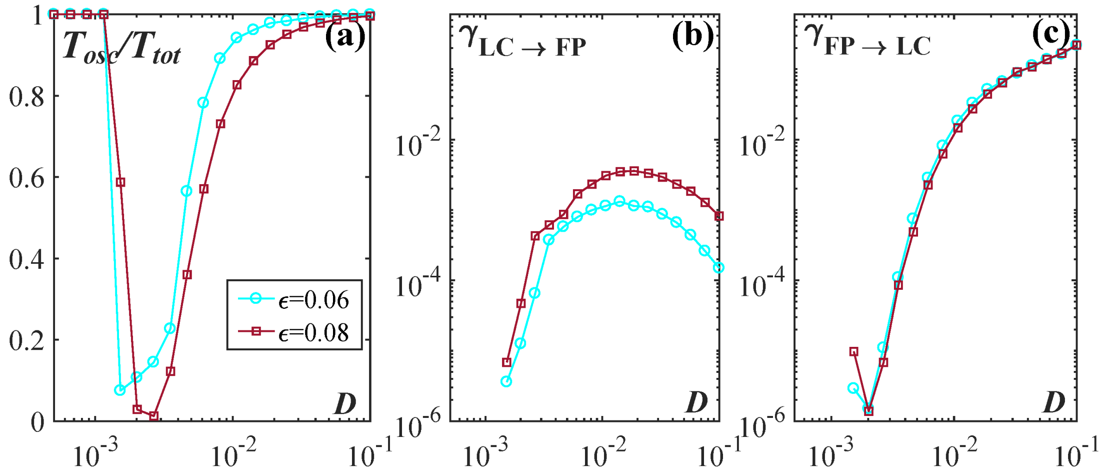

Figure 4.5: (a) Fraction of time spent in the oscillatory metastable state T_{osc}/T_{tot} as a function of noise for $\varepsilon \in \{0.06, 0.08\}$. (b) and (c) Numerically estimated transition rates from the oscillatory to the quasi-stationary metastable states, $\gamma_{LC \to FP}(D)$ and *vice versa*, $\gamma_{FP \to LC}(D)$. The remaining parameters are $I_0 = 0.95, \beta = 4.2$.

been distinguished by considering the corresponding coupling weight series. Specifically, as shown in Fig 3.7 (b), the difference $\Delta\kappa(t) = |\kappa_1(t) - \kappa_2(t)|$ is much larger for the quasi-stationary than for the oscillatory solutions. Thus, by setting the threshold to $\Delta\kappa_{thr} = 0.6$, we were able to identify the system's states and trace the associated transitions. Figure 4.5(a) indicates a non-monotone dependence of $T_{osc}/T_{tot}(D)$, implying that the switching process near the resonant noise level becomes strongly biased in favor of the quasi-stationary state, even more so for faster adaptivity. The biased switching process arises from the geometry of the phase space, whose structure is asymmetrical with respect to the separatrix between the coexisting attractors: the limit cycle lies much closer to the separatrix than the stationary states.

The nonlinear response to noise may be understood in terms of the competition between the transition processes from and to the limit cycle attractor. These processes are characterized by the transition rates from the stability basin of the limit cycle attractor to that of the stationary states $\gamma_{LC\to FP}$ and *vice versa*, $\gamma_{FP\to LC}$. We have numerically estimated these quantities as the reciprocal values of the corresponding mean first-passage times [290]. Figures 4.5(b)-(c) corroborate that the dependencies $\gamma_{LC\to FP}(D)$ and $\gamma_{FP\to LC}(D)$ are qualitatively distinct: the former displays a maximum at the resonant noise level, whereas the latter just increases monotonously with noise. For small noise $D \lesssim 10^{-3}$, one observes virtually no switching to the quasi-stationary state, in accordance with the fact that the corresponding oscillation frequency is identical to the deterministic one. For increasing noise, the competition between the two processes is resolved such that for an intermediate (large) noise intensity, the impact of $\gamma_{LC\to FP}$ ($\gamma_{FP\to LC}$) becomes prevalent. The large values of $\gamma_{FP\to LC}$ found for quite strong noise $D \gtrsim 0.04$ reflect the fact that the system spends most of the time in the oscillatory metastable state, with only short excursions to the quasi-stationary state. Moreover, the fact that ISR is more pronounced for higher adaptivity rates is reflected in the curve $\gamma_{LC\to FP}(D)$ for $\varepsilon = 0.1$ lying substantially above that for $\varepsilon = 0.06$, as shown in Fig. 4.5(b). Large deviations from the oscillatory metastable state are quite rare.

4.1.2.3 Local stability of the limit cycle attractor: the impact of scale separation

To understand why the interplay of adaptivity rate and noise results in a stronger resonant effect for larger ε, we have investigated the susceptibility of the limit cycle attractor to external perturbation. The latter can be quantified by calculating the determinant of the Jacobian $detJ = |\frac{\partial(\dot\varphi_1,\dot\varphi_2,\dot\kappa_1,\dot\kappa_2)}{\partial(\varphi_1,\varphi_2,\kappa_1,\kappa_2)}|$ for (4.1) with $D = 0$,

$$detJ = \varepsilon^2 \cos(\kappa_1 - \kappa_2)(\kappa_1 \cos(\varphi_1 - 2\varphi_2) + \cos\varphi_1(\kappa_1 + 2\kappa_2\cos(\varphi_1 - \varphi_2) + 2\cos\varphi_2)),$$

along the whole orbit of the limit cycle, whereby larger values indicate a more pronounced local instability.

Fig. 4.6 shows how the determinant of the Jacobian changes with the phase variable φ_1 for $\varepsilon = 0.06$ (blue line) and $\varepsilon = 0.1$ (orange line), respectively. For smaller ε, one may identify two particular points where the determinant of the Jacobian is the largest, i.e. where the

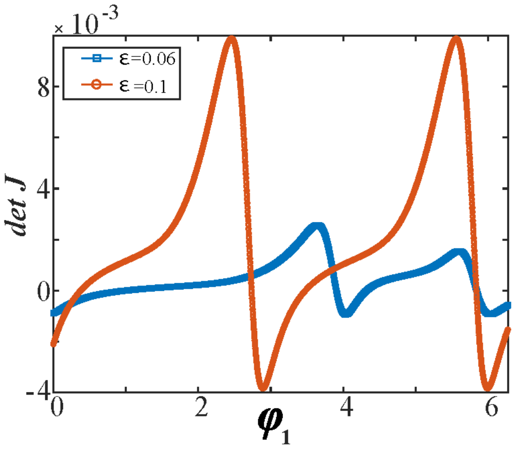

Figure 4.6: Determinant of the Jacobian calculated along the limit cycle orbit as a function of the phase variable for $\varepsilon \in \{0.06, 0.1\}$ with $I_0 = 0.95, \beta = 4.2$. This quantity indicates the sensitivity of certain sections of the orbit to external perturbation.

impact of external perturbation is felt the strongest. This implies that the perturbation is most likely to drive the system's trajectory away from the limit cycle attractor around these two sections of the orbit, which should lie closest to the boundary to the stability basins of the stationary states. Such a physical picture is maintained for larger ε, but one should stress that the sensitivity of limit cycle attractor to external perturbation substantially increases along the entire orbit, cf. Fig. 4.6. Translated to the stochastic system, this would imply that faster adaptivity enhances the impact of noise, contributing to a more pronounced ISR effect. This point will be addressed from another angle in the following subsection.

4.1.3 Facilitatory role of adaptivity in the resonant effect: slow-fast analysis

Though ISR is most pronounced for intermediate ε, it turns out that an additional subtlety in the mechanism of biased switching may be explained by employing the singular perturbation theory to the noiseless version of (4.1). In particular, by combining the critical manifold theory [47] and the averaging approach [255], we were able to explain the facilitatory role of plasticity in enhancing the resonant effect by showing that the adaptation drives the fast flow towards the parameter region where the stationary state is a focus rather than a node. It is well known that the response to noise in multi-timescale systems qualitatively depends on the character of stationary states. Indeed, using sample-paths approach and other advanced techniques, it has already been shown that such systems may exhibit fundamentally different scaling regimes with respect to the noise variance and the scale separation ratio [291, 292, 293]. Intuitively, one expects that the resonant effects are associated with the quasi-stationary states derived from foci rather than nodes [291], essentially because the local dynamics around the stationary state then involves an eigenfrequency.

Let us first briefly summarize the main results from section 3.1.2, concerning the layer and reduced problems for system (4.1) with $I_0 = 0.95, D = 0$. Within the layer problem, we obtain the fast flow dynamics

$$\begin{aligned}\dot{\varphi}_1 &= I_0 - \sin\varphi_1 + \kappa_1 \sin(\varphi_2 - \varphi_1)\\ \dot{\varphi}_2 &= I_0 - \sin\varphi_2 + \kappa_2 \sin(\varphi_1 - \varphi_2),\end{aligned} \tag{4.2}$$

by treating the slow variables $\kappa_1, \kappa_2 \in [-1, 1]$ as additional system parameters. One may formally obtain (4.2) by setting $\varepsilon = 0$ in (4.1) with $D = 0$. Depending on κ_1 and κ_2, the fast flow dynamics is almost always monostable, exhibiting either a stable equilibrium or a limit cycle attractor, apart from a small region of bistability near the main diagonal where they coexist, as shown in Fig. 4.7(a). The maximal stability region of the oscillatory regime, encompassing both the domain where the oscillatory solution is monostable and where it coexists with a stable equilibrium, is indicated by the gray shading in Fig. 4.7(a). The latter has been determined by the method of numerical continuation, starting from a periodic solution. Note that each periodic solution above the main diagonal has a $\mathbb{Z}_2$ symmetry-related counterpart below the diagonal. The periodic solutions typically emanate from SNIPER bifurcations, which comprise two branches where either κ_1 or κ_2 are almost constant and close to zero.

By averaging over the different attractors of the fast flow dynamics, we have obtained multiple stable sheets of the slow flow [255]. The explicit procedure consists in determining the time average $\langle \varphi_2 - \varphi_1 \rangle_t = h(\kappa_1, \kappa_2)$ by iterating (4.2) for each fixed set (κ_1, κ_2) [181, 255], and then substituting these averages into the equations of the slow flow

$$\begin{aligned}\kappa_1' &= [-\kappa_1 + \sin(h(\kappa_1, \kappa_2) + \beta)]\\ \kappa_2' &= [-\kappa_2 + \sin(-h(\kappa_1, \kappa_2) + \beta)],\end{aligned} \tag{4.3}$$

where the prime refers to a derivative over the rescaled time variable $T := t/\varepsilon$. The arrows in Fig. 4.7(a) show the vector fields on the two stable sheets of the slow flow (4.3) associated with the stationary and the periodic attractors of the fast flow.

Fig. 4.7(b) shows the vector fields associated with each of the attractors (fixed point or limit cycle), presented within its respective (κ_1, κ_2) stability region. In the small region of the (κ_1, κ_2) plane supporting coexisting stable solutions of the fast flow, the corresponding vector field of the slow flow is consists of two overlapping sheets, since the value of the average $f(\kappa_1, \kappa_2)$ depends on the initial conditions.

Within the described slow-fast approach, the subtle influence of adaptivity on the mechanism behind the ISR may be explained as follows. Figure 4.7(b) shows a projection of a typical $(\kappa_1(t), \kappa_2(t))$ trajectory of the full system (4.1) corresponding to a switching episode between the metastable states associated with a limit cycle attractor and a stable equilibrium of the deterministic system, see the time traces in Fig. 4.7(c)-(d). One observes that for the oscillating regime, the coupling dynamics always remains close to the SNIPER bifurcation of the fast flow, cf. Fig. 4.7(a), which makes the oscillations quite susceptible to noise. Recall that the fast flow is typically monostable. Thus, switching events in the full system are associated with the fast flow undergoing the SNIPER bifurcation: either a direct one, leading

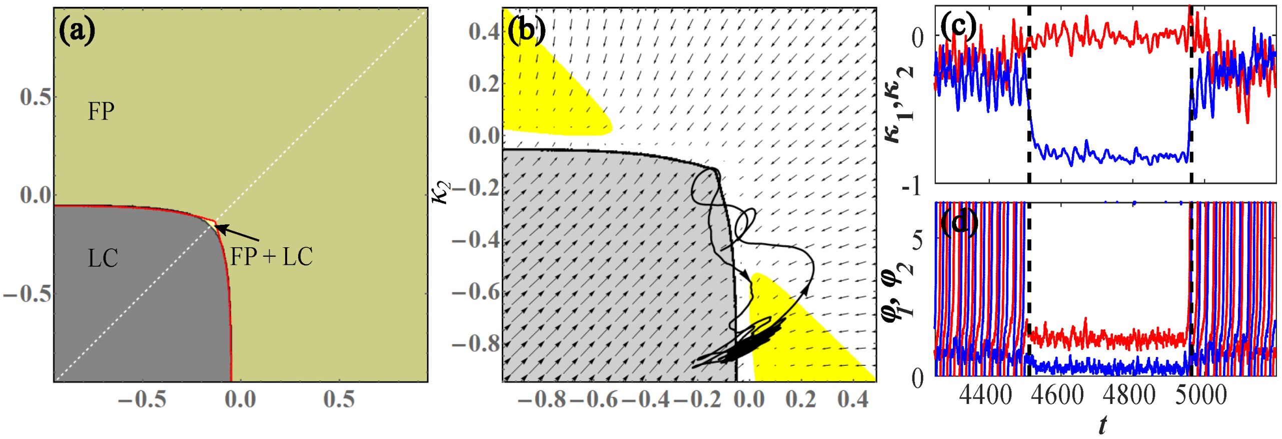

Figure 4.7: (a) Attractors of the fast flow (4.2) in terms of κ_1 and κ_2, now treated as system parameters. The fast flow is typically monostable, admitting either a stable fixed point (FP) or a stable limit cycle (LC), apart from a small region of bistability (FP+LC) around the main diagonal. (b) Vector field of the slow flow (4.3) determined by considering only the stable regimes of the fast flow for $\beta = 4.2$, $I_0 = 0.95$. Within the yellow-highlighted regions, stable fixed point of the fast flow is a focus rather than the node. The displayed orbit $(\kappa_1(t), \kappa_2(t))$ corresponds to a switching episode from the oscillatory state to the quasi-stationary state and back (evolution direction indicated by arrows). (c) and (d) show the time traces of phases and couplings during this switching episode.

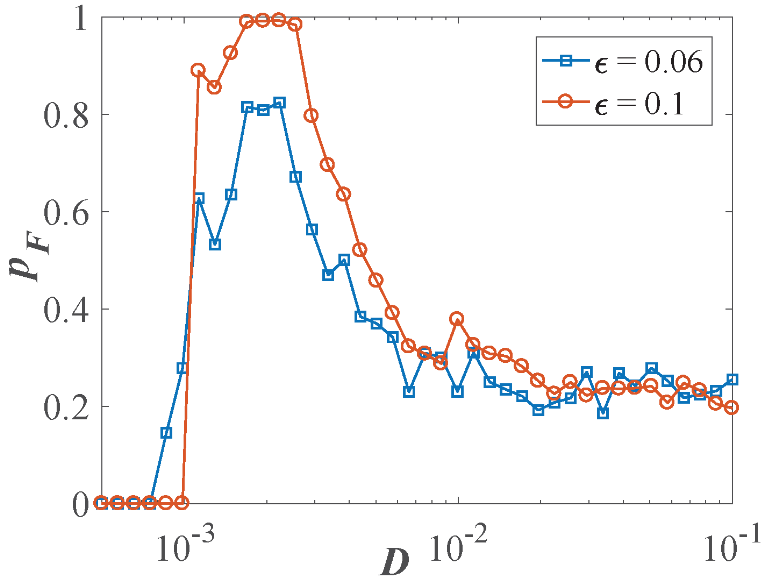

Figure 4.8: Conditional probability $p_F(D)$ for $\varepsilon = 0.06$ (blue squares) and $\varepsilon = 0.1$ (orange circles).

from the oscillatory to the stationary regime, or an inverse one, unfolding in the opposite direction.

For (κ_1, κ_2) values immediately after the SNIPER bifurcation toward the quiescent state, the stable equilibrium of the fast flow is a node. Nevertheless, for noise levels where ISR is most pronounced, we find that the coupling dynamics guides the system into the region where the equilibrium is a stable focus rather than a node, see the yellow highlighted region in Fig. 4.7(b). We have verified that this feature is a hallmark of the resonant effect by numerically calculating the conditional probability p_F that the events of crossing the SNIPER bifurcation are followed by the system's orbit visiting the (κ_1, κ_2) region where the stable equilibrium is a focus. The $p_F(D)$ dependencies for two characteristic ε values at fixed $\beta = 4.2$ plotted in Fig. 4.8 indeed show a maximum for the resonant noise levels, corresponding to the minima of the frequency dependencies in Fig. 4.2(a). From this we infer that the local dynamics near the focus causes a form of a *trapping* effect due to which the phase variables remain in the associated quasi-stationary states much longer than when the metastable states derive from the nodes of the fast flow. Small noise below the resonant values is insufficient to drive the system to the regions featuring focal equilibria, whereas for too strong noise, the stochastic fluctuations completely take over, washing out the quasi-stationary regime. The trapping effect is enhanced for the faster adaptivity rate, as evinced by the fact that the curve $p_F(D)$ for $\varepsilon = 0.1$ lies above the one for $\varepsilon = 0.06$, see Fig. 4.8.

4.2 *ISR due to noise-enhanced stabilization of an unstable fixed point*

By studying the paradigmatic example of two adaptively coupled stochastic active rotators with local dynamics in the oscillatory regime near the bifurcation threshold, we demonstrate a novel generic scenario for inverse stochastic resonance. In particular, the phenomenon arises due to a trapping effect associated with noise-enhanced stability of an unstable fixed point. To explain the details of the underlying mechanism, we perform a slow-fast analysis of the corresponding noiseless system, whereby we demonstrate that noise induces "tunneling" through the bifurcation threshold, temporarily stabilizing an unstable fixed point of the deterministic system.

4.2.1 Model and deterministic dynamics of the full system

In this section, we will consider the same model from the previous section (4.1), but with local dynamics in the *oscillatory* $(I_0 > 1)$ rather than the excitable regime, keeping the parameter $I_0 = 1.05$ fixed near the bifurcation threshold. The plasticity parameter is set to $\beta = \pi$, such that the modality of the phase-dependent adaptivity rule resembles the spike-timing-dependent plasticity (STDP) in neuronal systems [84, 85, 86, 288, 289], whose typical form [182, 289] favors a causal relationship between the pre- and post-synaptic neuron firing times [206, 207]. For an illustration of the considered STDP-like rule, refer to Fig. 2.1 which shows how the stationary values of the couplings depend on $\varphi_2 - \varphi_1$. The full model now reads:

$$\begin{aligned}
\dot{\varphi_1} &= I_0 - \sin\varphi_1 + \kappa_1 \sin(\varphi_2 - \varphi_1) + \sqrt{D}\xi_1(t) \\
\dot{\varphi_2} &= I_0 - \sin\varphi_2 + \kappa_2 \sin(\varphi_1 - \varphi_2) + \sqrt{D}\xi_2(t) \\
\dot{\kappa_1} &= \varepsilon(-\kappa_1 - \sin(\varphi_2 - \varphi_1)) \\
\dot{\kappa_2} &= \varepsilon(-\kappa_2 + \sin(\varphi_2 - \varphi_1)).
\end{aligned} \tag{4.4}$$

The following sections concern the noiseless ($D = 0$) dynamics of the system. We will first provide a numerical analysis of the multistability in the full system with finite scale separation, and then perform a slow-fast analysis considering the singular perturbation limit, which will allows us to gain a deeper understanding of the mechanism behind ISR.

4.2.1.1 Stationary states

The deterministic system of the full system is invariant to $\mathbb{Z}_2$ symmetry (exchange of indices), which implies that the solutions appear in pairs sharing the same stability properties. The specific feature of the plasticity rule $\beta = \pi$ is that it confines the dynamics of the couplings to a symmetry invariant subspace, namely, $\kappa_1(t) = -\kappa_2(t) \equiv \kappa(t)$, which is readily seen from adding the equations for the coupling dynamics. This reduces the deterministic version of the original system (4.1) to the following three-dimensional form

$$\begin{aligned}
\dot{\varphi_1} &= I_0 - \sin\varphi_1 + \kappa \sin(\varphi_2 - \varphi_1) \\
\dot{\varphi_2} &= I_0 - \sin\varphi_2 + \kappa \sin(\varphi_2 - \varphi_1) \\
\dot{\kappa} &= \varepsilon(-\kappa - \sin(\varphi_2 - \varphi_1)).
\end{aligned} \tag{4.5}$$

By numerically solving the corresponding eigenvalue problem, we have verified that (4.5) has no stable fixed points. Rather, the system possesses two pairs of $\mathbb{Z}_2$ symmetry-related fixed points: a pair of saddle nodes and a pair of saddle foci, whereby the following conditions hold for each of the fixed points:

$$\begin{aligned}
{\kappa_1}^* &= -{\kappa_2}^* \\
{\varphi_1}^* &= \pi - {\varphi_2}^*.
\end{aligned} \tag{4.6}$$

The maximal real part of the eigenvalues of the foci displays a power-law dependence on the scale separation, tending to zero in the singular limit $\varepsilon \to 0$, cf. Fig 4.9. The stable manifolds of the saddle points determine the separatrices between the coexisting limit cycle attractors.

4.2.1.2 Multistability of oscillatory regimes in the full system

As far as oscillatory states are concerned, our numerical experiments show that (4.5) exhibits multistability of three periodic solutions which lie within the invariant subspace $\kappa_1(t) = -\kappa_2(t)$, namely

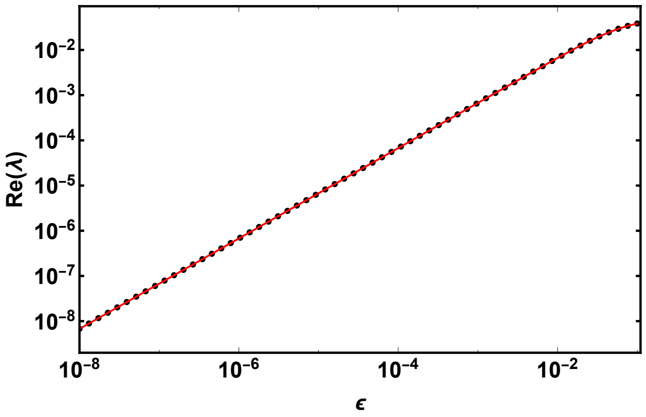

Figure 4.9: The dependence of the maximal real part of the eigenvalues of the two foci Re(λ) on timescale separation ε reveals that the values tend to zero as a power law in the singular limit ($\varepsilon \to 0$).

1. two non-zero coupling solutions with a constant phase shift **lying off the synchronization manifold**, related by the exchange symmetry of indices;

2. zero-coupling solutions with the fast variables synchronized in-phase, **lying on the synchronization manifold**.

These regimes are illustrated in Fig. 4.10, which shows the time traces of both variables, alongside the respective basins of attraction.

Nevertheless, the existence of these solutions critically depends on ε. In particular, for intermediate ε, the two periodic solutions off the synchronization manifold undergo a sequence of period-doubling bifurcations, eventually vanishing in a homoclinic bifurcation, as they collide with the unstable manifold of the foci (which have two stable directions in the κ subspace). Fig. 4.11 shows the corresponding bifurcation diagram, constructed by the method of numerical continuation, such that the final state for the given ε value was taken as the initial state for the incremented ε value. The system is multistable until $\varepsilon \approx 0.382$, above which one lying on the synchronization manifold (effectively uncoupled units) remains the only attractor.

4.2.2 Slow-fast analysis

A deeper understanding of the ingredients relevant for gaining insight into the mechanism of inverse stochastic resonance can be gained within the framework of fast-slow analysis. In the present section, we will first study the layer problem by determining the stationary and periodic solutions of the fast flow, and then demonstrate that this particular value of β also gives rise to the invariance of the fast flow to time-reversal symmetry.

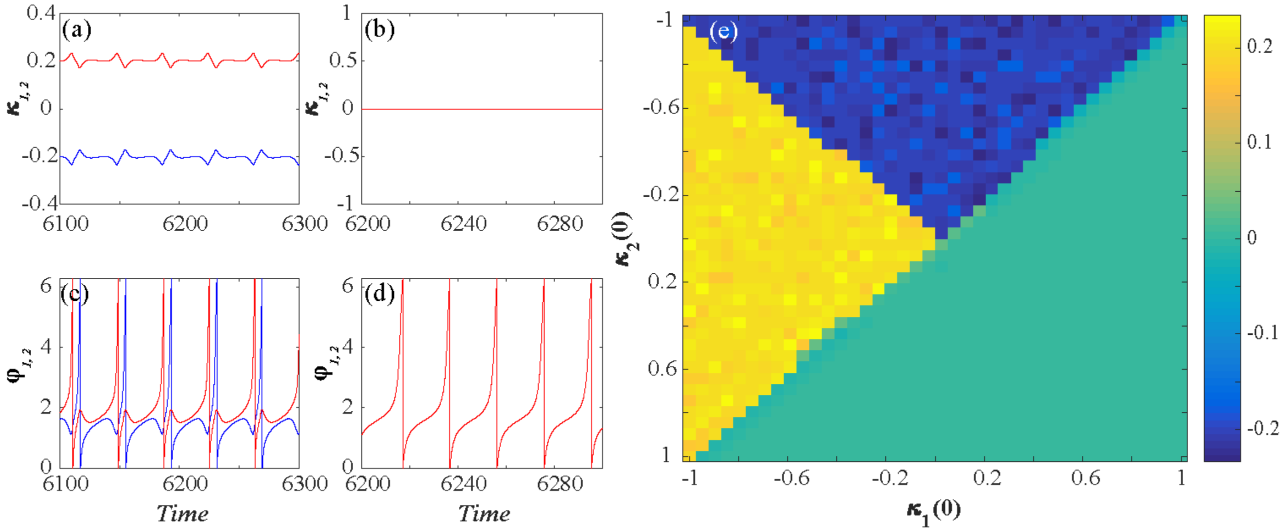

Figure 4.10: Multistability of the full system (4.5) for $I_0 = 1.05, \beta = \pi, \varepsilon = 0.01, D = 0$. (a)-(d) The left/middle column refers to the dynamics of the two periodic solutions off/on the synchronization manifold. The basins of attraction of all three regimes are shown in (e), whereby the yellow and the blue regions correspond to initial conditions leading to the two solutions off the synchronization manifold, whereas the green domain indicates those leading to the solution lying on the synchronization manifold.

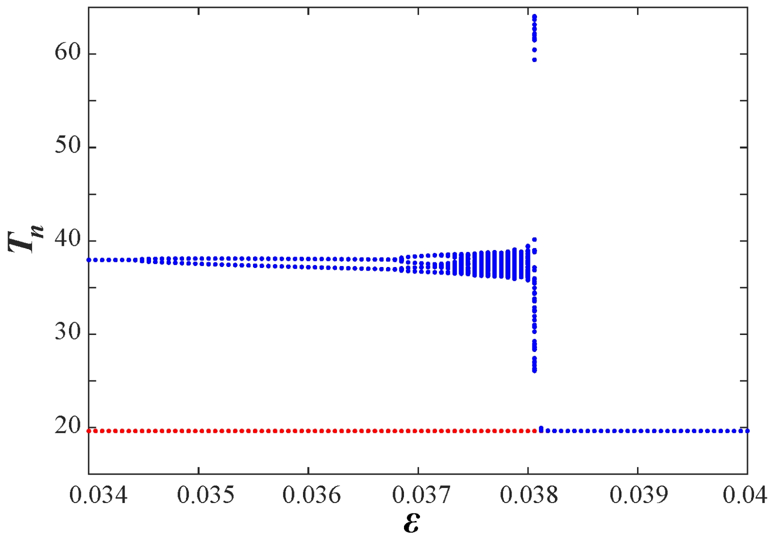

Figure 4.11: Numerical bifurcation diagram obtained by determining the first return times T_n to the Poincare cross-section $\varphi_1 = 4.5$ for system (4.5) with $I_0 = 1.05, \beta = \pi, D = 0$, constructed by the method of numerical continuation. The blue dots refer to a representative periodic solution off the synchronization manifold, while the red dots correspond to the periodic solution on the synchronization manifold.

4.2.2.1 Layer problem: stationary states and periodic orbits of the fast flow

Let us now consider the layer problem, defined on the fast timescale, formally obtained by setting $\varepsilon = 0$ in the multiscale system (4.5),

$$\begin{aligned}\dot{\varphi}_1 &= I_0 - \sin\varphi_1 + \kappa \sin(\varphi_2 - \varphi_1)\\ \dot{\varphi}_2 &= I_0 - \sin\varphi_2 + \kappa \sin(\varphi_2 - \varphi_1),\end{aligned} \tag{4.7}$$

where $\kappa \in [-1, 1]$ is treated as an additional system parameter.

To classify the stationary states of the fast flow, we will apply the coordinate transformation $(\varphi_1, \varphi_2) \mapsto (\Phi, \delta\varphi) = (\frac{\varphi_1+\varphi_2}{2}, \frac{\varphi_1-\varphi_2}{2})$, such that the fast flow (4.7) becomes

$$\begin{aligned}\delta\dot{\varphi} &= -\sin\delta\varphi\cos\Phi\\ \dot{\Phi} &= I_0 - \cos\delta\varphi(\sin\Phi + 2\kappa\sin\delta\varphi).\end{aligned} \tag{4.8}$$

From the second equation in (4.8), one readily finds that the fast flow cannot possess any fixed points on the synchronization manifold for oscillatory local dynamics, since $\delta\varphi = 0$ cannot satisfy the system for $I_0 > 1$. Therefore, the stationary solutions $(\varphi_1^*, \varphi_2^*)$ may arise only from the condition $\cos\Phi = 0$, namely,

$$\cos\frac{\varphi_1^* + \varphi_2^*}{2} = 0 \Rightarrow \frac{\varphi_1^* + \varphi_2^*}{2} = \frac{\pi}{2} + n\pi, n \in \mathbb{Z} \Rightarrow \varphi_1^* + \varphi_2^* = \pi$$

A numerical bifurcation analysis reveals that the fast flow (4.7) exhibits either two fixed points or none at all, depending on κ and I_0, cf. Fig. 4.12 (a). The two fixed points are a saddle point $SP \equiv (\varphi_{1SP}, \varphi_{2SP})$ and a center $CP \equiv (\varphi_{1CP}, \varphi_{2CP})$ whose relative positions for fixed I_0 depend on the value of κ. The structure of the fast flow is organized around the **saddle-center bifurcation** which occurs at $\kappa = \kappa_{SC} \approx -0.1674$ for $I_0 = 1.05$. In this bifurcation scenario, the two fixed points get annihilated as a homoclinic orbit associated with the saddle collapses onto the center, as illustrated in Fig. 4.12 (b)-(c). Nevertheless, the two fixed points re-emerge at the symmetrical weight value $\kappa = -\kappa_{SC} \approx 0.1674$.

To gain a complete picture of the multistable dynamics of the fast flow, we have shown illustrative examples of the phase portraits and the associated vector fields for $\kappa < \kappa_{SC}$ and $\kappa > \kappa_{SC}$ in Figures 4.13(a) and 4.13(b), respectively. For $\kappa \in [-1, \kappa_{SC})$, the fast flow exhibits a limit cycle attractor, essentially derived from the local dynamics of the units, cf. the orbit indicated in orange in Fig. 4.13(a). Apart from the attracting periodic orbit, one observes two additional types of closed orbits, namely the homoclinic connections to the saddle point (SP), shown by blue and green, as well as periodic orbits around the center point (CP), an example of which is indicated in purple. On the other hand, for $\kappa > \kappa_{SC}$, the fast flow exhibits bistability of two oscillatory solutions, featuring the coexistence of a limit cycle inherited from the local dynamics of units and a limit cycle associated with the former homoclinic orbits, cf. Fig. 4.13(b).

The counterpart of the center point of the fast flow in the full system (4.5) is a weakly unstable focus. This difference originates from the fact that for finite scale separation, the

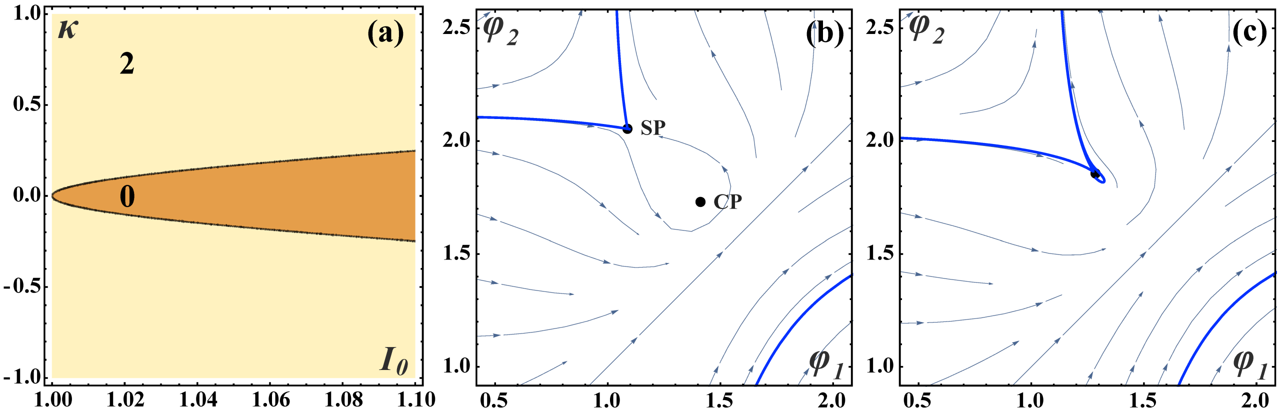

Figure 4.12: (a) The variation of the number of fixed points of the fast flow (4.7) in the (κ, I_0) plane, showing that it admits two or none fixed points. The saddle-center bifurcation scenario accounting for the change in the number of fixed points is shown in (b) and (c), obtained for $I_0 = 1.05$ with $\kappa = -0.2 < \kappa_{SC}$ in (b) and $\kappa = -0.1674 \approx \kappa_{SC}$ in (c). The homoclinic orbit of the saddle point SP, shown in blue, gradually engulfs the center point CP as the fixed points eventually collide and disappear at $\kappa = \kappa_{SC}$.

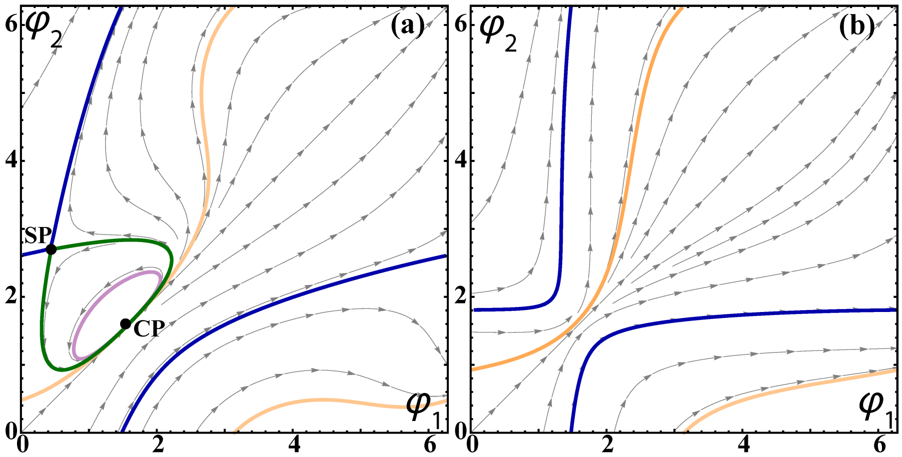

Figure 4.13: Multistable dynamics of the fast flow (4.7) for $I_0 = 1.05$ (a) below $(\kappa = -0.8)$ and (b) above the saddle-center bifurcation $(\kappa = -0.08)$. In (a), the system has two unstable fixed points, a saddle (SP) and a center (CP), and exhibits three types of closed orbits: a limit cycle attractor (orange) derived from the local dynamics of the units, homoclinic connections to SP (blue and green), and subthreshold oscillations around the center (purple). In (b), the system exhibits bistability between two oscillatory states, shown in orange and blue.

number and stability of fixed points depend on ε. In particular, the associated eigenvalues show that the fixed points of the full system are a pair of saddles (all eigenvalues real, one eigenvalue positive) and a pair of weakly unstable foci, rather than centers. The unstable foci are in fact saddle-foci, with two real negative eigenvalues and a pair of complex conjugate eigenvalues with positive real parts. However, as we have already shown in Fig. 4.9, it turns out that, as the singular limit $\varepsilon \to 0$ is approached, the maximal real part of the eigenvalues of the unstable foci tends to zero according to a power law dependency, corroborating the consistency of the slow-fast analysis with the dynamics of the full system in the singular limit.

4.2.2.2 Time-reversal symmetry of the fast flow

The appearance of the center point in the dynamics of the fast flow (4.7) is associated with its invariance to time-reversal symmetry. To show this explicitly, we will derive the symmetry-preserving map R, assuming that it has the form

$$R = \begin{cases} \varphi_1 \to X - \varphi_2, \\ \varphi_2 \to X - \varphi_1, \\ t \to -t, \end{cases}$$

where X has to be determined.

After applying R to (4.7), the indices in the l.h.s. of $\dot{\varphi}_1$ and $\dot{\varphi}_2$ are exchanged, while the coupling term remains unchanged:

$$\begin{aligned} \dot{\varphi}_2 &= I_0 - \sin(X - \varphi_2) + \kappa \sin(\varphi_2 - \varphi_1) \\ \dot{\varphi}_1 &= I_0 - \sin(X - \varphi_1) + \kappa \sin(\varphi_2 - \varphi_1). \end{aligned}$$

Thus, X must satisfy the condition

$$\sin(X - \varphi_i) = \sin \varphi_i, i = \{1,2\} \iff X = (2k+1)\pi, k \in \mathbb{Z},$$

which leads to the symmetry-preserving map

$$R = \begin{cases} \varphi_1 \to \pi - \varphi_2, \\ \varphi_2 \to \pi - \varphi_1, \\ t \to -t \end{cases} \tag{4.9}$$

The invariance of (4.7) under R can readily be illustrated by superimposing the vector field plots of the system before and after applying the time-reversal transformation (4.9), cf. Fig. 4.14. Since the two vector fields coincide, one infers that the fast flow (4.7) is invariant to time-reversal symmetry.

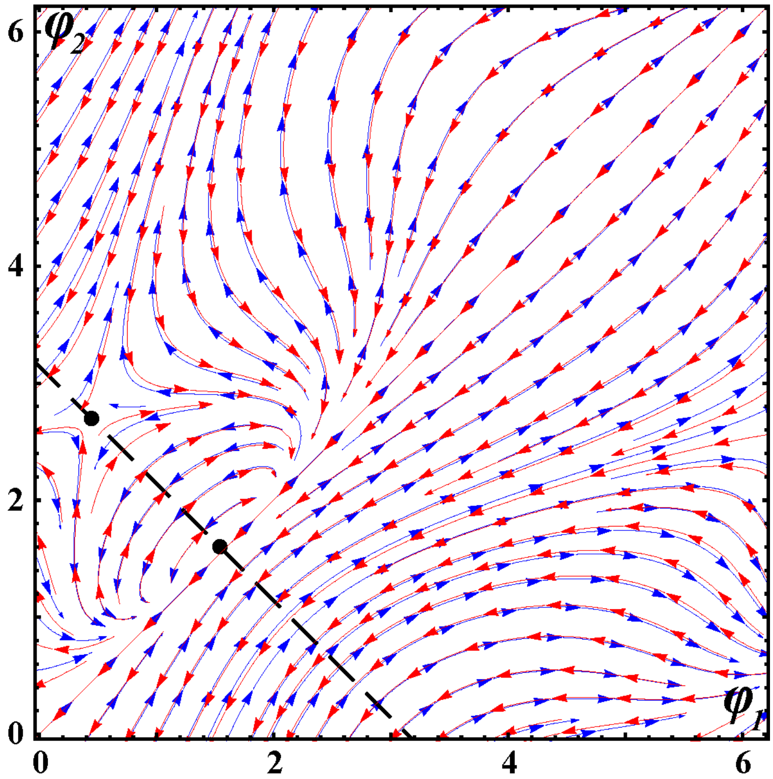

Figure 4.14: Time-reversal symmetry of the fast flow for $I_0 = 1.05, \kappa = -0.8$. The dashed line connects the saddle point and the center. Since the vector fields before (blue) and after (red) applying the time-reversal transformation 4.9 coincide, the fast flow is invariant under time-reversal.

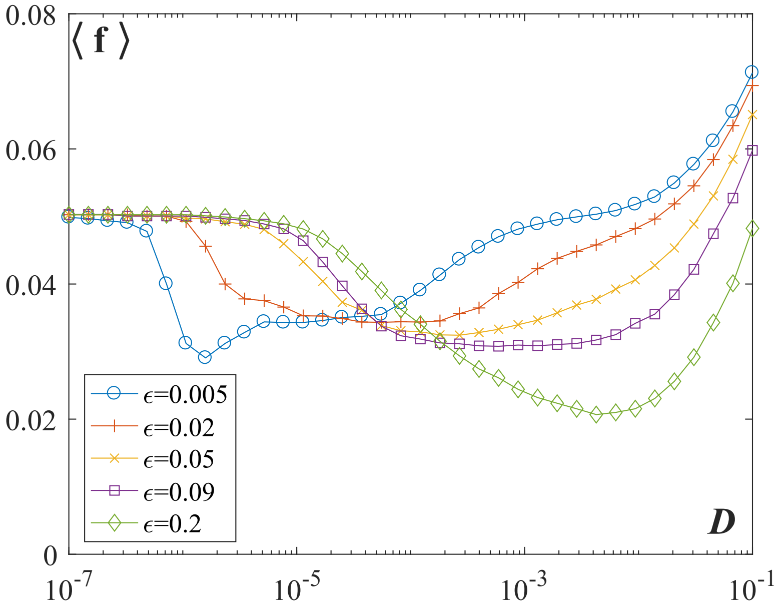

Figure 4.15: Observation of inverse stochastic resonance in system (4.4) with $I_0 = 1.05$. A family of dependencies $\langle f \rangle(D)$ for scale separations $\varepsilon \in \{0.005, 0.02, 0.05, 0.09, 0.2\}$.

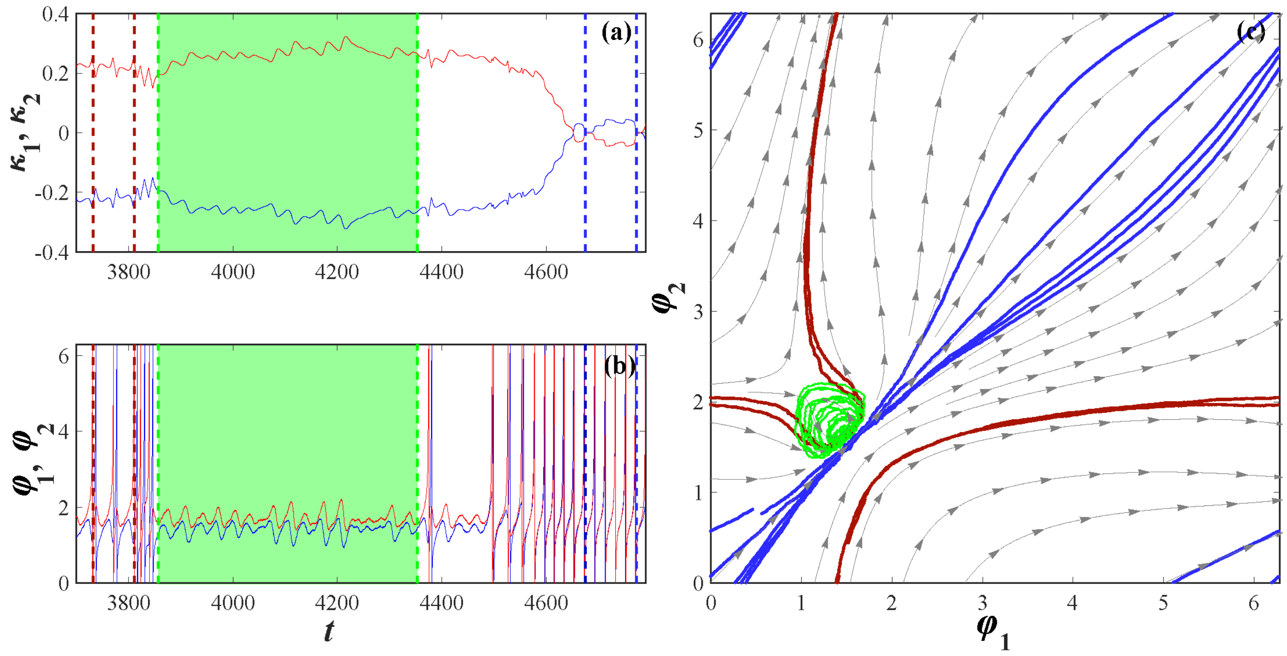

Figure 4.16: (a) and (b) show the time traces of $\kappa_i(t)$ and $\varphi_i(t), i \in \{1,2\}$ respectively, with an episode during which the system remains in the vicinity of an unstable fixed point highlighted in green. The parameters are $I_0 = 1.05, \varepsilon = 0.035, \beta = \pi, D = 10^{-4}$. (c) The orbits conforming to the two metastable states characterized by large-amplitude oscillations of phases are shown in red and blue, whereas the subthreshold oscillations are indicated in green. Superimposed is the vector field of the fast flow, corresponding to the limit $\varepsilon \to 0$.

4.2.3 Numerical observation of ISR and the trapping effect

We find that system (4.5) exhibits the characteristic non-monotone response to noise in which the oscillation frequency of the phases $\langle f \rangle$ displays a minimum at an intermediate noise level, see Fig. 4.15. In contrast to the mechanism described in section 3.1, the onset of ISR here does not *qualitatively* depend on the adaptivity rate. Instead, the dependence of the system's nonlinear response to noise on ε is only *quantitative* whereby the resonant noise level shifts to larger values with increasing ε. Our exhaustive numerical simulations, in which we performed stochastic averaging over an ensemble of 100 different process realizations, indicate that the effect persists for slow adaptivity rates, cf. the example of the $\langle f(D) \rangle$ for $\varepsilon = 0.005$ in Fig. 4.15. Moreover, our slow-fast analysis also corroborates that all ingredients required for the ISR effect remain in the singular perturbation limit $\varepsilon \to 0$. The persistence of the ISR effect has also been numerically confirmed for faster adaptivity rates of the order $\varepsilon \sim 0.1$. In this case, we have observed that the minima of the $\langle f(D) \rangle$ curves become deeper with ε, suggesting that the effect becomes more pronounced for higher adaptivity rates.

Using the elements of singular perturbation theory, and in particular, the described layer dynamics, one may explain the mechanism behind ISR as follows. In the presence of noise, the described attractors of the fast flow (4.7) become metastable states. Nevertheless, in con-

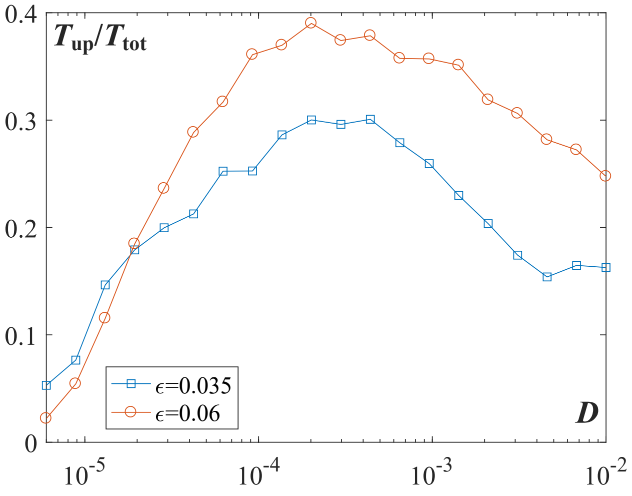

Figure 4.17: Numerically estimated fraction of time spent in the vicinity of the unstable fixed point T_{up}/T_{tot} as a function of noise for $\varepsilon = 0.035$ (squares) and $\varepsilon = 0.06$ (circles). Note that the positions of the maxima coincide with the corresponding resonant noise levels from Fig. 4.15. The remaining system parameters are set to $I_0 = 1.05, \beta = \pi$.

trast to the case of two adaptively coupled excitable units from section 3.1, slow stochastic fluctuations here involve not only switching between the metastable states, but also include *subthreshold oscillations* derived from periodic orbits around the center point. These subthreshold oscillations account for the trapping effect, which results in reducing the oscillation frequency. An example of time series $\kappa_i(t)$ and $\varphi_i(t), i \in \{1,2\}$ obtained for an intermediate $\varepsilon = 0.035$, shown in Fig. 4.16(a)-(b), indeed involves three characteristic episodes, including visits to two distinct oscillatory metastable states and an extended stay in the vicinity of the center, cf. the stochastic orbits $(\varphi_1(t), \varphi_2(t))$ and the vector field of the fast flow in Fig. 4.16(c). In the case of finite scale separation, the trapping effect is manifested as the noise-enhanced stability of an unstable fixed point. The prevalence of subthreshold oscillations changes with noise in a non-monotone fashion, see the inset in Fig. 4.16(c), becoming maximal around the resonant noise level where the frequency dependence on noise exhibits a minimum, cf. Fig. 4.17 and Fig. 4.15. The fraction of time spent in the metastable state corresponding to subthreshold oscillations has been estimated by a threshold-based numerical procedure analogous to the one already described in section 4.1.

4.2.3.1 Degradation of ISR for different rules of adaptation

The present subsection concerns the robustness of ISR with respect to different plasticity rules, viz. its persistence as the plasticity parameter β is changed. For plasticity rules $\beta \lesssim \pi$, it has been found that the effect persists in a small interval below $\beta = \pi$. For instance, for fixed $\varepsilon = 0.05$, the effect is observed within the interval $\beta \in (\pi - 0.15, \pi)$. In this β range, the trapping efficiency of the phase space area around the weakly unstable focus is still sufficient to give rise to the nonlinear response to noise. The degradation of the resonant effect for decreasing β is illustrated in Fig. 4.18. Beyond the given β interval, the phase synchronized oscillations with constant bidirectional coupling remain the only stable

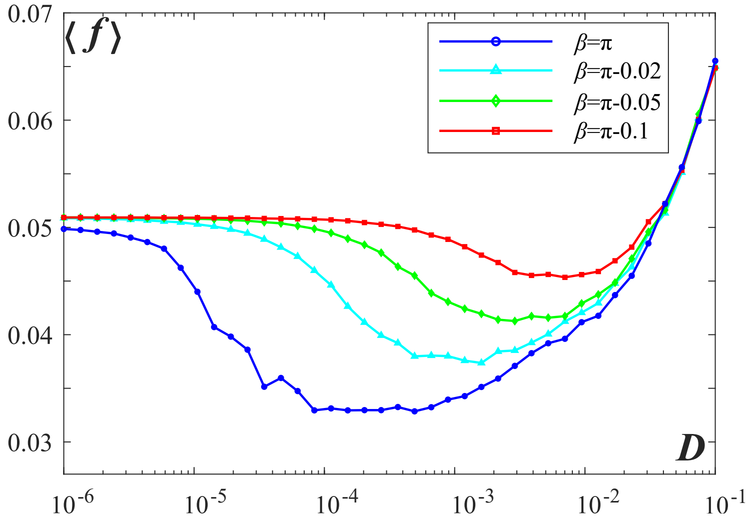

Figure 4.18: Family of $\langle f\rangle(D)$ curves over $\beta \lesssim \pi$ for system (4.4) with $I_0 = 1.05$. The resonant effect is suppressed with reducing β.

solution of the deterministic system. This physical picture is only marginally perturbed by noise and there is no reduction of the oscillation frequency.

For plasticity rules $\pi < \beta < 4.391$, the dynamics is qualitatively different than the one for $\beta \lesssim \pi$ because the fast flow admits two coexisting stable fixed points (not shown). Note that the two stable fixed points are created as nodes at $\beta \approx 4.391$, but become foci as β decreases below $\beta \approx 4.1295$. Under the influence of noise, one finds switching between the two quasi-stationary metastable states, but no nonlinear response to noise is observed.

4.3 *Two mechanisms of ISR in classical neuronal models*

So far, we have demonstrated two novel paradigmatic scenarios for ISR considering the examples of coupled Type I excitable oscillators, whose local dynamics is near a SNIPER bifurcation, either in the excitable or the oscillatory regime. Nevertheless, one may show that the onset of ISR and the underlying mechanisms do not depend on the excitability class of the local dynamics. In particular, it has recently been demonstrated that a single Type II Fitzhugh-Nagumo relaxation oscillator exhibits the qualitatively same form of non-monotone dependence on noise [94], with the mechanism involving noise-induced subthreshold oscillations that follow the maximal canard of an unstable focus. In that case, it has been established that the trapping effect and the related subthreshold oscillations are triggered due to the *phase-sensitive excitability* of a limit cycle.

Moreover, we have verified that the same model of neuronal dynamics, set to different parameter regimes, may exhibit the two generic scenarios of ISR we described. In particular,

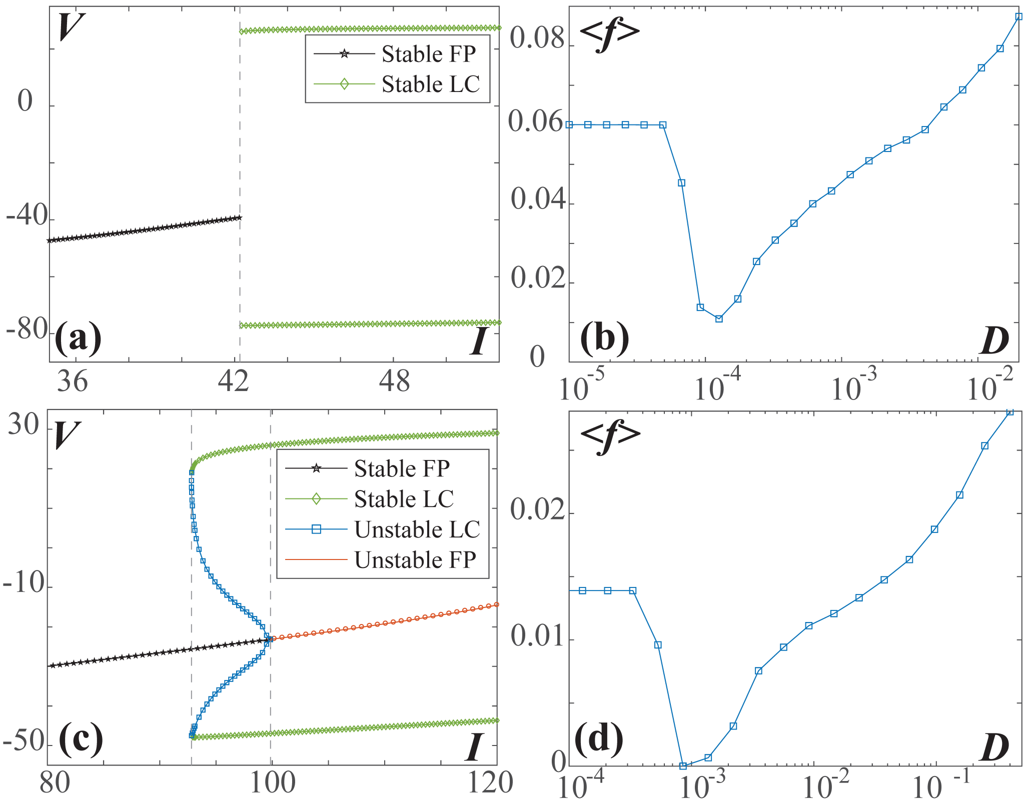

Figure 4.19: (a) The bifurcation diagram for the Morris-Lecar model in the vicinity of the *supercritical* Hopf bifurcation, showing the dependence of the membrane potential amplitudes V on the external bias current I. (b) illustrates the $\langle f \rangle(D)$ dependence for the Morris-Lecar neural oscillator at $I = 43$. (c) $V(I)$ bifurcation diagram for the Morris-Lecar model near the *subcritical* Hopf bifurcation. (d) The characteristic non-monotone dependence $\langle f \rangle(D)$ for the Morris-Lecar model from (c), with the bifurcation parameter $I = 95$ set to the bistable regime. The remaining parameters of the Morris-Lecar model for both cases are specified in the main text.

the Morris-Lecar neuron model is given by

$$\begin{aligned}
C\frac{dv}{dt} &= -g_{fast}m(v)(v - E_{Na}) - g_{slow}W(v - E_K) - g_{leak}(v - E_{leak}) + I \\
\frac{dv}{dt} &= \phi\frac{W_\infty(v) - W}{\tau(v)} \\
m(v) &= 0.5[1 + \tanh(\frac{v - \beta_m}{\gamma_m})] \\
W_\infty(v) &= [1 + \tanh(\frac{v - \beta_w}{\gamma_w})] \\
\tau(v) &= 1/\cosh(\frac{v - \beta_w}{2\gamma_w}),
\end{aligned}$$

where v and W denote the membrane potential and the slow recovery variable, respectively. The external bias current I is the bifurcation parameter. By an appropriate selection of the system parameters, the dynamics can be set to the vicinity of a supercritical or a subcritical Hopf bifurcation [294].

In the first case, obtained for $E_{Na} = 50\ mV, E_K = -100\ mV, E_{leak} = -70\ mV, g_{fast} =$

$20\ mS/cm^2, g_{slow} = 20\ mS/cm^2, g_{leak} = 2\ mS/cm^2, \phi = 0.15, C = 2\ \mu F/cm^2, \beta_m = -1.2\ mV, \beta_w = -13\ mV, \gamma_m = 18\ mV, \gamma_w = 10\ mV$, the model is monostable under the variation of I, and ISR is observed slightly above the Hopf bifurcation ($I = 43\mu A/cm^2$) due to **noise-enhanced stability of an unstable fixed point**, cf. Fig. 4.19(a)-(b).

In the second case, conforming to the parameter set $E_{Na} = 120\ mV, E_K = -84\ mV, E_{leak} = -60\ mV, g_{fast} = 4.4\ mS/cm^2, g_{slow} = 8\ mS/cm^2, g_{leak} = 2\ mS/cm^2, \phi = 0.04, C = 20\ \mu F/cm^2, \beta_m = -1.2\ mV, \beta_w = 2\ mV, \gamma_m = 18\ mV, \gamma_w = 30\ mV$, the model displays bistability between a limit cycle and a stable equilibrium in a range of I values just below the Hopf threshold. There, ISR emerges due to a mechanism based on **biased switching**, see the bifurcation diagram $V(I)$ in Fig. 4.19(c) as well as the dependence of the oscillation frequency on noise for $I = 95\ \mu A/cm^2$ in Fig. 4.19(d).

4.4 *Controlling CR by nonlinear feedback*

Coherence resonance is a phenomenon in which the regularity of noise-induced oscillations becomes maximal at an intermediate noise level [108, 159, 160, 161, 162, 163, 164, 165, 166, 167, 168, 169, 170]. A number of recent studies have addressed the *control* of the statistical features of noise-induced spiking in (coupled) excitable systems, i. e. mechanisms of enhancing or suppressing CR. In networks of coupled oscillators, efficient control mechanisms include time-delayed feedback [276, 277, 278, 279, 280, 281, 282], network topology [283], spatial heterogeneity of bifurcation parameters [285], as well as multiplexing it to another layer which exhibits SISR [284]. In the present section, we will study the control of CR due to an interaction between stochastic fluctuations and a slowly adapting feedback. Our main finding is that the filtered feedback employed in our model provides an efficient means of controlling this effect, whose prominence can be substantially enhanced or suppressed by a corresponding choice of the feedback gain. To explicitly demonstrate that our extension of singular perturbation theory to stochastic systems can be used to predict the statistical features of the noise-induced spiking, including its regularity, we will compare the regularity of oscillations arising in the original multiscale system to that of the limiting case of infinite time scale separation. Note that the present study strongly relies on the findings from section 3.2.

4.4.1 Paradigmatic model for the control of CR via a slowly adapting feedback

This study concerns a stochastic excitable system subjected to a slow control via a low-pass filtered feedback whose general form is

$$\begin{aligned} \dot{v} &= f(v,\mu) + \sqrt{D}\xi(t) \\ \dot{\mu} &= \varepsilon(-\mu + \eta g(v)), \end{aligned} \tag{4.10}$$

where the small parameter $0 < \varepsilon \ll 1$ determines the timescale separation between the fast variable $v(t)$ and the slow feedback variable $\mu(t)$. The fast dynamics $\dot{v} = f(v, 0)$ is excitable and is influenced by Gaussian white noise $\xi(t)$ of variance D. Moreover, the slow feedback variable μ controls its excitability properties. The parameter η is the control gain or feedback strength, such that for $\eta = 0$ one recovers a classical noise-driven excitable system [67]. Systems like (4.10) conform both to spontaneous dynamics of classical neuronal models, such as the Izhikevich model [258], but may also be associated with dynamics of neuronal populations (where the collective dynamics is reduced to the evolution of the phase variable, such as the active rotator model) influenced by a slowly changing environment.

The simplest possible, yet paradigmatic choice of a model with excitable local dynamics is given by the active rotator. We have introduced the adaptation by considering a positive phase-dependent periodic function $g(\varphi) = 1 - \sin\varphi$, namely

$$\begin{aligned} \dot{\varphi} &= I_0 - \sin\varphi + \mu + \sqrt{D}\xi(t), \\ \dot{\mu} &= \varepsilon\left(-\mu + \eta\left(1 - \sin\varphi\right)\right), \end{aligned} \tag{4.11}$$

where the fast dynamics of the phase $\varphi \in S^1$ and the slow dynamics of the feedback variable $\mu \in \mathbb{R}$ involve a timescale separation defined by the small parameter $0 < \varepsilon \ll 1$. The excitability of the fast subsystem is controlled by the parameter I_0 and the slowly adapting feedback variable μ, characterized by the feedback strength parameter η which affects the fast dynamics via feedback. Moreover, the excitable fast dynamics is influenced by Gaussian white noise $\xi(t)$ of variance D.

In the absence of feedback and noise, i. e. for fixed $\mu = 0$ and $D = 0$, the fast subsystem undergoes a SNIPER bifurcation at $I_0 = 1$. Nevertheless, in the presence of feedback, the deterministic dynamics is governed by the term $I_0 + \mu(t)$ which can induce switching between the excitable equilibrium ($|I_0 + \mu| < 1$) and the oscillatory regime ($|I_0 + \mu| > 1$). This adaptation rule provides a positive feedback for the spikes and oscillations, since μ increases when $\varphi(t)$ is oscillating and drives the system towards the oscillatory regime, while in the vicinity of the equilibrium ($\sin\varphi \approx 1$) the control signal effectively vanishes.

The following subsections, we will provide the analysis of the deterministic dynamics of the system within the singular perturbation theory, and then extend the slow-fast approach to the noise-driven system.

4.4.1.1 Slow-fast analysis of the deterministic system

The layer problem, formally obtained by setting $\varepsilon = 0$ in (4.11), concerns the fast subsystem

$$\dot{\varphi} = I_0 + \mu - \sin\varphi, \tag{4.12}$$

where μ is treated as an additional parameter. Depending on the value of μ, (4.12) with $D = 0$ may be either in the excitable ($\mu < 1 - I_0$) or in the oscillatory ($\mu > 1 - I_0$) regime. Conversely, in order to consider the reduced problem, defined on the slow timescale, we rescale time as $T = \varepsilon t$ and set $\varepsilon = 0$ in the rescaled system, obtaining

$$\mu'(T) = -\mu(T) + \eta(1 - \sin\varphi(T)), \tag{4.13}$$

where the prime denotes the derivative with respect to the slow time T. Recall from section 3.2.2 that, by combining adiabatic elimination in the case of the stable equilibrium and averaging over fast oscillations in the case of oscillatory layer dynamics, we were able to derive a reduced slow system, which describes both the slow dynamics on the critical manifold, corresponding to the stable equilibrium of the fast flow, and the slow averaged dynamics corresponding to the oscillatory solution of the fast flow:

$$\mu'(T) = -\mu(T) + \eta(1 - I_0 - \mu(T) + \Omega(\mu(T))). \tag{4.14}$$

where the oscillation frequency $\Omega(\mu)$ is defined as follows

$$\Omega(\mu) = \begin{cases} 0, & \mu < 1 - I_0 \\ \sqrt{(I_0 + \mu)^2 - 1}, & \mu > 1 - I_0 \end{cases}.$$

4.4.1.2 Slow-fast analysis of the stochastic system

Let us now present a summary of our analysis of the stochastic dynamics of (4.11), using the method of stochastic averaging to extend the singular perturbation theory to stochastic systems. In particular, the goal is to derive the equation for the slow dynamics, analogous to (4.14), that would account for the averaged effect of noise in the layer dynamics

$$\mu'(T) = -\mu(T) + \eta(1 - \langle \sin\varphi(t)\rangle_t), \tag{4.15}$$

where $\langle \sin\varphi(t)\rangle_t$ is the stochastic average for solutions of the stochastic fast equation (4.12), calculated as follows

$$\langle \sin\varphi(t)\rangle_t = \lim_{t\longrightarrow\infty} \frac{1}{t}\int_0^t \sin\varphi(t)\mathrm{d}t' = \int_0^{2\pi} \rho(\varphi;\mu,D)\sin\varphi \mathrm{d}\varphi. \tag{4.16}$$

The stationary probability density $\rho(\varphi;\mu,D)$ is the solution of the stationary Fokker-Planck equation for the stochastic layer dynamics. The mean frequency, obtained by time averaging of the layer dynamics (4.12), is given by

$$\Omega_D(\mu) = I_0 + \mu - \langle \sin\varphi(t)\rangle_t, \tag{4.17}$$

which depends on both D and μ via (4.16). After inserting (4.17) into (4.15), the equation for the slow dynamics of $\mu(T)$ reads

$$\mu'(T) = -\mu(T) + \eta(1 - I_0 - \mu + \Omega_D(\mu(T))), \tag{4.18}$$

i.e. it is of the same form as in the deterministic case (4.14).

The numerical bifurcation diagram with respect to D and η is obtained by simultaneously solving for the stationary solution of the Fokker-Planck equation for the layer dynamics (3.38) and the equation for the stationary solution of the slow subsystem. The diagram,

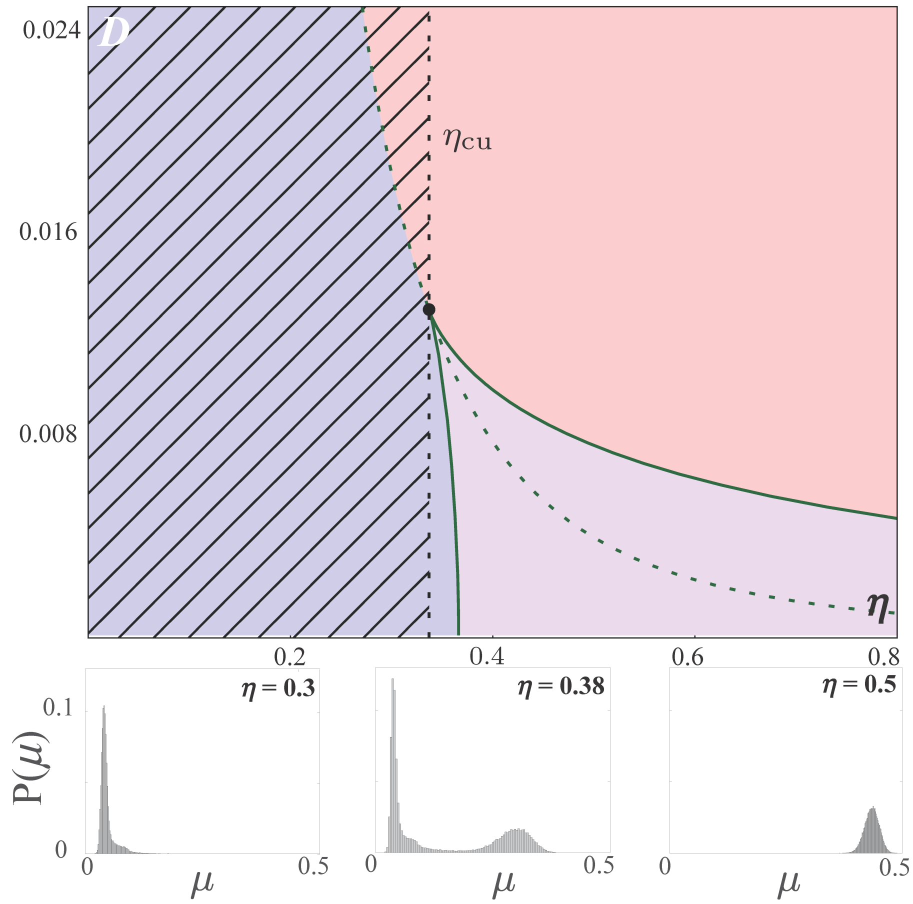

Figure 4.20: Comparison between the bifurcation diagram obtained within singular perturbation theory (upper panel) and numerical simulations for the full system with finite scale separation (lower panel). Upper panel: Stability domains for different dynamical regimes: noise-induced spiking (blue), noise-perturbed oscillations (red), and noise induced bursting (violet). The green dashed line refers to $\mu = \mu_c = 1 - I_0$. Enhanced coherence resonance can be found in the hatched region. Lower panels: Stationary distributions of $\mu(T)$, obtained from numerical simulations of the full system (4.11) with $\varepsilon = 0.005$, $D = 0.008$ and $\eta \in \{0.3, 0.38, 0.5\}$.

shown in Fig 4.20, reveals three characteristic (D, η) regions featuring noise-induced spiking, noise-perturbed spiking, and stochastic busting. For an illustration of the regimes, refer to Figure 3.14. Moreover, our numerical simulations for finite values of ε (lower panels in Fig. 4.20) show that the slowly varying control variable $\mu(T)$ is distributed around the stationary values from the limiting problem $\varepsilon = 0$, see also Figure 3.16. In the following, we will show that by varying the feedback strength within the region of noise-induced spiking, one can enhance or suppress coherence resonance.

4.4.2 Enhancing or suppressing CR by adjusting the feedback strength

The phenomenon of CR is well-known for noise-induced oscillations in excitable systems such as the classical model of the active rotator [161], given by the fast equation (4.12) without adaptation ($\eta = 0$ and therefore also $\mu = 0$), as well as in other phase models such as Adler's equation [155, 295] and the theta neuron [156]. In this section we demonstrate a novel mechanism of control of CR, showing that the effect may be enhanced or suppressed by introducing a slowly adapting variable that, depending on the feedback strength, produces a positive or a negative feedback to noise-induced spikes, effectively driving the system in a self-adjusted way towards or away from the bifurcation threshold.

CR may be characterized by studying how the regularity of noise-induced oscillations changes with the noise intensity. As a measure of the variability of spike timing, one can use the so-called jitter, which represents the coefficient of variation of the interspike interval [149, 273]. In particular, for any 2π-periodic spiking variable φ, the spiking times t_k are defined as the first passage times $\varphi(t_k) = 2\pi k$, $k \in \mathbb{N}$. Then, the corresponding interspike intervals are given by $\tau_k = t_k - t_{k-1}$, such that the coefficient of variation of their distribution is defined as

$$R(D) = \frac{\sqrt{\langle \tau_k^2 \rangle - \langle \tau_k \rangle^2}}{\langle \tau_k \rangle}.$$

Since smaller values of the coefficient of variation indicate a higher regularity of noise-induced oscillations, the effect of CR is reflected in the curve $R(D)$ having a minimum at an intermediate noise level.

The control mechanism is based on coupling the excitable system to a slowly adapting variable, which gives rise to a multiscale system with a finite scale separation. Nevertheless, we show that the introduced extension of singular perturbation theory to stochastic systems may still be used to predict the impact of control on CR with sufficient accuracy. In particular, we were able to predict the statistical features of the response of the full system (4.11) to noise by considering a stochastic equation of the layer dynamics (4.12) where the control variable is replaced by its stationary value obtained from the corresponding reduced problem (4.13). This has allowed us to determine the $R(D)$ dependencies for the stochastic layer dynamics corresponding to different values of feedback strength, which show a good match to the $R(D)$ dependencies for the full system.

Let us now compare the $R(D)$ dependencies obtained for the *full* system (4.11) for a given η value and for the *fast* subsystem (4.12) with the corresponding stochastic averages $\mu^*(D;\eta)$ substituted into μ. In the former case, R can be determined from direct numerical simulations of (4.11), while in the latter case, $\mu^*(D;\eta)$ displays a strongly nonlinear dependence both on η and D, see also Figs. 3.12(a) and 3.13. In particular, for fixed η slightly below the cusp value η_{cu}, the strongly nonlinear dependence of μ^* on D has a substantial impact on the resonant behavior reflected in the form of $R(D)$.

Figure 4.21 displays the $R(D)$ dependence for different values of the feedback strength η, comparing the numerical results for the fast subsystem (4.12) with stationary values $\mu^*(D;\eta)$ substituted as fixed μ, to numerical simulations of the multiscale system (4.11) for $\varepsilon = 0.005$. While for $0 < \eta < \eta_{cu}$ one finds that CR can be substantially enhanced, cf. the $R(D)$ dependencies for $\eta = 0$ and $\eta = 0.3$. On the other hand, the resonant effect can be readily suppressed by introducing negative values of the feedback strength η, see the $R(D)$ curves for $\eta = -0.2$ in Fig. 4.21. This implies that the adaptive feedback we employ provides an

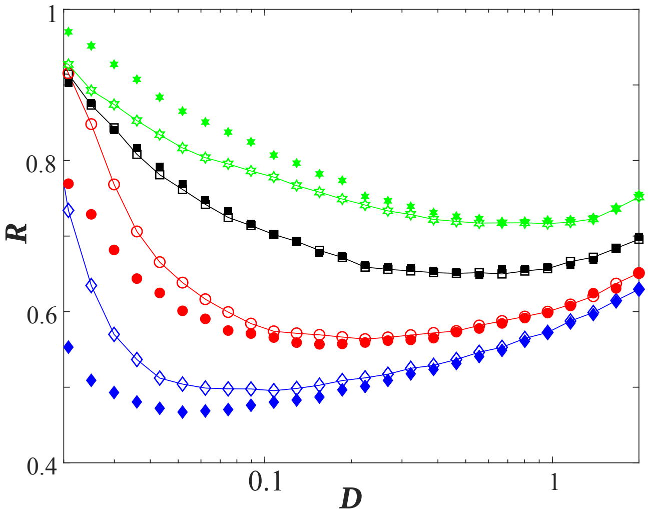

Figure 4.21: Enhancement or suppression of CR by a slowly adapting feedback control. The connected lines with empty symbols refer to $R(D)$ dependencies for the full system (4.11) at different values of the feedback strength: $\eta = -0.2$ (green hexagonals), $\eta = 0$ (black squares), $\eta = 0.2$ (red circles), and $\eta = 0.3$ (blue diamonds), having fixed $I_0 = 0.95, \varepsilon = 0.005$. The unconnected filled symbols indicate the corresponding $R(D)$ dependencies obtained from numerical simulations of the layer equation 4.12 with stationary $\mu^*(D)$.

efficient *control of coherence resonance*. Such an effect has already been demonstrated in [278, 279, 280] by using a delayed feedback control of Pyragas type. However, this control method requires the feedback delay time as an additional control parameter to be well adapted to the maximum resonance frequency.

4.5 *Chapter summary and discussion*

In the present chapter, devoted to the study of resonant effects in noisy coupled systems whose local dynamics is near the bifurcation threshold, we have presented two new generic scenarios for inverse stochastic resonance (ISR) as well as a novel method of controlling coherence resonance (CR). Let us now provide a summary of these results and establish their importance in the context of theoretical developments and applications to neuroscience.

Understanding the conditions which give rise to ISR in coupled excitable systems may be crucial to understanding the prevalence of the effect in neural networks, whose activity depends on the interplay of excitability, coupling properties, and noise. Considering a model that involves the classical ingredients of neuronal dynamics, such as excitable behavior and coupling plasticity, we have demonstrated two paradigmatic scenarios for inverse stochastic resonance. According to one scenario, the phenomenon arises in systems with multistable deterministic dynamics where at least one of the attractors is a stable equilibrium. Due to the structure of the phase space, and in particular the position of the separatrices, the switching dynamics between the associated metastable states becomes biased at an intermediate noise level, such that the longevity of the quasi-stationary states substantially increases or they may even turn into absorbing states. In the other scenario, an oscillatory system possesses a weakly unstable fixed point, whose stability is enhanced due to the action of noise. The latter results in a trapping effect, such that the system exhibits subthreshold oscillations whose prevalence is noise-dependent and is found to be maximal at the resonant noise level. Both scenarios involve classical facilitatory effects of noise, such as crossing the separatrices or stochastic mixing across the bifurcation threshold, which should warrant the ubiquity of ISR. In terms of the robustness of the effect, we have demonstrated that the onset of ISR is independent on the excitability class of local dynamics, and moreover, that the same model of neuronal dynamics, depending on the particular parameters, may display two different scenarios for ISR.

Previous studies have mostly concerned ISR due to biased switching in the case of individual units with bistable dynamics close to a subcritical Hopf bifurcation, involving coexistence of a stable equilibrium and an oscillatory solution [68, 173, 174, 175, 176]. In contrast to that, we have found the same mechanism for emergent oscillations in coupled units with excitable local dynamics. Moreover, ISR is found to be promoted by the multiscale structure of the system, which has been confirmed both for the case of coupled systems with slow adaptive couplings and for the case of single units with inherent multiscale dynamics. The latter has been reported for a single Fitzhugh-Nagumo oscillator just above the supercritical Hopf bifurcation, where ISR occurs due to phase sensitive excitability of the relaxation oscillations [94].

Given that ISR has so far been observed at the level of individual neuron models [94, 173, 174, 176], motifs of units with neuron-like dynamics [172, 193], and neural networks [177], it is reasonable to expect that the phenomenon is universal to neuronal dynamics, affecting both emergent oscillations and systems of coupled oscillators. The presented mechanisms appear to be generic and should be expected in other systems comprised of units with local dynamics near a bifurcation threshold. It is already known that ISR plays important functional roles in neuronal systems, including the reduction of spiking frequency in the absence of neuromodulators, the triggering of stochastic bursting, i.e. of on-off tonic spiking activity, the suppression of pathologically long short-term memories [68, 174, 176, 178], and most notably, may contribute to the generation of UP-DOWN states, characteristic for spontaneous and induced activity in cortical networks [180, 260]. These findings along with our results suggest that ISR may provide a generic means of controlling and optimizing the firing rate in multi-timescale systems, which can be applied to neuronal activity, calcium signaling, and other types of cell dynamics.

Moreover, considering the paradigmatic model of a single active rotator influenced by slowly adaptive feedback which promotes spiking behavior, we have demonstrated that filtered feedback provides efficient control of CR, which can be substantially enhanced or suppressed by a corresponding choice of the feedback gain. The advantage of the control mechanism presented in the thesis compared to other control mechanisms, such as the one of Pyragas type [278, 279, 280], is that it involves only a single control parameter, namely the control gain. We suspect that such a control mechanism may even provide for a self-consistent control of spiking regularity in stochastic neuronal dynamics, e.g. in the Izhikevich neuron model.

Chapter 5

Conclusions

This thesis presents a systematic overview of assorted self-organizing phenomena in coupled excitable systems arising due the interplay of multiple timescale dynamics and noise. In particular, considering paradigmatic models, we have been able to demonstrate and analyze emergent phenomena such as **macroscopic excitability, slow stochastic fluctuations, stochastic bursting, inverse stochastic resonance**, and **coherence resonance**. These phenomena are based on mechanisms of self-organization, namely *synchronization of noise-induced oscillations, noise-induced switching, noise-enhanced stabilization of deterministically unstable structures*, and *noise-induced multistability*. Our results provide important advancements to contemporary studies in nonlinear dynamics, both in terms of the discovery of novel phenomena and their analysis, as well as from a methodological standpoint. Moreover, the present results may fundamentally increase our ability to characterize, predict and control biological systems, such as neuronal networks. Let us now summarize the scientific contributions of this thesis.

5.1 *Conceptual advancements*

1. Extension of the notion of excitability to coupled systems.

At variance with the classical notion of excitability which refers to the dynamics of individual units, this thesis extends the concept of excitability to *coupled* systems. In particular, we have analyzed the excitability of motifs consisting of two active rotators and assemblies of coupled neuronal maps. In the former case, we have classified different threshold-like responses of the coupled system to perturbation [181]. Concerning the latter, we were the first to introduce the concept of *macroscopic excitability* which refers to the scenario where a population of units acts like an excitable element [191].

2. Discovery of two generic mechanisms for inverse stochastic resonance.

We have identified two generic scenarios for inverse stochastic resonance (ISR), one based on biased switching and the other associated with noise-enhanced stabilization of a deterministically unstable fixed point. The effect has been demonstrated both in the case of self-sustained oscillators near the bifurcation threshold and for emergent oscillations in coupled excitable systems. The particular type of slow dynamics, such as phase-dependent plasticity, have been shown to be capable of enhancing the resonant effect. The two mechanisms of ISR have been proven to be independent on the excitability class of local dynamics [193, 194].

So far, ISR has been observed for Type II excitable units with bistable local dynamics near the subcritical Hopf bifurcation [68, 173, 174, 175]. Our results support the idea that ISR may be a more widespread effect, observed in a wide range of systems. Since ISR has already been found in models of individual neurons [94, 173, 174, 176], motifs of units with neuron-like dynamics [172, 193], as well as neural networks [177], it is likely that ISR universal to neuronal dynamics, where it has already been suggested to play a number of important functional roles [68, 174, 176, 178, 180, 260].

3. Discovery of a new method of control of coherence resonance.

We have introduced a novel nonlinear control mechanism of coherence resonance, demonstrating how the resonant effect may be enhanced or suppressed by introducing a slowly adapting feedback to a stochastic excitable system. The adaptation rule provides a positive feedback for the noise-induced rare spikes and oscillations, while in the vicinity of the equilibrium the control signal effectively vanishes [192]. Compared with other types of control, like the one based on the Pyragas scheme of control via delayed feedback [278, 279, 280], the advantage of our method is that it features only one control parameter, namely the feedback strength.

4. Discovery of two types of slow fluctuations in stochastic excitable multiscale systems.

We have investigated switching dynamics in multiscale systems for small, but *finite* timescale separation, having found that it gives rise to two different effects, namely *slow stochastic fluctuations* and *stochastic bursting*. Considering a motif of two adaptively coupled stochastic excitable units, we have found that slow stochastic fluctuations qualitatively depend on the scale separation between the fast and slow variables, such that a larger separation gives rise to switching between two modes of noise-induced oscillations, whereas a smaller separation induces switching between metastable states derived from coexisting attractors of the deterministic dynamics [181]. For the paradigmatic system of a stochastic excitable unit with a slowly adapting feedback, we have demonstrated how the interaction of multiscale dynamics and noise may give rise to *stochastic bursting*, having explained it in terms of switching between metastable states derived from the deterministic version of the system by invoking an analogy with the Eyring-Kramers process in a double-well potential [192].

5.2 *Methodological advancements*

1. Extension of mean-field theory to coupled stochastic maps.

The mean-field method has so far been applied exclusively to the class of continuous-time systems, while effective models for discrete assemblies of coupled maps have been lacking due to the inability to implement the Fokker-Planck formalism to discrete-time systems. Using a cumulant approach complemented by the Gaussian closure hypothesis, we have derived the first effective model for the collective dynamics of coupled stochastic maps [191].

2. Extension of multiscale analysis methods to stochastic systems (stochastic averaging).

Within singular perturbation theory, one may consider two limiting problems corresponding to infinite timescale separation in a multiscale system, namely the layer problem, defined on the fast timescale, and the reduced problem, defined on the slow timescale. We have introduced a novel averaging approach for treating the reduced problem. The case of oscillatory layer dynamics in *deterministic* multiscale problems has typically been treated by performing the averaging over fast oscillations and inserting the obtained averages into the reduced problem dynamics. We have extended this idea to stochastic oscillatory layer dynamics, introducing the method of **stochastic averaging**. By this method, the noise-induced or noise-perturbed oscillations in layer dynamics are considered by solving for the stationary solution of the corresponding Fokker-Planck equation [192].

3. Extension of phase-response theory to coupled systems.

We have studied the stimulus-response relationship of an assembly of coupled neuronal maps, showing that the derived effective model is not only capable of successfully treating the asymptotic, but also the transient collective dynamics of an assembly of coupled stochastic maps. We have established that the effective model is capable of reproducing the phase response curves of the exact system and the assembly's response to external stimulation of finite amplitude and duration with sufficient accuracy [191].

5.3 *Outlook*

The presented results potentially have interdisciplinary applications. For instance, the newly-introduced concept of macroscopic excitability, which refers to the scenario in which a population of excitable elements acts like an excitable element itself, may be relevant to slow stochastic fluctuations unfolding on the intermediate (mesoscopic) scale of the brain's hierarchical organization [296], where assemblies are comprised of microcolumns or cortical columns [297, 298, 299]. Moreover, given that our motif model involves ingredients inherent to neuronal systems, such as excitability, plasticity and noise, the results on switching dynamics can be interpreted in the context of neuroscience: the scenario of switching under slow adaptation implies that a binary neuron motif may display slow alternation between two effectively unidirectional weight configurations, promoting opposite direction of information flow, whereas the scenario found for faster adaptation, if extended to networks, may be considered as a paradigm for UP-DOWN states, typical for cortical dynamics [180, 260]. Concerning inverse stochastic resonance, it is already known that it plays a number of important functional roles in neuronal systems (triggering on-off tonic spiking activity, the suppression of pathologically long short-term memories [68, 174, 176, 178], and the formation of UP-DOWN states [180, 260]). Considering that models of individual neurons [94, 173, 174, 176], motifs of units with neuron-like dynamics [172, 181], and neural networks [177] have all been shown to exhibit the effect, it stands to reason that the phenomenon should be universal to neuronal dynamics. The scenarios for the onset of the effect presented in this thesis appear to be generic and should be expected in other biological systems comprised of units with local dynamics near a bifurcation threshold. Finally, our results on the new general method of control of coherence resonance via filtered feedback may have applications in neuroscience and engineering.

The novel averaging methods developed within our analysis have advanced the theoretical knowledge on multiscale stochastic systems on a fundamental level, shifting the paradigm from singular perturbation theory to understanding the effects of finite scale separation, primarily related to switching dynamics. Moreover, our mean-field model for coupled stochastic maps has set the stage for a more systematic exploration of spontaneous and induced collective dynamics of assemblies of map neurons by analytical means. We believe that the introduced techniques can be successfully applied for treating emergent behavior in a wide range of stochastic multiscale systems, allowing for an extension towards understanding critical transitions in systems with complex network topologies and interacting networks.

Bibliography

[1] H. Haken, *Synergetics: An Introduction. Nonequilibrium Phase Transition and Self-Organization in Physics, Chemistry, and Biology, Third Revised and Enlarged Edition* (Springer-Verlag, Berlin, 1983).

[2] H. Haken, *Synergetics, Introduction and Advanced Topics* (Springer, Berlin, 2004).

[3] M. M. Waldrop, *Complexity: The Emerging Science at the Edge of Order and Chaos* (Viking, London, 1992).

[4] Y. Bar-Yam, "General Features of Complex Systems" in *Encyclopedia of Life Support Systems* (EOLSS UNESCO Publishers, Oxford, 2002).

[5] R. Cen, Astrophys. J. Lett. **785**, L21 (2014).

[6] S. Jungblut and C. Dellago, Eur. J. Phys. E **39**, 77 (2016).

[7] A. Baas, Geomorphology **48**, 309 (2002).

[8] I. D. Couzin and J. Krause, Adv. Study. Behav. **32**, 1 (2003).

[9] S. Camazine, J-L. Deneubourg, N. R. Franks, J. Sneyd, G. Theraulaz, and E. Bonabeau, *Self-Organization in Biological Systems* (Princeton University Press, Princeton, 2003).

[10] B. S. Kerner, Phys. Rev. Lett. **81**, 3797 (1998).

[11] P. Krugman, *The Self Organizing Economy* (Blackwell Publishers, Hoboken, 1995).

[12] C. Fuchs, Cybernetics and Human Knowing **12**, 37 (2005).

[13] B. de Boer, "Self-organization and language evolution" in *The Oxford Handbook of Language Evolution*, eds. K. R. Gibson, and M. Tallerman (Oxford University Press, Oxford, 2011).

[14] E. Bullmore and O. Sporns, Nat. Rev. Neurosci. **10**, 186 (2009).

[15] J. W. Krakauer, A. A. Ghazanfar, A. Gomez-Marin, M. A. MacIver, and D. Poeppel, Neuron **93**, 480 (2017).

[16] R. Ellis, Philos. Psychol. **13**, 173 (2000).

[17] P. Perruchet and A. Vinter, Behav. Brain Sci. **25**, 297 (2002).

[18] H. Haken, “Self-Organization in Physics”, in *Nonlinear Dynamics of Transcritical Flows. Lecture Notes in Engineering, vol 13*, eds. H. L. Jordan, H. Oertel, and K. Robert (Springer, Berlin, Heidelberg, 1985).

[19] F. Paslack, *Urgeschichte der Selbstorganisation* (Vieweg, Braunschweig, 1991).

[20] A. Palmer, *Reading Lucretius in the Renaissance* (Harvard University Press, Cambridge, 2014).

[21] R. Descartes, *Discourse on Method and the Meditations* (Penguin, London, 1968).

[22] I. Kant, *Critique of Judgement* (Clarendon Press, Oxford, 2008).

[23] W. R. Ashby, J. Gen. Physchol. **37**, 125 (1947).

[24] P. Asaro, “Heinz von Foerster and the Bio-Computing Movements of the 1960s” in *An Unfinished Revolution? Heinz von Foerster and the Biological Computer Laboratory BCL 1958–1976*, eds. A. Müller, and K. H. Müller (Edition Echoraum, Vienna, 2007).

[25] H. von Foerster, “On self-organizing systems and their environments” in *Understanding Understanding: Essays on Cybernetics and Cognition* (Springer, New York, 2003).

[26] H. von Foerster and G. Pask, Cybernetica **3**, 258 (1961).

[27] H. von Foerster and G. Pask, Cybernetica **4**, 20 (1961).

[28] N. Wiener, *Cybernetics: or Control and Communication in the Animal and the Machine*, 2nd ed. (MIT Press, Cambridge, 1961).

[29] I. Prigogine, Bull. Cl. Sci. Acad. R. Belg. **31**, 600 (1945).

[30] `nobelprize.org/prizes/chemistry/1977/prigogine/lecture`

[31] L. Zuchowsky, Stud. Hist. Philos. M. P. **63**, 86 (2018).

[32] H. A. Simon, *The Sciences of the Artificial* (MIT Press, Cambridge, 1981).

[33] J. Goldstein, Emergence **1**, 49 (1999).

[34] T. de Wolf and T. Holvoet, “Emergence Versus Self-Organisation: Different Concepts but Promising When Combined” in *Engineering Self-Organising Systems*, eds. S. A. Brueckner, S. G. di Marzo, A. Karageorgos, and R. Nagpal (Springer, Berlin, Heidelberg, 2005).

[35] M. Benham-Hutchins, and T. Clancy, JONA **40**, 352 (2010).

[36] E. Estrada, *The Structure of Complex Networks: Theory and Applications* (Oxford University Press, Oxford, 2011).

[37] A.-L. Barabási, *Linked: How Everything Is Connected to Everything Else and What It Means for Business, Science, and Everyday Life* (Plume, New York, 2003).

[38] G. Caldarelli and M. Catanzaro, *Networks: A Very Short Introduction* (Oxford University Press, Oxford, 2012).

[39] S. Strogatz, *Nonlinear Dynamics and Chaos: with Applications to Physics, Biology, Chemistry, and Engineering* (Perseus Books Publishing, New York, 1994).

[40] U. Feudel, Int. J. Bifurcation Chaos **18**, 1607 (2008).

[41] U. Feudel, A. N. Pisarchik, and K. Showalter, Chaos **28**, 033501 (2018).

[42] I. Franović and V. Klinshov, Chaos **28**, 023111 (2018).

[43] F. Sorrentino and E. Ott, Phys. Rev. Lett. **100**, 114101 (2008).

[44] F. Vazquez, V. M. Eguiluz, and M. S. Miguel, Phys. Rev. Lett. **100**, 108702 (2008).

[45] N. Caporale and Y. Dan, Ann. Rev. Neurosci. **31**, 25 (2008).

[46] C. Furusawa and K. Kaneko, Phys. Rev. Lett. **90**, 088102 (2003).

[47] C. Kuehn, *Multiple Time Scale Dynamics* (Springer, Switzerland, 2015).

[48] M. Krupa, B. Sandstede, and P. Szmolyan, J. Differ. Equ. **133**, 49 (1997).

[49] M. Desroches, J. Guckenheimer, B. Krauskopf, C. Kuehn, H. M. Osinga, and M. Wechselberger, SIAM Rev. **54**, 211 (2012).

[50] M. Lichtner, M. Wolfrum, and S. Yanchuk, SIAM J. Math. Anal. **43**, 788 (2011).

[51] H. Jardon-Kojakhmetov and C. Kuehn (2019), `arxiv.org/abs/1901.01402`.

[52] M. Scheffer, et al., Nature **461**, 53 (2009).

[53] C. Meisel, A. Klaus, C. Kuehn, and D. Plenz, PloS Comput. Biol. **11**, e1004097 (2015).

[54] L. Cocchi, L. L. Gollo, A. Zalesky, and M. Breakspear, Prog. Neurobiol. **158**, 132 (2017).

[55] C. Meisel and C. Kuehn, PloS One **7**, e30371 (2012).

[56] G. Schöner and J. A. Kelso, Science **239**, 1513 (1988).

[57] C. Kuehn, Physica D **240**, 1020 (2011).

[58] Y. Kuramoto, in *International Symposium on Mathematical Problems in Theoretical Physics, Lecture Notes in Physics*, ed. H. Araki (Springer, New York, 1975).

[59] K. Wiesenfeld, P. Colet, and S. H. and Strogatz, Phys. Rev. Lett. **76**, 404 (1996).

[60] F. Dörfler, M. Chertkov, and F. Bullo, Proc. Natl. Acad. Sci. U.S.A. **110**, 2005 (2013).

[61] J. Aldridge, and E. K. Pye, Nature **259**, 670 (1976).

[62] D. C. Michaels, E. P. Matyas, and J. Jalife, Circ. Res. **61**, 704, (1987).

[63] M. Komarov, S. Gupta, and A. Pikovsky, EPL **106**, 40003 (2014).

[64] S. Gupta, A. Campa, and S. Ruffo, *Statistical Physics of Synchronization* (Springer, Cham, 2018).

[65] E. Meron, Phys. Rep. **218**, 1 (1992).

[66] T. Isele and E. Schöll, New J. Phys. **17**, 023058 (2015).

[67] B. Lindner, J. Garcia-Ojalvo, A. Neiman, and L. Schimansky-Geier, Phys. Rep. **392**, 321 (2004).

[68] B. A. Schmerl and M. D. McDonnell, Phys. Rev. E **88**, 052722 (2013).

[69] A. Destexhe and M. Rudolph-Lilith, *Neuronal Noise* (New York, Springer, 2012).

[70] M. D. McDonnell and L. M. Ward, Nat. Rev. Neurosci. **12**, 415 (2011).

[71] G. Buzsáki, *Rhythms of the Brain* (Oxford University Press, Oxford, 2009).

[72] A. Destexhe and D. Contreras, Science **314**, 85 (2006).

[73] E. M. Izhikevich, Int. J. Bifurc. **10**, 1171 (2000).

[74] E. M. Izhikevich, *The Dynamical Systems in Neuroscience: Geometry of Excitability and Bursting* (MIT Press, Cambridge, 2007)

[75] K. Ikeda, Opt. Commun. **30**, 257 (1979).

[76] D. Pieroux and T. Erneux, Phys. Rev. A **53**, 2765 (1996).

[77] R. J. Field and M. Burger, *Oscillations and Traveling Waves in Chemical Systems* (Wiley, New York, 1985).

[78] V. Petrov, S. K. Scott, and K. Showalter, J. Chem. Phys. **97**, 6191 (1992).

[79] I. T. Georgiou, A. K. Baja, and M. Corless, Int. J. Nonlin. Mech. **33**, 275 (1998).

[80] Z. H. Wang and H. Y. Hu, Nonlinear Dyn. **25**, 317 (2001).

[81] D. Ludwig, D. D. Jones, and C. S. Holling, J. Anima. Ecol. **47**, 315 (1978).

[82] S. Rinaldi and M. Scheffer, Ecosystems **3**, 507 (2000).

[83] L. F. Abbott and S. Nelson, Nat. Neurosci. **3**, 1178 (2000).

[84] H.-X. Wang, R. C. Gerkin, D. W. Nauen, and Bi G.-Q., Nat. Neurosci. **8**, 187 (2005).

[85] S. Song, K. D. Miller, and L. F. Abbott, Nat. Neurosci. **3**, 919 (2000).

[86] R. C. Froemke and Y. Dan, Nature **416**, 433 (2002).

[87] M. Krupa and P. Szmolyan, J. Differ. Equ. **174**, 312 (2001).

[88] N. Fenichel, J. Differ. Equ. **31**, 53 (1979).

[89] J. Mitry, M. McCarthy, N. Kopell, and M. Wechselberger, J. Math. Neurosci. **3**, 12 (2013).

[90] P. Szmolyan and M. Wechselberger, J. Differ. Equ. **177**, 419 (2001).

[91] M. Wechselberger, SIAM J. Appl. Dyn. Syst. **4**, 101 (2005).

[92] M. Wechselberger, Trans. Am. Math. Soc. **364**, 3289 (2012).

[93] N. Wiener and A. Rosenblueth, Arch. Inst. Cardiol. Mex. **16**, 205 (1946).

[94] I. Franović, O. E. Omel’chenko, and M. Wolfrum, Chaos **28**, 071105 (2018).

[95] K. Motokawa, Tohoku J. Exp. Med. **50**, 307 (1949).

[96] J. P. Green, N. J. Giarman, and W. T. Salte, Am. J. Physiol. **171**, 174 (1952).

[97] J. W. Gebhard, J. Exp. Psychol. **44**, 132 (1952).

[98] J. W. Gebhard, Psychol. Bull. **50**, 73 (1953).

[99] A. T. Winfree, *The Geometry of Biological Time* (Springer, New York, 1980).

[100] J. D. Murray, *Mathematical Biology* (Springer, Berlin–Heidelberg–New York, 1993).

[101] B. Hille, *Ionic Channels of Excitable Membranes* (Sinauer Associates, Sunderland, 2001).

[102] L. Glass, Nature **410**, 277 (2001).

[103] C. O. Weiss and R. Vilaseca, *Dynamics of Lasers* (VCH, Weinheim, 1991).

[104] A. M. Yacomotti, P. Monnier, F. Raineri, B. B. Bakir, C. Seassal, R. Raj, and J. A. Levenson, Phys. Rev. Lett. **97**, 143904 (2006).

[105] R. Kapral and K. Showalter (Eds.), *Chemical Waves and Patterns* (Kluwer Academic Publishers, Dordrecht, 1995).

[106] G. Bucchioni, A. Cavallo, D. Ippolito, G. Marton, and U. Castiello, Brain Cogn. **81**, 176 (2013).

[107] G. Dumas, G. C. de Guzman, E. Tognoli, and J. A. S. Kelso, PNAS **35**, E3726 (2014).

[108] A. Ganopolski and S. Rahmstorf, Phys. Rev. Lett. **88**, 038501 (2002).

[109] J. M. Carlson, J. S. Langer, and B. E. Shaw, Rev. Mod. Phys. **66**, 657 (1994).

[110] A. L. Hodgkin, J. Physiol. **107**, 165 (1948).

[111] A. L. Hodgkin and A. F. Huxley, J. Physiol. **117**, 500 (1952).

[112] `nobelprize.org/prizes/medicine/1963/summary`

[113] J. Rinzel and G. B. Ermentrout, "Analysis of neural excitability and oscillations" in *Methods in Neural Modeling*, eds. C. Koch and I. Segev (MIT Press, London, 1989).

[114] I. A. Khovanov, A. V. Polovinkin, D. G. Luchinsky, and P. V. E. McClintock, Phys. Rev. E **87**, 032116 (2013).

[115] P. de Maesschalck and M. Wechselberger, J. Math. Neurosci. **5**, 16 (2015).

[116] S. Shinomoto and Y. Kuramoto, Prog. Theor. Phys. **75**, 1105 (1986).

[117] G. B. Ermentrout and N. Kopell, SIAM J. Appl. Math, **46**, 233 (1986).

[118] C. Börger, S. Epstein, and N. Kopell, PNAS **105**, 18023 (2008).

[119] R. Osan, J. Rubin, and B. Ermentrout, SIAM J. Appl. Math. **62**, 1197 (2002).

[120] S. McKennoch, T. Voegtlin, and L. Bushnell, Neural Comput. **21**, 9 (2008).

[121] R. FitzHugh, Biophysical J. **1**, 445 (1961).

[122] J. Nagumo, S. Arimoto, and S. Yoshizawa, Proc. IRE **50**, 2061 (1962).

[123] A. M. Pertsov, E. A. Ermakova, and A. V. Panfilov, Physica D **14**, 117 (1984).

[124] V. S. Zykov, Biofizika **31**, 862 (1986).

[125] Y. Zhao, S. A. Billings, D. Coca, Y. Guo, R. I. Ristic, and L. DeMatos, Int. J. Bifurcat. Chaos. **21**, 3249 (2011).

[126] F. J. L. Capelle, and D. Durrer, Circ. Res. **47**, 454 (1980).

[127] J. J. Tyson and J. P. Keener, Physica D **29**, 215 (1987).

[128] R. T. Faghih, M. Sc. thesis. *The FitzHugh-Nagumo model dynamics with an application to the hypothalamic pituitary adrenal axis* (MIT, 2010).

[129] S. Brandstetter, M. A. Dahlem and E. Schöll, Philos. T. R. Soc. A **368**, 391 (2010).

[130] I. Franović, K. Todorović, M. Perc, N. Vasović, and N. Burić, Phys. Rev. E **92**, 062911 (2015).

[131] S. R. Eydam, I. Franović, and M. Wolfrum, Phys. Rev. E **99**, 042207 (2019).

[132] R. FitzHugh, Bull. Math. Biophys. **7**, 252 (1955).

[133] A. Tonnelier, Phys. Rev. E **90**, 022701 (2014).

[134] E. E. Benoit, J. L. Callot, F. Diener, and M. M. Diener, Collect. Math **32**, 37 (1981).

[135] M. Broens and K. Bar-Eli, J. Phys. Chem. **95**, 8706 (1991).

[136] B. Peng, V. Gaspar, and K. Showalter, Phil. Trans. R. Soc. Lond. A **337**, 275 (1991).

[137] S. M. Baer and T. Erneux, SIAM J. Appl. Math. **46**, 721 (1986).

[138] M. Krupa and P. Szmolyan, SIAM J. Math. Anal. **33**, 286 (2001).

[139] C. H. Henry and R. F. Kazarinov, Rev. Mod. Phys. **68**, 801 (1996).

[140] M. San Miguel and J. M. Sancho, Phys. Lett. A **90**, 455 (1982).

[141] N. Ho and A. Destexhe, J. Neurophysiol. **84**, 1488 (2000).

[142] H. Treutlein, K. Schulten, and Ber. Bunsenges, Phys. Chem. **89**, 710 (1985).

[143] W. Ebeling, H. Herzel, W. Richert, and L. Schimansky-Geier, Zeitschr. Angew. Mathem. Mechanik **66**, 161 (1986).

[144] D. Sigeti and W. Horsthemke, J. Stat. Phys. **54**, 1217 (1989).

[145] C. Kurrer and K. Schulten, Physica D **50**, 311 (1991).

[146] C. Kurrer,and K. Schulten, Int. J. Neural Systems **7**, 399 (1996).

[147] P. S. Landa, J. Commun. Techn. Electron. **47**, 1321 (2002).

[148] U. Hillenbrand, Phys. Rev. E **66**, 021909 (2002).

[149] A. Pikovsky and J. Kurths, Phys. Rev. Lett. **78**, 775 (1997).

[150] H. Gang, T. Ditzinger, C. Z. Ning, and H. Haken, Phys. Rev. Lett. **71**, 807 (1993).

[151] A. Longtin, Phys. Rev. E **55** 868 (1997).

[152] A. Neiman, P. I. Saparin, and L. Stone, Phys. Rev. E **56** 270 (1997).

[153] J. R. Pradines, G. V. Osipov, and J. J. Collins, Phys. Rev. E **60**, 6407 (1999).

[154] L. I and J.-M. Liu, Phys. Rev. Lett. **74**, 3161 (1995).

[155] M. Qian, M.-P. Qian, and X.-J. Zhang, Phys. Lett. A. **309**, 371 (2003).

[156] W. Lim, S.-Y. Kim, and S. Lee, J. Korean Phys. Soc. **50**, 219 (2007).

[157] Y. Wang, D. T. W. Chik, and Z. D. Wang, Phys. Rev. E **61**, 740 (2000).

[158] A. N. Pisarchik, V. A. Maksimenko, A. V. Andreev, et al., Sci Rep **9**, 18325 (2019).

[159] A. M. Lacasta, F. Sagués, and J. M. Sancho, Phys. Rev. E **66**, 045105 (2002).

[160] K. Pakdaman, S. Tanabe, and T. Shimokawa, Neural Networks **14**, 895 (2001).

[161] M. Qian, G.-X. Wang, and X.-J. Zhang, Phys. Rev. E **62**, 6469 (2000).

[162] S. Wu, W. Ren, K. He, and Z. Huang, Phys. Lett. A **279**, 347 (2001).

[163] P. L. Gong, J. X. Xu, and S.J. Hu, Chaos Soliton. Fract. **13**, 885 (2002).

[164] S.-G. Lee, A. Neiman, and S. Kim, Phys. Rev. E **57**, 3292 (1998).

[165] J. L. A. Dubbeldam, B. Krauskopf, and D. Lenstra, Phys. Rev. E **60**, 6580 (1999).

[166] S. Zhong and H. Xin, Chem. Phys. Lett. **321**, 309 (2000).

[167] D. E. Postnov, S. K. Han, T. G. Yim, and O. V. Sosnovtseva, Phys. Rev. E **59**, R3791 (1999).

[168] G. Giacomelli, M. Giudici, S. Balle, and J.R. Tredicce, Phys. Rev. Lett. **84**, 3289 (2000).

[169] Z. Hou and H. Xin, J. Phys. Chem. A **103**, 6181 (1999).

[170] E. Manjarrez, J. G. Rojas-Piloni, I. Méndez, L. Martínez, and D. Vélez D, Neurosci. Lett. **326**, 93 (2002).

[171] R. E. L. DeVille, E. Vanden-Eijnden, and C. B. Muratov, Phys. Rev. E **72**, 031105 (2005)

[172] B. S. Gutkin, J. Jost, and H. C. Tuckwell, EPL **81** 20005 (2008).

[173] H. C. Tuckwell, J. Jost, and B. S. Gutkin, Phys. Rev. E **80** 031907 (2009).

[174] M. Uzuntarla, J. R. Cressman, M. Ozer, and E. Barreto, Phys. Rev. E **88** 042712 (2013).

[175] M. Uzuntarla, Phys. Lett. A **377**, 2585 (2013).

[176] M. Uzuntarla, J. J. Torres, P. So., M. Ozer, and E. Barreto, Phys. Rev. E **95**, 012404 (2017).

[177] M. Uzuntarla, E. Barreto, and J. J. Torres, PLoS Comput. Biol. **13**, e1005646 (2017).

[178] A. Buchin, S. Rieubland, M. Häusser, B. S. Gutkin, and A. Roth, PLoS Comput. Biol. **12**, e1005000 (2016).

[179] I. Franović and V. Klinshov, EPL **116**, 48002 (2016).

[180] T. T. G. Hahn, J. M. McFarland, S. Berberich, B. Sakmann, and M. R. Mehta, Nat. Neurosci. **15**, 1531 (2012).

[181] I. Bačić, S. Yanchuk, M. Wolfrum, and I. Franović, EPJ ST **227**, 177 (2018).

[182] L. Lücken, O. V. Popovych, P. A Tass, and S. Yanchuk, Phys. Rev. E **93**, 032210 (2016).

[183] D. V. Kasatkin, and V. I. Nekorkin, Radiophys. Quantum Electron. **58**, 877 (2016).

[184] D. Kasatkin, S. Yanchuk, E. Schöll, and V. Nekorkin, Phys. Rev. E **96**, 062211 (2017).

[185] I. Franović, K. Todorović, N. Vasović, and N. Burić, Phys. Rev. E **89**, 022926 (2014).

[186] I. Franović, K. Todorović, N. Vasović, and N. Burić, Phys. Rev. E **87**, 012922 (2013).

[187] I. Franović, K. Todorović, N. Vasović, and N. Burić, Chaos **22**, 033147 (2012).

[188] V. Klinshov and I. Franović, Phys. Rev. E **92**, 062813 (2015).

[189] M. A. Zaks, X. Sailer, L. Schimansky-Geier, and A. B. Neiman, Chaos **15**, 026117 (2005).

[190] B. Sonnenschein, M. A. Zaks, A. B. Neiman, and L. Schimansky-Geier, EPJ ST **222**, 2517 (2013).

[191] I. Franović, O. V. Maslennikov, I. Bačić, and V. I. Nekorkin, Phys. Rev. E **96**, 012226 (2017).

[192] I. Franović, S. Yanchuk, S. Eydam, I. Bačić, and M. Wolfrum, Chaos **30**, 083109 (2020).

[193] I. Bačić, V. Klinshov, V. I. Nekorkin, M. Perc, and I. Franović, EPL **124** 40004 (2018).

[194] I. Bačić and I. Franović, Chaos **30**, 033123 (2020).

[195] V. S. Zykov and E. Bodenschatz, Annu. Rev. Condens. Matter Phys. **9**, 435 (2018).

[196] Q. Dai, M. Zhang, H. Cheng, et al., Nonlinear Dyn. **91**, 1723 (2018).

[197] M. A. L. Nicolelis and M. A. Lebedev, Nat. Rev. Neurosci., **10**, 530 (2009).

[198] C. Zhou, L. Zemanova, G. Zamora, C. Hilgetag, and J. Kurths, Phys. Rev. Lett. **97**, 238103 (2006).

[199] O. Sporns, D. Chialvo, M. Kaiser, and C. C. Hilgetag, Trends Cogn. Sci. **8**, 418 (2004).

[200] O. Sporns, *Networks of the Brain* (MIT Press, Cambridge, Massachusetts, 2011).

[201] O. Sporns and R. Kotter, PLoS Biol. **2**, e369 (2004).

[202] I. Franović and V. Miljković, Chaos Soliton. Fract. **44**, 122 (2011).

[203] I. Franović and V. Miljković, Chaos Soliton. Fract. **45**, 527 (2012).

[204] I. Franović and V. Miljković, EPL **92**, 68007 (2010).

[205] Y. L. Maistrenko, B. Lysyansky, C. Hauptmann, O. Burylko, and P. A. Tass, Phys. Rev. E **75**, 066207 (2007).

[206] T. Aoki and T. Aoyagi, Phys. Rev. Lett. **102**, 034101 (2009).

[207] T. Aoki and T. Aoyagi, Phys. Rev. E **84**, 066109 (2011).

[208] Y. Baibolatov, M. Rosenblum, Z. Z. Zhanabaev, M. Kyzgarina, and A. Pikovsky, Phys. Rev. E **80**, 046211 (2009).

[209] W. Gerstner, H. Sprekeler, and G. Deco, Science **338**, 60 (2012).

[210] S. E. Folias and P. C. Bressloff, Phys. Rev. Lett. **95**, 208107 (2005).

[211] S. E. Folias and P. C. Bressloff, SIAM J. Appl. Math. **65**, 2067 (2005).

[212] C. R. Laing, W. C. Troy, B. Gutkin, and G. B. Ermentrout, SIAM J. Appl. Math. **63**, 62 (2002).

[213] P. C. Bressloff, Phys. Rev. E **82**, 051903 (2010).

[214] M. A. Buice and J. D. Cowan, Phys. Rev. E **75**, 051919 (2007).

[215] N. Brunel and V. Hakim, Neural Comput. **11**, 1621 (1999).

[216] H. Hasegawa, Phys. Rev. E **67**, 041903 (2003).

[217] N. F. Rulkov, Phys. Rev. E **65**, 041922 (2002).

[218] N. F. Rulkov, I. Timofeev, and M. Bazhenov, J. Comput. Neurosci. **17**, 203 (2004).

[219] D. Q. Wei and X. S. Luo, Europhys. Lett. **77**, 68004 (2007).

[220] Q. Y. Wang, Z. Duan, M. Perc, and G. Chen, Europhys. Lett. **83**, 50008 (2008).

[221] C. A. S. Batista, A. M. Batista, J. A. C. de Pontes, R. L. Viana, and S. R. Lopes, Phys. Rev. E **76**, 016218 (2007).

[222] B. Ibarz, J. M. Casado, and M. A. F. Sanjuán, Phys. Rep. **501**, 1 (2011).

[223] E. M. Izhikevich, Neural Comput. **18**, 245 (2006).

[224] E. M. Izhikevich, and G. M. Edelman, Proc. Natl. Acad. Sci. USA **105**, 3593 (2008).

[225] V. I. Nekorkin, and L. V. Vdovin, Izv. Vyssh. Uchebn. Zaved. Prikladn. Nelinejn. Din **15**, 36 (2007).

[226] M. Courbage, V. I. Nekorkin, and L. V. Vdovin, Chaos **17**, 043109 (2007).

[227] O. V. Maslennikov and V. I. Nekorkin, Phys. Rev. E **90**, 012901 (2014).

[228] O. V. Maslennikov, D. V. Kasatkin, N. F. Rulkov, and V. I. Nekorkin, Phys. Rev. E **88**, 042907 (2013).

[229] O. V. Maslennikov, V. I. Nekorkin, and J. Kurths, Phys. Rev. E **92**, 042803 (2015).

[230] O. V. Maslennikov and V. I. Nekorkin, Commun. Nonlinear Sci. Numer. Simul. **23**, 10 (2015).

[231] O. V. Maslennikov and V. I. Nekorkin, Chaos **23**, 023129 (2013).

[232] O. V. Maslennikov and V. I. Nekorkin, "Map-Based Approach to Problems of Spiking Neural Network Dynamics" in *Nonlinear Dynamics and Complexity*, eds. V. Afraimovich, A. C. J. Luo, and X. Fu (Springer International Publishing, Switzerland, 2014).

[233] I. Franović, K. Todorović, M. Perc, N. Vasović, and N. Burić, Phys. Rev. E **92**, 062911 (2015).

[234] L. Arnold, *Random Dynamical Systems*, (SpringerVerlag, Berlin, 1999).

[235] J. A. Acebrón, A. R. Bulsara, and W.-J. Rappel, Phys. Rev. E **69**, 026202 (2004).

[236] M. Gaudreault, J. M. Berbert, and J. Viñals, Phys. Rev. E **83**, 011903 (2011).

[237] P. Kaluza, C. Strege, and H. Meyer-Ortmanns, Phys. Rev. E **82**, 036104 (2010).

[238] V. I. Nekorkin and O. V. Maslennikov, Radiophys. Quantum Electron. (Engl. Transl.) **54**, 56 (2011).

[239] M. Courbage, O. V. Maslennikov, and V. I. Nekorkin, Chaos Soliton. Fract. **45**, 645 (2012).

[240] O. V. Maslennikov and V. I. Nekorkin, Radiophys. Quantum Electron. (Engl. Transl.) **55**, 198 (2012).

[241] C. W. Gardiner, *Handbook of Stochastic Methods for Physics, Chemistry and the Natural Sciences*, 3rd ed. (Springer-Verlag, Berlin, 2004).

[242] N. W. Schultheiss, A. A. Prinz, and R. J. Butera (eds.) *Phase Response Curves in Neuroscience: Theory, Experiment, and Analysis* (Springer, New York, 2012).

[243] P. A. Tass, *Phase Resetting in Medicine and Biology: Stochastic Modeling and Data Analysis* (Springer, Berlin–Heidelberg, 2007).

[244] C. C. Canavier, Scholarpedia **1**, 1332 (2006).

[245] W. Gerstner, W. M. Kistler, R. Naud, and L. Paninski, *Neuronal Dynamics: From Single Neurons to Networks and Models of Cognition* (Cambridge University Press, Cambridge, 2014).

[246] L. F. Abbott and P. Dayan, *Theoretical Neuroscience* (The MIT Press, 2005).

[247] C. Clopath, L. Büsing, E. Vasilaki, and W. Gerstner, Nat. Neurosci. **13**, 344 (2010).

[248] O. Popovych, S. Yanchuk, and P. A. P. Tass, Sci. Rep. **3**, 2926 (2013).

[249] V.-C. Oriol, M. Ronny, R. Sten, and L. Schimansky-Geier, Phys. Rev. E **83**, 036209 (2011).

[250] G. B. Ermentrout and D. Kleinfeld, Neuron **29**, 33 (2001).

[251] L. Lücken, D. P. Rosin, V. M. Worlitzer, and S. Yanchuk, Chaos **27**, 13114 (2017).

[252] I. Franović, M. Perc, K. Todorović, S. Kostić, and N. Burić, Phys. Rev. E **92**, 062912 (2015).

[253] S. Yanchuk, S. Ruschel, J. Sieber, and M. Wolfrum, Phys. Rev. Lett. **123**, 053901 (2019).

[254] J. A. Kromer, R. D. Pinto, B. Lindner, and L. Schimansky-Geier, EPL **108**, 20007 (2014).

[255] A. Shilnikov, Int. J. Bifurcat. Chaos **18**, 2141 (2008).

[256] G. Pavliotis and A. Stuart, *Multiscale Methods: Averaging and Homogenization* (Springer, Berlin–Heidelberg, 2008).

[257] M. Galtier and G. Wainrib, Phys. Rev. E **2**, 13 (2012).

[258] E. M. Izhikevich, IEEE Trans. Neural Netw. **15**, 1063 (2004).

[259] E. J. Doedel, R. C. Paffenroth, A. R. Champneys, T. F. Fairgrieve, Y. A. Kuznetsov, B. Sandstede, and X. Wang, *AUTO-07p: Continuation and bifurcation software for ordinary differential equations* (Montreal, Canada, 2007), URL: indy.cs.concordia.ca/auto/

[260] V. V. Vyazovskiy and K. D. Harris, Nat. Rev. Neurosci. **14**, 443 (2013).

[261] P. H. Dannenberg, J. C. Neu, and S. W. Teitsworth, Phys. Rev. Lett. **113**, 020601 (2014).

[262] E. Hunsberger, M. Scott, and C. Eliasmith, Neural Comput. **26**, 1600 (2014).

[263] B. Neiman and D. F. Russell, Phys. Rev. Lett. **88**, 138103 (2002).

[264] L. Ryashko and E. Slepukhina, Phys. Rev. E **96**, 032212 (2017).

[265] C. Zheng and A. Pikovsky, Phys. Rev. E **98**, 042148 (2018).

[266] A. Fiasconaro, B. Spagnolo, and S. Boccaletti, Phys. Rev. E **72**, 061110 (2005).

[267] R. N. Mantegna and B. Spagnolo, Phys. Rev. Lett. **76**, 563 (1996).

[268] S. Ciuchi, F. de Pasquale, and B. Spagnolo, Phys. Rev. E **47**, 3915 (1993).

[269] N. V. Agudov, A. A. Dubkov, and B. Spagnolo, Physica A **325**, 144 (2003).

[270] G. Augello, D. Valentia, and B. Spagnolo, Eur. Phys. J. B **78**, 225 (2010).

[271] A. Zakharova, A. Feoktistov, T. Vadivasova and E. Schöll, EPJ ST **222**, 2481 (2013).

[272] N. Semenova, A. Zakharova, V. Anishchenko, and Eckehard Schöll, Phys. Rev. Lett. **117**, 014102 (2016).

[273] B. Lindner and L. Schimansky-Geier, Phys. Rev. E **60**, 7270 (1999).

[274] V. A. Makarov, V. I. Nekorkin, and M. G. Velarde, Phys. Rev. Lett. **86**, 3431 (2001).

[275] L. H. Gammaitoni, P. Hänggi, P. Jung, and F. Marchesoni, Rev. Mod. Phys. **70**, 223 (1998).

[276] J. Hizanidis and E. Schöll, Phys. Rev. E **78**, 066205 (2008).

[277] J. Hizanidis, A. Balanov, A. Amann, and E. Schöll, Phys. Rev. Lett. **96**, 244104 (2006).

[278] R. Aust, P. Hövel, J. Hizanidis, and E. Schöll, Eur. Phys. J. Spec. Top. **187**, 77 (2010).

[279] N. Kouvaris, L. Schimansky-Geier, and E. Schöll, Eur. Phys. J. Spec. Top. **191**, 29 (2010).

[280] N. B. Janson, A. Balanov, and E. Schöll, Phys. Rev. Lett. **93**, 010601 (2004).

[281] V. Semenov, A. Feoktistov, T. Vadivasova, E. Schöll, and A. Zakharova, Chaos **25**, 033111 (2015).

[282] B. Hauschildt, N. B. Janson, A. Balanov, and E. Schöll, Phys. Rev. E **74**, 051906 (2006).

[283] M. Masoliver, N. Malik, E. Schöll, and A. Zakharova, Chaos **27**, 101102 (2017).

[284] M. E. Yamakou and J. Jost, Phys. Rev. E **100**, 022313 (2019).

[285] C. Zhou, J. Kurths, and B. Hu, Phys. Rev. Lett. **87**, 098101 (2001).

[286] C. Morris and H. Lecar, Biophys. J. **35**, 193 (1981).

[287] D. O. Hebb, *The Organization of Behavior: A Neuropsychological Approach* (John Wiley & Sons, New York, 1949).

[288] O. V. Popovych, S. Yanchuk, and P. A. Tass, Sci. Rep. **3**, 2926 (2013).

[289] A. Morrison, M. Diesmann, and W. Gerstner, Biol. Cybern. **98**, 459 (2008).

[290] P. Hänggi, P. Talkner, and M. Borkovec, Rev. Mod. Phys. **62**, 251 (1990).

[291] N. Berglund and B. Gentz, *Noise-Induced Phenomena in Slow-Fast Dynamical Systems* (Springer, Berlin, 2006).

[292] C. Laing and G. J. Lord (eds.), *Stochastic Methods in Neuroscience* (Oxford University Press, London, 2009).

[293] J. Touboul and G. Wainrib, Physica D **307**, 42 (2015).

[294] H. Wang, L. Wang, L. Yu, and Y. Chen, Phys. Rev. E **83**, 021915 (2011).

[295] T. Ditzinger, C. Z. Ning, and G. Hu, Phys. Rev. E **50**, 3508 (1994).

[296] W. J. Freeman, *Neurodynamics: An Exploration in Mesoscopic Brain Dynamics* (Springer-Verlag, London, 2000).

[297] H. Liljenström, Scholarpedia **7**, 4601 (2012).

[298] G. Deco, V. K. Jirsa, P. A. Robinson, M. Breakspear, and K. Friston, PloS Comput. Biol. **4**, e1000092 (2008).

[299] J. L. P. Velazquez and R. Wennberg, *Coordinated Activity in the Brain: Measurements and Relevance to Brain Function and Behavior* (Springer, New York, 2009).

Curriculum Vitae

Born in Subotica, Republic of Serbia on June 12th, 1992, Iva Bačić completed elementary and secondary education in her hometown. As a student of the gymnasium “Svetozar Marković”, she attended numerous seminars in Petnica Science Center. In 2010, she enrolled in the Bachelor of Science program Theoretical and Experimental physics at the Faculty of Physics, University of Belgrade. In 2014, after graduating with a GPA of 9.44/10, she continued her education, enrolling in the same program at the Master of Science level. Within research for her MSc thesis, she visited the SOLEIL synchrotron in France. Under the supervision of Dr. Aleksandar Milosavljević, an Associate Research Professor at the Institute of Physics Belgrade, she completed her MSc thesis entitled *Inner-Shell Action Spectroscopy of Trapped Substance P Peptide Ions and their Nanosolvated Complexes*. Following the defense of her thesis and graduation with a GPA of 9.67/10 in 2015, Iva started her doctoral studies at the Faculty of Physics, specializing in statistical physics and nonlinear dynamics. Under the supervision of Dr. Igor Franović, an Associate Research Professor from the Scientific Computing Laboratory of the National Center of Excellence for the Study of Complex Systems at the Institute of Physics Belgrade, Iva studies self-organizing dynamics in coupled systems.

Since March 2016, Iva has been employed at the Institute of Physics Belgrade as a Research Assistant, participating in the National Project ON171017 *Modeling and Numerical Simulations of Complex Many-Body Systems* funded by the Ministry of Education, Science and Technological Development of the Republic of Serbia. Alongside this, she was also a participant in the DAAD bilateral project *Emergent dynamics in systems of coupled excitable units* in 2017 and 2018, within which she paid three visits to the Weierstrass Institute in Berlin, Germany. During the past decade, Iva was also an assistant in the Petnica Science Center, where she delivered lectures on a variety of topics and supervised several projects.

As a doctoral student, Iva published five peer-reviewed research papers whose contents provide the basis for the present thesis (Phys. Rev. E **96**, 012226 (2017); EPJ ST **227**, 177 (2018); EPL **124** 40004 (2018); Chaos **30**, 033123 (2020); and Chaos **30**, 083109 (2020)), along with an additional publication unrelated to her thesis (EPL **120**, 68001 (2017)). The latter was chosen for EPL’s *Highlights from the previous volumes*, while the main results were presented in Europhysics News **49** (3), 2018. Iva has presented her research at poster presentations and by giving contributed talks on several international conferences and workshops. She provided service to the scientific community by performing peer review for *Chaos: An Interdisciplinary Journal of Nonlinear Science*.

Изјава о ауторству

Име и презиме аутора – **Ива Бачић**

Број индекса – **2015/8018**

Изјављујем

да је докторска дисертација под насловом

Self-Organization in Coupled Excitable Systems: Interplay Between Multiple Timescale Dynamics and Noise

(Самоорганизација у спрегнутим ексцитабилним системима: садејство вишеструких временских скала и шума)

- резултат сопственог истраживачког рада;
- да дисертација у целини ни у деловима није била предложена за стицање друге дипломе према студијским програмима других високошколских установа;
- да су резултати коректно наведени и
- да нисам кршио/ла ауторска права и користио/ла интелектуалну својину других лица.

Потпис аутора

У Београду, 04. 09. 2020. год.

Iva Bačić

Изјава о истоветности штампане и електронске верзије докторског рада

Име и презиме аутора – **Ива Бачић**

Број индекса **– 2015/8018**

Студијски програм – **Физика**

Наслов рада – **Self-Organization in Coupled Excitable Systems: Interplay Between Multiple Timescale Dynamics and Noise (Самоорганизација у спрегнутим ексцитабилним системима: садејство вишеструких временских скала и шума)**

Ментор – **др Игор Франовић**

Изјављујем да је штампана верзија мог докторског рада истоветна електронској верзији коју сам предао/ла ради похрањивања у **Дигиталном репозиторијуму Универзитета у Београду.**

Дозвољавам да се објаве моји лични подаци везани за добијање академског назива доктора наука, као што су име и презиме, година и место рођења и датум одбране рада.

Ови лични подаци могу се објавити на мрежним страницама дигиталне библиотеке, у електронском каталогу и у публикацијама Универзитета у Београду.

Потпис аутора

У Београду, 04. 09. 2020. год.

Iva Bačić

Изјава о коришћењу

Овлашћујем Универзитетску библиотеку „Светозар Марковић“ да у Дигитални репозиторијум Универзитета у Београду унесе моју докторску дисертацију под насловом:

Self-Organization in Coupled Excitable Systems: Interplay Between Multiple Timescale Dynamics and Noise (Самоорганизација у спрегнутим ексцитабилним системима: садејство вишеструких временских скала и шума)

која је моје ауторско дело.

Дисертацију са свим прилозима предао/ла сам у електронском формату погодном за трајно архивирање.

Моју докторску дисертацију похрањену у Дигиталном репозиторијуму Универзитета у Београду и доступну у отвореном приступу могу да користе сви који поштују одредбе садржане у одабраном типу лиценце Креативне заједнице (Creative Commons) за коју сам се одлучио/ла.

1. Ауторство (CC BY)

2. Ауторство – некомерцијално (CC BY-NC)

3. Ауторство – некомерцијално – без прерада (CC BY-NC-ND)

4. Ауторство – некомерцијално – делити под истим условима (CC BY-NC-SA)

5. Ауторство – без прерада (CC BY-ND)

[✓ **6. Ауторство – делити под истим условима (CC BY-SA)**]

(Молимо да заокружите само једну од шест понуђених лиценци.
Кратак опис лиценци је саставни део ове изјаве).

Потпис аутора

Ivan Bačić

У Београду, 04. 09. 2020. год.

1. **Ауторство**. Дозвољавате умножавање, дистрибуцију и јавно саопштавање дела, и прераде, ако се наведе име аутора на начин одређен од стране аутора или даваоца лиценце, чак и у комерцијалне сврхе. Ово је најслободнија од свих лиценци.

2. **Ауторство – некомерцијално**. Дозвољавате умножавање, дистрибуцију и јавно саопштавање дела, и прераде, ако се наведе име аутора на начин одређен од стране аутора или даваоца лиценце. Ова лиценца не дозвољава комерцијалну употребу дела.

3. **Ауторство – некомерцијално – без прерада**. Дозвољавате умножавање, дистрибуцију и јавно саопштавање дела, без промена, преобликовања или употребе дела у свом делу, ако се наведе име аутора на начин одређен од стране аутора или даваоца лиценце. Ова лиценца не дозвољава комерцијалну употребу дела. У односу на све остале лиценце, овом лиценцом се ограничава највећи обим права коришћења дела.

4. **Ауторство – некомерцијално – делити под истим условима**. Дозвољавате умножавање, дистрибуцију и јавно саопштавање дела, и прераде, ако се наведе име аутора на начин одређен од стране аутора или даваоца лиценце и ако се прерада дистрибуира под истом или сличном лиценцом. Ова лиценца не дозвољава комерцијалну употребу дела и прерада.

5. **Ауторство – без прерада**. Дозвољавате умножавање, дистрибуцију и јавно саопштавање дела, без промена, преобликовања или употребе дела у свом делу, ако се наведе име аутора на начин одређен од стране аутора или даваоца лиценце. Ова лиценца дозвољава комерцијалну употребу дела.

6. **Ауторство – делити под истим условима**. Дозвољавате умножавање, дистрибуцију и јавно саопштавање дела, и прераде, ако се наведе име аутора на начин одређен од стране аутора или даваоца лиценце и ако се прерада дистрибуира под истом или сличном лиценцом. Ова лиценца дозвољава комерцијалну употребу дела и прерада. Слична је софтверским лиценцама, односно лиценцама отвореног кода.